

THE AUSTRALIAN NATIONAL UNIVERSITY

DOCTORAL THESIS

Lattice-Boltzmann Modelling of
Immiscible Fluid Displacement
in Geologic Porous Media

Author:

Zhe LI

Supervisors:

Prof. Adrian P. SHEPPARD

Dr. James E. MCCLURE

Dr. Andrew M. KINGSTON

*A thesis submitted in fulfillment of the requirements
for the degree of Doctor of Philosophy*

in the

Department of Applied Mathematics
Research School of Physics

© Copyright by Zhe LI 2019
All Rights Reserved

Declaration of Authorship

I, Zhe LI, declare that this thesis titled, “Lattice-Boltzmann Modelling of Immiscible Fluid Displacement in Geologic Porous Media” and the work presented in it are my own. I confirm that:

- This work was done wholly or mainly while in candidature for a research degree at this University.
- Where any part of this thesis has previously been submitted for a degree or any other qualification at this University or any other institution, this has been clearly stated.
- Where I have consulted the published work of others, this is always clearly attributed.
- Where I have quoted from the work of others, the source is always given. With the exception of such quotations, this thesis is entirely my own work.
- I have acknowledged all main sources of help.
- Where the thesis is based on work done by myself jointly with others, I have made clear exactly what was done by others and what I have contributed myself.

Signed: 

Date: 13/08/2019

“A theory is all the more impressive the simpler its premises, the greater the variety of phenomena it describes, and the broader its area of application. This is the reason for the profound impression made on me by classical thermodynamics. It is the only general physical theory of which I am convinced that, within its regime of applicability, it will never be overturned (this is for the special attention of the skeptics in principle)”

Albert Einstein

Abstract

Over the past two decades, multicomponent lattice-Boltzmann (LB) modelling has become a popular numerical technique to study the porous medium systems. For this technique to become a mature platform at a production level and to solve realistic problem that can be readily incorporated in the digital core analysis services for the oil and gas industries, there are still some challenges to resolve. This thesis intends to resolve some of issues confronted by the LB community. The first part of the thesis investigates the impact of the fundamental trade-off between image resolution and field of view on LB modelling. This is of practical value since 3D images of geological samples rarely have both sufficient resolution to capture fine structure and sufficient field of view to capture a full representative elementary volume of the medium. To optimise the simulations, it is important to know the minimum number of grid points that LB methods require to deliver physically meaningful results, and allow for the sources of measurement uncertainty to be appropriately balanced. We choose two commonly used multicomponent LB models, Shan-Chen and Rothman-Keller models, and study the behaviour of these two models when the phase interfacial radius of curvature and the feature size of the medium approach the discrete unit size of the computational grid. Both simple, small-scale test geometries and real porous media are considered. Models' behaviour in the extreme discrete limit is classified ranging from gradual loss of accuracy to catastrophic numerical breakdown. Based on this study, we provide guidance for experimental data collection and how to apply the LB methods to accurately resolve physics of interest for two-fluid flow in porous media. Resolution effects are particularly relevant to the study of low-porosity systems, including fractured materials, when the typical pore width may only be a few voxels across. The second part of the thesis explores the two-fluid displacement mechanism, especially the Haines jump dynamics and associated snap-off during drainage, by using a novel flux boundary condition, which is numerically more stable, and can more realistically replicate experiments given a prescribed capillary number. Irreversible events such as Haines jump in multiphase flow is what ultimately determines the hysteric behaviour of the porous medium systems. The high temporal resolution of LB methods makes it a suitable candidate to capture the dynamics of fast events (e.g. Haines jump in millisecond). We study the impacts of both the geometries of porous medium using persistent homology and the dynamic factors of fluids (i.e. viscosity ratio and capillary number) on the occurrence and frequency of snap-off events during drainage.

Acknowledgements

First of all I would like to thank my supervisor Prof. Adrian Sheppard for his great guidance and support throughout my PhD project. Adrian, being reservoir of almost all kinds of knowledge, is unarguably the mentor who introduced me to the great world of computational physics, which I truly enjoyed for the past five years. From my first little CUDA lattice-Boltzmann code (full of bugs, for sure) to eventually working on a much more mature and sophisticated platform with my associate supervisor James McClure, Adrian witnessed that I constantly stumbled around but gradually got up the learning curve. I want to thank Adrian for his great patience when educating me from literally all aspects of computer science to those of fluid mechanics, and I am also grateful that no matter how late I send him an email with tough questions, Adrian always comes up with something constructive and responds to me even around midnight.

I would like to thank my associate supervisor James McClure for his generous support, insightful guidance and patient education. Since our first meet during AGU 2015 to the delightful three-month visit at Blacksburg, James already becomes a good friend, who is just about as sharp as he is nice and unassuming. I would also like to thank James and Katharine for their warm hospitality during my visit.

I also want to thank all other members in my supervisor penal: I am very grateful to Dr. Andrew Kingston, a very warm person, for his constant encouragement; I want to thank Dr. Trond Varslot for the helpful discussion on LBM in general and the related low-resolution study; and I want to thank Dr. Shane Latham for helping to give me some (program-wise) advice and to fix bugs in my LB code. Moreover, I want to thank Prof. Vincent Graig for the helpful guidance on the surface chemistry, bubble dissolution and some insights on the bubble snap-off. I want to thank Dr. Anna Herring, kayak queen on the water, for not only being an awesome office mate, but also teaching me a lot on the subsurface flow, and most importantly, during my first AGU conference, took me to the Chinatown San Francisco to have some Thai. I want to thank Dr. Mohammad Saadatfar for his encouragement which indeed cheered me up during my low. I also want to thank Mrs. Jill Middleton and Mr. Robert Middleton for their help on the software-related issues. I am lucky to pursue my study at the department of Applied Mathematics with the great folks around who do not hesitate to lend me help and give me advice, and my thanks go to Prof. Mark Knackstedt, Dr. Vanessa Robins, Dr. Michael Turner, Prof. David Williams, Dr. Andrew Fogden, Dr. Robert Sok, Dr. Glenn Myers, Mr. Paul Jan Veldkamp, Mr. Tim Sawkins and Prof. Tim Senden; and also to my good friends and fellow PhD candidates: Dr. Wilfred Fullager, Dr. Thomas Li, Muidh Alheshibri, Carl Yang, Dr. Qianhao Cheng, Hijaz Hasnan, Dr. Mahsa Paziresh, and Dr. Virginia Mazzini.

I would also like to thank other good friends at school of physics who make my past few years so colourful and enjoyable. I am so grateful to my earlier mentor and also supervisor during my Honours, Prof. Lan Fu from department of Electronic Materials

Engineering: it was really a pleasant year to work with you and I truly appreciate your education, support and numerous invaluable advice on my career; I would also like to thank Prof. Fu's husband, Zhenghua Li, a pragmatic all-time problem solver, for his kind help to me and my family. I also want to thank my Honours advisers Prof. Chennupati Jagadish and Prof. Hoe Tan for their great support. In addition, my thanks go to other folks at school: Bijun Zhao, Dr. Xin Chen, Naiyin Wang, Dr. Yujie Ma, Jaret Yu-Heng Lee, Dr. Crystal Chin-Hsing Tien, Prakash Prasai, Dr. Ziyuan Li, Dr. Qian Gao, Dr. Kun Peng, Dr. Xiaoming Yuan, Dr. Fan Wang, Dr. Nian Jiang, Prof. Jiandong Ye, Dr. Fangfang Ren, Dr. Li Li, Dr. Tim Burgess, Ian Y. Wenas, Dr. Fengling Xian, Dr. Guogang Zhang, Dr. Zhiqing Zhong, Dr. Yanan Guo, Dr. Shuai Li, Dr. Haofeng Lu, Yunshi Chen and Chongjie Yong; and to my good friends when studying at ANU: Gu'an Wang, Yu Hao, Dr. Guangyuan Gao, Angus Donohoo, Tianshu Liu, Sin-Yee Keoh, Ning Ma, Hongji Zhang, and Chao Jiang.

Lastly, I thank my family for their unconditional love and encouragement. To my parents Tianjun Li and Chengrui Wu for being the best parents who provide me with constant source of support throughout my life, and who always back me up to dream big and never letting me give up on those dreams, my grandmother Peiyu Zhang for her tremendous love and care since birth, and most of all, my loving and supportive wife Emma N. Yu, without whom I would not have held up this journey.

Contents

Declaration of Authorship	iii
Abstract	vii
Acknowledgements	ix
1 Introduction and Background	1
1.1 Background	1
1.2 Research Questions	3
1.3 Research Objectives	4
2 Background Theory of Lattice-Boltzmann Method	7
2.1 Fundamentals of Lattice-Boltzmann Methods	8
2.2 Unit Conversion in LBM	18
2.3 Single-Relaxation-Time Multiphase Lattice-Boltzmann Methods	20
2.3.1 Shan-Chen Model	21
2.3.2 Rothman-Keller Model	23
2.4 Multi-Relaxation-Time Multiphase Lattice-Boltzmann Methods	25
2.4.1 Momentum Transport with Surface Tension Force	25
2.4.2 Mass Transport with Phase Segregation	33
3 Discretisation Limits of Multicomponent LB Models	47
3.1 Introduction	47
3.2 Methodology	49
3.3 Bubble Test	50
3.4 Static Capillary Tube Test	57
3.4.1 Flat Tube Case	59
3.4.2 Tilted Tube Case	63
3.4.3 Correlation with Unit Conversion	69
3.5 Primary Drainage in Square Capillary Tubes	70
3.5.1 Effect of Phase Saturation	71
3.5.2 Effect of Pressure Boundary Condition	73
3.5.3 Effect of Various Radius Tube	75
3.5.4 Effect of Porous Barrier	78
3.5.5 Effect of Capillary Tube Size	81
3.6 Primary Drainage in Porous Medium	83

3.7	Conclusions	86
4	Wetting Boundary in Lattice-Boltzmann Models	91
4.1	Wetting Boundary in Shan-Chen Model	92
4.2	Wetting Boundary in Rothman-Keller Model	94
4.3	Consequence in Porous Media Simulation	96
4.4	Introduction to Geometric Formulation	100
4.5	Proposed Wetting Boundary for RK Model	106
5	Two-fluid Flow in Porous Medium and Haines Jump Dynamics	109
5.1	Methods	110
5.1.1	Non-unity Viscosity Test	110
5.1.2	Total Flux Boundary Condition	112
5.2	Influence of Interfacial Spurious Currents	116
5.2.1	Capillary Filling in Square Tube	118
5.2.2	Drainage in Square Tube	124
5.3	Influence of LB Temporal Resolution	133
5.4	Results and Discussion	135
5.4.1	Overview of All Cases	135
5.4.2	Drainage Displacement Patterns	143
5.4.3	Preliminary Study: Haines Jump Velocity	153
5.4.4	Preliminary Study: Impact of Medium Geometry	159
5.5	Conclusions and Future Work	163
6	Conclusion and Future Work	167
A	Methods of Measuring Interfacial Curvature	173
A.1	Surface Fitting Method	173
A.2	Level-set Method:	174
B	Challenge of Low-Resolution Contact Angle Measurement	175
C	Pressure Boundary Condition in Shan-Chen Model	177
D	Characterisation of Bentheimer Sandstone Sample	181
E	Effect of Resolution on Dissolved Non-wetting Phase	183
F	Mean Curvature Measured by Level-set Method	185
F.1	Bubble Test	185
F.2	Flat Tube Test	186
F.3	Tilted Tube Test	187
G	Breakdown Examples of Primary Drainage in Square Tube	189
H	Snap-off Events During Drainage	193

I Young-Laplace Relation for Drainage in Square Tube	201
Bibliography	203

List of Figures

3.1	The one-dimensional NW and W fluid density profiles extracted from the bubble test	53
3.2	The bubble test of Laplace's law, where the mean curvature is measured by the surface fitting method for SC and RK models	54
3.3	Component densities of NW and W phases in SC model as a function of capillary pressure for a water-oil system	56
3.4	The maximum spurious currents extracted from the bubble tests for SC and RK models	57
3.5	Two-dimensional density profiles of SC and RK models in the static flat tube test	60
3.6	The mean curvature versus capillary pressure for SC and RK models in static flat tube tests	61
3.7	Derived contact angle is plotted against model parameters for SC and RK models in flat tube test	63
3.8	The mean curvature-capillary pressure measurements of the tilted tube test for SC and RK models	64
3.9	Three-dimensional surface contour plots of the zero phase field at $\bar{R}_{\text{tilted}} = 1.44 \text{ l.u.}$ in the tilted tube test for SC and RK models	65
3.10	Three-dimensional surface contour plots of the non-wetting phase pressure profiles in the tilted tube test for SC and RK models	66
3.11	The mean curvature-capillary pressure measured for RK model in a tilted tube of $\bar{R}_{\text{tilted}} = 1.85 \text{ l.u.}$	67
3.12	The mean curvature measured from the flat tube and the tilted tube tests for SC and RK models	68
3.13	The derived contact angle of the tilted tube test is plotted against model parameters for SC and RK models	68
3.14	Set-up of the primary drainage test in a square capillary tube	70
3.15	Comparison of different calculating methods of S_w for the primary drainage test in a square tube	72
3.16	Primary drainage curves of the RK model with capillary pressure extracted from different locations for R_{tube} of 2, 3, and 4 l.u.	75
3.17	Schematic of the set-up of the special tube test with corresponding one-dimensional density profiles for SC and RK models	76
3.18	Relative deviation in the capillary pressure of SC and RK models for different R_{tube} with same surface tension	77

3.19	Relative deviation in the capillary pressure of SC and RK models for different surface tension with same R_{tube}	78
3.20	Snapshots of the non-physical NW phase leakage (through porous plate) of RK model in the square tube primary drainage test	80
3.21	Primary drainage curves at various R_{tube} for SC and RK models in square capillary tubes	82
3.22	Primary drainage simulation in a μ CT image of Bentheimer sandstone with constant pressure boundary condition	85
4.1	A two-dimensional schematic illustrating the fluid-solid boundary at the corner of a square capillary tube	92
4.2	Two-dimensional density profiles of dissolved NW phase in the bulk W phase extracted from the end of the capillary tube, at different wetting conditions for SC model	93
4.3	Illustration of the phase field near the corner of a square tube for RK model	94
4.4	Two-dimensional density profiles of dissolved NW phase in the bulk W phase extracted from the end of the capillary tube, at different wetting conditions for RK model	95
4.5	Two-dimensional pressure profiles at the centre and the end of the flat square tube for SC and RK models	96
4.6	The three-dimensional fluid configurations in primary drainage simulation of a Bentheimer sandstone sample using flux boundary conditions at different capillary numbers	98
4.7	A illustration of the growth of a non-physical non-wetting phase ganglion during the drainage process in the Bentheimer sandstone sample	99
4.8	Two-dimensional illustrations of the propagation of the transport of dissolved non-wetting phase along the solid surface in primary drainage simulation of a Bentheimer sandstone	100
4.9	Three-dimensional fluid configurations in drainage simulations in the Bentheimer sandstone with different contact angles and boundary conditions	101
4.10	Schematic of the wetting boundary condition of <i>Akai's method</i> based on geometric formulation	103
4.11	Illustration of the phase field near the corner of a square tube for RK model for old and proposed wetting boundary conditions	107
5.1	Schematic of three-dimensional two-fluid co-current flow through parallel plate	111
5.2	Velocity profiles along the central line ($x = 51$) in the central plane ($z = 51$) of three-dimensional parallel plate system	111
5.3	Velocity profiles for Poiseuille flow along the central line $y = 20 \text{ l.u.}$ at the middle plane of the square tube ($z = 40 \text{ l.u.}$)	113

5.4	The time rate change of the saturation (scaled by the pore volume of the media) in the primary drainage simulations in square tube and Bentheimer sandstone μ CT image	114
5.5	The cross-sectional view of the velocity field $u_z(x, y)$ at the inlet boundary of NWR in Bentheimer sandstone primary drainage simulation for the case of $Q_z^{\text{LB}} = 1.72 \text{ l.u.}^3/\text{l.t.}$	115
5.6	Schematic of the capillary filling in a square tube	118
5.7	The wetting phase saturation as a function of simulation time for the capillary filling in a square tube of $R_{\text{tube}} = 5 \text{ l.u.}$	119
5.8	Three-dimensional vector plot of the velocity field for the capillary filling process in a square tube, with the two-dimensional cross-sectional view of the magnitude of the velocity field at the central plane of the domain.	120
5.9	Two-dimensional cross-sectional view of the z -component of the velocity for the capillary filling in a square tube of $R_{\text{tube}} = 5.0 \text{ l.u.}$ at $\phi_s = -0.7$ for $\alpha = 10^{-2}$, together with the slice-by-slice averaged LB pressure field along the flow direction, and measured velocity components within each bulk phase compared to the theoretical Poiseuille profiles.	122
5.10	Two-dimensional cross-sectional view of the z -component of the velocity for the capillary filling in a square tube of $R_{\text{tube}} = 5.0 \text{ l.u.}$ at $\phi_s = -0.7$ for $\alpha = 10^{-4}$, together with the slice-by-slice averaged LB pressure field along the flow direction, and measured velocity components within each bulk phase compared to the theoretical Poiseuille profiles.	123
5.11	Young-Laplace test where the interfacial mean curvature is plotted against the phase pressure difference normalised by the LB surface tension, for the process of capillary filling in a square tube.	125
5.12	Three-dimensional vector plot of the velocity field for the drainage process in a square tube, with the two-dimensional cross-sectional view of the magnitude of the velocity field at the central plane of the domain, for the case of $R_{\text{tube}} = 5.0 \text{ l.u.}$ with $\phi_s = -0.7$ and prescribed global $Ca = 5 \times 10^{-4}$	126
5.13	Two-dimensional cross-sectional view of the z -component of the velocity for the drainage in a square tube of $R_{\text{tube}} = 5.0 \text{ l.u.}$ at $\phi_s = -0.7$ and prescribed global $Ca = 5 \times 10^{-4}$ for $\alpha = 10^{-2}$, together with the slice-by-slice averaged LB pressure field along the flow direction, and measured velocity components within each bulk phase compared to the theoretical Poiseuille profiles.	127

5.14	Two-dimensional cross-sectional view of the z -component of the velocity for the drainage in a square tube of $R_{\text{tube}} = 5.0 \text{ l.u.}$ at $\phi_s = -0.7$ and prescribed global $Ca = 5 \times 10^{-4}$ for $\alpha = 10^{-4}$, together with the slice-by-slice averaged LB pressure field along the flow direction, and measured velocity components within each bulk phase compared to the theoretical Poiseuille profiles.	128
5.15	Demonstration of the deviations from the theoretical Poiseuille profile for the drainage in a square tube at the largest prescribed global capillary number for $\alpha = 10^{-2}$	129
5.16	Young-Laplace test, where the interfacial mean curvature is plotted against the phase pressure difference normalised by the LB surface tension, for the process of drainage in a square tube.	131
5.17	Mean interfacial curvature as a function of instantaneous capillary number calculated from the evolution of the phase field	132
5.18	For prescribed global $Ca = 10^{-3}$: NW phase distributions during drainage with different LB surface tension parameter α but at the same physical time	134
5.19	For prescribed global $Ca = 10^{-3}$: NW phase distributions during drainage at same S_w for the equivalent physical system, but with different LB surface tension parameter α	136
5.20	For prescribed global $Ca = 10^{-4}$: NW phase distributions during drainage at same S_w for the equivalent physical system, but with different LB surface tension parameter α	137
5.21	Classification of drainage flow patterns based on the capillary number and viscosity ratio of the LB primary drainage simulations	140
5.22	Schematic illustration of the flow patterns based on the 2D micromodels	141
5.23	The end-states of 3D NW phase configurations of all cases with $\alpha = 10^{-2}$ when the most advanced NW phase front reaches the wetting phase reservoir.	142
5.24	The end-states of 3D NW phase configurations of all cases with $\alpha = 10^{-4}$ when the most advanced NW phase front reaches the wetting phase reservoir.	142
5.25	Capillary pressure-saturation relationships ($P_c/\gamma_{wn}-S_{nw}$) of primary drainage simulations in a Bentheimer sandstone sample, with the snap-off events being highlighted by different colours and symbols. Two cases of $\alpha = \{10^{-2}, 10^{-4}\}$ at viscosity ratio $M = 0.8$ and $Ca = 10^{-5}$ are shown.	143
5.26	Three-dimensional non-wetting fluid distributions of case 3 for $\alpha = \{10^{-2}, 10^{-4}\}$, at a series of non-wetting phase saturations.	144
5.27	Visualisation of Haines jumps during drainage from LB simulation in n-decane/water system	146

5.28	Capillary pressure-saturation relationships ($P_c/\gamma_{wn}-S_{nw}$) of primary drainage simulations in a Bentheimer sandstone μ CT image, with the snap-off events being highlighted by different colours and symbols . . .	147
5.29	Three-dimensional non-wetting fluid distributions of case 1, 2, 4 and 5 for $\alpha = 10^{-2}$, at non-wetting phase saturation of 0.026	148
5.30	Three-dimensional non-wetting fluid distributions of case 1, 2, 4 and 5 for $\alpha = 10^{-2}$, at non-wetting phase saturation of 0.123	148
5.31	Three-dimensional non-wetting fluid distributions of case 1, 2, 4 and 5 for $\alpha = 10^{-2}$, at non-wetting phase saturation of 0.197	149
5.32	Three-dimensional non-wetting fluid distributions of case 1, 2, 4 and 5 for $\alpha = 10^{-2}$, at non-wetting phase saturation of 0.273	149
5.33	Three-dimensional non-wetting fluid distributions of case 1, 2, 4 and 5 for $\alpha = 10^{-4}$, at non-wetting phase saturation of 0.026	150
5.34	Three-dimensional non-wetting fluid distributions of case 1, 2, 4 and 5 for $\alpha = 10^{-4}$, at non-wetting phase saturation of 0.123	150
5.35	Three-dimensional non-wetting fluid distributions of case 1, 2, 4 and 5 for $\alpha = 10^{-4}$, at non-wetting phase saturation of 0.197	151
5.36	Three-dimensional non-wetting fluid distributions of case 1, 2, 4 and 5 for $\alpha = 10^{-4}$, at non-wetting phase saturation of 0.273	151
5.37	2D Velocity field in physical units for case 3 of $\alpha = \{3.57 \times 10^{-2}, 10^{-4}\}$, with spurious velocity concentrated at entrance, non-wetting/wetting phase interface and non-wetting/solid interface.	154
5.38	Illustration of manual measurement of local interfacial velocity for Haines jumps followed by snap-off events	156
5.39	Local interfacial velocity of Haines jumps followed by snap-off events in $\alpha = 3.57 \times 10^{-2}$	157
5.40	Direct comparison between indirectly measured interfacial velocity and LB velocity field for a Haines jump of case 3 of $\alpha = 3.57 \times 10^{-3}$	158
5.41	Local interfacial velocity of Haines jumps followed by snap-off events in $\alpha = 10^{-4}$	160
5.42	Persistent homology diagram of β_0 topological feature in the LB sub-domain, with partitioned two-dimensional slices of μ CT image highlighting the labelled pore bodies in which the snap-off events for both α take place	162
B.1	Illustration of the challenge of manually measuring the contact angle at small tube size in the flat tube test	176
C.1	Component densities of NW and W phase in the SC model as a function of wetting parameter in a static flat tube test at R_{tube} of 1.5 and 3.0 <i>l.u.</i>	177
C.2	Primary drainage curves for SC model at the tube size $R_{\text{tube}} = \{1.5, 2.0\}$ <i>l.u.</i> , where the boundary conditions are extracted from the flat tube test of $R_{\text{tube}} = \{1.5, 2.0\}$	178

C.3	Primary drainage curves for SC model at the tube size $R_{\text{tube}} = 2.0$ $l.u.$, where the density components $\rho_{\text{nw,major}}$, $\rho_{\text{nw,minor}}$ and $\rho_{\text{w,major}}$ at the boundaries are extracted from the flat tube test of $R_{\text{tube}} = 1.5$ $l.u.$, and $\rho_{\text{w,minor}}$ is fixed at 0.0005	179
D.1	The Pore and throat size distributions of the sub-domain of 256 $l.u.$ ³ of the Bentheimer sandstone sample	181
E.1	The dissolved non-wetting phase density of RK model is plotted against the wetting boundary control parameter for different tube sizes	184
F.1	The bubble test of Laplace's law, where the mean curvature is measured by the level-set method for SC and RK models	186
F.2	The mean curvature versus capillary pressure for SC and RK models in static flat tube tests measured by the surface fitting and level-set methods	187
F.3	The mean curvature versus capillary pressure for SC and RK models in static tilted tube tests measured by the surface fitting and level-set methods	188
G.1	Screen-shots of a breakdown process for SC model where the invading non-wetting phase snaps off after the entry in a primary drainage in square capillary tube	190
G.2	Screen-shots of a breakdown process for RK model where the invading non-wetting phase leaks through the porous plate after the entry in a primary drainage in square capillary tube	191
H.1	Visualisation of snap-off process for LB primary drainage simulation with snap-off event identifier 1/(5; 8)/752	194
H.2	Visualisation of snap-off process for LB primary drainage simulation with snap-off event identifier 1/(5; 49; 55)/752	195
H.3	Visualisation of snap-off process for LB primary drainage simulation with snap-off event identifier 1/(5; 49; 55)/752	195
H.4	Visualisation of snap-off process for LB primary drainage simulation with snap-off event identifier 3/(5; 8)/752	196
H.5	Visualisation of snap-off process for LB primary drainage simulation with snap-off event identifier 4/(15; 16)/709	196
H.6	Visualisation of snap-off process for LB primary drainage simulation with snap-off event identifier 4/8/752	197
H.7	Visualisation of snap-off process for LB primary drainage simulation with snap-off event identifier 5/2/627	198
H.8	Visualisation of snap-off process for LB primary drainage simulation with snap-off event identifier 5/(15; 16)/646	199

H.9	Visualisation of the consecutive snap-off/reconnection cycle for LB primary drainage simulation with snap-off event identifier 5/(15; 16)/646	200
I.1	Interfacial mean curvature measured by the surface fitting method is plotted against the phase pressure difference normalised by the LB surface tension, for the process of capillary filling in a square tube.	201
I.2	Interfacial mean curvature measured by the surface fitting method is plotted against the phase pressure difference normalised by the LB surface tension, for the process of drainage in a square tube.	202

List of Tables

2.1	Summary of Units in Lattice-Boltzmann Method	18
3.1	Numerical Behaviours of Multicomponent Lattice-Boltzmann Models .	50
3.2	Major Parameters in Bubble Test	51
3.3	Major Parameters in Flat/Tilted Tube Tests	59
3.4	Summary of Breakdown Due to Size of Porous Plate	79
5.1	Simulation Parameters of Primary Drainage for Haines Jumps and Snap-off Study with $\alpha = 3.57 \times 10^{-2}$	139
5.2	Simulation Parameters of Primary Drainage for Haines Jumps and Snap-off Study with $\alpha = 10^{-4}$	140

List of Abbreviations

BC	B oundary C ondition
BGK	B hatnagar- G ross- K rook (collision approximation)
BTE	B oltzmann T ransport E quation
CE	C hapman E nskog (analysis)
CT	C omputer T omography
GPGPU	G eneral P urpose G raphical P rocessing U nit
LBM	L attice B oltzmann M ethod (or M odel)
LGA	L attice G as A utomata
MRT	M ultiple R elaxation T ime
NSE	N avier- S okes E quation
NW	N on- W etting (phase)
NWR	N on- W etting phase R eservoir
PD	P rimary D rainage
RK	R othman- K eller (lattice-Boltzmann model)
SC	S han- C hen (lattice-Boltzmann model)
SRT	S ingle R elaxation T ime
TRT	T wo- R elaxation- T ime (collision)
W	W etting (phase)
WR	W etting phase R eservoir

List of Symbols

$\mathbf{a}^{(n)}$	expansion coefficient of rank- n Hermite polynomials	[-]
A_k	surface tension strength coefficient for SRT-RK model	[-]
$c_{s,p}$	physical speed of sound of fluid	m/s
$c_{s,LB}$	LB speed of sound of fluid	$l.u./l.t.$
f_i^k	LB single-particle distribution of velocity ξ_i for k_{th} fluid component	$kg/l.u.^3$
$f_i^{k,eq}$	LB equilibrium distribution function of ξ_i for k_{th} fluid	$kg/l.u.^3$
f_{LB}	LB continuum single-particle distribution	$kg/l.u.^3$
f_p	single-particle distribution function in physical unit	$kg \cdot s^3/m^6$
f_p^{eq}	equilibrium single-particle distribution function in physical unit	$kg \cdot s^3/m^6$
\mathbf{F}_k	total LB body force in SRT-SC model	$kg \ l.u./l.t.^2$
\mathbf{F}_k^{coh}	LB cohesive force in SRT-SC model	$kg \ l.u./l.t.^2$
\mathbf{F}_k^{ads}	LB adhesive force in SRT-SC model	$kg \ l.u./l.t.^2$
\mathbf{g}	body acceleration rate in physical unit	m/s^2
\mathbf{g}_k	LB body acceleration rate for k_{th} fluid	$l.u./l.t.^2$
\mathbf{G}	colour-gradient for SRT-RK model	$l.u.^{-1}$
G_{coh}	LB cohesion coefficient in SRT-SC model	[-]
$G_{ads, k}$	LB adhesion coefficient for k_{th} fluid in SRT-SC model	[-]
h	μ CT image resolution	$\mu m/l.u.$
$\mathcal{H}^{(n)}$	rank- n Hermite polynomial	[-]
\mathbb{I}	Identity matrix	[-]
m_p	molecular mass of fluid in physical unit	kg
m_{LB}	molecular mass of fluid in LB system	kg
m_0	physical-to-LB scaling factor for molecular mass	[-]
n_0	physical-to-LB scaling factor for number density	[-]
n_p	number density of fluid in physical unit	m^{-3}
n_{LB}	number density of fluid in LB unit	$l.u.^{-3}$
\mathbf{n}	unit normal vector of colour gradient	[-]
P_c	capillary pressure	Pa
P_{LB}	pressure in LB unit	$kg/l.u./l.t.^2$
\mathbb{P}_{LB}	LB momentum flux tensor	$kg/l.u./l.t.^2$
S_{nw}	non-wetting phase saturation	[-]
S_w	wetting phase saturation	[-]
$S_{\alpha\beta}$	capillary pressure tensor	$kg/l.u./l.t.^2$
t_p	time in physical unit	s
t_{LB}	time in LB unit	$l.t.$

t_i	LB lattice weighting coefficient for i_{th} velocity	[-]
\mathbf{u}_p	macroscopic fluid velocity in physical unit	m/s
\mathbf{u}_{LB}	macroscopic fluid velocity in LB unit	$l.u./l.t.$
\mathbf{v}_{LB}	general velocity in LB unit	$l.u./l.t.$
\mathbf{x}_p	space vector in physical unit	m
\mathbf{x}_{LB}	space vector in LB unit	$l.u.$
α	surface tension parameter in SRT-/MRT-RK model	[-]
β	interface parameter in SRT-/MRT-RK model	[-]
γ_{wn}	fluid-fluid interfacial tension	N m^{-1}
γ_{LB}	surface tension in LB unit	$\text{kg}/l.t.^2$
δt	LB iteration time step	$l.t.$
δt_p	physical-to-LB time conversion factor	$s/l.t.$
$\delta \rho$	density variation for MRT-RK model	kg
δp	pressure variation for MRT-RK model	$\text{kg}/l.u./l.t.^2$
$\delta_{\alpha\beta}$	Kronecker delta	[-]
ϵ	smallness parameter for Chapman-Enskog analysis	[-]
ζ_{LB}	LB kinematic bulk viscosity	$\text{kg}/l.u./l.t.^2$
κ_H	mean curvature in LB unit	$l.u.^{-1}$
ν_{LB}	LB kinematic viscosity	$l.u.^2/l.t.$
ξ_p	continuum velocity in physical unit	m/s
$\xi_{i,LB}$	discretised i_{th} velocity in LB unit	$l.u./l.t.$
ρ_{LB}	fluid density in LB system	kg
$\sigma_{\alpha\beta}$	viscous stress tensor	$\text{kg}/l.u./l.t.^2$
τ_i	LB relaxation time of i_{th} moment	$l.t.$
τ_p	continuum relaxation time in physical unit	s
τ_{LB}	LB continuum relaxation time	$l.t.$
φ_i	angle between colour gradient and ξ_i for SRT-RK model	[-]
ϕ	phase field for MRT-RK model	[-]
ϕ_s	fluid-solid phase field parameter for MRT-RK model	[-]
Φ	phase field for SRT-RK model	[-]
$\omega(\xi)$	weight function of velocity ξ for Hermite polynomials	[-]
Ω_i^k	LB collision operator of velocity ξ_i for k_{th} fluid component	$\text{kg}/l.u.^3$

Dedicated to my parents

Chapter 1

Introduction and Background

1.1 Background

Immiscible two-phase fluid flows in complex porous media are ubiquitous in nature and industrial applications, and underlay the transport of groundwater, enhanced oil and gas recovery, the chemical contaminant spreading in the vadose zone, and carbon dioxide (CO₂) sequestration, to name but a few. The phase distributions during flow depend on the intrinsic pore space structure, on the wettability of the solid phase, and on the external forcing. For the subsurface flow in particular, the interplay of three major forces, gravity, capillary, and viscous forces, gives rise to a wide range of macroscopic displacement patterns, which can be classified typically in phase diagrams of flow regimes (Lenormand, Touboul, and Zarcone, 1988; Zhang et al., 2011), or more recently, be characterised based on the Minkowski functionals (Schlüter et al., 2016; Herring et al., 2018; McClure et al., 2018). Understanding the physical fundamentals that govern the various displacement patterns is critical for the practical industrial applications since different flow processes can then be engineered to suit different needs, such as enhanced oil recovery or maximised carbon dioxide storage. Such study via various experiment techniques can be very expensive as it requires very specialised laboratory equipment, and also time-consuming, e.g. acquisition of the drilled core samples usually takes 0.5~1 year, and a full special core analysis may take another year for applications in oil industries (Alpak, Berg, and Zacharoudiou, 2018).

On the other hand, the modelling and associated simulations of immiscible multiphase fluid flows in porous media have also been extensively explored over the past three decades. The advent of X-ray micro-tomography (μ CT) imaging, a non-destructive 3D microscopy technique enables the full micro-structure of porous materials to be imaged with very high fidelity from the micron to the centimetre scales (Wildenschild and Sheppard, 2013). This is possible at both laboratory instruments and at synchrotron beam-lines; at the latter, it is now possible to capture the dynamics of fluid transport within the porous micro-structure at a time resolution of better than one second (Berg et al., 2013; Lovric et al., 2016). Even at laboratory facilities, both the rock micro-structure and the fluid distributions can be imaged with sufficient clarity to measure fluid-fluid interfacial curvatures and contact angles (Armstrong, Porter, and Wildenschild, 2012; Andrew, Bijeljic, and Blunt, 2014). As

a consequence of these recent enormous increases in imaging capabilities and even more striking advances in computational capabilities (further accelerated since 2005 through general purpose graphical processing unit (GPGPU) computing), direct numerical simulation of multi-fluid transport can be carried out with sufficient resolution and accuracy, and can be validated against some experiment (e.g. (Armstrong et al., 2016)).

However direct numerical simulation in complex heterogeneous geologic materials presents numerous challenges, particularly when one considers the difficulty of solving the underlying Navier-Stokes equations. Various modelling techniques have therefore been applied to the study of flow in porous materials, ranging from the conventional fluid dynamics methods (e.g. the volume-of-fluid method (Gueyffier et al., 1999; Pilliod and Puckett, 2004) and the level-set method (Osher and Sethian, 1988; Osher and Fedkiw, 2003; Prodanovic and Bryant, 2006) to the percolation-based pore-scale network models (Pereira et al., 1996; Bakke and Øren, 1997; Knackstedt, Sheppard, and Sahimi, 2001; Blunt, 2001; Caubit et al., 2009; Blunt et al., 2013)) and the phase-field method (Jacqmin, 1999; Yue et al., 2004). The most popular approach, however, is the lattice-Boltzmann (LB) method, whose most pronounced capability is to almost immediately deal with μ CT data sets, whereas other above-mentioned methods generally need pre-processing such as meshing of boundaries between solid and pore. Several review articles on single-/multiphase LB methods can be found, for example in Benzi, Succi, and Vergassola (1992), Chen and Doolen (1998), Lallemand and Luo (2000), Aidun and Clausen (2010), Chen et al. (2014), and Liu et al. (2016). LB methods are advantageous for solving multicomponent fluid flows in porous media with complex boundary conditions, and straightforward to implement in a scalable parallel manner (e.g. numerous works done on the parallel CPU: (Hou et al., 1995; Amati, Succi, and Piva, 1997; Kandhai et al., 1998; Krafczyk et al., 1998; Pohl et al., 2004; Pan, Prins, and Miller, 2004; Chopard et al., 2010)), particularly on GPU hardware (Tölke and Krafczyk, 2008; Bernaschi et al., 2010; Habich et al., 2011; Obrecht et al., 2013; Januszewski and Kostur, 2014; McClure, Prins, and Miller, 2014; Alpak et al., 2018).

Over the past two decades, there has been a large body of work on applying multiphase LB models in porous media. For example, Martys and Chen (1996) implemented a Shan-Chen (SC) multicomponent LB model to perform drainage and imbibition in the μ CT image of a Fontainebleau sandstone, and determined the relative permeability curves favourably with the experimental data; Schaap et al. (2007) also applied Shan-Chen multicomponent LB model to observed computed μ CT data from water-air and water-Soltrol displacement experiments in a glass bead porous system, from which a good agreement between simulated and observed water-air pressure-saturation characteristics was found. More works on using Shan-Chen-type multiphase LB models can be found for example in Pan, Hilpert, and Miller (2004), Sukop and Or (2004), Li, Pan, and Miller (2005), Harting et al. (2005), Sukop et al. (2008), Porter, Schaap, and

Wildenschild (2009), and Parmigiani et al. (2011). Tölke et al. (2002) have successfully applied Rothman-Keller-type multicomponent LB model to the water-air flow in a waste-water batch reactor and the saturation hysteresis effect in soil flow, and obtained qualitative agreement compared to the experiment. Additional work that relies on Rothman-Keller-type LB models can be found for example in Vogel et al. (2005), Ahrenholz et al. (2008), Ramstad, Øren, and Bakke (2010), Liu et al. (2014b), Liu, Zhang, and Valocchi (2015), and McClure et al. (2016). The free-energy based multicomponent LB models have also been under extensive research on exploring the displacement patterns and the potential prediction of relative permeability, such as the work by Zacharoudiou and Boek (2016), Zacharoudiou et al. (2017), Zacharoudiou, Boek, and Crawshaw (2018), and Alpak, Berg, and Zacharoudiou (2018).

1.2 Research Questions

Despite much progress, the most critical question that still remains open for debate is whether the multiphase lattice-Boltzmann modelling can give accurate and reliable pore-scale results; in other words, can it serve as an alternative and robust technique, and provide parallel insight compared to laboratory core analysis. To be more specific, we expand this critical question into several concrete sub-questions, to exemplify the requirement of accuracy and reliability:

- can LB model replicate the experimental boundary conditions to mimic the drainage and imbibition processes accurately and be numerically stable ?
- what is the consequence and how accurate would be the simulation results, if using different sets of LB parameters to match the same physical conditions, i.e. both the (experimental) boundary pumping rates and the fluid properties (e.g. interfacial tension and viscosity). This question is raised because, in practice, it always involves a trade-off between the computation time and the size of domain. Different sets of LB parameters can lead to different LB temporal resolution (i.e. physical time per LB iteration), thus different simulation time, given the same physical condition being matched, and this has a significant impact on the computation efficiency.
- the question above naturally leads to a more concrete issue: what is the impact of different LB temporal resolution on the ultimate simulated flow patterns and fluid distributions, especially for the fast pore-scale phenomena such as Haines jumps and snap-off, for which the current experimental techniques have difficulty in fully capturing the detailed dynamics (mainly due to the CT acquisition time).
- given the ‘notorious’ interfacial spurious velocity in all of the current multicomponent LB models, which is a long-standing unresolved problem despite numerous research attempting to eliminate such velocity, how is the interface movement affected by the spurious velocity and can LB modelling still capture the right physics ?

Besides the important questions above, another pragmatic question needs to be answered before the LB methods can be qualified as a robust numerical tool is how well LBM can cope with the low-resolution μ CT images. This is also critical because 3D images of geological samples are invariably a compromise between resolution and field of view, and if we want to better characterise the multiphase system (porous media plus fluids) to include more heterogeneity, simulations with lower image resolution could be the easiest and most straightforward approach. An μ CT image with coarsened resolution by a factor of 2, corresponds to a shrinkage of total simulation domain by a factor of 8, which would save thousands of hours of computation time¹. Therefore, it is of importance for researchers to be aware whether the image resolution coarsening will render the LB simulation results erroneous and possibly meaningless.

1.3 Research Objectives

The research presented here attempts to answer the important questions listed above to advance our understanding of multiphase lattice-Boltzmann modelling in practical applications. The specific objectives of this work are as follows, which also correspond to the sequence from Chapter 3 to 5:

1. Study the fundamentals of multicomponent LB models in terms of computational efficiency at low-resolution limits. The investigation is exclusively focused on the capillary-dominated flow in porous media. This objective is accomplished in Chapter 3:
 - to implement a variety of small-scale, simple-geometry, both static and dynamic tests, using either periodic or constant-pressure boundary condition with SC and RK models;
 - to develop testing cases at low resolution limits to illustrate problems in the traditional LB models, which can also be used as benchmark study for any novel LB models;
 - to characterise two models' different breakdown behaviours ranging from gradual loss of accuracy to catastrophic numerical instability at the resolution limit; and
 - to conclude both qualitatively and quantitatively the consequences of the models' breakdown behaviour and to discuss the ramifications for larger-scale simulations of fluid displacements in porous media.
2. Following the first objective, the influence of the wetting boundary condition (independent of resolution) is studied separately in Chapter 4. The consequence of implementing the widely used surface-energy-type wettability model

¹Such μ CT image coarsening may involve some complicated segmentation rules, and whether a voxel after coarsening becomes a fluid or solid node will depend on the specific image processing techniques; an alternative approach is to implement a greyscale lattice-Boltzmann method (e.g. Pereira (2016)) for images with unresolved regions.

in drainage simulation in a Bentheimer sandstone μ CT image has been explored. A new energy-based wettability model (still preliminary) is proposed to potentially overcome the breakdown caused by the existing model, but future work is needed to validate the proposed model.

3. Investigate the influence of the spurious velocity (present at fluid-fluid and fluid-solid interfaces) on the interfacial movement, using the state-of-the-art multi-relaxation-time colour-gradient based multicomponent model. Both drainage and imbibition processes have been studied, and the associated error is quantitatively analysed.
4. Explore the influence of temporal resolution of LB models on the flow patterns and fluid distributions, by using different sets of LB surface tension parameters, but still mapping to the equivalent macroscopic physical system (i.e. characterised by same dimensionless fluid mechanic number such as Reynolds number, capillary number and viscosity ratio).
5. Perform a series of drainage simulations under various reservoir conditions to study the Haines jump dynamics and snap-off which is caused by some of Haines jumps. The interfacial velocity profiles of the Haines jumps that lead to snap-off are measured, and the correlation of the peak jump velocity to the invading/defending fluid properties is discussed qualitatively. We characterise the snap-off events according to the pore body filled by the snapped-off ganglion and the throat where the invading phase breaks, by a novel geometry-topology analysis via persistent homology, and we summarise some geometric signatures shared by the frequent snap-off sites. The objective of this work is accomplished in Chapter 5.

Chapter 2

Background Theory of Lattice-Boltzmann Method

Fluid flow is simply a branch of transport phenomena in our everyday life, which can be described in general by the transport theory. A transport process involves temporal and spatial evolution of large amount of particles in certain medium, thus the physical foundation of the transport theory is statistical mechanics. When a system is in equilibrium, the motion of individual particles does not change the macroscopic state of the system. Therefore, the study of transport theory is within the regime of non-equilibrium statistical mechanics. More specifically, the study of transport theory can be loosely categorised into three levels: *microscopic*, *mesoscopic*, and *macroscopic* levels (Huang and Ding, 2008). In the context of this thesis which aims at solving the fluid flow problems, the governing equations at these three levels are the *Liouville equation*, the *Boltzmann transport equation* (BTE), and the *Navier-Stokes equation* (NSE), respectively (Groot and Mazur, 1984; Huang, 1987; Kardar, 2007).

On the microscopic level of description, the acquisition of the Liouville equation starts from the fundamental classical equations of motion, i.e. Hamiltonian mechanics. It is an equation of the phase density, and states that the phase density behaves like an incompressible fluid (Kardar, 2007), where the phase space for a system of N weakly-coupled particles, is a $6N$ -dimensional space consisting of $3N$ spatial coordinates and $3N$ momentum components, and a point in such phase space indicates a microstate of the system. Going from the Hamiltonian canonical equations to the Liouville equation, it is the starting point of the statistical mechanics; however, the full phase space density, for which the Liouville equation is solved for, still contains much more information than necessary for description of equilibrium properties of the system. The Liouville equation can be reduced to the Boltzmann transport equation by an iterative mathematical treatment, which is called BBGKY hierarchy of equations; this reduction process migrates the microscopic description to the mesoscopic description, and involves a set of approximations. The above ‘workflow’ is well within the regime of classical statistical mechanics which can be found in many standard textbooks, such as Huang (1987) and Kardar (2007), or in the relevant monographs (Harris, 2004; Cercignani, 1988), to name but a few.

On the macroscopic level of description, the Navier-Stokes equation describes the

motion of viscous fluid substance, which arises from applying Newton's second law to fluid motion. Since both Boltzmann transport equation and Navier-Stokes equation can be used to describe the same system, it leads naturally to the question of what the correlation is between the two descriptions. The Chapman-Enskog analysis bridges the theoretical gap between the two, and provides an effective way of correlating the macroscopic transport coefficient (e.g. viscosity) in NSE to the molecular counterparts described in BTE, and in fact, it can be shown that NSE can be recovered by performing the Chapman-Enskog analysis on BTE, subject to a series of approximations (Chapman, Burnett, and Cowling, 1970).

The Lattice-Boltzmann method (LBM) comes into place as a special discretised form of BTE, therefore LBM is also a mesoscopic approach of modelling viscous fluid flow. More details on the historical aspect of LBM can be found in the following sub-section. The rest of this chapter is arranged as follows: first, the discretisation of BTE into LBM is introduced; since BTE is usually in the physical units and LBM is in the so-called lattice-Boltzmann units, we integrate the discussion of physical unit mapping and mathematical discretisation together; then two major branches of LBM, i.e. single-relaxation-time (SRT) and multi-relaxation-time (MRT) LB models are introduced, and for the latter branch, how NS equation can be recovered from LB equation via Chapman-Enskog analysis is discussed in detail.

2.1 Fundamentals of Lattice-Boltzmann Methods

Overview

In this section, the fundamental theory of the lattice-Boltzmann method (LBM) is introduced. It is now known that LBM is a special discretised form of the Boltzmann transport equation (He and Luo, 1997). Historically, however, it originates from the lattice gas automata (LGA) method (Frisch, Hasslacher, and Pomeau, 1986; Wolfram, 1986), which simulates the behaviour of interactions of many single particles by a set of simple rules on a lattice grid. For each time step of the simulation, those particles perform consecutive "collision" and "advection" steps over discrete lattice mesh. While the LGA has shown potential for simulating multiphase fluid flow (Rothman and Keller, 1988; Rothman, 1988), it has been criticised due to its lack of Galilean invariance and its large statistical noise. LBM is proposed to overcome these limitations. Rather than modelling individual particles, it considers a particle distribution function $f_i^k(\mathbf{x}, t)$, which is governed by the lattice Boltzmann equation

$$f_i^k(\mathbf{x} + \boldsymbol{\xi}_i \delta_t, t + \delta_t) - f_i^k(\mathbf{x}, t) = \Omega_i^k(\mathbf{x}, t), \quad (2.1)$$

where $f_i^k(\mathbf{x}, t)$, in a multicomponent system, represents the probability to find the k_{th} fluid component at location \mathbf{x} and time t , moving in the direction corresponding to $\boldsymbol{\xi}_i$. δ_t is the discrete lattice time step, and $\Omega_i^k(\mathbf{x}, t)$ is the collision operator for the k_{th} fluid that transfers momentum between components of the lattice velocity vectors.

The velocity vector is discretised into a set of lattice velocity vectors $\boldsymbol{\xi}_i$. In this work, we implement the D3Q19 lattice model that corresponds to a three-dimensional lattice with 19 velocity vectors $\boldsymbol{\xi}_i$, $i = 0, 1, \dots, 18$ (Qian, d'Humières, and Lallemand, 1992). The choice of different number of discretised velocity sets is of course a trade-off between the model accuracy and the computation load, and there are many other available lattice structures, such as D2Q9, D3Q13, D3Q15, and D3Q27 (d'Humières, Lallemand, and Frisch, 1986; Qian, d'Humières, and Lallemand, 1992; Chen et al., 1992; d'Humières, Bouzidi, and Lallemand, 2001).

The most commonly used collision operator in the LB methods is based on the BGK approximation (Bhatnagar, Gross, and Krook, 1954; Qian, d'Humières, and Lallemand, 1992; d'Humières, 1992), for which the process of the non-equilibrium distribution evolving towards the local equilibrium state is characterised by a set of relaxation time parameter τ_i for each f_i^k . This naturally gives the so-called multiple-relaxation-time model with each τ_i being set individually, whereas in the single-relaxation-time model a single value is assigned to all τ_i .

For the rest of the section, we present a detailed account of the derivation of the lattice-Boltzmann equation 2.1 from the continuum Boltzmann transport equation, primarily based on the theoretical framework proposed by Shan, Yuan, and Chen (2006). Shan *et al.* formalised the framework by developing a systematic discretisation procedure of the continuum Boltzmann-BGK equation, to obtain the Navier-Stokes hydrodynamics and those beyond. We adapt the framework by incorporating the physical-to-LB unit conversion scheme to make it more self-consistent from a pragmatic perspective. In the following section 2.2, a practical procedure of setting up LB parameters to match certain experimental conditions is then introduced.

Derivation

In the three-dimensional space, we consider \mathbf{x} as the Cartesian coordinates and $\boldsymbol{\xi}$ as the coordinates in the velocity space. The continuum Boltzmann-BGK equation which determines the evolution of the single-particle distribution function $f_p(\mathbf{x}_p, \boldsymbol{\xi}_p, t_p)$ is given as:

$$\partial_{t_p} f_p + \boldsymbol{\xi}_p \cdot \nabla_p f_p + \mathbf{g} \cdot \nabla_{\boldsymbol{\xi}_p} f_p = -\frac{1}{\tau_p} [f_p - f_p^{eq}], \quad (2.2)$$

where the subscript ' p ' denotes that the quantity is in the physical unit, ∇_p is the spatial gradient, $\nabla_{\boldsymbol{\xi}_p}$ is the gradient in the velocity space, \mathbf{g} is the acceleration due to the body forces, and τ_p characterises the relaxation time of the collisions to equilibrium. For the following derivation, the body force will be neglected for simplicity. f_p^{eq} represents the local equilibrium distribution, i.e. so-called Maxwell-Boltzmann distribution, which is given by:

$$f_p^{eq} = m_p n_p \left(\frac{1}{2\pi c_{s,p}^2} \right)^{\frac{D}{2}} \exp \left[-\frac{(\boldsymbol{\xi}_p - \mathbf{u}_p)^2}{2c_{s,p}^2} \right], \quad (2.3)$$

where D is the dimension of the domain, m_p is the molecular mass of fluid particle, n_p is the number density, \mathbf{u}_p is the macroscopic fluid velocity, and $c_{s,p}$ is the speed of sound in the fluid. In practice, to perform LB simulation, one is usually given a set of μ CT images of rock samples as the simulation domain. One of the most important property of a μ CT image is the resolution h , for instance, in $\mu\text{m}/l.u.$, where $l.u.$ is short for *lattice unit*, which is the basic spatial unit in LB simulations. The two fundamental relations between the physical spatial coordinates and physical time scale and their counterparts in LB units are:

$$\mathbf{x}_p = h\mathbf{x}_{LB}, \quad (2.4a)$$

$$t_p = \frac{\delta t_p}{\sqrt{3}}t_{LB}, \quad (2.4b)$$

where \mathbf{x}_{LB} is in $l.u.$, t_{LB} is in *lattice time* ($l.t.$), i.e. the iteration step in LB simulations, and δt_p is the time converting factor in $s/l.t.$. The factor of $\sqrt{3}$ in the time relation is a consequence of projecting the regular LB lattice onto the Hermite basis when discretising the continuum Boltzmann equation, which will become more clear later.

Given the relations in equation 2.4, the coordinate of the velocity space and the macroscopic velocity in physical units can be related to their LB counterparts as:

$$\boldsymbol{\xi}_p = \frac{h}{\delta t_p}\sqrt{3}\boldsymbol{\xi}_{LB}, \quad (2.5a)$$

$$\mathbf{u}_p = \frac{h}{\delta t_p}\sqrt{3}\mathbf{u}_{LB}, \quad (2.5b)$$

where the macroscopic velocity in LB unit \mathbf{u}_{LB} is always given by $\mathbf{u}_{LB} = \mathbf{x}_{LB}/t_{LB}$. Based on the fundamental unit conversion relation, the equilibrium distribution function in physical unit can be expressed in terms of its LB counterpart as:

$$\begin{aligned} f_p^{eq}(\mathbf{x}_p, \boldsymbol{\xi}_p, t_p) &= m_p n_p \left(\frac{1}{2\pi c_{s,p}^2} \right)^{\frac{D}{2}} \exp \left[-\frac{(\boldsymbol{\xi}_p - \mathbf{u}_p)^2}{2c_{s,p}^2} \right] \\ &= m_0 m_{LB} \frac{n_0}{h^D} n_{LB} \left[\frac{1}{2\pi (\sqrt{3}c_{s,LB})^2} \right]^{\frac{D}{2}} \left(\frac{\delta t_p}{h} \right)^D \exp \left[-\frac{(\sqrt{3}\boldsymbol{\xi}_{LB} - \sqrt{3}\mathbf{u}_{LB})^2}{2 \times (\sqrt{3}c_{s,LB})^2} \right] \\ &= m_0 n_0 \frac{\delta t_p^D}{h^{2D}} f_{LB}^{eq}(\mathbf{x}_{LB}, \sqrt{3}\boldsymbol{\xi}_{LB}, t_{LB}), \end{aligned} \quad (2.6)$$

where the equilibrium distribution function in LB unit is given by:

$$\begin{aligned}
 f_{LB}^{eq}(\mathbf{x}_{LB}, \sqrt{3}\boldsymbol{\xi}_{LB}, t_{LB}) &= m_{LB} n_{LB} \left[\frac{1}{2\pi (\sqrt{3}c_{s, LB})^2} \right]^{\frac{D}{2}} \exp \left[-\frac{(\sqrt{3}\boldsymbol{\xi}_{LB} - \sqrt{3}\mathbf{u}_{LB})^2}{2 \times (\sqrt{3}c_{s, LB})^2} \right] \\
 &= \left(\frac{1}{\sqrt{3}} \right)^D m_{LB} n_{LB} \left(\frac{1}{2\pi c_{s, LB}^2} \right)^{\frac{D}{2}} \exp \left[-\frac{(\boldsymbol{\xi}_{LB} - \mathbf{u}_{LB})^2}{2c_{s, LB}^2} \right] \\
 &= \left(\frac{1}{\sqrt{3}} \right)^D f_{LB}^{eq}(\mathbf{x}_{LB}, \boldsymbol{\xi}_{LB}, t_{LB}).
 \end{aligned} \tag{2.7}$$

The molecular mass m_p is related to its LB counterpart by $m_p = m_0 m_{LB}$, where m_0 is a dimensionless scaling factor, and m_{LB} is usually taken as 1.0 kg. Similarly, the number density in physical unit is related to its LB counterpart by $n_p = \frac{n_0}{h^D} n_{LB}$, where n_0 is another dimensionless scaling constant. The LB speed of sound is given by $c_{s, p} = \sqrt{3}h/\delta t_p c_{s, LB}$. However, according to the LB literature, the LB speed of sound is simply $1/\sqrt{3}$ l.u./l.t. for commonly used LB lattice structures such as D2Q9 and D3Q19. This apparently does not make any physical sense, since $c_{s, p}$ is likely to not resemble any of actual physical systems given that the image resolution is a completely independent quantity. Therefore, Nourgaliev et al. (2003) called $c_{s, LB}$ the “pseudo-sound-speed” to reflect the inherent artificiality in the LB models. Likewise, the LB mean collision time τ_{LB} in equation 2.9 also carries an artificial meaning. In the later part of the section it will be shown why $c_{s, LB}$ must be $1/\sqrt{3}$ l.u./l.t..

Overall, the conversion of the distribution function between physical and LB units are given as:

$$\begin{aligned}
 f_p(\mathbf{x}_p, \boldsymbol{\xi}_p, t_p) &= \frac{m_0 n_0 \delta t_p^D}{h^{2D}} f_{LB}(\mathbf{x}_{LB}, \sqrt{3}\boldsymbol{\xi}_{LB}, t_{LB}) \\
 &= \frac{m_0 n_0 \delta t_p^D}{(\sqrt{3})^D h^{2D}} f_{LB}(\mathbf{x}_{LB}, \boldsymbol{\xi}_{LB}, t_{LB}).
 \end{aligned} \tag{2.8}$$

The corresponding continuum Boltzmann equation (neglecting the acceleration due to body forces) in LB units is then given by:

$$\partial_{t_{LB}} f_{LB} + \boldsymbol{\xi}_{LB} \cdot \nabla_{LB} f_{LB} = -\frac{1}{\tau_{LB}} (f_{LB} - f_{LB}^{eq}). \tag{2.9}$$

To seek the solution of equation 2.9 through discretisation, we first project the continuum LB-BGK equation onto Hermite basis, by expanding $f_{LB}(\mathbf{x}_{LB}, \sqrt{3}\boldsymbol{\xi}_{LB}, t_{LB})$ in terms of Hermite orthogonal polynomials in the velocity space $\boldsymbol{\xi}_{LB}$:

$$f_{LB}(\mathbf{x}_{LB}, \sqrt{3}\boldsymbol{\xi}_{LB}, t_{LB}) = \omega(\sqrt{3}\boldsymbol{\xi}_{LB}) \sum_{n=0}^{\infty} \frac{1}{n!} \mathbf{a}^{(n)}(\mathbf{x}_{LB}, t_{LB}) \mathcal{H}^{(n)}(\sqrt{3}\boldsymbol{\xi}_{LB}), \tag{2.10}$$

where both the expansion coefficient $\mathbf{a}^{(n)}$ and Hermite polynomial $\mathcal{H}^{(n)}$ are rank- n tensors, so the product on the right-hand side of the equation above denotes full tensor contraction. More properties on the Hermite polynomials can be found in Grad (1949), Shan, Yuan, and Chen (2006), and Chen (2011). The weight function associated with the Hermite polynomials in D -dimensional Cartesian coordinates \mathbf{x} is given by:

$$\omega(\boldsymbol{\xi}) = \frac{1}{(2\pi)^{D/2}} \exp\left(-\frac{\boldsymbol{\xi}^2}{2}\right), \quad (2.11)$$

and the n th-order Hermite polynomials is defined as:

$$\mathcal{H}(\boldsymbol{\xi}) = \frac{(-1)^n}{\omega(\boldsymbol{\xi})} \nabla^n \omega(\boldsymbol{\xi}), \quad (2.12)$$

which is a rank- n symmetric tensor. The first three polynomials are listed as follows which will be used in the later derivation:

$$\mathcal{H}^{(0)}(\boldsymbol{\xi}) = 1, \quad (2.13a)$$

$$\mathcal{H}_\alpha^{(1)}(\boldsymbol{\xi}) = \xi_\alpha, \quad (2.13b)$$

$$\mathcal{H}_{\alpha\beta}^{(2)}(\boldsymbol{\xi}) = \xi_\alpha \xi_\beta - \delta_{\alpha\beta}, \quad (2.13c)$$

where $\delta_{\alpha\beta}$ is the Kronecker delta function whose value is 1 if $\alpha = \beta$ and 0 otherwise. The expansion coefficient rank- n tensor $\mathbf{a}^{(n)}$ is given by:

$$\mathbf{a}^{(n)}(\mathbf{x}_{LB}, t_{LB}) = \int f_{LB}(\mathbf{x}_{LB}, \sqrt{3}\boldsymbol{\xi}_{LB}, t_{LB}) \mathcal{H}^{(n)}(\sqrt{3}\boldsymbol{\xi}_{LB}) d(\sqrt{3}\boldsymbol{\xi}_{LB}), \quad (2.14)$$

where in a D -dimension, $d(\sqrt{3}\boldsymbol{\xi}_{LB}) = (\sqrt{3})^D d\boldsymbol{\xi}_{LB}$. Here we list first three expansion coefficients which recover the familiar hydrodynamic quantities:

$$\begin{aligned} \mathbf{a}^{(0)}(\mathbf{x}_{LB}, t_{LB}) &= \int f_{LB}(\mathbf{x}_{LB}, \sqrt{3}\boldsymbol{\xi}_{LB}, t_{LB}) d(\sqrt{3}\boldsymbol{\xi}_{LB}) \\ &= \int \left(\frac{1}{\sqrt{3}}\right)^D f_{LB}(\mathbf{x}_{LB}, \boldsymbol{\xi}_{LB}, t_{LB}) (\sqrt{3})^D d\boldsymbol{\xi}_{LB} \\ &= \int f_{LB}(\mathbf{x}_{LB}, \boldsymbol{\xi}_{LB}, t_{LB}) d\boldsymbol{\xi}_{LB} \\ &= \rho_{LB}. \end{aligned} \quad (2.15)$$

Similarly, for the second expansion coefficient:

$$\begin{aligned} \mathbf{a}^{(1)}(\mathbf{x}_{LB}, t_{LB}) &= \int f_{LB}(\mathbf{x}_{LB}, \sqrt{3}\boldsymbol{\xi}_{LB}, t_{LB}) \sqrt{3}\boldsymbol{\xi}_{LB} d(\sqrt{3}\boldsymbol{\xi}_{LB}) \\ &= \sqrt{3} \int f_{LB}(\mathbf{x}_{LB}, \boldsymbol{\xi}_{LB}, t_{LB}) \boldsymbol{\xi}_{LB} d\boldsymbol{\xi}_{LB} \\ &= \rho_{LB}(\sqrt{3}\mathbf{u}_{LB}), \end{aligned} \quad (2.16)$$

and for the third coefficient:

$$\begin{aligned}
\mathbf{a}^{(2)}(\mathbf{x}_{LB}, t_{LB}) &= \int f_{LB}(\mathbf{x}_{LB}, \sqrt{3}\boldsymbol{\xi}_{LB}, t_{LB}) (3\boldsymbol{\xi}_{LB}\boldsymbol{\xi}_{LB} - \mathbb{I}) d(\sqrt{3}\boldsymbol{\xi}_{LB}) \\
&= 3 \int f_{LB}(\sqrt{3}\boldsymbol{\xi}_{LB}) (\boldsymbol{\xi}_{LB} - \mathbf{u}_{LB}) (\boldsymbol{\xi}_{LB} - \mathbf{u}_{LB}) d(\sqrt{3}\boldsymbol{\xi}_{LB}) \\
&\quad + 2\mathbf{u}_{LB} \int f_{LB}(\sqrt{3}\boldsymbol{\xi}_{LB}) \boldsymbol{\xi}_{LB} d(\sqrt{3}\boldsymbol{\xi}_{LB}) - \mathbf{u}_{LB}\mathbf{u}_{LB} \int f_{LB}(\sqrt{3}\boldsymbol{\xi}_{LB}) d(\sqrt{3}\boldsymbol{\xi}_{LB}) \\
&\quad - \mathbb{I} \int f_{LB}(\sqrt{3}\boldsymbol{\xi}_{LB}) d(\sqrt{3}\boldsymbol{\xi}_{LB}) \\
&= 3\mathbb{P}_{LB} + \rho_{LB} (3\mathbf{u}_{LB}\mathbf{u}_{LB} - \mathbb{I}),
\end{aligned} \tag{2.17}$$

where \mathbb{I} is the identity matrix, and the rank-2 momentum flux tensor \mathbb{P} is defined as:

$$\mathbb{P}_{LB} = \int f_{LB}(\mathbf{x}_{LB}, \boldsymbol{\xi}_{LB}, t_{LB}) (\boldsymbol{\xi}_{LB} - \mathbf{u}_{LB}) (\boldsymbol{\xi}_{LB} - \mathbf{u}_{LB}) d\boldsymbol{\xi}_{LB}. \tag{2.18}$$

In a short summary, the macroscopic hydrodynamic quantities are completely determined by the Hermite expansion coefficients as follows:

$$\rho_{LB} = \mathbf{a}^{(0)}, \tag{2.19a}$$

$$\rho_{LB}\mathbf{u}_{LB} = \mathbf{a}^{(1)}/\sqrt{3}, \tag{2.19b}$$

$$\mathbb{P}_{LB} = 1/3 \left[\mathbf{a}^{(2)} - \rho_{LB} (3\mathbf{u}_{LB}\mathbf{u}_{LB} - \mathbb{I}) \right]. \tag{2.19c}$$

Similarly, for the equilibrium distribution function, i.e. equation 2.7, its Hermite expansion coefficients $\mathbf{a}_0^{(n)}$ can also be calculated as:

$$\mathbf{a}_0^{(n)}(\mathbf{x}_{LB}, t_{LB}) = \int f_{LB}^{eq}(\mathbf{x}_{LB}, \sqrt{3}\boldsymbol{\xi}_{LB}, t_{LB}) \mathcal{H}^{(n)}(\sqrt{3}\boldsymbol{\xi}_{LB}) d(\sqrt{3}\boldsymbol{\xi}_{LB}). \tag{2.20}$$

Given the expression of $\omega(\boldsymbol{\xi})$ we could rewrite the equilibrium distribution as:

$$f_{LB}^{eq}(\mathbf{x}_{LB}, \sqrt{3}\boldsymbol{\xi}_{LB}, t_{LB}) = \frac{\rho_{LB}}{(\sqrt{3}c_{s,LB})^D} \omega\left(\frac{\sqrt{3}\boldsymbol{\xi}_{LB} - \sqrt{3}\mathbf{u}_{LB}}{\sqrt{3}c_{s,LB}}\right). \tag{2.21}$$

If we change the dummy variable as:

$$\boldsymbol{\eta}_{LB} = \frac{\sqrt{3}\boldsymbol{\xi}_{LB} - \sqrt{3}\mathbf{u}_{LB}}{\sqrt{3}c_{s,LB}}, \tag{2.22}$$

then the equilibrium expansion coefficient becomes:

$$\mathbf{a}_0^{(n)}(\mathbf{x}_{LB}, t_{LB}) = \rho_{LB} \int \omega(\boldsymbol{\eta}_{LB}) \mathcal{H}^{(n)}(\sqrt{3}c_{s,LB} + \sqrt{3}\mathbf{u}_{LB}) d\boldsymbol{\eta}_{LB}, \tag{2.23}$$

which gives:

$$\begin{aligned} \mathbf{a}_0^{(0)} &= \rho_{LB} \int \omega(\boldsymbol{\eta}_{LB}) d\boldsymbol{\eta}_{LB} \\ &= \rho_{LB}, \end{aligned} \quad (2.24)$$

and

$$\begin{aligned} \mathbf{a}_0^{(1)} &= \rho_{LB} \int \omega(\boldsymbol{\eta}_{LB}) (\sqrt{3}c_{s,LB}\boldsymbol{\eta}_{LB} + \sqrt{3}\mathbf{u}_{LB}) d\boldsymbol{\eta}_{LB} \\ &= \rho_{LB}(\sqrt{3}\mathbf{u}_{LB}), \end{aligned} \quad (2.25)$$

and

$$\begin{aligned} \mathbf{a}_0^{(2)} &= \rho_{LB} \int \omega(\boldsymbol{\eta}_{LB}) \left[(\sqrt{3}c_{s,LB}\boldsymbol{\eta}_{LB} + \sqrt{3}\mathbf{u}_{LB})(\sqrt{3}c_{s,LB}\boldsymbol{\eta}_{LB} + \sqrt{3}\mathbf{u}_{LB}) - \mathbb{I} \right] d\boldsymbol{\eta}_{LB} \\ &= 3\rho_{LB}\mathbf{u}_{LB}\mathbf{u}_{LB} + \rho_{LB}(3c_{s,LB}^2 - 1)\mathbb{I}. \end{aligned} \quad (2.26)$$

Overall, given the above expansion coefficients and according to equation 2.10, the equilibrium distribution can be explicitly written as:

$$\begin{aligned} f_{LB}^{eq}(\mathbf{x}_{LB}, \sqrt{3}\boldsymbol{\xi}_{LB}, t_{LB}) &= \omega(\sqrt{3}\boldsymbol{\xi}_{LB})\rho_{LB} \left\{ 1 + 3\mathbf{u}_{LB} \cdot \boldsymbol{\xi}_{LB} \right. \\ &\quad \left. + \frac{1}{2} [(3\mathbf{u}_{LB}\mathbf{u}_{LB} + (3c_{s,LB}^2 - 1)\mathbb{I}) : (3\boldsymbol{\xi}_{LB}\boldsymbol{\xi}_{LB} - \mathbb{I})] + \mathcal{O}(n \geq 3) \right\} \\ &= \omega(\sqrt{3}\boldsymbol{\xi}_{LB})\rho_{LB} \left\{ 1 + 3\mathbf{u}_{LB} \cdot \boldsymbol{\xi}_{LB} + \frac{9}{2}\mathbf{u}_{LB}\mathbf{u}_{LB} : \boldsymbol{\xi}_{LB}\boldsymbol{\xi}_{LB} - \frac{3}{2}u_{LB}^2 \right. \\ &\quad \left. + \frac{1}{2} (3c_{s,LB}^2 - 1) (3\xi_{LB}^2 - D) + \mathcal{O}(n \geq 3) \right\}. \end{aligned} \quad (2.27)$$

Because of the orthogonality of the Hermite polynomials, the moments of the distribution functions up to N th order is exactly preserved by truncation of the higher-order terms in its Hermite expansions, which serves as the foundations of the discretisation scheme. As a result, the distribution function that is expanded in equation 2.10 can be approximated by its projection onto a Hilbert subspace spanned by the first N Hermite polynomials without changing first N moments (as in equation 2.19): (Shan, Yuan, and Chen, 2006)

$$\begin{aligned} f_{LB}(\mathbf{x}_{LB}, \sqrt{3}\boldsymbol{\xi}_{LB}, t_{LB}) &\approx f_{LB}^N(\mathbf{x}_{LB}, \sqrt{3}\boldsymbol{\xi}_{LB}, t_{LB}) \\ &= \omega(\sqrt{3}\boldsymbol{\xi}_{LB}) \sum_{n=0}^N \frac{1}{n!} \mathbf{a}^{(n)}(\mathbf{x}_{LB}, t_{LB}) \mathcal{H}^{(n)}(\sqrt{3}\boldsymbol{\xi}_{LB}), \end{aligned} \quad (2.28)$$

which means that f_{LB}^N has exactly the same moments as the original f_{LB} does. This ensures that the fluid system and the associated theoretical framework can be built by a finite set of macroscopic quantities.

For the discretisation of the velocity space, first, utilising the Gauss-Hermite quadrature, the integrand on the right-hand side of equation 2.14 can be expressed as:

$$f_{LB}^N(\mathbf{x}_{LB}, \sqrt{3}\boldsymbol{\xi}_{LB}, t_{LB}) \mathcal{H}^{(n)}(\sqrt{3}\boldsymbol{\xi}_{LB}) = \omega(\sqrt{3}\boldsymbol{\xi}_{LB}) p(\mathbf{x}_{LB}, \sqrt{3}\boldsymbol{\xi}_{LB}, t_{LB}), \quad (2.29)$$

where $p(\mathbf{x}_{LB}, \sqrt{3}\boldsymbol{\xi}_{LB}, t_{LB})$ is a polynomial in $\boldsymbol{\xi}_{LB}$ of a degree no more than $2N$, and thus the expansion coefficient $\mathbf{a}^{(n)}$ in equation 2.14 can be exactly written as a weighted sum of the function values of $p(\mathbf{x}_{LB}, \sqrt{3}\boldsymbol{\xi}_{LB}, t_{LB})$:

$$\begin{aligned} \mathbf{a}^{(n)} &= \int \omega(\sqrt{3}\boldsymbol{\xi}_{LB}) p(\mathbf{x}_{LB}, \sqrt{3}\boldsymbol{\xi}_{LB}, t_{LB}) d(\sqrt{3}\boldsymbol{\xi}_{LB}) \\ &= \sum_{i=0}^{q-1} t_i p(\mathbf{x}_{LB}, \sqrt{3}\boldsymbol{\xi}_{i, LB}, t_{LB}) \\ &= \sum_{i=0}^{q-1} \frac{t_i}{\omega(\sqrt{3}\boldsymbol{\xi}_{i, LB})} f_{LB}^N(\mathbf{x}_{LB}, \sqrt{3}\boldsymbol{\xi}_{i, LB}, t_{LB}) \mathcal{H}^{(n)}(\sqrt{3}\boldsymbol{\xi}_{i, LB}), \end{aligned} \quad (2.30)$$

where t_i and $\sqrt{3}\boldsymbol{\xi}_{i, LB}$, $i = 0, 1, \dots, q-1$ are the weights and abscissae of a Gauss-Hermite quadrature of a degree $\geq 2N$.

A quadrature formula is usually named by three numbers as in $E_{D,n}^d$, where d is the number of points employed by the quadrature, D is the dimension of the quadrature, and n is the algebraic degree of precision (Shan, Yuan, and Chen, 2006). These quadratures directly map to the commonly seen lattice structures in LB models. For example, the Gauss-Hermite quadrature giving rise to the D3Q19 lattice with $q = 19$ in LBM, is annotated as $E_{3,5}^{19}$, i.e. a three-dimensional degree-5 precision quadrature with 19 abscissae. $E_{3,5}^{19}$ has three groups of abscissae $\sqrt{3}\boldsymbol{\xi}_{i, LB}$, namely, the stable group $(0, 0, 0)$ with the weight $t_0 = 1/3$; the orthogonal group $(\pm\sqrt{3}, 0, 0)$, $(0, \pm\sqrt{3}, 0)$, and $(0, 0, \pm\sqrt{3})$ with $t_i = 1/18$ for $i = 1, 2, \dots, 6$; and the diagonal group $(\pm\sqrt{3}, \pm\sqrt{3}, 0)$, $(\pm\sqrt{3}, 0, \pm\sqrt{3})$, and $(0, \pm\sqrt{3}, \pm\sqrt{3})$, with $t_i = 1/36$ for $i = 7, 8, \dots, 18$. For more quadratures that give for example D3Q15 or D3Q27 lattices please see Shan, Yuan, and Chen (2006). Now it becomes clear to readers why a factor of $\sqrt{3}$ is introduced early in equation 2.4 and is used throughout our derivation. This is essentially to map the Gauss-Hermite quadrature to a regular spatial grid such that the actual abscissae $\boldsymbol{\xi}_{i, LB}$ has the increment of 1 *l.u.* for $i > 0$.

It is noted that the set of discrete distribution functions $f^N(\mathbf{x}_{LB}, \boldsymbol{\xi}_{i, LB}, t_{LB})$, $i = 0, 1, \dots, q-1$ completely determines $f^N(\mathbf{x}_{LB}, \boldsymbol{\xi}_{LB}, t_{LB})$ and thus its first N moments. The superscript N is thus omitted hereafter, and $f_{LB}(\sqrt{3}\boldsymbol{\xi}_{i, LB})$ is short for $f_{LB}(\mathbf{x}_{LB}, \sqrt{3}\boldsymbol{\xi}_{i, LB}, t_{LB})$. Now explicitly write the first three expansion coefficients according to equation 2.30, and considering the macroscopic hydrodynamic quantities

given in equations 2.15 to 2.17, after some algebra we obtain:

$$\rho_{LB} = \sum_{i=1}^{q-1} \frac{t_i f_{LB}(\sqrt{3}\xi_{i,LB})}{\omega(\sqrt{3}\xi_{i,LB})}, \quad (2.31a)$$

$$\rho_{LB}(\sqrt{3}\mathbf{u}_{LB}) = \sum_{i=1}^{q-1} \frac{t_i f_{LB}(\sqrt{3}\xi_{i,LB})\sqrt{3}\xi_{i,LB}}{\omega(\sqrt{3}\xi_{i,LB})}, \quad (2.31b)$$

$$3\mathbb{P} + \rho_{LB}(3\mathbf{u}_{LB}\mathbf{u}_{LB} - \mathbb{I}) = \sum_{i=1}^{q-1} \frac{t_i f_{LB}(\sqrt{3}\xi_{i,LB})(3\xi_{i,LB}\xi_{i,LB} - \mathbb{I})}{\omega(\sqrt{3}\xi_{i,LB})}. \quad (2.31c)$$

If we further define that:

$$f_{i,LB}(\mathbf{x}_{LB}, t_{LB}) = \frac{t_i f_{LB}(\sqrt{3}\xi_{i,LB})}{\omega(\sqrt{3}\xi_{i,LB})}, \quad (2.32)$$

the commonly seen equations of macroscopic hydrodynamic quantities in terms of discretised velocity $\xi_{i,LB}$ in the LB literature are obtained:

$$\rho_{LB} = \sum_{i=0}^{q-1} f_{i,LB}, \quad (2.33a)$$

$$\rho_{LB}\mathbf{u}_{LB} = \sum_{i=0}^{q-1} f_{i,LB}\xi_{i,LB}, \quad (2.33b)$$

$$\mathbb{P}_{LB} + \rho_{LB}\mathbf{u}_{LB}\mathbf{u}_{LB} = \sum_{i=0}^{q-1} f_{i,LB}\xi_{i,LB}\xi_{i,LB}, \quad (2.33c)$$

and the discretised equilibrium distribution function can be written as:

$$\begin{aligned} f_{i,LB}^{eq}(\mathbf{x}_{LB}, t_{LB}) &= \frac{t_i f_{LB}^{eq}(\sqrt{3}\xi_{i,LB})}{\omega(\sqrt{3}\xi_{i,LB})} \\ &= t_i \rho_{LB} \left\{ 1 + 3\mathbf{u}_{LB} \cdot \xi_{i,LB} + \frac{9}{2}\mathbf{u}_{LB}\mathbf{u}_{LB} : \xi_{i,LB}\xi_{i,LB} - \frac{3}{2}u_{LB}^2 \right. \\ &\quad \left. + \frac{1}{2}(3c_{s,LB}^2 - 1)(3\xi_{i,LB}^2 - D) + \mathcal{O}(n \geq 3) \right\}, \end{aligned} \quad (2.34)$$

where it can be seen that if $c_{s,LB}$ is set as $1/\sqrt{3}$, and neglecting the higher-order terms, the discretised equilibrium distribution functions recovers the commonly seen form such as equation 2.52 in the later section. This also reflects the artificial feature carried by the current LB models - that is, $c_{s,LB}$, although being called the speed of sound, comes more as a result of mathematical manipulation, and does not resemble any of real physical meaning usually seen in the classical thermodynamics context.

Based on the definition of equation 2.32, the relation between macroscopic quantities and the discretised equilibrium distribution functions can also be obtained after

some algebra:

$$\rho_{LB} = \sum_{i=0}^{q-1} f_{i, LB}^{eq} \quad (2.35a)$$

$$\rho_{LB} \mathbf{u}_{LB} = \sum_{i=0}^{q-1} f_{i, LB}^{eq} \boldsymbol{\xi}_{i, LB} \quad (2.35b)$$

$$\rho_{LB} \mathbf{u}_{LB} \mathbf{u}_{LB} + \rho_{LB} c_{s, LB}^2 \mathbb{I} = \sum_{i=0}^{q-1} f_{i, LB}^{eq} \boldsymbol{\xi}_{i, LB} \boldsymbol{\xi}_{i, LB} \quad (2.35c)$$

In terms of the discrete Boltzmann-BGK equation, firstly we can directly evaluate equation 2.9 at $\boldsymbol{\xi}_{i, LB}$ to obtain:

$$\partial_{t_{LB}} f_{LB}(\boldsymbol{\xi}_{i, LB}) + \boldsymbol{\xi}_{i, LB} \cdot \nabla_{LB} f_{LB}(\boldsymbol{\xi}_{i, LB}) = -\frac{1}{\tau_{LB}} [f_{LB}(\boldsymbol{\xi}_{i, LB}) - f_{LB}^{eq}(\boldsymbol{\xi}_{i, LB})], \quad (2.36)$$

and multiplying $(1/\sqrt{3})^D$ on both sides of the equation above to change $f_{LB}(\boldsymbol{\xi}_{i, LB})$ to $f_{LB}(\sqrt{3}\boldsymbol{\xi}_{i, LB})$; and lastly multiplying the constant $t_i/\omega(\sqrt{3}\boldsymbol{\xi}_{i, LB})$, we obtain the discrete-velocity Boltzmann-BGK equation for $f_{i, LB}(\mathbf{x}_{LB}, t_{LB})$ as follows:

$$\partial_{t_{LB}} f_{i, LB} + \boldsymbol{\xi}_{i, LB} \cdot \nabla_{LB} f_{i, LB} = -\frac{1}{\tau_{LB}} (f_{i, LB} - f_{i, LB}^{eq}). \quad (2.37)$$

The discretisation of space and time is then performed, via first-order upwind finite-difference approximation to equation 2.37 to obtain the celebrated lattice-Boltzmann BGK equation 2.41. It should be noted, as pointed out by Cao et al. (1997), this particular discretisation scheme is merely a reflection of historical evolution of the LB models, which first originated from the lattice gas automaton method; but as we show in this section that LB model is simply a discrete form of continuum Boltzmann equation, various mature discretisation methods used in the computational fluid dynamics can also be applied to equation 2.37. Although in this thesis only the simplest upwind finite-difference method is introduced, readers are refer to the reported works for other techniques, such as the Runge-Kutta based finite-difference LBM by Cao et al. (1997), finite-volume LBM by Nannelli and Succi (1992), and finite-element LBM by Lee and Lin (2001), to name but a few.

Following the historical path (Wolf-Gladrow, 2000), the discretised space and time are coupled as:

$$\xi_{i, x} = \frac{\delta x}{\delta t}, \quad \xi_{i, y} = \frac{\delta y}{\delta t}, \quad \xi_{i, z} = \frac{\delta z}{\delta t}, \quad (2.38)$$

where the subscript ‘LB’ is neglected hereafter for more clarity. In a regular grid, this implies that $\delta x = \delta y = \delta z = \delta t$. Again, such a discretisation relation is not necessary and any standard finite difference method serves the purpose of discretising equation

2.37. An upwind discretisation of equation 2.37 is then given by:

$$\begin{aligned}
& \frac{f_i(\mathbf{x}, t + \delta t) - f_i(\mathbf{x}, t)}{\delta t} + \xi_{i,x} \frac{f_i(x + \delta x, t + \delta t) - f_i(\mathbf{x}, t + \delta t)}{\delta x} \\
& + \xi_{i,y} \frac{f_i(y + \delta y, t + \delta t) - f_i(\mathbf{x}, t + \delta t)}{\delta y} \\
& + \xi_{i,z} \frac{f_i(z + \delta z, t + \delta t) - f_i(\mathbf{x}, t + \delta t)}{\delta z} \\
& = -\frac{1}{\tau}(f_i - f_i^{eq}).
\end{aligned} \tag{2.39}$$

Given the relation 2.38, the equation above can be rearranged as:

$$\frac{f_i(\mathbf{x}, t + \delta t) - f_i(\mathbf{x}, t)}{\delta t} + \frac{f_i(\mathbf{x} + \boldsymbol{\xi}\delta t, t + \delta t) - f_i(\mathbf{x}, t + \delta t)}{\delta t} = -\frac{1}{\tau}(f_i - f_i^{eq}). \tag{2.40}$$

Simplifying the equation above, it finally leads to the celebrated single-relaxation-time lattice-Boltzmann BGK equation (in LB units):

$$f_i(\mathbf{x} + \boldsymbol{\xi}_i\delta t, t + \delta t) - f_i(\mathbf{x}, t) = -\frac{\delta t}{\tau}(f_i - f_i^{eq}). \tag{2.41}$$

2.2 Unit Conversion in LBM

The physical-to-LB unit conversion has been touched briefly in equations 2.4 and 2.5 in the previous sub-section, to facilitate the full derivation from the physical Boltzmann transport equation to the lattice-Boltzmann equation. In this sub-section more details are introduced for the unit conversion of other relevant quantities that are important for modelling multiphase flow. There are three fundamental units in the LB modelling: the lattice unit (*l.u.*), the lattice time (*l.t.*), and the mass (kg), from which a series of relevant quantities can be constructed, as is summarised in Table 2.1.

TABLE 2.1: Summary of Units in Lattice-Boltzmann Method

Quantity	Symbol	Unit in LBM
Length	x_{LB}	<i>l.u.</i>
Time	t_{LB}	<i>l.t.</i>
Velocity	v_{LB}	$\text{l.u.} \cdot \text{l.t.}^{-1}$
Mass	m_{LB}	kg
Number Density	n_{LB}	l.u.^{-3}
Density	ρ_{LB}	$\text{kg} \cdot \text{l.u.}^{-3}$
Kinematic Viscosity	ν_{LB}	$\text{l.u.}^2 \cdot \text{l.t.}^{-1}$
Pressure	P_{LB}	$\text{kg} \cdot \text{l.u.}^{-1} \cdot \text{l.t.}^{-2}$
Surface Tension	γ_{LB}	$\text{kg} \cdot \text{l.t.}^{-2}$

In practical pore-scale two-phase simulations, one is usually given a sets of digitised μ CT images of certain rock type to start with, and the most relevant parameter here is the resolution of the μ CT image (*h*). As mentioned, the LB units are linked to the physical units by several scaling factors, among which, the image resolution *h* is the

most fundamental one, and all of the rest scaling factors can be derived from it. More specifically, the unit conversion procedure can be performed as follows:

1. Given a physical system, the resolution of the μ CT image (h), the density of the fluid (ρ_{phys}), the dynamic viscosity of the fluid (μ_{phys}) or the kinematic viscosity ($\nu_{\text{phys}} = \mu_{\text{phys}}/\rho_{\text{phys}}$), and the interfacial tension (γ_{phys}) are known.
2. By relating the physical density of the fluid to its LB counterpart, the density-related scaling factor $m_0 n_0$ (see equation 2.47) can be determined.
3. Once $m_0 n_0$ is determined, one has the freedom to set either the LB surface tension γ_{LB} or the LB kinematic viscosity ν_{LB} , but it is noted that only one of the two can be set freely. For example, if choosing to set γ_{LB} first, the time conversion factor δt_{phys} (in the unit of s/l.t.) can be immediately determined by $\sigma_{\text{phys}} = \frac{m_0 n_0}{(\delta t_{\text{phys}}/\sqrt{3})^2} \gamma_{\text{LB}}$; this also automatically determines the LB viscosity by $\nu_{\text{phys}} = \frac{\sqrt{3} h^2}{\delta t_{\text{phys}}} \nu_{\text{LB}}$, and vice versa.
4. After determining the scaling factors $m_0 n_0$ and δt_{phys} , all the other quantities, such as the LB pressure, are set accordingly.

All the key unit conversion relations, together with some extra notes, are summarised as follows for reference:

1. *length*:

$$x_{\text{phys}} = h x_{\text{LB}}, \quad (2.42)$$

where h is the resolution of the μ CT image of certain reservoir rock type, in the unit of m/l.u..

2. *time*:

$$t_{\text{phys}} = \frac{\delta t_{\text{phys}}}{\sqrt{3}} t_{\text{LB}}, \quad (2.43)$$

where δt_{phys} is the time conversion factor in the unit of s/l.t., and t_{LB} is usually the iteration step in the LB simulations. The factor $\sqrt{3}$ is due to the mathematical details of the Gauss-Hermite quadrature when discretising the continuum physical quantities into their LB counterparts, and see more discussion under equation 2.30.

3. *velocity*:

$$\mathbf{u}_{\text{phys}} = \frac{h}{\delta t_{\text{phys}}/\sqrt{3}} \mathbf{u}_{\text{LB}}. \quad (2.44)$$

4. *mass*:

$$m_{\text{phys}} = m_0 m_{\text{LB}}, \quad (2.45)$$

where m_0 is a dimensionless scaling factor for the molecular mass of fluid.

5. *number density*:

$$n_{\text{phys}} = \frac{n_0}{h^3} n_{\text{LB}}, \quad (2.46)$$

where the physical and LB number densities are in the units of m^{-3} and l.u.^{-3} , respectively. n_0 is a dimensionless scaling factor for the number density of fluid.

6. *density*:

$$\rho_{\text{phys}} = \frac{m_0 n_0}{h^3} \rho_{\text{LB}}, \quad (2.47)$$

where, in practice, it is usually the product $m_0 n_0$ that is calculated, by setting $\rho_{\text{LB}} = 1.0 \text{ kg l.u.}^{-3}$, which is a common choice for immiscible LB models (e.g. section 2.4).

7. *kinematic viscosity*:

$$\nu_{\text{phys}} = \frac{h^2}{\delta t_{\text{phys}}/\sqrt{3}} \nu_{\text{LB}}. \quad (2.48)$$

This relation is obtained by retaining the consistent Reynolds number (Re) between the physical and LB systems: $Re = \frac{u_{\text{phys}} x_{\text{phys}}}{\nu_{\text{phys}}} = \frac{u_{\text{LB}} x_{\text{LB}}}{\nu_{\text{LB}}}$.

8. *interfacial tension*:

$$\gamma_{\text{phys}} = \frac{m_0 n_0}{(\delta t_{\text{LB}}/\sqrt{3})^2} \gamma_{\text{LB}}. \quad (2.49)$$

9. *pressure*:

$$P_{\text{phys}} = \frac{m_0 n_0}{h(\delta t_{\text{phys}}/\sqrt{3})^2} P_{\text{LB}}. \quad (2.50)$$

2.3 Single-Relaxation-Time Multiphase Lattice-Boltzmann Methods

After reviewing the fundamentals of the LB theory and how the model can be set up in practical simulations, now it is time to introduce the concrete multicomponent LB models for the two-phase flow study. In this and next sections, the multicomponent LB models based on the single-relaxation-time (SRT) and multi-relaxation-time (MRT) collision operators are introduced, respectively. Although the SRT-based LBM is less advanced compared to the multi-relaxation-time (MRT) ones, in terms of the numerical stability and the range of viscosity ratio etc., they can be algorithmically easily implemented and are usually used to perform quick proof-of-concept demonstrations.

In this section, two commonly used SRT multicomponent models, Shan-Chen (SC) model, and colour-gradient based Rothman-Keller (RK) model, are briefly introduced, as they are used in the low-resolution characterisation study in Chapter 3. Here only the algorithm-wise implementations of SC and RK models are discussed; regarding the physics of how LB method can recover the macroscopic Navier-Stokes equation (with surface tension force), it will be studied in detail when introducing the MRT multicomponent model in the next section 2.4, and we conducted all of the practical simulations with MRT-LB model in Chapter 5.

Overall, to handle multiple fluid components, the collision operator in equation 2.41 must be revised to incorporate the surface tension forces between the fluids. Therefore, on top of the normal BGK collision process, the surface tension and the

associated phase segregation is realised (1) by adding a body force which only becomes non-negligible where there is a large density gradient, (2) by adding extra terms in the equilibrium distribution functions, or (3) by adding an extra perturbation process after the normal BGK collision. The Shan-Chen (SC) model (Martys and Chen, 1996; Pan, Hilpert, and Miller, 2004; Huang et al., 2007) introduced in section 2.3.1 uses external body force to realise the surface tension, whereas the Rothman-Keller (RK) model, also known as colour-gradient model (Gunstensen et al., 1991; Grunau, Chen, and Eggert, 1993; Latva-Kokko and Rothman, 2005a; Liu, Valocchi, and Kang, 2012), introduced in section 2.3.2 chooses to use perturbation process. The MRT model introduced in section 2.4, however, uses the approach of adding extra terms in the equilibrium distribution functions to realise the surface tension.

2.3.1 Shan-Chen Model

The key feature of Shan-Chen model is that two external forces, cohesion and adhesion forces, are introduced. The cohesion force determines the excess free energy of mixing, causes the fluid components to phase separate and gives the resulting fluid-fluid interfaces a surface tension. The adhesion force incorporates different wetting conditions by adding excess free energy to the interaction with solid surfaces. The excess energies are provided through attractive or repulsive forces between nearest-/next nearest-neighbouring particles, arising from modifying the momentum values in the equilibrium distribution function on which the collision operator depends. In this work, we use a single-relaxation-time, Bhatnagar-Gross-Krook (BGK) collision operator for SC model, which is given by (Qian, d’Humières, and Lallemand, 1992):

$$\Omega_i^k(\mathbf{x}, t) = -\frac{1}{\tau_k} \left[f_i^k(\mathbf{x}, t) - f_i^{k,eq}(\mathbf{x}, t) \right], \quad (2.51)$$

where τ_k is the relaxation parameter for k_{th} fluid component, which describes how quickly the system relaxes to the equilibrium. The kinematic viscosity of k_{th} fluid, ν_k , is linked to τ_k by: $\nu_k = (2\tau_k - 1)/6$. The equilibrium distribution function $f_i^{k,eq}$ is given by (Qian, d’Humières, and Lallemand, 1992):

$$f_i^{k,eq}(\mathbf{x}, t) = \rho_k t_i \left[1 + \frac{\boldsymbol{\xi}_i \cdot \mathbf{u}_k^{eq}}{c_s^2} + \frac{(\boldsymbol{\xi}_i \cdot \mathbf{u}_k^{eq})^2}{2c_s^4} - \frac{|\mathbf{u}_k^{eq}|^2}{2c_s^2} \right], \quad (2.52)$$

where ω_i is the weighting factor associated with D3Q19 lattice, which is given by $t_i = 1/3$ ($i = 0$), $t_i = 1/18$ ($i = 1, 2, \dots, 6$), and $t_i = 1/36$ ($i = 7, 8, \dots, 18$); $c_s = 1/\sqrt{3}$ is the speed of sound for the lattice. The macroscopic density and momentum of the k_{th} fluid component are defined as $\rho_k = \sum_i f_i^k$ and $\rho_k \mathbf{u}_k = \sum_i f_i^k \boldsymbol{\xi}_i$, respectively. The total fluid density ρ is given by $\rho = \sum_k \rho_k$.

The macroscopic equilibrium velocity \mathbf{u}_k^{eq} in equation (2.52) is given by:

$$\mathbf{u}_k^{eq} = \mathbf{u}' + \frac{\tau_k \mathbf{F}_k}{\rho_k}, \quad (2.53)$$

where \mathbf{u}' is a weighted velocity among fluid components (also known as the common velocity), and is given by:

$$\mathbf{u}' = \frac{\sum_k \frac{\rho_k \mathbf{u}_k}{\tau_k}}{\sum_k \frac{\rho_k}{\tau_k}}. \quad (2.54)$$

Note in the current SC model the body force is incorporated by directly adding the resultant momentum to the equilibrium velocity; there are however many other forcing schemes, for example, the explicit forcing method, developed recently by Porter et al. (2012), has shown enhanced numerical stability and coverage of larger viscosity ratio (0.001 \sim 1000).

In equation (2.53), \mathbf{F}_k is the total force exerted on k_{th} fluid component, and is normally written as:

$$\mathbf{F}_k = \mathbf{F}_k^{\text{coh}} + \mathbf{F}_k^{\text{ads}} + \rho_k \mathbf{g}_k, \quad (2.55)$$

where $\mathbf{F}_k^{\text{coh}}$ is the fluid-fluid cohesive force, $\mathbf{F}_k^{\text{ads}}$ is the fluid-solid adhesive force, and $\rho_k \mathbf{g}_k$ is the gravitational force on k_{th} fluid. The fluid-fluid interaction force $\mathbf{F}_k^{\text{coh}}$ at site \mathbf{x} is calculated as the sum of forces between the k_{th} fluid particle at \mathbf{x} , and the k'_{th} fluid particle at neighbouring sites of \mathbf{x} , given as:

$$\mathbf{F}_k^{\text{coh}}(\mathbf{x}, t) = -G_{\text{coh}} \rho_k(\mathbf{x}, t) \sum_i t_i \rho_{k'}(\mathbf{x} + \boldsymbol{\xi}_i \delta_t, t) \boldsymbol{\xi}_i, \quad (2.56)$$

where G_{coh} is the cohesion coefficient. Based on equation (2.56) it is the product of G_{coh} and the total fluid density ρ that controls the strength of the fluid-fluid interaction. Systematic study of the dependence of phase separation on $G_{\text{coh}}\rho$ has been done, which shows that there is a threshold value for $G_{\text{coh}}\rho$, beyond which a stable immiscibility among different fluid phases can be achieved (Schaap et al., 2007; Huang et al., 2007). To determine the correspondence between $G_{\text{coh}}\rho_{\text{total}}$ to the macroscopic interfacial tension, a calibration such as a bubble test is needed.

Similarly, the fluid-solid interaction force $\mathbf{F}_k^{\text{ads}}$ takes the form as:

$$\mathbf{F}_k^{\text{ads}}(\mathbf{x}, t) = -G_{\text{ads},k} \rho_k(\mathbf{x}, t) \sum_i t_i s(\mathbf{x} + \boldsymbol{\xi}_i \delta_t, t) \boldsymbol{\xi}_i, \quad (2.57)$$

where $s(\mathbf{x}, t)$ is an indicator function that is 1 for a solid node and 0 for a fluid node, and $G_{\text{ads},k}$ is the adhesion coefficient that controls the surface force for k_{th} fluid component. The adhesion coefficients for the non-wetting and wetting phases should satisfy $G_{\text{ads},\text{nw}} - G_{\text{ads},\text{w}} > 0$, and setting $G_{\text{ads},\text{nw}} = G_{\text{ads},\text{w}}$ models a neutral wetting condition. For simulations in this thesis, we choose to set $G_{\text{ads},\text{w}} = 0$ and vary $G_{\text{ads},\text{nw}}$ between 0 and 1; another common parametrisation, which is to set $G_{\text{ads},\text{nw}} = -G_{\text{ads},\text{w}}$ (Pan, Hilpert, and Miller, 2004; Huang et al., 2007), is in fact equivalent to our setting, provided that $|G_{\text{ads},\text{nw}} - G_{\text{ads},\text{w}}|$ is same in two cases.

For D3Q19 lattice, the overall pressure, for example in a two-phase system is given by:

$$P(\mathbf{x}) = c_s^2(\rho_1 + \rho_2) + \frac{G_{\text{coh}}\rho_1\rho_2}{3}, \quad (2.58)$$

which is determined by the sum of two fluids, with an extra non-linear term considering the non-ideal gas law that explicitly depends on the fluid-fluid cohesive interactions. The total macroscopic fluid velocity \mathbf{u} is given by $\rho\mathbf{u} = \sum_k \rho_k \mathbf{u}_k + \frac{1}{2} \sum_k \mathbf{F}_k$. Overall, for SC model, the input parameters for a two-phase system include G_{coh} , which controls the strength of macroscopic surface tension, and $G_{\text{ads,nw}}$ and $G_{\text{ads,w}}$ that realise different wetting conditions.

2.3.2 Rothman-Keller Model

The RK model, also known as the colour-gradient model, was the first multicomponent lattice-Boltzmann model, originally proposed by Gunstensen et al. (1991) as a development of the lattice gas model (Rothman and Keller, 1988), and was further developed by Grunau, Chen, and Eggert (1993) to incorporate variable density and viscosity ratios. The RK model has been criticised for its larger spurious current at the phase interface than that of SC model (Hou et al., 1997) and a “lattice pinning” phenomenon that results in a loss of Galilean invariance (Latva-Kokko and Rothman, 2005a). It was not until Latva-Kokko and Rothman (2005a) revised the recolouring step in the collision operator for RK model that these issues were effectively addressed. Generally, in the context of RK model, fluid particles of different species are labelled as red and blue fluid particles, with particle distribution functions of f_i^R and f_i^B , respectively. The collision operator for RK model consists of three parts (Liu, Valocchi, and Kang, 2012):

$$\Omega_i^k = (\Omega_i^k)^{(3)}[(\Omega_i^k)^{(1)} + (\Omega_i^k)^{(2)}], \quad (2.59)$$

where the superscript k is either R or B for red or blue fluid, respectively. $(\Omega_i^k)^{(1)}$ is the normal single-relaxation-time BGK collision operator which has the same form as for SC model (i.e. equation (2.51)), and the kinematic viscosity for each fluid component is still $\nu_{R,B} = (2\tau_{R,B} - 1)/6$. $(\Omega_i^k)^{(2)}$ is the perturbation operator that produces interfacial tension, while $(\Omega_i^k)^{(3)}$ is the recolouring operator that forces particles of each fluid to congregate together to ensure immiscibility.

The macroscopic density for k_{th} fluid component is given by $\rho_k = \sum_i f_i^k$, and the total fluid density is $\rho = \rho_R + \rho_B$. In the BGK collision operator $(\Omega_i^k)^{(1)}$, the equilibrium distribution function $f_i^{k,eq}$ is defined the same as in equation (2.52) for SC model, except that \mathbf{u}_k^{eq} is replaced with the total macroscopic fluid velocity \mathbf{u} , which can be obtained from $\rho\mathbf{u} = \sum_i \sum_k f_i^k \xi_i$. The original perturbation operator $(\Omega_i^k)^{(2)}$ proposed by Gunstensen et al. (1991) and Grunau, Chen, and Eggert (1993) was designed for 2D hexagonal lattice, and it has been shown that a direct extension of it to D2Q9 or D3Q19 lattice cannot recover the Navier-Stokes equations for multiphase fluid flow. In this work we adopt an improved perturbation operator proposed by Liu, Valocchi, and Kang (2012) for D3Q19, which has been shown to recover the correct interfacial force term in the Navier-Stokes equations with reduced spurious current.

This $(\Omega_i^k)^{(2)}$ is given by:

$$(\Omega_i^k)^{(2)}(f_i^k) = f_i^k + \frac{A_k}{2} |\mathbf{G}| \left[t_i \frac{(\boldsymbol{\xi}_i \cdot \mathbf{G})^2}{|\mathbf{G}|^2} - B_i \right], \quad (2.60)$$

where A_k is a free parameter that controls the surface tension, and $B_0 = -1/3$, $B_{1-6} = 1/18$ and $B_{7-18} = 1/36$ from (Liu, Valocchi, and Kang, 2012). \mathbf{G} is the colour gradient, which is the gradient of the phase field: $\mathbf{G} = \nabla \Phi$, where the phase field is given by:

$$\Phi(\mathbf{x}, t) = \frac{\rho_R(\mathbf{x}, t) - \rho_B(\mathbf{x}, t)}{\rho_R(\mathbf{x}, t) + \rho_B(\mathbf{x}, t)}. \quad (2.61)$$

To minimise the discretisation error, the spatial derivative in the definition of the colour gradient \mathbf{G} is evaluated by applying 9-point difference stencils (Liu, Valocchi, and Kang, 2012):

$$\mathbf{G}(\mathbf{x}) = 3 \sum_i t_i \Phi(\mathbf{x} + \boldsymbol{\xi}_i \delta_t) \boldsymbol{\xi}_i. \quad (2.62)$$

The recolouring operator $(\Omega_i^k)^{(3)}$ modified by Latva-Kokko and Rothman (2005a) is defined as follows:

$$(\Omega_i^k)^{(3)}(f_i^R) = \frac{\rho_R}{\rho} f_i^* + \beta \frac{\rho_R \rho_B}{\rho^2} \cos(\varphi_i) \sum_k f_i^{k,eq}|_{\mathbf{u}=0}, \quad (2.63a)$$

$$(\Omega_i^k)^{(3)}(f_i^B) = \frac{\rho_B}{\rho} f_i^* - \beta \frac{\rho_R \rho_B}{\rho^2} \cos(\varphi_i) \sum_k f_i^{k,eq}|_{\mathbf{u}=0}, \quad (2.63b)$$

where f_i^* is the total particle distribution function after BGK collision and perturbation steps, but prior to the streaming. β is another free parameter that controls the thickness of the phase interface (the interface becomes thicker as β decreases), and it is suggested to be between 0 and 1 to ensure the positive distribution functions and numerical stability. The values of β is 1 in this work. φ_i is the angle between the colour gradient and discrete velocity vectors, which can be obtained from:

$$\cos(\varphi_i) = \frac{\boldsymbol{\xi}_i \cdot \mathbf{G}}{|\boldsymbol{\xi}_i| |\mathbf{G}|}. \quad (2.64)$$

The macroscopic surface tension in RK model can be derived analytically, and is linked to the model parameter A_k by (Liu, Valocchi, and Kang, 2012):

$$\gamma = \frac{2}{9} (A_R + A_B) \tau, \quad (2.65)$$

where $\tau_R = \tau_B = \tau$ is assumed, and in this work $A_R = A_B$ is set for simplicity. The contact angle is related to the phase field on the wall nodes, and is predicted by (Latva-Kokko and Rothman, 2005b):

$$\cos \theta = \Phi(\mathbf{x}_{\text{wall}}) = \frac{\rho_{\text{wall,R}} - \rho_{\text{wall,B}}}{\rho_{\text{wall,R}} + \rho_{\text{wall,B}}}, \quad (2.66)$$

where $\rho_{\text{wall},R}$ and $\rho_{\text{wall},B}$ are densities of red and blue fluids on wall nodes. The pressure for k_{th} fluid is $p_k = c_s^2 \rho_k$ and the overall pressure is given by:

$$P(\mathbf{x}) = c_s^2(\rho_R + \rho_B). \quad (2.67)$$

Overall, for RK model, the input parameter for a two-phase system include A_R and A_B that determine the macroscopic surface tension, β that controls the phase interfacial thickness, and $\rho_{\text{wall},R}$ and $\rho_{\text{wall},B}$ that realise different wetting conditions.

A distinct feature of the RK model is that macroscopic physical quantities, such as surface tension and contact angle can be predicted in advance, unlike the SC model where the relation between macroscopic quantities and model parameters (i.e. G_{coh} and G_{ads}) can only be obtained through a set of calibrations.

2.4 Multi-Relaxation-Time Multiphase Lattice-Boltzmann Methods

In this section, a colour-gradient based multi-relaxation-time model is introduced. The algorithm-wise implementation of this MRT-LB model has been presented in detail in McClure, Prins, and Miller (2014), however, a systematic theoretical study on the macroscopically recovered momentum and mass transport equations and the associated errors (due to truncation of higher order terms) is still lacking in the literature. Therefore, here we focus on the derivation of recovering the macroscopic momentum transport (i.e. Navier-Stokes equation) and the mass transport (i.e. the continuity equation). Overall, the MRT-LB model by McClure, Prins, and Miller (2014) is an efficient two-phase model, by simultaneously solving the momentum and the mass transport equations on separate LB lattices to maximise the computation efficiency. These two equations are coupled via the colour gradient, which is the key element that gives rise to the interfacial tension. The momentum transport equation is solved for the distribution of pressure and velocity fields, while the mass transport is solved for the phase field, which indicates the evolution of the interface in an incompressible fluid context. In the following two sub-sections, using the standard Chapman-Enskog analysis (Chapman, Burnett, and Cowling, 1970; Mohamad, 2011; Huang and Ding, 2008), the derivations from the respective LB evolution equation to the corresponding macroscopic transport equation will be presented in detail.

2.4.1 Momentum Transport with Surface Tension Force

The MRT-LB evolution equation that accounts for the two-phase momentum transport is given by:

$$f_i(\mathbf{x} + \boldsymbol{\xi}_i \delta_t, t + \delta_t) - f_i(\mathbf{x}, t) = -\Lambda_{ij} \left[f_j(\mathbf{x}, t) - f_j^{(\text{eq})}(\mathbf{x}, t) \right]. \quad (2.68)$$

In order to recover its macroscopic counterpart, we first Taylor expand the equation above up to $\mathcal{O}(\epsilon^2)$: (Guo and Shu, 2013)

$$D_i f_i + \frac{\delta_t}{2} D_i^2 f_i = -\Lambda'_{ij}(f_j - f_j^{(\text{eq})}), \quad (2.69)$$

where $D_i = \partial_t + e_{i\alpha} \partial_\alpha$, and $\Lambda'_{ij} = \Lambda_{ij}/\delta_t$. If writing the equation above in a ‘bra-ket’ vector form, it becomes:

$$\mathbf{D} |\mathbf{f}\rangle + \frac{\delta_t}{2} \mathbf{D}^2 |\mathbf{f}\rangle = -\mathbf{\Lambda}'(|\mathbf{f}\rangle - |\mathbf{f}^{(\text{eq})}\rangle), \quad (2.70)$$

where $\mathbf{D} = \text{diag}\{\mathbf{D}_0, \mathbf{D}_1, \dots, \mathbf{D}_{18}\}$, and $\mathbf{\Lambda}' = \mathbf{\Lambda}'/\delta_t$. In the moment space of the distribution, we have correspondingly:

$$\hat{\mathbf{D}} |\mathbf{m}\rangle + \frac{\delta_t}{2} \hat{\mathbf{D}}^2 |\mathbf{m}\rangle = -\mathbf{S}'(|\mathbf{m}\rangle - |\mathbf{m}^{(\text{eq})}\rangle), \quad (2.71)$$

where $\hat{\mathbf{D}} = \mathbf{M} \mathbf{D} \mathbf{M}^{-1} = \partial_t \mathbb{I} + \hat{\mathbf{C}}_\alpha \partial_\alpha$, $\hat{\mathbf{C}}_\alpha = \mathbf{M} \mathbf{C}_\alpha \mathbf{M}^{-1}$, $\mathbf{C}_\alpha = \text{diag}\{\xi_{0\alpha}, \xi_{1\alpha}, \dots, \xi_{18\alpha}\}$, \mathbb{I} is the identity tensor, and $\mathbf{S}' = \mathbf{S}/\delta_t$, where \mathbf{S} is the relaxation parameter which, for D3Q19 lattice being implemented in our LB code, is given by: (d’Humières et al., 2002)

$$\mathbf{S} = \text{diag}(0, s_e, s_\varepsilon, 0, s_q, 0, s_q, 0, s_q, s_\nu, s_\pi, s_\nu, s_\pi, s_\nu, s_\nu, s_\nu, s_m, s_m, s_m), \quad (2.72)$$

and the moments for D3Q19 lattice are given by:

$$|\mathbf{m}\rangle = (\delta\rho, e, \varepsilon, j_x, q_x, j_y, q_y, j_z, q_z, 3p_{xx}, 3\pi_{xx}, p_{ww}, \pi_{ww}, p_{xy}, p_{yz}, p_{xz}, m_x, m_y, m_z)^T, \quad (2.73)$$

where the ‘ket’ notation indicates a column vector. The above 19 moments are the density variation ($m_0 = \delta\rho$) which literally just gives the pressure variation¹ $\delta p = c_s^2 \delta\rho = \delta\rho/3$, the part of the kinetic energy independent of the density ($m_1 = e$), the part of the kinetic energy square independent of the density and kinetic energy ($m_2 = \varepsilon = e^2$), the momentum flux ($m_{3,5,7} = j_{x,y,z}$), the energy flux ($m_{4,6,8} = q_{x,y,z}$), the symmetric traceless viscous stress tensor ($m_9 = 3p_{xx}$, $m_{11} = p_{ww}$, and $m_{13,14,15} = p_{xy,yz,xz}$), the vectors of quadratic order ($m_{10} = 3\pi_{xx}$, and $m_{12} = \pi_{ww}$), and the vectors of cubic order ($m_{16,17,18} = m_{x,y,z}$) (d’Humières et al., 2002).

The equilibrium moment functions in D3Q19 lattice with the surface tension terms are as follows (Tölke, Freudiger, and Krafczyk, 2006; Ahrenholz et al., 2008; McClure,

¹First, note that in our MRT based multicomponent LB model, the LB speed of sound c_s that relates the density variation to the pressure variation, is merely a mathematical constant from the standard Chapman-Enskog analysis used to recover the macroscopic equation, and does not resemble any physical meaning in a classic thermodynamics context. Therefore, in many literature, e.g. in Ahrenholz et al. (2008), the introduction of c_s is even skipped and simply $\delta p = \delta\rho/3$ is given, to avoid any confusion. Second, although the first moment $\delta\rho$ is called the density variation in the original work by d’Humières et al. (2002), our MRT model only deals with strictly incompressible fluid with constant density, and the existence of $\delta\rho$ is only for calculating the pressure field by $\delta p = \delta\rho/3$.

Prins, and Miller, 2014):

$$m_0^{(\text{eq})} = \delta\rho, \quad (2.74\text{a})$$

$$m_1^{(\text{eq})} = e^{(\text{eq})} = -11\delta\rho + \frac{19}{\rho_0}(j_x^2 + j_y^2 + j_z^2) - 19\alpha|\nabla\phi|, \quad (2.74\text{b})$$

$$m_2^{(\text{eq})} = \varepsilon^{(\text{eq})} = w_\varepsilon\delta\rho + \frac{w_\varepsilon j}{\rho_0} \mathbf{j} \cdot \mathbf{j}, \quad (2.74\text{c})$$

$$m_3^{(\text{eq})} = j_x = \rho_0 u_x, \quad (2.74\text{d})$$

$$m_5^{(\text{eq})} = j_y = \rho_0 u_y, \quad (2.74\text{e})$$

$$m_7^{(\text{eq})} = j_z = \rho_0 u_z, \quad (2.74\text{f})$$

$$m_4^{(\text{eq})} = -\frac{2}{3}j_x, \quad (2.74\text{g})$$

$$m_6^{(\text{eq})} = -\frac{2}{3}j_y, \quad (2.74\text{h})$$

$$m_8^{(\text{eq})} = -\frac{2}{3}j_z, \quad (2.74\text{i})$$

$$\begin{aligned} m_9^{(\text{eq})} &= 3P_{xx}^{(\text{eq})} + \frac{1}{2}\alpha|\nabla\phi|(2n_x^2 - n_y^2 - n_z^2) \\ &= \frac{1}{\rho_0} [2j_x^2 - (j_y^2 + j_z^2)] + \frac{1}{2}\alpha|\nabla\phi|(2n_x^2 - n_y^2 - n_z^2), \end{aligned} \quad (2.74\text{j})$$

$$m_{11}^{(\text{eq})} = P_{ww}^{(\text{eq})} + \frac{1}{2}\alpha|\nabla\phi|(n_y^2 - n_z^2) = \frac{1}{\rho_0}(j_y^2 - j_z^2) + \frac{1}{2}\alpha|\nabla\phi|(n_y^2 - n_z^2), \quad (2.74\text{k})$$

$$m_{13}^{(\text{eq})} = P_{xy}^{(\text{eq})} + \frac{1}{2}\alpha|\nabla\phi|n_x n_y = \frac{j_x j_y}{\rho_0} + \frac{1}{2}\alpha|\nabla\phi|n_x n_y, \quad (2.74\text{l})$$

$$m_{14}^{(\text{eq})} = P_{yz}^{(\text{eq})} + \frac{1}{2}\alpha|\nabla\phi|n_y n_z = \frac{j_y j_z}{\rho_0} + \frac{1}{2}\alpha|\nabla\phi|n_y n_z, \quad (2.74\text{m})$$

$$m_{15}^{(\text{eq})} = P_{xz}^{(\text{eq})} + \frac{1}{2}\alpha|\nabla\phi|n_x n_z = \frac{j_x j_z}{\rho_0} + \frac{1}{2}\alpha|\nabla\phi|n_x n_z, \quad (2.74\text{n})$$

$$m_{10}^{(\text{eq})} = 3\pi_{xx}^{(\text{eq})} = 3w_{xx}P_{xx}^{(\text{eq})}, \quad (2.74\text{o})$$

$$m_{12}^{(\text{eq})} = \pi_{ww}^{(\text{eq})} = w_{xx}P_{ww}^{(\text{eq})}, \quad (2.74\text{p})$$

$$m_{16}^{(\text{eq})} = m_x^{(\text{eq})} = 0, \quad (2.74\text{q})$$

$$m_{17}^{(\text{eq})} = m_y^{(\text{eq})} = 0, \quad (2.74\text{r})$$

$$m_{18}^{(\text{eq})} = m_z^{(\text{eq})} = 0, \quad (2.74\text{s})$$

where $w_\varepsilon = 3$, $w_{\varepsilon j} = -11/2$, and $w_{xx} = 0$, according to d'Humières et al. (2002). Also, it is noted that the equilibrium moments m_1 , m_9 , m_{11} , m_{13} , m_{14} , and m_{15} are perturbed by adding the colour-gradient related terms to generate the correct surface tension force. In these perturbed terms, the phase field is defined as:

$$\phi = \frac{\rho_n - \rho_w}{\rho_n + \rho_w}, \quad (2.75)$$

and the corresponding unit normal vector of the colour gradient $\nabla\phi$ is given as:

$$\mathbf{n} = \frac{\nabla\phi}{|\nabla\phi|}. \quad (2.76)$$

Following the Chapman-Enskog analysis, we assume that the moment distribution functions can be expressed as:

$$|\mathbf{m}\rangle = \sum_{n=0}^{\infty} \epsilon^n |\mathbf{m}^{(n)}\rangle, \quad (2.77)$$

where ϵ is the smallness parameter, and it can be usually given by the Knudsen number (Kn), which is defined as the ratio of the molecular mean free path to the characteristic length of the fluid system. The time and space can also be expanded in the power series of the smallness parameter as:

$$\partial_t = \epsilon \partial_{t_1} + \epsilon^2 \partial_{t_2}, \quad (2.78)$$

and

$$\partial_\alpha = \epsilon \partial_{1\alpha}, \quad (2.79)$$

and then we can get the moment equations on different order of ϵ as follows:

$$|\mathbf{m}^{(0)}\rangle = |\mathbf{m}^{(\text{eq})}\rangle, \quad (2.80a)$$

$$\hat{D}_1 |\mathbf{m}^{(0)}\rangle = -\mathbf{S}' |\mathbf{m}^{(1)}\rangle, \quad (2.80b)$$

$$\partial_{t_2} |\mathbf{m}^{(0)}\rangle + \hat{D}_1 \left(\mathbf{I} - \frac{\mathbf{S}}{2} \right) |\mathbf{m}^{(1)}\rangle = -\mathbf{S}' |\mathbf{m}^{(2)}\rangle, \quad (2.80c)$$

on the order of $\mathcal{O}(\epsilon^0)$, $\mathcal{O}(\epsilon^1)$ and $\mathcal{O}(\epsilon^2)$, respectively, where $\hat{D}_1 = \partial_{t_1} \mathbf{I} + \hat{C}_\alpha \partial_{1\alpha}$. For the conserved moments we know that:

$$m_0^{(n)} = \delta \rho^{(n)} = 0, \quad (2.81a)$$

$$m_3^{(n)} = j_x^{(n)} = 0, \quad (2.81b)$$

$$m_5^{(n)} = j_y^{(n)} = 0, \quad (2.81c)$$

$$m_7^{(n)} = j_z^{(n)} = 0, \quad \text{for } n > 0, \quad (2.81d)$$

On the order of $\mathcal{O}(\epsilon^1)$, we have the conserved moment for m_0 :

$$\partial_{t_1} (\delta \rho) + \partial_{1x} (\rho_0 u_x) + \partial_{1y} (\rho_0 u_y) + \partial_{1z} (\rho_0 u_z) = 0, \quad (2.82)$$

for m_3 :

$$\begin{aligned} \partial_{t_1} (\rho_0 u_x) + \partial_{1x} \left[\delta p + \frac{j_x^2}{\rho_0} + \frac{1}{2} \alpha |\nabla \phi| \left(\frac{2}{3} n_x^2 - \frac{1}{3} n_y^2 - \frac{1}{3} n_z^2 - \frac{1}{3} \right) \right] \\ + \partial_{1y} \left[\frac{j_x j_y}{\rho_0} + \frac{1}{2} \alpha |\nabla \phi| n_x n_y \right] \\ + \partial_{1z} \left[\frac{j_y j_z}{\rho_0} + \frac{1}{2} \alpha |\nabla \phi| n_y n_z \right] = 0, \end{aligned} \quad (2.83)$$

for m_5 :

$$\begin{aligned} \partial_{t_1}(\rho_0 u_y) + \partial_{1x} \left[\frac{j_x j_y}{\rho_0} + \frac{1}{2} \alpha |\nabla \phi| n_x n_y \right] \\ + \partial_{1y} \left[\delta p + \frac{j_y^2}{\rho_0} + \frac{1}{2} \alpha |\nabla \phi| \left(-\frac{1}{3} n_x^2 + \frac{2}{3} n_y^2 - \frac{1}{3} n_z^2 - \frac{1}{3} \right) \right] \\ + \partial_{1z} \left[\frac{j_y j_z}{\rho_0} + \frac{1}{2} \alpha |\nabla \phi| n_y n_z \right] = 0, \end{aligned} \quad (2.84)$$

and for m_7 :

$$\begin{aligned} \partial_{t_1}(\rho_0 u_z) + \partial_{1x} \left[\frac{j_x j_z}{\rho_0} + \frac{1}{2} \alpha |\nabla \phi| n_x n_z \right] \\ + \partial_{1y} \left[\frac{j_y j_z}{\rho_0} + \frac{1}{2} \alpha |\nabla \phi| n_y n_z \right] \\ + \partial_{1z} \left[\delta p + \frac{j_z^2}{\rho_0} + \frac{1}{2} \alpha |\nabla \phi| \left(-\frac{1}{3} n_x^2 - \frac{1}{3} n_y^2 + \frac{2}{3} n_z^2 - \frac{1}{3} \right) \right] = 0. \end{aligned} \quad (2.85)$$

where the following relation

$$\delta p = c_s^2 \delta \rho = \delta \rho / 3, \quad (2.86)$$

is used for the fluid pressure variation (also see the footnote when introducing equation 2.73). It is noted that although the density variation $\delta \rho$ is constantly seen here during the derivation, it is the pressure variation δp (and its distribution) that is of key interest in the modelling. Hence, although on the order of $\mathcal{O}(\epsilon^1)$, from equation 2.82 we have recovered the continuity equation as follows:

$$\partial_{t_1}(\delta \rho) + \partial_{1\alpha}(\rho_0 u_\alpha) = 0, \quad (2.87)$$

it can be seen as a by-product when performing Chapman-Enskog analysis on the LB evolution equation 2.68. What $\delta \rho$ really gives is the pressure field $\delta p = \delta \rho / 3$, and the fluid density is always a constant in our incompressible LB model. The actual mass transport is modelled by a separate LB evolution equation 2.114 which will be discussed in the next sub-section.

Also, from equations 2.83, 2.84, and 2.85, given that $n_x^2 + n_y^2 + n_z^2 = 1$, we can recover the Euler equation with the continuum surface force $\mathbf{F} = \nabla \cdot \mathbf{S}$, where \mathbf{S} is the capillary stress tensor:

$$\partial_{t_1}(\rho_0 u_\alpha) + \partial_{1\beta}(\rho_0 u_\alpha u_\beta) = -\partial_{1\alpha}(\delta p) + \partial_{1\beta} S_{\alpha\beta}, \quad (2.88)$$

where the capillary pressure tensor \mathbf{S} takes the form as:

$$S_{\alpha\beta} = \frac{1}{2} \alpha |\nabla \phi| (\delta_{\alpha\beta} - n_\alpha n_\beta), \quad (2.89)$$

or in the matrix form as:

$$S_{\alpha\beta} = \frac{1}{2}\alpha|\nabla\phi| \begin{pmatrix} n_y^2 + n_z^2 & -n_x n_y & -n_x n_z \\ -n_x n_y & n_x^2 + n_z^2 & -n_y n_z \\ -n_x n_z & -n_y n_z & n_x^2 + n_y^2 \end{pmatrix}, \quad (2.90)$$

which satisfies the required isotropy for an interfacial force (Reis and Phillips, 2007).

On the order of $\mathcal{O}(\epsilon^2)$, we have for the conserved moment m_0 :

$$\partial_{t_2}(\delta\rho) = 0, \quad (2.91)$$

for m_3 :

$$\begin{aligned} \partial_{t_2}(\rho_0 u_x) + \partial_{1x} \left[\frac{1}{19} \times \frac{1}{3} \left(1 - \frac{s_e}{2} \right) e^{(1)} + \left(1 - \frac{s_\nu}{2} \right) P_{xx}^{(1)} \right] \\ + \partial_{1y} \left[\left(1 - \frac{s_\nu}{2} \right) P_{xy}^{(1)} \right] \\ + \partial_{1z} \left[\left(1 - \frac{s_\nu}{2} \right) P_{xz}^{(1)} \right] = 0, \end{aligned} \quad (2.92)$$

for m_5 :

$$\begin{aligned} \partial_{t_2}(\rho_0 u_y) + \partial_{1x} \left[\left(1 - \frac{s_\nu}{2} \right) P_{xy}^{(1)} \right] \\ + \partial_{1y} \left[\frac{1}{19} \times \frac{1}{3} \left(1 - \frac{s_e}{2} \right) e^{(1)} + \frac{1}{2} \left(1 - \frac{s_\nu}{2} \right) (P_{ww}^{(1)} - P_{xx}^{(1)}) \right] \\ + \partial_{1z} \left[\left(1 - \frac{s_\nu}{2} \right) P_{yz}^{(1)} \right] = 0, \end{aligned} \quad (2.93)$$

and for m_7 :

$$\begin{aligned} \partial_{t_2}(\rho_0 u_z) + \partial_{1x} \left[\left(1 - \frac{s_\nu}{2} \right) P_{xz}^{(1)} \right] \\ + \partial_{1y} \left[\left(1 - \frac{s_\nu}{2} \right) P_{yz}^{(1)} \right] \\ + \partial_{1z} \left[\frac{1}{19} \times \frac{1}{3} \left(1 - \frac{s_e}{2} \right) e^{(1)} - \frac{1}{2} \left(1 - \frac{s_\nu}{2} \right) (P_{ww}^{(1)} + P_{xx}^{(1)}) \right] = 0. \end{aligned} \quad (2.94)$$

where $e^{(1)}$, $P_{xx}^{(1)}$, $P_{xy}^{(1)}$, $P_{yz}^{(1)}$, $P_{xz}^{(1)}$, and $P_{ww}^{(1)}$ are to be determined from the equations on $\mathcal{O}(\epsilon^1)$.

Before solving for the terms $e^{(1)}$ and so on, note that from the recovered Euler equation 2.88, we can get a relation which turns out to be very useful for the subsequent derivations²:

$$\partial_{t_1}(\rho_0 u_\alpha u_\alpha) = -u_\alpha \partial_{1\beta}(\delta p) - u_\beta \partial_{1\alpha}(\delta p) + \mathcal{O}(u^3), \quad (2.95)$$

where $\mathcal{O}(u^3)$ will be omitted, and some order-of-magnitude relations (i.e. $\delta\rho \sim \mathcal{O}(u)$,

²However, to obtain this relation it in fact requires $\delta\rho = \rho_0$, which implies that our current MRT-LBM model is not fully compatible with the presumed incompressible setting. The derivation of the relation is shown at the end of this sub-section.

$\delta p \sim \mathcal{O}(u^3)$, $S_{\alpha\beta} \sim \mathcal{O}(u^3)$) are used to give the equation above. Equipped with equation (2.95), we have:

$$e^{(1)} = -38 \times \frac{\delta_t}{s_e} (\delta p \partial_{1x} u_x + \delta p \partial_{1y} u_y + \delta p \partial_{1z} u_z), \quad (2.96a)$$

$$P_{xx}^{(1)} = -\frac{\delta_t}{3s_\nu} (4\delta p \partial_{1x} u_x - 2\delta p \partial_{1y} u_y - 2\delta p \partial_{1z} u_z), \quad (2.96b)$$

$$P_{ww}^{(1)} = -\frac{\delta_t}{s_\nu} (2\delta p \partial_{1y} u_y - 2\delta p \partial_{1z} u_z), \quad (2.96c)$$

$$P_{xy}^{(1)} = -\frac{\delta_t}{s_\nu} (\delta p \partial_{1x} u_y + \delta p \partial_{1y} u_x), \quad (2.96d)$$

$$P_{yz}^{(1)} = -\frac{\delta_t}{s_\nu} (\delta p \partial_{1y} u_z + \delta p \partial_{1z} u_y), \quad (2.96e)$$

$$P_{xz}^{(1)} = -\frac{\delta_t}{s_\nu} (\delta p \partial_{1x} u_z + \delta p \partial_{1z} u_x). \quad (2.96f)$$

The above equations are derived from the Euler equation 2.88 by neglecting the surface tension term since $S_{\alpha\beta} \sim \mathcal{O}(u^3)$.

Now substituting equation (2.96) into equation (2.92) we get on $\mathcal{O}(\epsilon^2)$ for m_3 :

$$\begin{aligned} \partial_{t_2}(\rho_0 u_x) &= \partial_{1x} \left[2\delta\rho\nu \left(\partial_{1x} u_x - \frac{1}{3} \nabla \cdot \mathbf{u} \right) + \delta\rho\zeta(\nabla \cdot \mathbf{u}) \right] \\ &\quad + \partial_{1y} [\delta\rho\nu(\partial_{1x} u_y + \partial_{1y} u_x)] \\ &\quad + \partial_{1z} [\delta\rho\nu(\partial_{1x} u_z + \partial_{1z} u_x)], \end{aligned} \quad (2.97)$$

and substituting equation (2.96) into equation (2.93) we have on $\mathcal{O}(\epsilon^2)$ for m_5 :

$$\begin{aligned} \partial_{t_2}(\rho_0 u_y) &= \partial_{1x} [\delta\rho\nu(\partial_{1x} u_y + \partial_{1y} u_x)] \\ &\quad + \partial_{1y} \left[2\delta\rho\nu \left(\partial_{1y} u_y - \frac{1}{3} \nabla \cdot \mathbf{u} \right) + \delta\rho\zeta(\nabla \cdot \mathbf{u}) \right] \\ &\quad + \partial_{1z} [\delta\rho\nu(\partial_{1y} u_z + \partial_{1z} u_y)], \end{aligned} \quad (2.98)$$

and substituting equation (2.96) into equation (2.94) we have on $\mathcal{O}(\epsilon^2)$ for m_7 :

$$\begin{aligned} \partial_{t_2}(\rho_0 u_z) &= \partial_{1x} [\delta\rho\nu(\partial_{1x} u_z + \partial_{1z} u_x)] \\ &\quad + \partial_{1y} [\delta\rho\nu(\partial_{1y} u_z + \partial_{1z} u_y)] \\ &\quad + \partial_{1z} \left[2\delta\rho\nu \left(\partial_{1z} u_z - \frac{1}{3} \nabla \cdot \mathbf{u} \right) + \delta\rho\zeta(\nabla \cdot \mathbf{u}) \right], \end{aligned} \quad (2.99)$$

where the kinematic shear viscosity is given by:

$$\nu = \frac{1}{3} \left(\frac{1}{s_\nu} - \frac{1}{2} \right) \delta_t, \quad (2.100)$$

and the kinematic bulk viscosity is given by

$$\zeta = \frac{2}{9} \left(\frac{1}{s_e} - \frac{1}{2} \right) \delta_t. \quad (2.101)$$

To enable various viscosity ratios between two phases, we set the LB kinematic viscosity a linear interpolation spatially dependent on the phase field value: (Tölke, Prisco, and Mu, 2013)

$$\nu = \frac{1+\phi}{2}\nu_{\text{nw}} + \frac{1-\phi}{2}\nu_{\text{w}}, \quad (2.102)$$

and if choosing $\rho_{\text{nw}} = \rho_{\text{w}} = 1.0$, the viscosity ratio is simply $M = \nu_{\text{nw}}/\nu_{\text{w}}$, which can be achieved by using prescribed $s_{\nu,\text{nw}}$ and $s_{\nu,\text{w}}$.

Following the reported work by Ginzburg and d'Humières (2003), the relaxation rates in our model is set in a ‘two-relaxation-time’ (TRT) fashion as:

$$s_e = s_\varepsilon = s_\pi = s_\nu, \quad s_q = s_m = 8 \frac{(2 - s_\nu)}{(8 - s_\nu)}. \quad (2.103)$$

In summary, combining the equations on $\mathcal{O}(\epsilon^1)$ and $\mathcal{O}(\epsilon^2)$ we obtain the continuity equation:

$$\partial_t(\delta\rho) + \partial_\alpha(\rho_0 u_\alpha) = 0, \quad (2.104)$$

and for the momentum transport we have:

$$\partial_t(\rho_0 u_\alpha) + \partial_\beta(\rho_0 u_\alpha u_\beta) = -\partial_\alpha p + \partial_\beta \sigma_{\alpha\beta} + \partial_\beta S_{\alpha\beta}, \quad (2.105)$$

where the viscous stress tensor $\sigma_{\alpha\beta}$ is given by:

$$\sigma_{\alpha\beta} = (\delta\rho)\nu \left[(\partial_\alpha u_\beta + \partial_\beta u_\alpha) - \frac{2}{3} \partial_\gamma u_\gamma \delta_{\alpha\beta} \right] + (\delta\rho)\zeta \partial_\gamma u_\gamma \delta_{\alpha\beta}, \quad (2.106)$$

and the capillary stress tensor $S_{\alpha\beta}$ is given by:

$$S_{\alpha\beta} = \frac{1}{2} \alpha |\nabla\phi| (\delta_{\alpha\beta} - n_\alpha n_\beta). \quad (2.107)$$

Incidental Note

This note introduces how the equation 2.95 is obtained. The contribution of this part of the thesis is to identify a critical constraint of the current MRT-LB formulation, which also applies to other variants of MRT-LB models by Tölke, Freudiger, and Krafczyk (2006), Ahrenholz et al. (2008), and Tsuji, Jiang, and Christensen (2016). It has an important implication on the simulation of non-unitary density ratio cases.

Multiplying equation 2.88 by another set of velocity we can get:

$$\underbrace{u_\gamma \partial_{t_1}(\rho_0 u_\alpha)}_{=\partial_{t_1}(\rho_0 u_\alpha u_\gamma) - \rho_0 u_\alpha \partial_{t_1} u_\gamma} + \underbrace{u_\gamma \partial_{1\beta}(\rho_0 u_\alpha u_\beta)}_{=\partial_{1\beta}(\rho_0 u_\alpha u_\beta u_\gamma) - \rho_0 u_\alpha u_\beta \partial_{1\beta} u_\gamma} = -u_\gamma \partial_{1\alpha}(\delta p), \quad (2.108)$$

Then rearranging the equation above we get:

$$\partial_{t_1}(\rho_0 u_\alpha u_\gamma) = \underbrace{\rho_0 u_\alpha \partial_{t_1} u_\gamma + \rho_0 u_\alpha u_\beta \partial_{1\beta} u_\gamma}_{\text{call it } \Pi_{\alpha\gamma}} - \partial_{1\beta}(\rho_0 u_\alpha u_\beta u_\gamma) - u_\gamma \partial_{1\alpha}(\delta p). \quad (2.109)$$

The simplification of the term $\Pi_{\alpha\gamma}$ is as follows:

$$\begin{aligned}
\Pi_{\alpha\gamma} &= u_\alpha [\rho_0 \partial_{t_1} u_\gamma + \rho_0 u_\beta \partial_{1\beta} u_\gamma] \\
&= u_\alpha [\partial_{t_1} (\rho_0 u_\gamma) - u_\gamma \partial_{t_1} \rho_0 + \partial_{1\beta} (\rho_0 u_\beta u_\gamma) - u_\gamma \partial_{1\beta} (\rho_0 u_\beta)] \\
&= u_\alpha [\partial_{t_1} (\rho_0 u_\gamma) + \partial_{1\beta} (\rho_0 u_\beta u_\gamma) - u_\gamma \partial_{t_1} \rho_0 - u_\gamma \partial_{1\beta} (\rho_0 u_\beta)] \\
&= -u_\alpha \partial_{1\gamma} (\delta p) - u_\alpha u_\gamma [\partial_{t_1} \rho_0 + \partial_{1\beta} (\rho_0 u_\beta)],
\end{aligned} \tag{2.110}$$

where the second term on the right-hand side is zero if $\delta\rho = \rho_0$, since on the order of $\mathcal{O}(\epsilon^1)$ we have recovered $\partial_{t_1}(\delta\rho) + \partial_{1\beta}(\rho_0 u_\beta) = 0$. Currently, the condition of $\delta\rho = \rho_0$ is obviously an incompatibility to the incompressible setting of the LB model: ρ_0 is the (constant) phase density which can be a linear interpolation spatially dependent on the phase field:

$$\rho_0 = \frac{1+\phi}{2}\rho_n + \frac{1-\phi}{2}\rho_w, \tag{2.111}$$

but $\delta\rho$ is the pressure variation (or more precisely, $\delta p = \delta\rho/3$); in other words, the pressure $\delta\rho$ and the density ρ_0 should have been completely decoupled, but they are currently subject to the constraint $\delta\rho = \rho_0$, in order to recover the targeted Navier-Stokes equation. For unitary density ratio, this constraint should not cause any problem since for pressure it is the difference that matters; for close-to-one density ratio, the error caused by this incompatibility may also be limited. However, future work is needed to appropriately resolve this issue, possibly by using some other approaches to model the case of non-unitary density ratio.

2.4.2 Mass Transport with Phase Segregation

The mass transport (i.e. convection-diffusion equation) is solved separately, using the velocity field from momentum transport as the input. To the author's knowledge, the study of the macroscopically recovered mass transport equation (incorporated with recolouring scheme) is still lacking in the literature, thus it is necessary to investigate the limitations and the associated error terms (due to higher-order truncation) to better understand the model behaviour. Similar to the momentum transport formulation, the mass transport is also modelled in a collision-streaming fashion, but on a D3Q7 lattice for more efficient computation. First, for D3Q7 lattice according to Wolfram (1986) the isotropic relations of the lattice take as follows:

$$\sum_i t_i = 1, \tag{2.112a}$$

$$\sum_i t_i e_{i\alpha} e_{i\beta} = k_2 |c|^2 \delta_{\alpha\beta}, \tag{2.112b}$$

$$\sum_i t_i e_{i\alpha} e_{i\beta} e_{i\gamma} e_{i\delta} = k_4 |c|^4 \delta_{\alpha\beta\gamma\delta}, \tag{2.112c}$$

where e_i is the discretised velocity for D3Q7 lattice with $i = 0, 1, 2, \dots, 6$, and its norm is $|e_i| = 1$. The weight coefficient is $t_0 = 1/3$ and $t_q = 1/9$ for $q = 1, 2, \dots, 6$. The LB speed of sound for D3Q7 lattice is $c_s^2 = 2/9$. The coefficient k_2 and k_4 are linked to

the lattice property as:

$$k_2|c|^2 = k_4|c|^2 = 2t_q|c|^2 = c_s^2 = 2/9. \quad (2.113)$$

The LB evolution equations are given by, for NW and W phases, respectively, as follows:

$$R_i(\mathbf{x} + \delta_t \mathbf{e}_i, t + \delta_t) - R_i(\mathbf{x}, t) = -\frac{\delta_t}{\tau_{m,nw}} \left[R_i(\mathbf{x}, t) - R_i^{(eq)}(\mathbf{x}, \mathbf{u}, t) \right], \quad (2.114a)$$

$$B_i(\mathbf{x} + \delta_t \mathbf{e}_i, t + \delta_t) - B_i(\mathbf{x}, t) = -\frac{\delta_t}{\tau_{m,w}} \left[B_i(\mathbf{x}, t) - B_i^{(eq)}(\mathbf{x}, \mathbf{u}, t) \right], \quad (2.114b)$$

where $\tau_{m,n}$ and $\tau_{m,w}$ are the relaxation parameters of mass transport for NW and W phases, respectively. Here we use R_i (short for ‘Red’) and B_i (short for ‘Blue’) to denote the distribution functions for NW and W phase, respectively. For simplicity we take $\tau_{m,n} = \tau_{m,w} = \tau_m$, and in the end we will take $\tau_m = 1$.

Firstly we can decouple the collision and the streaming steps explicitly as follows, the collision step is:

$$R_i^{\dagger\dagger}(\mathbf{x}, t) = R_i(\mathbf{x}, t) - \frac{1}{\tau_m} \left[R_i(\mathbf{x}, t) - R_i^{(eq)}(\mathbf{x}, \mathbf{u}, t) \right], \quad (2.115a)$$

$$B_i^{\dagger\dagger}(\mathbf{x}, t) = B_i(\mathbf{x}, t) - \frac{1}{\tau_m} \left[B_i(\mathbf{x}, t) - B_i^{(eq)}(\mathbf{x}, \mathbf{u}, t) \right], \quad (2.115b)$$

where the double dagger superscript denotes the post-collision, post-recolouring distribution functions. The streaming step is:

$$R_i(\mathbf{x} + \delta_t \mathbf{e}_i, t + \delta_t) = R_i^{\dagger\dagger}(\mathbf{x}, t), \quad (2.116a)$$

$$B_i(\mathbf{x} + \delta_t \mathbf{e}_i, t + \delta_t) = B_i^{\dagger\dagger}(\mathbf{x}, t). \quad (2.116b)$$

The equilibrium distribution function for the mass transport are given by:

$$R_i^{(eq)} = t_i \left[\rho_n \left(1 + \frac{\mathbf{e}_i \cdot \mathbf{u}}{c_s^2} \right) + \beta \frac{\rho_n \rho_w}{\rho_n + \rho_w} (\mathbf{n} \cdot \mathbf{e}_i) \right], \quad (2.117a)$$

$$B_i^{(eq)} = t_i \left[\rho_w \left(1 + \frac{\mathbf{e}_i \cdot \mathbf{u}}{c_s^2} \right) - \beta \frac{\rho_n \rho_w}{\rho_n + \rho_w} (\mathbf{n} \cdot \mathbf{e}_i) \right], \quad (2.117b)$$

where \mathbf{u} is the colour-blind macroscopic fluid velocity given by solving the momentum transport (i.e. the Navier-Stokes equation). The recolouring step, which promotes the phase separation, is embedded in the last term in R_i^{eq} and B_i^{eq} . The same coefficient β , which is also seen in equation 2.63 in the SRT-RK model, determines the thickness of the interfacial region. The unit normal vector of the colour gradient is given by:

$$\mathbf{n} = \frac{\nabla \phi}{|\nabla \phi|}, \quad (2.118)$$

where the phase field is defined as:

$$\phi = \frac{\rho_n - \rho_w}{\rho_n + \rho_w}. \quad (2.119)$$

Furthermore, the phase densities are given by:

$$\rho_n = \sum_i R_i, \quad \rho_w = \sum_i B_i, \quad (2.120)$$

and the phase density and the phase field can be linked as follows: (Halliday, Hollis, and Care, 2007)

$$\rho_n = \frac{1}{2}\rho(1 + \phi), \quad (2.121a)$$

$$\rho_w = \frac{1}{2}\rho(1 - \phi), \quad (2.121b)$$

where the colour-blind density $\rho = \rho_n + \rho_w$. According to the molecular capillary relation, for diffused flat interface, the one-dimensional theoretical phase field takes the form as follows: (Rowlinson and Widom, 1982; Anderson, McFadden, and Wheeler, 1998; Latva-Kokko and Rothman, 2005a; Halliday, Hollis, and Care, 2007)

$$\phi(x) = \tanh[\beta(x - x_0)], \quad (2.122)$$

where x_0 corresponds to the position of exact zero phase field. The 1D relation above can be well extended to a 2D lattice, e.g., D2Q9 (Halliday, Hollis, and Care, 2007), and since D3Q7 lattice only has orthogonal velocity links, the same extension applies as:

$$\phi(s) = \tanh(\beta s), \quad (2.123)$$

where s measures the distance in the direction of \mathbf{n} , with $s = 0$ corresponding to the centre of the interface. The actual phase field given by the LB model, however, is only an approximation of the theoretical relation above; nevertheless it still gives us an useful relation as follows:

$$\nabla\phi \approx \beta \operatorname{sech}^2(\beta s)\mathbf{n} = \beta(1 - \phi^2)\mathbf{n}. \quad (2.124)$$

The relation above will come very handy when dealing with one of the recolouring term:

$$\beta \left(\frac{\rho_n \rho_w}{\rho_n + \rho_w} \right) n_\alpha = \frac{\rho}{4} \partial_\alpha \phi, \quad (2.125)$$

since $\frac{\rho_n \rho_w}{\rho_n + \rho_w} = \frac{\rho}{4}(1 - \phi^2)$ according to equation 2.121.

Now we perform the Chapman-Enskog analysis for the mass transport LB equation 2.114. Again, assuming it is possible to expand the mass distribution functions as

follows:

$$R_i(\mathbf{x}, t) = \sum_{n=0}^{\infty} \epsilon^n R_i^{(n)}(\mathbf{x}, t), \quad (2.126a)$$

$$B_i(\mathbf{x}, t) = \sum_{n=0}^{\infty} \epsilon^n B_i^{(n)}(\mathbf{x}, t), \quad (2.126b)$$

where it is taken up to $n = 2$ for the following derivation, and the power expansions in time and space are similar to those for the momentum transport:

$$\partial_t = \epsilon \partial_{t_1} + \epsilon^2 \partial_{t_2}, \quad (2.127)$$

for time and

$$\partial_\alpha = \epsilon \partial_{1\alpha}, \quad (2.128)$$

where ϵ is again the smallness parameter which can be approximated by the Knudsen number (Kn). The Zeroth-order approximation of R_i and B_i are simply the equilibrium mass distributions given in equation 2.117. Then it is straightforward to work out some basic relations for NW and W phases (considering the lattice isotropic relations 2.112):

$$\sum_i R_i^{(0)} = \rho_n, \quad (2.129a)$$

$$\sum_i R_i^{(0)} e_{i\alpha} = \rho_n u_\alpha + k_2 \beta \frac{\rho_n \rho_w}{\rho_n + \rho_w} n_\alpha, \quad (2.129b)$$

$$\sum_i R_i^{(0)} e_{i\alpha} e_{i\beta} = c_s^2 \rho_n \delta_{\alpha\beta}, \quad (2.129c)$$

and similarly for the W phase:

$$\sum_i B_i^{(0)} = \rho_w, \quad (2.130a)$$

$$\sum_i B_i^{(0)} e_{i\alpha} = \rho_w u_\alpha - k_2 \beta \frac{\rho_n \rho_w}{\rho_n + \rho_w} n_\alpha, \quad (2.130b)$$

$$\sum_i B_i^{(0)} e_{i\alpha} e_{i\beta} = c_s^2 \rho_w \delta_{\alpha\beta}. \quad (2.130c)$$

Based on equation 2.129(a) and 2.130(a), it implies that:

$$\sum_i R_i^{(n \geq 1)} = 0, \quad \sum_i B_i^{(n \geq 1)} = 0. \quad (2.131)$$

However, it should be noted that the first- and second-order moments are not necessarily zero: $\sum_i R_i^{(n \geq 1)} e_{i\alpha} \neq 0$ and $\sum_i R_i^{(n \geq 1)} e_{i\alpha} e_{i\beta} \neq 0$. Furthermore, we can define some net mass flux terms, for example, the post-collision (i.e. equation 2.115) net mass flux as:

$$\mathbf{q}^{\dagger\dagger}(\mathbf{x}, t) = \mathbf{q}_R^{\dagger\dagger}(\mathbf{x}, t) - \mathbf{q}_B^{\dagger\dagger}(\mathbf{x}, t), \quad (2.132)$$

where

$$q_{R\alpha}^{\dagger\dagger} = \sum_i R_i^{\dagger\dagger} e_{i\alpha}, \quad q_{B\alpha}^{\dagger\dagger} = \sum_i B_i^{\dagger\dagger} e_{i\alpha}. \quad (2.133a)$$

Similarly we can also define post-propagation pre-collision (i.e. equation 2.116) net mass flux as:

$$\mathbf{q}(\mathbf{x}, t) = \mathbf{q}_R(\mathbf{x}, t) - \mathbf{q}_B(\mathbf{x}, t), \quad (2.134)$$

where

$$q_{R\alpha} = \sum_i R_i e_{i\alpha}, \quad q_{B\alpha} = \sum_i B_i e_{i\alpha}. \quad (2.135a)$$

Now let us work out the various net mass fluxes above. First, by just considering equation 2.115 we could already figure out the post-collision net mass flux $q_\alpha^{\dagger\dagger}$:

$$\begin{aligned} q_\alpha^{\dagger\dagger} &= \sum_i R_i^{\dagger\dagger}(\mathbf{x}, t) e_{i\alpha} - \sum_i B_i^{\dagger\dagger}(\mathbf{x}, t) e_{i\alpha} \\ &= \left(1 - \frac{1}{\tau_m}\right) \left[\sum_i R_i e_{i\alpha} - \sum_i B_i e_{i\alpha} \right] + \frac{1}{\tau_m} \left[\sum_i R_i^{(0)} e_{i\alpha} - \sum_i B_i^{(0)} e_{i\alpha} \right] \\ &= \left(1 - \frac{1}{\tau_m}\right) q_\alpha + \frac{1}{\tau_m} \left(\rho \phi u_\alpha + 2k_2 \beta \frac{\rho_n \rho_w}{\rho_n + \rho_w} n_\alpha \right), \end{aligned} \quad (2.136)$$

and if we take $\tau_m = 1$ we could immediately get:

$$\begin{aligned} q_\alpha^{\dagger\dagger} &= \rho \phi u_\alpha + 2k_2 \beta \frac{\rho_n \rho_w}{\rho_n + \rho_w} n_\alpha \\ &= \sum_i R_i^{(0)}(\mathbf{x}, t) e_{i\alpha} - \sum_i B_i^{(0)}(\mathbf{x}, t) e_{i\alpha}, \quad \text{for } \tau_m = 1. \end{aligned} \quad (2.137)$$

For q_α , however, it takes more algebra to work out, since it involves post-propagation (mass) distribution functions, i.e. $R_i(\mathbf{x}, t)$ and $B_i(\mathbf{x}, t)$, and solving $\sum_i R_i(\mathbf{x}, t) e_{i\alpha}$ directly is kind of troublesome since there is no formula that can be used. Nevertheless, the trick here is to note that these post-propagation distributions are equal to their pre-propagation counterparts $R_i^{\dagger\dagger}(\mathbf{x} - \mathbf{e}_i \delta_t, t - \delta_t)$ and $B_i^{\dagger\dagger}(\mathbf{x} - \mathbf{e}_i \delta_t, t - \delta_t)$, and solving for instance $\sum_i R_i^{\dagger\dagger}(\mathbf{x} - \mathbf{e}_i \delta_t, t - \delta_t) e_{i\alpha}$ is much easier since we can still utilise equation 2.115. Therefore we have:

$$\begin{aligned} q_\alpha &= \sum_i R_i(\mathbf{x}, t) e_{i\alpha} - \sum_i B_i(\mathbf{x}, t) e_{i\alpha} \\ &= \sum_i R_i^{\dagger\dagger}(\mathbf{x} - \mathbf{e}_i \delta_t, t - \delta_t) e_{i\alpha} - \sum_i B_i^{\dagger\dagger}(\mathbf{x} - \mathbf{e}_i \delta_t, t - \delta_t) e_{i\alpha}. \end{aligned} \quad (2.138)$$

To resolve equation 2.138, Halliday, Hollis, and Care (2007) introduces three approximations:

1. In the continuum applications, the interfacial phase field is always close to equilibrium such that the time variation can be neglected. This means that we can

ignore the δ_t time step difference and obtain:

$$R_i^{\dagger\dagger}(\mathbf{x} - \mathbf{e}_i \delta_t, t - \delta_t) \approx R_i^{\dagger\dagger}(\mathbf{x} - \mathbf{e}_i \delta_t, t), \quad (2.139a)$$

$$B_i^{\dagger\dagger}(\mathbf{x} - \mathbf{e}_i \delta_t, t - \delta_t) \approx B_i^{\dagger\dagger}(\mathbf{x} - \mathbf{e}_i \delta_t, t). \quad (2.139b)$$

2. Then we can Taylor expand the right-hand side of equation 2.139 and only retain up to the first-order spatial derivatives, which is the second approximation. Thus we have as follows:

$$R_i^{\dagger\dagger}(\mathbf{x} - \mathbf{e}_i \delta_t, t) \approx R_i^{\dagger\dagger}(\mathbf{x}, t) - \partial_{1\alpha}(R_i^{\dagger\dagger} e_{i\alpha}), \quad (2.140a)$$

$$B_i^{\dagger\dagger}(\mathbf{x} - \mathbf{e}_i \delta_t, t) \approx B_i^{\dagger\dagger}(\mathbf{x}, t) - \partial_{1\alpha}(B_i^{\dagger\dagger} e_{i\alpha}). \quad (2.140b)$$

3. The third approximation is, during the derivation of q_α shown below, to assume:

$$R_i(\mathbf{x}, t) \approx R_i^{(0)}(\mathbf{x}, t) + \epsilon R_i^{(1)}(\mathbf{x}, t), \quad (2.141a)$$

$$B_i(\mathbf{x}, t) \approx B_i^{(0)}(\mathbf{x}, t) + \epsilon B_i^{(1)}(\mathbf{x}, t), \quad (2.141b)$$

which means to neglect the higher-order terms $R_i^{(2)}$ and $B_i^{(2)}$. This approximation is mainly to simplify the calculation (which will come clear in the due part).

Based on the first two approximations above, the net mass flux for the post-propagation distributions are thus given as:

$$\begin{aligned} q_\alpha &\approx \sum_i \left[R_i^{\dagger\dagger}(\mathbf{x}, t) - B_i^{\dagger\dagger}(\mathbf{x}, t) \right] e_{i\alpha} - \partial_{1\beta} \sum_i \left[R_i^{\dagger\dagger}(\mathbf{x}, t) - B_i^{\dagger\dagger}(\mathbf{x}, t) \right] e_{i\alpha} e_{i\beta} \\ &= q_\alpha^{\dagger\dagger} - \partial_{1\beta} \sum_i \left[R_i^{\dagger\dagger}(\mathbf{x}, t) - B_i^{\dagger\dagger}(\mathbf{x}, t) \right] e_{i\alpha} e_{i\beta} \\ &= \rho \phi u_\alpha + 2k_2 \beta \frac{\rho_n \rho_w}{\rho_n + \rho_w} n_\alpha - \partial_{1\beta} \sum_i \left[R_i^{\dagger\dagger}(\mathbf{x}, t) - B_i^{\dagger\dagger}(\mathbf{x}, t) \right] e_{i\alpha} e_{i\beta}, \end{aligned} \quad (2.142)$$

where the first term in equation 2.142 is simply $q_\alpha^{\dagger\dagger}$, given by equation 2.137. For the second term of equation 2.142, we use equation 2.115 to replace $R_i^{\dagger\dagger}(\mathbf{x}, t)$ and $B_i^{\dagger\dagger}(\mathbf{x}, t)$:

$$\begin{aligned} R_i^{\dagger\dagger}(\mathbf{x}, t) - B_i^{\dagger\dagger}(\mathbf{x}, t) &= \left(1 - \frac{1}{\tau_m} \right) [R_i(\mathbf{x}, t) - B_i(\mathbf{x}, t)] + \frac{1}{\tau_m} [R_i^{(0)}(\mathbf{x}, t) - B_i^{(0)}(\mathbf{x}, t)] \\ &= [R_i^{(0)}(\mathbf{x}, t) - B_i^{(0)}(\mathbf{x}, t)] + \left(1 - \frac{1}{\tau_m} \right) [R_i^{(1)}(\mathbf{x}, t) - B_i^{(1)}(\mathbf{x}, t)], \end{aligned} \quad (2.143)$$

where the approximation 3 mentioned above has been used. Hence the second term of equation 2.142 becomes:

$$\begin{aligned}
 -\sum_i \partial_{1\beta} \left[R_i^{\dagger\dagger}(\mathbf{x}, t) - B_i^{\dagger\dagger}(\mathbf{x}, t) \right] e_{i\alpha} e_{i\beta} &= \overbrace{-\partial_{1\beta} \sum_i \left[R_i^{(0)}(\mathbf{x}, t) - B_i^{(0)}(\mathbf{x}, t) \right] e_{i\alpha} e_{i\beta}}^{\text{term (1)}} \\
 &\quad - \underbrace{\left(1 - \frac{1}{\tau_m} \right) \partial_{1\beta} \sum_i \left[R_i^{(1)}(\mathbf{x}, t) - B_i^{(1)}(\mathbf{x}, t) \right] e_{i\alpha} e_{i\beta}}_{\text{term (2)}}.
 \end{aligned} \tag{2.144}$$

Considering the relations in equation 2.129 and 2.130, the term (1) of equation 2.144 can be further simplified as follows:

$$\begin{aligned}
 -\partial_{1\beta} \sum_i \left[R_i^{(0)}(\mathbf{x}, t) - B_i^{(0)}(\mathbf{x}, t) \right] e_{i\alpha} e_{i\beta} &= -\partial_{1\beta} (c_s^2 \rho_n \delta_{\alpha\beta} - c_s^2 \rho_w \delta_{\alpha\beta}) \\
 &= -c_s^2 \partial_{1\alpha} (\rho \phi).
 \end{aligned} \tag{2.145}$$

For the term (2) in equation 2.144, we could utilise equation 2.153 which connects $R_i^{(1)}$ and $B_i^{(1)}$ to $R_i^{(0)}$ and $B_i^{(0)}$ on the order $\mathcal{O}(\epsilon^1)$. Therefore the term (2) can be simplified as follows:

$$\begin{aligned}
 -\left(1 - \frac{1}{\tau_m} \right) \partial_{1\beta} \sum_i \left[R_i^{(1)}(\mathbf{x}, t) - B_i^{(1)}(\mathbf{x}, t) \right] e_{i\alpha} e_{i\beta} \\
 = -\left(1 - \frac{1}{\tau_m} \right) (-\tau_m) \partial_{1\beta} \sum_i e_{i\alpha} e_{i\beta} (\partial_{t_1} + \partial_{1\gamma} e_{i\gamma}) R_i^{(0)} \\
 + \left(1 - \frac{1}{\tau_m} \right) (-\tau_m) \partial_{1\beta} \sum_i e_{i\alpha} e_{i\beta} (\partial_{t_1} + \partial_{1\gamma} e_{i\gamma}) B_i^{(0)}.
 \end{aligned} \tag{2.146}$$

in which the first term on the right-hand side of equation 2.146 can be simplified as:

$$\begin{aligned}
 -\left(1 - \frac{1}{\tau_m} \right) (-\tau_m) \partial_{1\beta} \sum_i e_{i\alpha} e_{i\beta} (\partial_{t_1} + \partial_{1\gamma} e_{i\gamma}) R_i^{(0)} \\
 = (\tau_m - 1) \partial_{1\beta} \left[\partial_{t_1} \sum_i e_{i\alpha} e_{i\beta} R_i^{(0)} + \partial_{1\gamma} \sum_i e_{i\alpha} e_{i\beta} e_{i\gamma} R_i^{(0)} \right] \\
 = (\tau_m - 1) \partial_{t_1} \partial_{1\alpha} (c_s^2 \rho_n) \\
 + (\tau_m - 1) \left[\partial_{1\alpha} \rho_n \partial_{1\gamma} u_\gamma + k_2 \beta \partial_{1\alpha} \left(\frac{\rho_n \rho_w}{\rho_n + \rho_w} \right) \partial_{1\gamma} n_\gamma \right],
 \end{aligned} \tag{2.147}$$

and similarly the second term on the right-hand side of equation 2.146 is as follows:

$$\begin{aligned}
& \left(1 - \frac{1}{\tau_m}\right) (-\tau_m) \partial_{1\beta} \sum_i e_{i\alpha} e_{i\beta} (\partial_{t_1} + \partial_{1\gamma} e_{i\gamma}) B_i^{(0)} \\
&= -(\tau_m - 1) \partial_{t_1} \partial_{1\alpha} (c_s^2 \rho_w) \\
&\quad - (\tau_m - 1) \left[\partial_{1\alpha} \rho_w \partial_{1\gamma} u_\gamma - k_2 \beta \partial_{1\alpha} \left(\frac{\rho_n \rho_w}{\rho_n + \rho_w} \right) \partial_{1\gamma} n_\gamma \right].
\end{aligned} \tag{2.148}$$

Overall, the term (2) of equation 2.144 is given by:

$$\begin{aligned}
& - \left(1 - \frac{1}{\tau_m}\right) \partial_{1\beta} \sum_i \left[R_i^{(1)}(\mathbf{x}, t) - B_i^{(1)}(\mathbf{x}, t) \right] e_{i\alpha} e_{i\beta} \\
&= (\tau_m - 1) \left[c_s^2 \partial_{t_1} \partial_{1\alpha} (\rho\phi) + \partial_{1\alpha} (\rho\phi) \partial_{1\gamma} u_\gamma + 2k_2 \beta \partial_{1\alpha} \left(\frac{\rho_n \rho_w}{\rho_n + \rho_w} \right) \partial_{1\gamma} n_\gamma \right].
\end{aligned} \tag{2.149}$$

Hence, considering equation 2.145 and 2.149, we are able to work out the expression for equation 2.144 as:

$$\begin{aligned}
& - \sum_i \partial_{1\beta} \left[R_i^{\dagger\dagger}(\mathbf{x}, t) - B_i^{\dagger\dagger}(\mathbf{x}, t) \right] e_{i\alpha} e_{i\beta} \\
&= -c_s^2 \partial_{1\alpha} (\rho\phi) \\
&\quad + (\tau_m - 1) \left[c_s^2 \partial_{t_1} \partial_{1\alpha} (\rho\phi) + \partial_{1\alpha} (\rho\phi) \partial_{1\gamma} u_\gamma + 2k_2 \beta \partial_{1\alpha} \left(\frac{\rho_n \rho_w}{\rho_n + \rho_w} \right) \partial_{1\gamma} n_\gamma \right].
\end{aligned} \tag{2.150}$$

If we again set $\tau_m = 1$, and substitute equation 2.150 into equation 2.142 we eventually obtain the net mass flux of the post-propagation distributions as follows:

$$q_\alpha = \rho\phi u_\alpha - c_s^2 \partial_{1\alpha} (\rho\phi) + 2k_2 \beta \frac{\rho_n \rho_w}{\rho_n + \rho_w} n_\alpha, \quad \text{for } \tau_m = 1, \tag{2.151}$$

where it can be easily seen, by comparing to equation 2.137:

$$q_\alpha = q_\alpha^{\dagger\dagger} - c_s^2 \partial_\alpha (\rho\phi), \quad \text{for } \tau_m = 1, \tag{2.152}$$

that $\partial_{1\alpha}$ is replaced by the normal ∂_α .

After working out the net mass flux terms, which is an important prerequisite for the subsequent derivation, now we can perform the Taylor expansion for equation 2.114, on the order of $\mathcal{O}(\epsilon^1)$:

$$(\partial_{t_1} + \partial_{1\alpha} e_{i\alpha}) R_i^{(0)} = -\frac{1}{\tau_m} R_i^{(1)}, \tag{2.153a}$$

$$(\partial_{t_1} + \partial_{1\alpha} e_{i\alpha}) B_i^{(0)} = -\frac{1}{\tau_m} B_i^{(1)}, \tag{2.153b}$$

and on the order of $\mathcal{O}(\epsilon^2)$:

$$\partial_{t_2} R_i^{(0)} + (\partial_{t_1} + \partial_{1\alpha} e_{i\alpha}) \left(1 - \frac{\delta_t}{2\tau_m}\right) R_i^{(1)} = -\frac{1}{\tau_m} R_i^{(2)}, \quad (2.154a)$$

$$\partial_{t_2} B_i^{(0)} + (\partial_{t_1} + \partial_{1\alpha} e_{i\alpha}) \left(1 - \frac{\delta_t}{2\tau_m}\right) B_i^{(1)} = -\frac{1}{\tau_m} B_i^{(2)}, \quad (2.154b)$$

where, for visual clarity $\delta_t = 1$ is used hereafter.

On the order of $\mathcal{O}(\epsilon^1)$, if summing equation 2.153 over i for each phase we can get:

$$\partial_{t_1} \rho_n + \partial_{1\alpha} (\rho_n u_\alpha) + k_2 \beta \partial_{1\alpha} \left[\frac{\rho_n \rho_w}{\rho_n + \rho_w} n_\alpha \right] = 0, \quad (2.155a)$$

$$\partial_{t_1} \rho_w + \partial_{1\alpha} (\rho_w u_\alpha) - k_2 \beta \partial_{1\alpha} \left[\frac{\rho_n \rho_w}{\rho_n + \rho_w} n_\alpha \right] = 0, \quad (2.155b)$$

where it can be seen that, if neglecting the terms due to the recolouring algorithm, the convection equation for each phase is indeed recovered on the $\epsilon^{-1} t_1^*$ scale. If taking the difference of equation 2.155(a) and 2.155(b) we then get:

$$\partial_{t_1} (\rho \phi) + \partial_{1\alpha} (\rho \phi u_\alpha) = -2k_2 \beta \partial_{1\alpha} \left[\frac{\rho_n \rho_w}{\rho_n + \rho_w} n_\alpha \right] \quad (2.156)$$

Also, on $\mathcal{O}(\epsilon^1)$, by multiplying equation 2.153 with the lattice velocity $e_{i\alpha}$ and summing over i , we obtain:

$$\partial_{t_1} \sum_i e_{i\beta} R_i^{(0)} + \partial_{1\alpha} \sum_i e_{i\alpha} e_{i\beta} R_i^{(0)} = -\frac{1}{\tau_m} \sum_i e_{i\beta} R_i^{(1)}, \quad (2.157a)$$

$$\partial_{t_1} \sum_i e_{i\beta} B_i^{(0)} + \partial_{1\alpha} \sum_i e_{i\alpha} e_{i\beta} B_i^{(0)} = -\frac{1}{\tau_m} \sum_i e_{i\beta} B_i^{(1)}, \quad (2.157b)$$

which can be straightforwardly simplified by considering equation 2.129 and 2.130:

$$\partial_{t_1} (\rho_n u_\beta) + \partial_{t_1} \left[k_2 \beta \frac{\rho_n \rho_w}{\rho_n + \rho_w} n_\beta \right] + c_s^2 \partial_{1\beta} \rho_n = -\frac{1}{\tau_m} \sum_i e_{i\beta} R_i^{(1)}, \quad (2.158a)$$

$$\partial_{t_1} (\rho_w u_\beta) - \partial_{t_1} \left[k_2 \beta \frac{\rho_n \rho_w}{\rho_n + \rho_w} n_\beta \right] + c_s^2 \partial_{1\beta} \rho_w = -\frac{1}{\tau_m} \sum_i e_{i\beta} B_i^{(1)}, \quad (2.158b)$$

and can be further simplified as:

$$\partial_{t_1} (\rho \phi u_\alpha) + 2k_2 \beta \partial_{t_1} \left[\frac{\rho_n \rho_w}{\rho_n + \rho_w} n_\alpha \right] + c_s^2 \partial_{1\alpha} (\rho \phi) = -\frac{1}{\tau_m} \sum_i e_{i\alpha} (R_i^{(1)} - B_i^{(1)}). \quad (2.159)$$

Again, for the term on the right-hand side of equation 2.159 we need to use the third approximation mentioned before (i.e. $R_i^{(1)} \approx R_i - R_i^{(0)}$ and similar to $B_i^{(1)}$),

such that the equation above becomes:

$$\begin{aligned}
\partial_{t_1}(\rho\phi u_\alpha) + 2k_2\beta\partial_{t_1}\left[\frac{\rho_n\rho_w}{\rho_n+\rho_w}n_\alpha\right] + c_s^2\partial_{1\alpha}(\rho\phi) \\
= -\frac{1}{\tau_m}\sum_i e_{i\alpha}(R_i - B_i) - \frac{1}{\tau_m}\sum_i e_{i\alpha}(R_i^{(0)} + B_i^{(0)}) \\
= \frac{1}{\tau_m}(q_\alpha^{\dagger\dagger} - q_\alpha),
\end{aligned} \tag{2.160}$$

where the expressions for q_α and $q_\alpha^{\dagger\dagger}$ are given in equation 2.137 and (2.151) for $\tau_m = 1$.

On the order $\mathcal{O}(\epsilon^2)$, similarly, we can sum equation 2.154 over i to obtain:

$$\partial_{t_2}\rho_n + \left(1 - \frac{1}{2\tau_m}\right)\partial_{1\alpha}\sum_i e_{i\alpha}R_i^{(1)} = 0, \tag{2.161a}$$

$$\partial_{t_2}\rho_w + \left(1 - \frac{1}{2\tau_m}\right)\partial_{1\alpha}\sum_i e_{i\alpha}B_i^{(1)} = 0, \tag{2.161b}$$

where equation 2.131 is used during the derivation. Considering again equation 2.153 to replace $R_i^{(1)}$ with $R_i^{(0)}$, we can then evaluate the right-hand side of equation 2.161 as follows:

$$\begin{aligned}
\sum_i e_{i\alpha}R_i^{(0)} &= -\tau_m\sum_i e_{i\alpha}(\partial_{t_1} + \partial_{1\beta}e_{i\beta})R_i^{(0)} \\
&= -\tau_m\partial_{t_1}\sum_i e_{i\alpha}R_i^{(0)} - \tau_m\partial_{1\beta}\sum_i e_{i\alpha}e_{i\beta}R_i^{(0)} \\
&= -\tau_m\left[\partial_{t_1}(\rho_n u_\alpha) + k_2\beta\partial_{t_1}\left(\frac{\rho_n\rho_w}{\rho_n+\rho_w}n_\alpha\right) + c_s^2\partial_{1\alpha}\rho_n\right],
\end{aligned} \tag{2.162}$$

and similarly:

$$\sum_i e_{i\alpha}B_i^{(0)} = -\tau_m\left[\partial_{t_1}(\rho_w u_\alpha) - k_2\beta\partial_{t_1}\left(\frac{\rho_n\rho_w}{\rho_n+\rho_w}n_\alpha\right) + c_s^2\partial_{1\alpha}\rho_w\right]. \tag{2.163}$$

Then substitute equation 2.162 and 2.163 into equation 2.161 we get:

$$\partial_{t_2}\rho_n - (\tau_m - \frac{1}{2})\partial_{1\alpha}\left\{\partial_{t_1}(\rho_n u_\alpha) + k_2\beta\partial_{t_1}\left[\frac{\rho_n\rho_w}{\rho_n+\rho_w}n_\alpha\right] + c_s^2\partial_{1\alpha}\rho_n\right\} = 0, \tag{2.164a}$$

$$\partial_{t_2}\rho_w - (\tau_m - \frac{1}{2})\partial_{1\alpha}\left\{\partial_{t_1}(\rho_w u_\alpha) - k_2\beta\partial_{t_1}\left[\frac{\rho_n\rho_w}{\rho_n+\rho_w}n_\alpha\right] + c_s^2\partial_{1\alpha}\rho_w\right\} = 0, \tag{2.164b}$$

which can be rewritten as:

$$\partial_{t_2}\rho_n - D\partial_{1\alpha}\partial_{1\alpha}\rho_n - \frac{D}{c_s^2}\partial_{1\alpha}\left\{\partial_{t_1}(\rho_n u_\alpha) + k_2\beta\partial_{t_1}\left[\frac{\rho_n\rho_w}{\rho_n+\rho_w}n_\alpha\right]\right\} = 0, \tag{2.165a}$$

$$\partial_{t_2}\rho_w - D\partial_{1\alpha}\partial_{1\alpha}\rho_w - \frac{D}{c_s^2}\partial_{1\alpha}\left\{\partial_{t_1}(\rho_w u_\alpha) - k_2\beta\partial_{t_1}\left[\frac{\rho_n\rho_w}{\rho_n+\rho_w}n_\alpha\right]\right\} = 0, \tag{2.165b}$$

where the diffusion coefficient D is given by:

$$D = c_s^2 \left(\tau_m - \frac{1}{2} \right). \quad (2.166)$$

It can be seen that equation 2.165 indeed recovers the diffusion equation on the $\epsilon^{-2}t_2^*$ scale, if neglecting the third term for each phase. Taking the difference between equation 2.165(a) and 2.165(b) we obtain:

$$\partial_{t_2}(\rho\phi) - D\partial_{1\alpha}\partial_{1\alpha}(\rho\phi) = \frac{D}{c_s^2}\partial_{1\alpha} \left\{ \partial_{t_1}(\rho\phi u_\alpha) + 2k_2\beta\partial_{t_1} \left[\frac{\rho_n\rho_w}{\rho_n + \rho_w} n_\alpha \right] \right\}, \quad (2.167)$$

and note that the right-hand side of equation above is part of equation 2.159, thus we can substitute equation 2.159 into equation 2.167 to get:

$$\begin{aligned} \partial_{t_2}(\rho\phi) - D\partial_{1\alpha}\partial_{1\alpha}(\rho\phi) &= \frac{D}{c_s^2} \left[-c_s^2\partial_{1\alpha}(\rho\phi) + \frac{1}{\tau_m} (q_\alpha^{\dagger\dagger} - q_\alpha) \right] \\ &= \frac{D}{c_s^2} [-c_s^2\partial_{1\alpha}(\rho\phi) + c_s^2\partial_{1\alpha}(\rho\phi)] \\ &= 0, \quad \text{for } \tau_m = 1, \end{aligned} \quad (2.168)$$

where equation 2.152 is used during the derivation, and note that when $\tau_m = 1$, the diffusion coefficient becomes $D = c_s^2/2$.

Now we can combine equation 2.156 and equation 2.168 to obtain:

$$\begin{aligned} \partial_t(\rho\phi) + \partial_\alpha(\rho\phi u_\alpha) &= -2k_2\beta\partial_\alpha \left[\frac{\rho_n\rho_w}{\rho_n + \rho_w} n_\alpha \right] + D\partial_\alpha\partial_\alpha(\rho\phi) \\ &= -\frac{c_s^2}{2}\partial_\alpha(\rho\partial_\alpha\phi) + \frac{c_s^2}{2}\partial_\alpha[\partial_\alpha(\rho\phi)] \\ &= \frac{c_s^2}{2}\partial_\alpha(\phi\partial_\alpha\rho), \end{aligned} \quad (2.169)$$

where equation 2.125 is used and note that $k_2|c|^2 = c_s^2$. We hereafter rewrite the evolution equation above as:

$$\partial_t(\rho\phi) + \partial_\alpha(\rho\phi u_\alpha) = \frac{c_s^2}{2}\partial_\alpha(\phi\partial_\alpha\rho). \quad (2.170)$$

To obtain the evolution equation of the phase field, we need further manipulation of all equations above: recalling that for the Chapman-Enskog analysis being performed above, we always start from the relevant equation for each phase, and after the sum over the discretised velocity index i , we take the difference between each phase, which is why we get an evolution equation for $\rho\phi = \rho_n - \rho_w$. Alternatively, for the equation on $\mathcal{O}(\epsilon^1)$ and $\mathcal{O}(\epsilon^2)$, we can take the sum, not the difference, of two phases to obtain an evolution equation for $\rho = \rho_n + \rho_w$. Therefore, if summing equation 2.153(a) and 2.153(b), we immediately get, on the order $\mathcal{O}(\epsilon^1)$, as follows:

$$\partial_{t_1}\rho + \partial_{1\alpha}(\rho u_\alpha) = 0, \quad (2.171)$$

which is the continuity equation for the colour-blinded phase. Similarly, if summing equation 2.165(a) and 2.165(b), we get on the order $\mathcal{O}(\epsilon^2)$:

$$\partial_{t_2}\rho - \frac{D}{c_s^2}\partial_{t_1}\partial_{1\alpha}(\rho u_\alpha) - D\partial_{1\alpha}\partial_{1\alpha}\rho = 0, \quad (2.172)$$

where it is noted that the second term on the left-hand side of the equation above can be rewritten using equation 2.171 such that $\partial_{t_1}\partial_{1\alpha}(\rho u_\alpha) = -\partial_{t_1}\partial_{t_1}\rho$. If combining the two time scales by doing ($\epsilon^1 \times$ equation 2.171 + $\epsilon^2 \times$ equation 2.172) we get:

$$\partial_t\rho + \partial_\alpha(\rho u_\alpha) + \frac{D}{c_s^2}\partial_t\partial_t\rho = D\partial_\alpha\partial_\alpha\rho. \quad (2.173)$$

Neglecting the second-order time derivative of the total density ρ ($= \rho_n + \rho_w$), and noting that when $\tau_m = 1$ the diffusion coefficient $D = c_s^2/2$, we thus have two evolution equations for $\rho\phi$ and ρ :

$$\partial_t(\rho\phi) + \partial_\alpha(\rho\phi u_\alpha) = \frac{c_s^2}{2}\partial_\alpha(\phi\partial_\alpha\rho), \quad (2.174a)$$

$$\partial_t\rho + \partial_\alpha(\rho u_\alpha) = \frac{c_s^2}{2}\partial_\alpha\partial_\alpha\rho. \quad (2.174b)$$

If multiplying equation 2.174(b) by the phase field ϕ , we get:

$$\phi\partial_t\rho + \phi\partial_\alpha(\rho u_\alpha) = \frac{c_s^2}{2}\phi\partial_\alpha\partial_\alpha\rho, \quad (2.175)$$

and if subtracting equation 2.175 from equation 2.174(a) we get:

$$\rho\partial_t\phi + \rho u_\alpha\partial_\alpha\phi = \frac{c_s^2}{2}\partial_\alpha\rho\partial_\alpha\phi, \quad (2.176)$$

which, noting that $D = c_s^2/2$, can be rearranged to obtain the evolution equation of the phase field as:

$$\partial_t\phi + u_\alpha\partial_\alpha\phi = \frac{D}{\rho}\partial_\alpha\rho\partial_\alpha\phi, \quad \text{for } \tau_m = 1, \quad (2.177)$$

or in the vector notation as:

$$\partial_t\phi + \mathbf{u} \cdot \nabla\phi = \frac{D}{\rho}\nabla\rho \cdot \nabla\phi, \quad \text{for } \tau_m = 1. \quad (2.178)$$

It is noted that the right-hand side of equation 2.177 is not zero, which indicates an error term in the recovered phase field evolution equation. This error terms essentially comes from the recolouring term in equation 2.117. The recolouring term is designed to suppress the inter-phase diffusion as well as to achieve phase segregation. Without the recolouring term, a standard convection-diffusion equation for the phase field will be recovered; ideally it is expected the inter-phase diffusion can be exactly cancelled by introducing a recolouring term; however, as it has just been shown, our recolouring scheme introduces an error term indicating that the interface accelerates with respect to the local fluid. The similar observation has also been made in the work of Halliday,

Hollis, and Care (2007), where a slightly different LB evolution equation is used.

Currently, the error term in the phase field equation remains one of the unresolved issues in our multicomponent LB model. The consequence of the error term, however, will be shown negligible based on the results in sections 5.1.2, where it is demonstrated that the evolution of the interface complies with the imposed boundary injection condition with decent accuracy (i.e. Figure 5.4). In terms of mitigation, the idea by Hollis, Halliday, and Law (2007) may be borrowed to revise the current recolouring formulation by imposing extra kinematic condition on the interface; since the current error term makes the interface move faster than the bulk fluid, a perturbation term introducing more viscous damping on the interface can be a potential remedy.

Chapter 3

Discretisation Limits of Multicomponent LB Models

3.1 Introduction

Over the past two decades, there have been a large body of work on applying multiphase LB models in the study of fluid flows in porous media. In section 1.1 we had a brief review of many examples applying different types of multiphase LB models in porous media applications. Despite the progress (most of which focus on the proof-of-concept that multiphase LB models can be applied to the realistic porous media), there has been relatively little study of the models' ability to make optimal use of 3D imagery by considering the minimum number of grid points that are needed to represent geometric features such as pore throats. This is important since 3D images of geological samples are inevitably a compromise between resolution and field of view. Pan, Hilpert, and Miller (2004) studied how the primary drainage LB simulations are affected by different resolution levels in both simple geometry and artificial sphere packing system. But the resolution of the model was not pushed to the extreme discrete limits, and this work did not focus on identifying shortcomings in the model's behaviour at low resolution and the potential implications for simulation studies. Moreover, for the Shan-Chen (SC) multicomponent LB model used in Pan, Hilpert, and Miller (2004) and many other works, concerns regarding to the numerical stability arises from the relatively narrow range of available model parameters and the need to fine-tune the pressure boundary condition. The latter has been studied by Schaap et al. (2007) who proposed an approach of identifying a stable pressure boundary condition empirically. It is natural to ask whether this approach would break down in some way if the resolution is pushed to the extreme discrete limit and what the consequences of this breakdown would be. As a result, it is also natural to examine if other mainstream multiphase LB models are suitable to be applied at the low resolution. McClure et al. (2016) compared LB drainage and imbibition sequence at different resolutions in a sphere packing system, using Rothman-Keller (RK) multicomponent LB model, and has shown that small features such as pendular rings will always tend to matter in real systems. However the focus of this work was not on examining the RK model at extremely low resolution as well as what the associated

breakdown behaviour will arise. Alongside these studies, there are also several works that compares the SC model, RK model, and free energy LB model (Hou et al., 1997; Huang, Wang, and Lu, 2011; Yang and Boek, 2013), but none of them have focused on the models' breakdown behaviour at the resolution limits.

Given the existing literature reviewed above, although some treatments have been introduced to overcome some shortcomings in the multicomponent LB models, overall the coverage is limited and the focus of most works is on generating positive outcomes. There is still an important question to ask: what will happen if we perform multiphase LB simulations on μ CT images with coarsened resolution? Ultimately, if we want to better characterise the multiphase system (porous media plus fluids) to include more heterogeneity, simulations with lower image resolution could be the easiest and most straightforward approach. An μ CT image with coarsened resolution by a factor of 2, corresponds to the shrink of total simulation domain by a factor of 8, which would save thousands of hours of computation time. However, it is critical for researcher to be aware whether the resolution coarsening will render the LB modelling erroneous and meaningless. Therefore, the goal of this chapter is to explore the discretisation limits of multicomponent LB models by pushing the fluid-fluid interfacial radius of curvature and the feature size of the simulation domain down to the discrete unit size of the computational grid, i.e. what is the coarsest computational grid that can be used to simulate a given system, and in what ways do the simulations break down as these limits are approached?

Throughout this investigation, we attempt to study some of the fundamentals of multicomponent LB models in terms of computational efficiency at low-resolution limits. Thus, to suit that need, we select two of the most commonly used single-relaxation-time multicomponent LB models: the SRT Shan-Chen (SC) model and the SRT Rothman-Keller (RK) model¹, where the details of these two models have been introduced in sections 2.3.1 and 2.3.2. Single-relaxation-time model can be easily implemented, hence it could serve as a quick proof-of-concept demonstration for our low-resolution study. Hence, in this chapter the study of SRT models constitutes the major part of our survey. The more state-of-the-art multi-relaxation-time (MRT) model (section 2.4) is also investigated in the dynamic drainage simulations. It is noted that MRT models focus more on the enhanced numerical stability and improved capacity of simulating systems with non-unity viscosity and density ratios, but most of models' low-resolution-limit behaviour (classified in Table 3.1), as will be discussed in the due parts of this chapter, is more closely linked to the feature of diffused interface models (to which LB methods belong) and wetting boundary conditions in multicomponent LB models. Therefore, the conclusions of our study apply more broadly to multicomponent LB models in general, regardless of whether SRT or MRT collision operators are used and whether the system is of unitary or non-unitary viscosity/density ratios. The SRT-based SC and RK model have been implemented with CUDA/C++ programming language on a single GPU card, with the algorithm

fully adopted from the work by Tölke (2008). For the algorithm and numerical performance of the MRT-base colour gradient model, please see McClure, Prins, and Miller (2014).

Our investigation is focused on capillary-dominated flow in porous media, and we restrict ourselves to unity viscosity and density ratios. In all such systems the Reynolds number is very low and Stokes flow can be assumed. In the rest of the sub-sections, we implement a variety of small-scale, simple-geometry, both static and dynamic tests, using either periodic or constant-pressure boundary condition with SC and RK models. These testing cases developed here can also be used as benchmark study for any novel LB models. For each test, we characterise SC and RK models' breakdown behaviours ranging from gradual loss of accuracy to catastrophic numerical instability at the resolution limit; and in the end of the chapter, we discuss the consequences of the models' breakdown behaviour and the ramifications for larger-scale simulations of fluid displacements in realistic porous media.

3.2 Methodology

Our goals are to identify these limits and to explore the nature of the loss of accuracy, thereby helping to understand the potential consequences for larger scale simulations. We classify the errors that appear in the SC and RK models at low resolution into the categories defined in Table 3.1. For type I behaviour, the simulated results are still well bound by the relevant physics laws, but there are discrepancies between theoretical relations and simulations. This loss of accuracy arises due to progressive change of the resolution or certain model parameters. Type II behaviour denotes non-physical behaviour of the models that cannot be predicted by any known physics laws. For example, in section 3.5 it shows that the dissolved non-wetting phase accumulating at the solid surface forms conduction layer which leads to the breakthrough of the capillary tube at a much lower entry pressure than that predicted by the theory. Type III behaviour denotes the numerical instability which sometimes leads to non-a-number (NaN) situations and complete program failure ensues.

We perform a series of simple tests with known results, and classify the breakdown of accuracy as one of error types. The behaviour of both multi-component models are evaluated primarily by examining the mean curvature of the fluid-fluid interfaces in the simulation. The fluid-fluid interface is defined as the level set of a real-valued function defined on a grid. At low-resolution limit it should be noted the accuracy of measuring the curvature of an interface will be degraded. Therefore, the mean interfacial curvature is measured by two methods: one that involves fitting a surface to the interface (i.e. the 'surface fitting' method) (Herring et al., 2017) and the

¹It is noted that there is also another popular multicomponent lattice-Boltzmann model, the free-energy model, which is also commonly seen in the porous media applications. However, considering the time frame of the thesis project and the time to develop the corresponding GPU-parallel code, we did not attempt to exhaust all multicomponent LB models and thus decided to only examine the two most popular ones, i.e. SC and RK models.

other that computes curvature directly from the real-valued function using a level-set approach (i.e. the ‘level-set’ method). More information of these two methods are introduced in Appendix A.

TABLE 3.1: Numerical Behaviours of Multicomponent Lattice-Boltzmann Models

Descriptions	
Type I	Progressive loss of accuracy
Type II	Transition to nonphysical behaviour
Type III	Complete numerical instability and program failure

3.3 Bubble Test

The static bubble test is frequently used to calibrate multicomponent LB models by providing a relation between the macroscopic surface tension and the model parameters (Hou et al., 1997; Tölke et al., 2002; Huang et al., 2007; Liu, Valocchi, and Kang, 2012; McClure, Prins, and Miller, 2014). Here we aim to determine the smallest bubble that the models can simulate, to explore how SC and RK models behave differently at limits of large curvatures, and to categorise their behaviour according to Table 3.1. We also investigate the fluid-fluid interface thickness and compare the magnitudes of interface spurious currents for SC and RK models.

To carry out the bubble test, we place a pure bubble of non-wetting (NW) phase whose radius is R_{initial} inside a $65 \times 65 \times 65$ domain of wetting (W) phase. We set $\rho_{\text{nw},\text{major}} = \rho_{\text{w},\text{major}} = 1.0$ with $\rho_{\text{nw},\text{minor}} = \rho_{\text{w},\text{minor}} = 0.0$, where $\rho_{\text{nw},\text{minor}}$ ($\rho_{\text{w},\text{minor}}$) is the dissolved density of NW (W) phase inside the W (NW) phase. All dimensional and model related parameters are summarised in Table 3.2. For the sake of the continuity with later discussions, we use the naming of NW and W phases for the bubble and its ambient fluid respectively, even though such naming has no meaning until a solid phase is present. Periodic boundary conditions are applied in all directions. As the system reaches equilibrium, we measure the mean curvature of the bubble κ_H (defined as $\kappa_H = \frac{1}{2} \left(\frac{1}{r_1} + \frac{1}{r_2} \right)$, where r_1 and r_2 are the principal radii of curvature and are equal for spherical interfaces) as well as the capillary pressure P_c across the phase interface, which is calculated as $P_c = P_{\text{nw}} - P_{\text{w}}$, where P_{nw} and P_{w} are volume-averaged pressure values taken away from the interface. R_{final} and P_c should follow the Young-Laplace law:

$$P_c = \gamma_{\text{wn}} \kappa_H = \gamma_{\text{wn}} \frac{2}{R_{\text{final}}}, \quad (3.1)$$

where R_{final} is the final radius of the bubble at equilibrium. The mean curvature of the bubble is measured by both surface fitting and level-set methods. For the case of a spherical bubble, R_{final} is conventionally measured by a method proposed by Hou et al. (1997), which defines R_{final} through the equation $\rho_{\text{max}} \pi R_{\text{final}}^2 + (L^2 - \pi R_{\text{final}}^2) \rho_{\text{min}} = \bar{\rho} L^2$ in a 2D case, where L^2 is the area of the computational domain, $\bar{\rho}$ is the average density of the NW phase, i.e. $\bar{\rho} = \sum_{\mathbf{x}} \rho_{\text{nw}} / L^2$, and ρ_{max} and ρ_{min} are

the maximum and minimum of the NW phase density over the entire domain. Then, the calculated R_{final} can be used to derive the corresponding mean curvature by assuming the bubble a perfect sphere. We performed curvature measurements using the method of Hou et al. (1997), as well as the surface fitting and level-set methods, to help validate our curvature measurement methods.

TABLE 3.2: Major Parameters in Bubble Test

	SC Model	RK Model
Domain Size (N_x, N_y, N_z)	(65, 65, 65)	
Initial NW density	$\rho_{\text{nw},\text{major}} = 1.0$ $\rho_{\text{nw},\text{minor}} = 0.0$	
Initial W density	$\rho_{\text{w},\text{major}} = 1.0$ $\rho_{\text{w},\text{minor}} = 0.0$	
Relaxation parameter τ	$\tau_{\text{nw}} = 1.0$ $\tau_{\text{w}} = 1.0$	
Other parameters	$G_{\text{coh}} = 1.5, 2.0, 2.5$ 3.0, 3.5, 4.0	$A_{\text{R}} = A_{\text{B}} = 0.001, 0.005,$ 0.01, 0.05, 0.1, 0.5

In terms of the initial condition, the equilibrium velocity \mathbf{u}_k^{eq} was set to zero to initialise $f_i^{k,eq}$, and initial values of f_i^k were also set to $f_i^{k,eq}$ for both models. The stopping criterion for simulations is chosen as:

$$\sup \left\{ \frac{\sum_{\mathbf{x}} [\rho_{\text{nw}}(\mathbf{x}, t) - \rho_{\text{nw}}(\mathbf{x}, t - 200)]^2}{\sum_{\mathbf{x}} [\rho_{\text{nw}}(\mathbf{x}, t)]^2}, \frac{\sum_{\mathbf{x}} [\rho_{\text{w}}(\mathbf{x}, t) - \rho_{\text{w}}(\mathbf{x}, t - 200)]^2}{\sum_{\mathbf{x}} [\rho_{\text{w}}(\mathbf{x}, t)]^2} \right\} < 5 \times 10^{-15}, \quad (3.2)$$

where t is the simulation step size, set as 1. This stopping mechanism is applied throughout the simulations in this chapter.

For the SC model, as already mentioned, it is the product of the cohesive coefficient G_{coh} and the sum of major and minor densities that determines the macroscopic surface tension. According to reported works (Schaap et al., 2007; Huang et al., 2007), for $1.5 \leq G_{\text{coh}}\rho_{\text{total}} \leq 4.4$, a reasonably immiscible two-phase system can be achieved for a range of surface tensions, where ρ_{total} is the sum of initial $\rho_{\text{nw},\text{major}}$ and $\rho_{\text{w},\text{minor}}$. It is noted that for $G_{\text{coh}}\rho_{\text{total}}$ greater than 4.4, the SC model becomes numerically unstable (a type III breakdown). Therefore we select several G_{coh} values, $\{1.5, 2.0, 2.5, 3.0, 3.5, 4.0\}$, for the SC model (note that ρ_{total} is unity according to the initial condition).

For the RK model, according to equation 2.60, the macroscopic surface tension is determined by the free parameters A_{R} and A_{B} . Here we examine a few representative $A_{\text{R}} (= A_{\text{B}})$ values: $\{0.001, 0.005, 0.01, 0.05, 0.1, 0.5\}$, across three orders of magnitude. Like the SC model, if $A_{\text{R},\text{B}} \gtrsim 0.6$, the RK model becomes numerically unstable. The free parameter β is set 1.0, corresponding to the thinnest numerical stable phase interface (Liu, Valocchi, and Kang, 2012).

Given the model parameters mentioned above and in Table 3.2, a quick order of magnitude estimation of the physical scale of the simulations can be made. According to the discussion on the unit conversion in section 2.2, the physical capillary pressure is related to the size of physical lattice units of the μ CT image, and the physical as well as LB interfacial tension. If assuming an oil-water system with a interfacial tension of 0.0378 N/m, and a resolution of 10 μ m per lattice units ($l.u.$), for SC model, based on the fitting results shown Figure 3.2, with $1.5 \leq G_{\text{coh}} \leq 4.0$, the capillary pressure ranges between 0 \sim 4100 Pa. For RK model, the model parameter $A_{\text{R,B}}$ of 0.001 \sim 0.5 gives the capillary pressure of 0 \sim 2600 Pa. In terms of the physical time scale, if a typical water kinematic viscosity of 10^{-6} m²/s is assumed, the physical time is 10^{-5} seconds per lattice time ($l.t.$), i.e. it takes 100,000 time steps to simulate one physical second.

Starting with different R_{initial} and allowing the system to relax to an equilibrium state, we can obtain bubbles with various sizes. Figure 3.1 shows the examples of 1D phase density profiles of the bubbles at equilibrium with a bubble radius of ~ 10.0 $l.u.$, for both SC and RK models. The phase density was extracted along the central line of a central plane of the domain. For SC model, it can be seen that as G_{coh} decreases, which corresponds to a decreased surface tension, both the dissolved densities $\rho_{\text{nw,minor}}$ and $\rho_{\text{w,minor}}$ increase. On the other hand, for RK model the amount of the dissolved phase in another fluid is negligible and is not affected by the model parameter $A_{\text{R,B}}$ which controls the surface tension. The SC model's immiscibility can be improved by using a larger G_{coh} , but we will show in the section 3.4 that once the solid phase is added, even a G_{coh} of 2.0 can lead to numerical instabilities. Most likely as a consequence of this, simulations described in the literature use lower values of G_{coh} (Schaap et al., 2007; Huang et al., 2007). In short, employing the SC model involves a trade-off between miscibility and numerical stability, while for RK model one can choose a surface tension without affecting numerical stability, but it's challenging to simulate any genuine miscibility. Fluid-fluid interface thicknesses can be estimated from this data by fitting the 1D density profile with a $\tanh(2x/\epsilon)$ function (Rowlinson and Widom, 1982), where ϵ is a measure of the interface width. This gives the interface thickness of ~ 5 $l.u.$ for the RK model at all $A_{\text{R,B}}$ with $\beta = 1.0$, and $4 \sim 6$ $l.u.$ for the SC model with G_{coh} ranging from 4.0 down to 1.5.

By measuring a series of bubble radii and the corresponding capillary pressure, the Young-Laplace law in equation (3.1) can be tested. Figure 3.2 summarises the bubble test results for both models, where P_c normalised by the fitted lattice surface tension γ_{wn} is plotted against the mean curvature κ_H . The capillary pressure is normalised to allow meaningful comparison among all results. The uncertainties associated with the estimation of P_c are due to the measurement of the volume-averaged P_{nw} and P_{w} from the bulk NW and W phases; the pressure must be sampled in the bulk phase well away from the interface. The surface tension is calculated as the slope of the linear fit to the P_c versus κ_H data, based on equation (3.1). All the fitted surface tension values agree well with reported works for the SC model (Schaap et al., 2007) and the

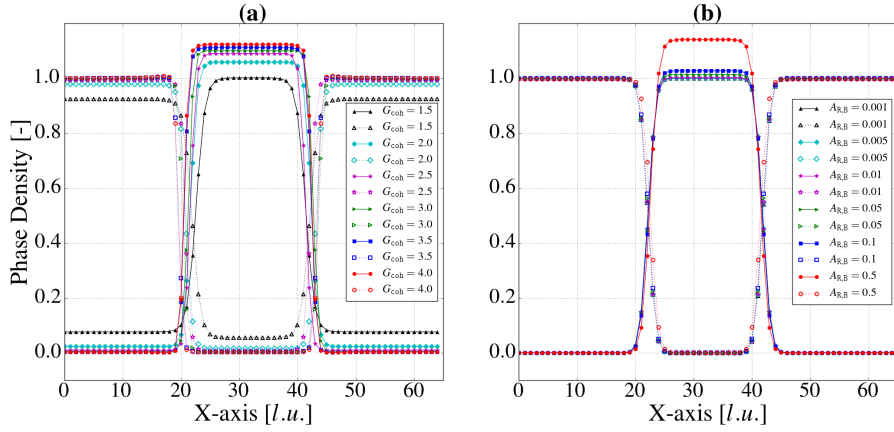


FIGURE 3.1: The NW and W fluid density profiles along the central line ($y = 33$) in the central plane ($z = 33$) for (a) SC model, and (b) RK model. The solid symbols with solid lines are of the non-wetting phase, and blank symbols with dotted lines are of the wetting phase. The density profiles are obtained at a mean curvature of about $0.2 \text{ } l.u.^{-1}$, which corresponds to a bubble radius of $10 \text{ } l.u.$. For SC model, the amount of dissolved density of one phase in another is dependent on G_{coh} that controls the surface tension, whereas for RK model, the dissolved phase is negligible, and is not affected by $A_{R,B}$ that controls the surface tension.

RK model (Liu, Valocchi, and Kang, 2012).

As can be seen from Figure 3.2, the RK model shows good agreement with Laplace's law for mean curvature up to $\kappa_H \approx 0.7 \text{ } l.u.^{-1}$ (corresponding to a bubble diameter of $5.71 \text{ } l.u.$), according to both curvature measurements. Beyond this the capillary pressure-curvature relation deviates progressively from the Laplace's law, which we classify as a type I breakdown behaviour². Given that the average interfacial thickness of RK model ($\beta = 1.0$) is $\sim 5.0 \text{ } l.u.$ as calculated based on Figure 3.1, this breakdown behaviour is clearly caused by the fact that the bubble diameter becomes comparable to the interfacial thickness, so that interfaces on opposite sides of the bubble overlap, preventing the NW fluid pressure inside the bubble from reaching a plateau. Consequently, even in the centre of the bubble the NW fluid pressure is significantly lower than it would be in the bulk, leading to an exaggerated measurement of capillary pressure. Such breakdown is a predictable, indeed inevitable consequence of finite interface thickness, and in fact as we shall see in section 3.4, the RK model suffers no fundamental breakdown at this radius and can accurately simulate situations with much higher interfacial curvatures. For $\kappa_H \gtrsim 0.7 \text{ } l.u.^{-1}$, the surface fitting method gives larger curvature values than the method of Hou et al. (1997): for the smallest bubble, an infeasible mean curvature of $\sim 2.75 \text{ } l.u.^{-1}$ is given by the surface fitting method (shown as the rightmost data point in the inset of Figure 3.2(d)). This is again due to the degraded NW phase density inside the bubble, such that the threshold used by the surface fitting method to construct an isosurface becomes inappropriate in the bubble interior. At this point, both LBM and measurement method are approaching the limits of accuracy, and it should be noted that the

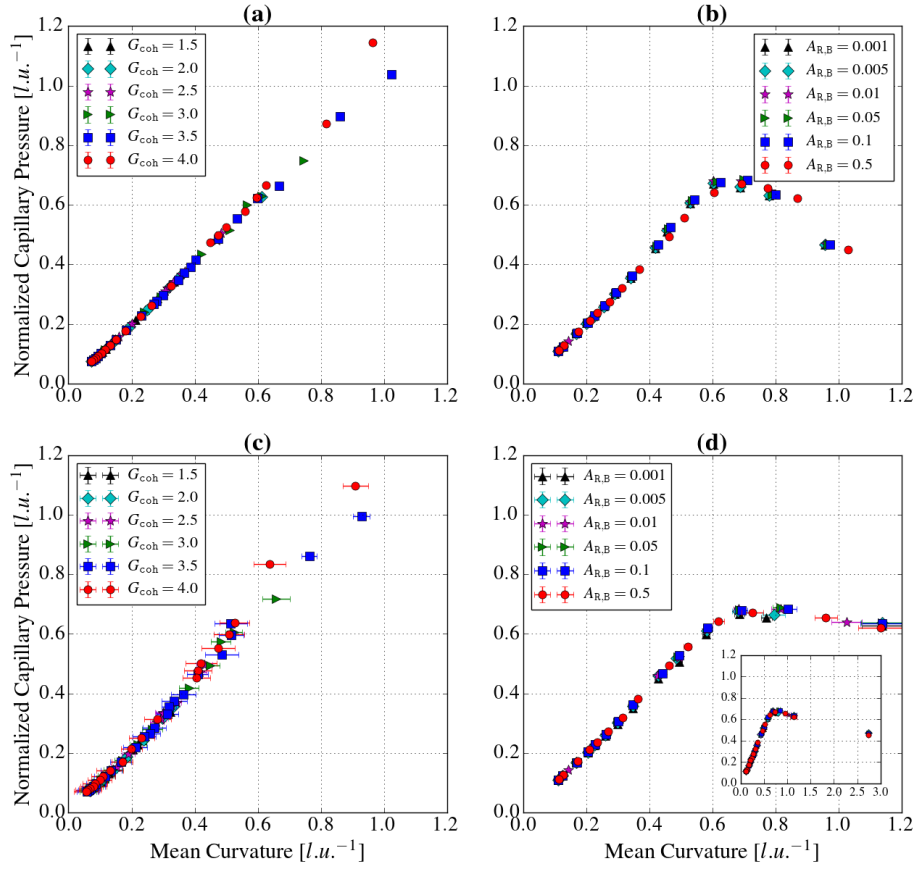


FIGURE 3.2: The bubble test of Laplace’s law, where the mean curvature is measured by the method proposed by Hou et al. (1997) for (a) SC model and (b) RK model, and by the surface fitting method for (c) SC model, and (d) RK model. The measured capillary pressure is normalised by the fitted surface tension for each G_{coh} and $A_{\text{R,B}}$. In (d), as discussed in the text, the surface fitting method over-estimates the mean curvature for the smallest bubble; the inset shows the full data set. Error bars for the surface fitting method arise from statistical variation between localised measurements. For more details of curvature measurement, see Appendix A.

lattice-Boltzmann model can still give reasonable results. Overall, for RK model as a strictly immiscible model, we are able to obtain bubbles of radii as low as $\sim 2.0 \text{ l.u.}$, and although the pressure at such a small radius is degraded due to the proximity of the phase interface, the bubble remains stable and spherical.

For SC model different behaviour is observed depending on G_{coh} . More specifically, for $G_{\text{coh}} = 3.5$ and 4.0 , whose minimum bubble sizes are similar to the RK model (i.e. the bubble diameter is $\sim 4.0 \text{ l.u.}$), the breakdown apparent in the RK model is not

²The deviation from the Laplace’s law in RK model is indeed a type I error, since type I error is predictable as the model is pushed to the low-resolution limit. In contrast, the type II error (transition to nonphysical behaviour), such as the nonphysical attraction of dissolved NW phase to the solid surface which is discussed in the later section, is not a feature of the model that can be predicted.

observed. This is expected, since based on the density profiles in Figure 3.1, the average interfacial thickness involves as small as 4.0 *l.u.*. However, for $G_{\text{coh}} \leq 3.0$, the curvature measurement stops at $\kappa_H \approx 0.75$ or less, beyond which the bubble completely dissolves. In fact, as G_{coh} decreases, the maximum mean curvature beyond which the initial NW bubble dissolves decreases correspondingly. The phenomena observed here are two folds: (a) in contrast to the RK model, the solubility of the SC model is strongly dependent on the curvature, as is directly shown in Figure 3.2; (b) the solubility (or more specifically the immiscibility) of the SC model also depends on the system's surface tension, since the maximum mean curvature decreases with a decreased G_{coh} , and a smaller G_{coh} gives a smaller system's surface tension. For the dissolution issue observed in phenomenon (a), it is convenient to refer to the Kelvin equation (Israelachvili, 2011) which describes the effect of curvature (and thereby capillary pressure) on the relative solubility of a liquid or a solid in a liquid. In the context of the bubble test where the dissolution of the NW bubble is of interest, the Kelvin equation can be conveniently written as:

$$\ln \left(\frac{\rho_{\text{nw,minor}}}{\rho_0} \right) = \frac{V_{\text{m}}}{RT} P_c, \quad (3.3)$$

where ρ_0 refers to the amount of the dissolved NW density in bulk W phase at zero capillary pressure (i.e. a plane interface), V_{m} is the molar volume of the NW phase, and R is the universal gas constant (i.e. $8.314 \text{ JK}^{-1}\text{mol}^{-1}$). The curvature-dependent solubility for the SC model has been investigated by Schaap et al. (2007), whose results is re-plotted here in Figure 3.3, where the same multicomponent SC model was used to model a water-Soltrol system. Figure 3.3 shows that the dissolved NW phase (i.e. Soltrol) density $\rho_{\text{nw,minor}}$ increases with increased capillary pressure, which qualitatively agrees with equation (3.3). However, at capillary pressure of $\sim 700 \text{ Pa}$, the magnitude of the left hand-side of equation (3.3) is ~ 0.7 . In reality, given that Soltrol density (790 kg/m^3) is close to water density, we can perform a quick order-of-magnitude estimation of the right hand-side of equation (3.3) by using the molar volume of water as an approximation (i.e. $18.016 \text{ mL} \cdot \text{mol}^{-1}$ at 277K (Chieh, 2009)), which gives $V_{\text{m}} P_c R^{-1} T^{-1} \sim 10^{-5}$. Therefore, the dissolved fluid concentration changes far more rapidly with small pressure changes in the SC model than in the real world. As the curvature increases, larger capillary pressure is needed, and more NW phase will dissolve into the W phase. The sensitivity of concentration on pressure means that the SC model is constantly being driven out of equilibrium by small changes capillary pressure. For this test, the main consequence is that small bubbles have an exaggerated tendency to dissolve into the surrounding fluid and it is not possible to simulate the type of partially-miscible but pre-equilibrated system that is common in laboratory experiments. Nevertheless, there are also circumstances that partial miscibility is a desired feature, such as vapour-liquid systems; for such applications, readers are referred to the work by Yuan and Schaefer (2006), where an improved SC model incorporated with many commonly used equations of state is studied. Overall,

in the context of immiscible simulations, using a larger G_{coh} would certainly suppress the dissolution of the phases, thereby improving the immiscibility; it, however, comes at a cost of reduced numerical stability as will be shown in the following discussion;

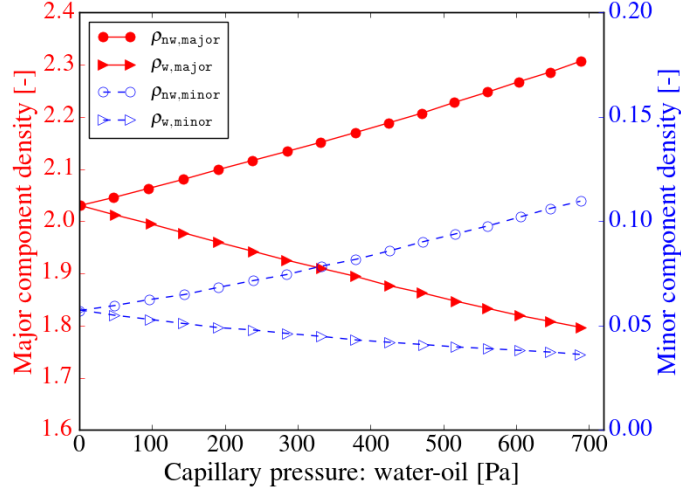


FIGURE 3.3: Component densities of NW and W phases in the SC model as a function of capillary pressure for a water-oil system, with the water-oil interfacial tension of 0.0378 N/m, computed by Schaap et al. (2007). While this was used to help calibrate the model in Schaap et al. (2007), we point out that it demonstrates the sensitivity of solubility to component pressure which lies at the heart of most problems with the SC model, and which violates the Kelvin equation. The simulation setup is similar to the flat tube test in this work (see section 3.4.1). $\rho_{nw,major}$ and $\rho_{w,minor}$ are extracted from within the bulk NW phase, and $\rho_{w,major}$ and $\rho_{nw,minor}$ from within the bulk W phase. Note that G_{coh} defined in Schaap et al. (2007) is 36 times smaller than that defined in this work. In Schaap et al. (2007), $G_{\text{coh}} = 0.025$ with $\rho_{\text{total}} = 2.088$ is used as the initial conditions, which, converted to the setting in this work, is equivalent to have $G_{\text{coh}} = 1.87$ with $\rho_{\text{total}} = 1.0$. We obtained the similar trend in the phase density components by using $G_{\text{coh}} = 2.0$ with $\rho_{\text{total}} = 1.0$ as the initial conditions, at the same tube size.

Lastly, we compare the level of spurious currents for SC and RK models. Ideally, at equilibrium, the velocity field in the bubble test over the simulation domain should be zero. However due to the imbalance of discretised forces, especially near curved phase interfaces, an artificial velocity field is present, and this unwanted velocity field is called the spurious current (Connington and Lee, 2012). Spurious currents are an universal problem for multicomponent LB models. The magnitude of spurious currents becomes larger as the system's surface tension increases, since the fluid-fluid interaction force is larger, increasing the imbalance of these discretised forces. Large spurious currents can prevent the system from achieving a true equilibrium state and even cause numerical instability (type III breakdown). Figure 3.4 summarises the maximum spurious current (extracted from fluid-fluid interface) for SC and RK models, plotted against mean curvature measured by the method of Hou et al. (1997). Overall, the RK model exhibits smaller spurious currents than the SC model, except

for the case of smallest surface tension ($G_{\text{coh}} = 1.5$) in the SC model and largest surface tension in the RK model ($A_{\text{R,B}} = 0.5$). However, it should be noted that for SC model more recently, Porter et al. (2012) replaced the velocity-shift forcing scheme (i.e. equation (2.53)) with the more accurate one by Guo, Zheng, and Shi (2002), and have shown much reduced spurious current. The reduced spurious current in RK model is because of the use of modified perturbation collision operator (i.e. equation (2.60)) that improves the isotropy in surface tension calculation, and the recolouring collision operator (i.e. equation (2.63)) further reduces the spurious currents. It is also noted that, both the interfacial curvature and the capillary pressure do not strongly influence the magnitude of the spurious current. For both models, as G_{coh} or $A_{\text{R,B}}$ increases, the level of spurious currents increases correspondingly. In particular, for SC model with $G_{\text{coh}} > 3.0$, the spurious currents are comparable to the lattice speed of sound c_s , thus at the proximity of the low Mach-number limit for incompressible LB models (Latt et al., 2008). Therefore, to avoid numerical instabilities due to large spurious currents, $1.6 \leq G_{\text{coh}} \leq 2.0$ is usually used for SC model (Huang et al., 2007). In this regime, the interfacial widths in the SC and RK models are the same, eliminating the SC model's potential advantage of generating thin phase interfaces at large G_{coh} .

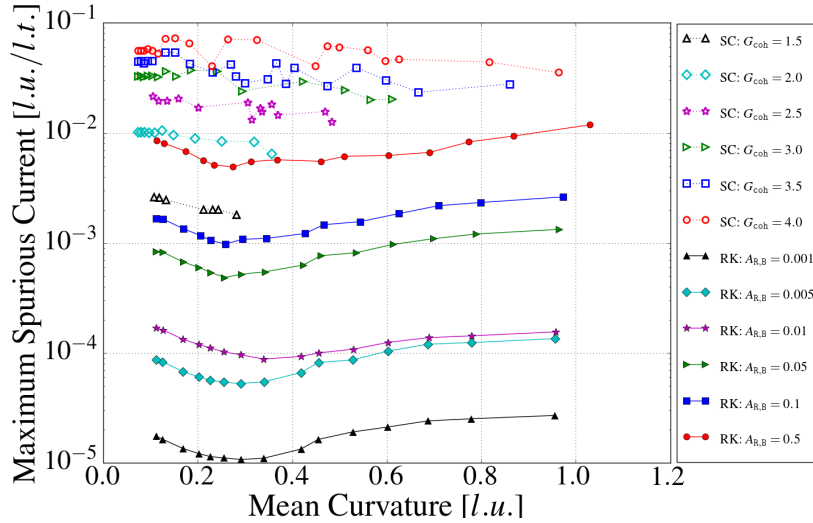


FIGURE 3.4: The maximum spurious currents for SC and RK models' bubble test at different model parameters G_{coh} and $A_{\text{R,B}}$. Mean curvatures are measured by the method of Hou et al. (1997).

3.4 Static Capillary Tube Test

In this section, solid boundaries ("walls") are added, with the NW and W fluids enclosed in a square-shaped capillary tube (Schaap et al., 2007; Huang et al., 2007; Ramstad, Øren, and Bakke, 2010). The NW phase is placed in the middle of the tube with the W phase at the ends, and the total masses of NW and W phases are set equal. Being able to achieve high curvatures with a high NW fluid saturation avoids

the complete dissolution that plagued the SC model in the bubble test. Periodic boundary conditions are applied at ends of the tube. For the fluid-solid interface, the standard bounce-back condition is used (Cornubert, d’Humières, and Levermore, 1991). This is the simplest scenario for simulating a single pore in real porous rocks. In this test, by varying the wetting conditions (adjusting $G_{\text{ads},k}$ for SC model and $\Phi(\mathbf{x}_{\text{wall}})$ for RK model), we explore the models’ behaviour through the capillary pressure - mean curvature relation. Two configurations are tested: a flat tube and a tube tilted at 45° to all coordinate axes. A flat tube is an ideal simplification of the real pore space, and the flat sides of the tube give perfectly aligned wall nodes. The tilted tube introduces a complex "staircase" structure along its side walls, as occurs in voxelated representations of real porous media.

For the case of the flat tube, the simulations were performed for wall to wall tube sizes of 3.0, 4.0, 6.0, and 8.0 $l.u.$, corresponding to inscribed tube radii (R_{tube}) of 1.5, 2.0, 3.0, and 4.0 $l.u.$. As a reference, we also performed simulations at $R_{\text{tube}} = 20.0$ $l.u.$, for which we have higher resolution to measure the mean curvature. For the case of the tilted tube, the tube is oriented at 45° to each axis (i.e. the tube axis is parallel to the (1, 1, 1) Cartesian vector). The tilted tube is constructed by geometrically transforming the axis-aligned flat tube. The actual size of the tilted tube, e.g. the effective cross-sectional area, is discretised and therefore not identical to the original flat tube. In addition, the ‘zigzag’ of the staircase walls means that one can only talk about a length-averaged tube size. We calculate the average inscribed radius of a tilted tube \bar{R}_{tilted} as:

$$\bar{R}_{\text{tilted}} = \frac{1}{2} \sqrt{\frac{V_{\text{tilted}}}{\sqrt{N_x^2 + N_y^2 + N_z^2}}}, \quad (3.4)$$

where V_{tilted} is the volume of the tilted tube in voxels, and (N_x, N_y, N_z) is the domain size for the tilted tube. For $R_{\text{tube}} = \{1.5, 2.0, 3.0, 4.0, 20.0\}$ $l.u.$ in the flat tube, after being tilted the calculated inscribed radii are $\bar{R}_{\text{tilted}} = \{1.44, 1.85, 2.83, 3.79, 17.73\}$ $l.u.$.

In terms of the model parameters, for the RK model, a mediate surface tension parameter $A_R (=A_B)$ of 0.01 is chosen. There is no a-priori preference to choose a particular $A_{R,B}$, since according to the bubble test, as long as $A_{R,B} < 0.5$, the model’s behaviour (e.g. numerical stability and interfacial thickness etc.) is relatively insensitive to $A_{R,B}$. Following equation 2.66, to achieve contact angles in the range $[0^\circ, 90^\circ]$ (defined with respect to the wetting phase), the phase field on the wall nodes $\Phi(\mathbf{x}_{\text{wall}})$ is varied in the range $[-1.0, 0.0]$. For the SC model, following results from the bubble test, we set the fluid-fluid interaction coefficient G_{coh} as 2.0 to avoid potential numerical instabilities while maintaining reasonable immiscibility. The wetting fluid-solid interaction coefficient $G_{\text{ads},w}$ is kept 0.0 while different contact angles are achieved by varying the non-wetting fluid-solid coefficient $G_{\text{ads},nw}$ in the range $[0.0, 2.0]$. For SC model, there is no theoretically predicted relation³ between contact angle and $G_{\text{ads},k}$.

The restriction of $G_{\text{ads},\text{nw}} \leq 2.0$ is because the SC model exhibits a type III breakdown for $G_{\text{ads},\text{nw}} > 2.0$ for small inscribed radii in a tilted tube (e.g. $R_{\text{tube}} = 1.5 \text{ l.u.}$), due to very large spurious currents near the fluid-solid interface. Nevertheless, as will be shown in the following sections, the use of $G_{\text{ads},\text{nw}} \leq 2.0$ is already sufficient to generate the contact angle from 0° to 90° . All parameters used in the flat and tilted tube tests are summarised in Table 3.3.

TABLE 3.3: Major Parameters in Flat/Tilted Tube Tests

	SC Model	RK Model
Initial NW density	$\rho_{\text{nw},\text{major}} = 1.0$	
	$\rho_{\text{nw},\text{minor}} = 0.0$	
Initial W density	$\rho_{\text{w},\text{major}} = 1.0$	
	$\rho_{\text{w},\text{minor}} = 0.0$	
Relaxation parameter τ	$\tau_{\text{nw}} = 1.0$	
	$\tau_{\text{w}} = 1.0$	
Inscribed radius of the tube	$R_{\text{tube}} = 1.50, 2.00, 3.00, 4.00, 20.00 \text{ l.u.}$	
	$R_{\text{tilted}} = 1.44, 1.85, 2.83, 3.79, 17.73 \text{ l.u.}$	
Model parameter 1	$G_{\text{coh}} = 2.0$	$A_{\text{R,B}} = 0.01$
Model parameter 2	$G_{\text{ads},\text{nw}} = 0.0 \sim 2.0$	$\Phi(\mathbf{x}_{\text{wall}}) = -0.1 \sim 0.0$
	$G_{\text{ads},\text{w}} = 0.0$	

3.4.1 Flat Tube Case

In the flat tube test, the simulation domain has a dimension of $(N_x, N_y, N_z) = (R_{\text{tube}} + 2, R_{\text{tube}} + 2, 80)$, where the constant ‘2’ accounts for the one-voxel thick wall layer of the tube. Before investigating models’ contact angle and capillary pressure-curvature relations, we first check the morphology of NW and W phases. Figure 3.5 shows, at an inscribed tube radius of 4.0 l.u. , the longitudinal (i.e. along z -axis) and cross-sectional (i.e. x - y plane) density profiles of SC and RK models at a contact angle near 45° , where the cross-sectional profiles are plotted in red for NW phase and in blue for W phase for visual clarity. Four cross-sectional density profiles are shown, corresponding to NW phase and W phase at the centre and ends of the tube. For both models, the cross-sectional density profiles at the centre of the tube look reasonable, as W phase is present in the corners while NW phase occupies the centre of the tube. This is not entirely physical, however, as the wetting film thickness is a function of the lattice unit size (Chen et al., 2015). More seriously, at the ends of the tube, we see non-physical accumulation of the NW phase at the walls (and especially the corners) and a corresponding repulsion of the W phase.

An analysis of what causes the peculiar accumulation/repulsion phenomena for both SC and RK models can be found in Chapter 4. In the static tube test, the

³Readers are noted that the excellent work by Huang et al. (2007), where an equation relating the contact angle to the SC model parameters G_{coh} , $G_{\text{ads},\text{nw}}$ and $G_{\text{ads},\text{w}}$ is given, is not a theoretical derivation of the contact angle from the SC model theory; on the other hand, the authors proposed an approximation of the contact angle determination, which is a direct substitution of SC cohesion parameters for the Young’s equation.

accumulation of dissolved NW phase near the solid surface is a type II breakdown behaviour, i.e., it is a gradual transition, but the behaviour is entirely non-physical and can therefore have quite unexpected consequences. One potential consequence of this phenomenon is that the models may not be able to support trapped NW phase ganglia at different pressures: for example, in a real porous medium, if two trapped NW ganglia with different capillary pressures are connected via a narrow throat filled with W phase, then the dissolved NW phase accumulating on the walls could allow non-physical transport of NW phase, allowing the ganglia pressures to equalise. In section 3.5.4 we will see that for primary drainage in a simple geometry, the pathway generated by the dissolved NW phase on the solid surface can cause dramatic, non-physical fluid transport; and in section 3.6 where primary drainage in a realistic porous medium is studied, it is shown that the non-physical NW fluid transport generates NW ganglia that are hard to distinguish from ganglia of physical origin (e.g. arising from snap-off). Lastly, it is noted that the SC model has another, more serious problem in the scenario of two disconnected ganglia due to the sensitivity of fluid-fluid solubility to pressure: in the SC model a difference in pressure of two ganglia results in a concentration gradient in the NW fluid dissolved in the W fluid between the two ganglia, causing the ganglia pressures and consequently their boundary curvature/radii to equilibrate rapidly for any choice of model parameters.

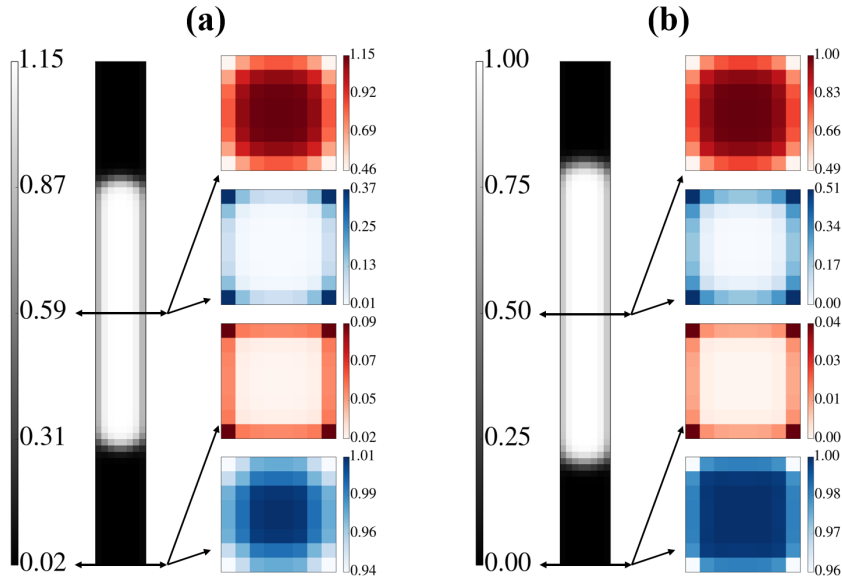


FIGURE 3.5: Longitudinal (i.e. along z -axis) and cross-sectional (i.e. x - y plane) density profiles for (a) SC model, and (b) RK model at a contact angle of $\sim 45^\circ$, in which $G_{\text{ads}, \text{nw}} = 0.7$ for SC model and $\Phi(\mathbf{x}_{\text{wall}}) = -0.63$ for RK model, at an inscribed tube radius of $4.0 \text{ } l.u.$. In each sub-plot, the grey-scale image is the longitudinal density of the NW phase, and on its right, four cross-sectional density profiles correspond to (from top to bottom): NW phase (in red) and W phase (in blue) densities extracted from the centre of the tube, and NW phase and W phase densities extracted from the ends of the tube. The colour-bar of each cross-sectional density profile has its own scale, in order to highlight the spacial variation of the phase density.

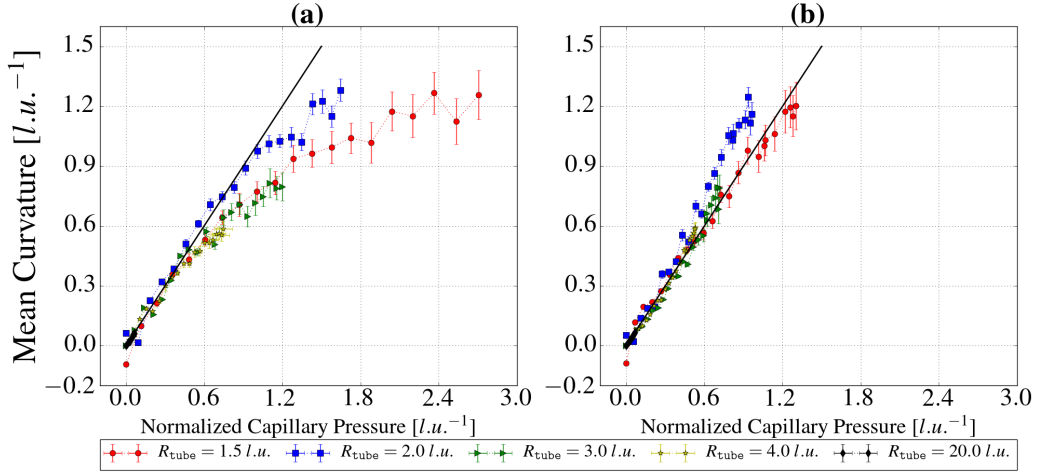


FIGURE 3.6: Plots of calculated mean curvature versus normalised capillary pressure for (a) SC model, and (b) RK model. The black line in each sub-plot is the one-to-one prediction line corresponding to Laplace's law. The error bar in the mean curvature is due to the averaging of mean curvature values of cloud points on the interface (more details in the support information S1). The error bar in the capillary pressure is due to the calculation of a volume-averaged pressure. Note that for $R_{\text{tube}} = 1.5$ and 2.0 l.u. , the fluid density data is up-sampled by linear interpolation to provide sufficient data points for the surface fitting method.

The capillary pressure - mean curvature measurements at different inscribed radii are shown in Figure 3.6 for SC and RK models, to test if the Laplace's law is recovered (for mean curvature measured by level-set method see Appendix F). The local fluid pressure at each grid point is calculated based on equation 2.58 and equation 2.67 for SC and RK models, respectively. Then the capillary pressure is obtained by taking the difference between the volume-averaged pressure in the bulk NW phase and that in the bulk W phase. Since the surface tension in SC and RK models differ by an order of magnitude, the capillary pressure is normalised by the surface tension obtained from the bubble test. A range of capillary pressure is obtained by setting $0.0 \leq G_{\text{nw,ads}} \leq 2.0$ for SC model and $-1.0 \leq \Phi_{\text{wall}} \leq 0.0$ for RK model. The mean curvature is measured by the surface fitting and the level-set methods. It is noted that, due to the surface fitting algorithm (explained in Appendix A), the resolution of the cases of $R_{\text{tube}} = 1.5$ and 2.0 l.u. is so low that not enough cloud points can be found to calculate the curvature values. Therefore, linear interpolation is used to double and treble the original density data for $R_{\text{tube}} = 2.0$ and 1.5 l.u. , respectively, before applying the surface fitting method.

For both models at the inscribed radius $R_{\text{tube}} = 1.5 \text{ l.u.}$, small negative mean curvature values are observed at neutral wetting condition (i.e. when the capillary pressure is close to zero), which is within the measurement error, and is due to the fact that at such a low resolution, the density information cannot be perfectly translated

to a measurable interfacial curvature. Comparing the SC and RK models, we make several observations:

First, when the resolution is high enough at $R = 20.0 \text{ } l.u.$, both models follow the prediction line within measurement uncertainty. This follows from the bubble test results in section 3.3, since the interface is predominantly many voxels away from the wall and should not suffer any degradation of accuracy.

Second, at $R_{\text{tube}} = 4.0$ and $3.0 \text{ } l.u.$, SC and RK models still follow the prediction lines well for low mean curvature (i.e. large contact angle). For the SC model at $R_{\text{tube}} = 4.0 \text{ } l.u.$, the simulation becomes progressively less accurate (type I breakdown behaviour) for $\kappa_H \gtrsim 0.4 \text{ } l.u.^{-1}$, corresponding to a radius of curvature $r_{\text{curv}} \lesssim 5.0 \text{ } l.u.$, and at $R_{\text{tube}} = 3.0 \text{ } l.u.$ accuracy is not degraded until at $\kappa_H \approx 0.5 \text{ } l.u.^{-1}$, (i.e. $r_{\text{curv}} \approx 4.0 \text{ } l.u.$). For the RK model, accuracy does not degrade until slightly higher mean curvatures: $\kappa_H \approx 0.5 \text{ } l.u.^{-1}$ for $R_{\text{tube}} = 4.0 \text{ } l.u.$ (i.e. $r_{\text{curv}} \approx 4.0 \text{ } l.u.$), and $\kappa_H \approx 0.6 \text{ } l.u.^{-1}$ for $R_{\text{tube}} = 3.0 \text{ } l.u.$ (i.e. $r_{\text{curv}} \approx 3.3 \text{ } l.u.$).

Third, given that the range of the curvature values in Figure 3.6, it indicates that we can explore higher curvatures in the SC model with the tube test than the bubble test, because the dissolution is suppressed via adjusting the mass ratio of NW to W phase, while still confining the fluids in very small space. For the RK model, the tube test does not exhibit the apparent breakdown due to the finite interface thickness that was observed in the bubble test (i.e. Figure 3.2 (b) and (d)), since the long NW fluid blob in the tube allows accurate bulk pressure measurement even at high curvatures. This demonstrates that the apparent loss of accuracy in the bubble test was a result of measurement failure rather than a breakdown of the simulation. It also indicates that for SC and RK models in general, the range of influence of the wall on a single fluid density can be as thin as $\sim 1.5 \text{ } l.u.$, and this is much smaller if compared to the fluid-fluid interface ($4.0 \sim 6.0 \text{ } l.u.$).

Overall, our results suggest that in the regime of high curvature where Laplace's law is not accurately recovered (i.e. type I breakdown behaviour), the curvatures appear too high in the RK model and too low in the SC model. This is the case for both the curvature measurement methods used here (results from the level-set method can be found in Appendix F), but we cannot rule out that this might also be a measurement artefact.

Figure 3.7 shows the contact angle against the model's wettability parameter, $G_{\text{ads,nw}}$ for SC model and $\Phi_{\text{wall}}(\mathbf{x})$ for RK model. Note that the contact angle is not measured directly, but is derived from the mean curvature. For large tubes, the contact angle can be directly measured, for example, by measuring the angle between the tangent to a contour line representing the fluid-fluid interface and the side-wall of the tube. However, for small tubes it is challenging to identify the presence of a fluid-fluid-solid triple-contact line, so the angle of the tangent line is highly uncertain. More information about this can be found in Appendix B. Therefore, in this work the contact angle is calculated based on the mean curvature and the tube size, given the following relation between the contact angle θ and the mean curvature for an angular

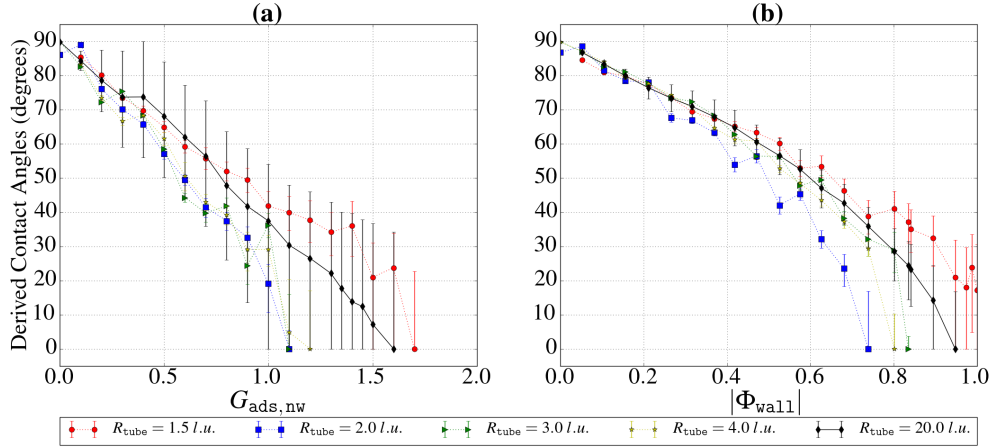


FIGURE 3.7: Derived contact angle plotted against model parameters for (a) SC model, and (b) RK model. For the SC model, the wetting condition is adjusted by varying the adhesion coefficient of NW phase $G_{\text{ads},\text{nw}}$, while keeping the adhesion coefficient of W phase $G_{\text{ads},\text{w}}$ fixed at 0.0. For RK model, the wettability is changed by varying the phase field on wall nodes Φ_{wall} . Contact angle is derived from tube size and measured mean curvature using equation (3.5).

tube (Princen, 1969; Ramstad, Øren, and Bakke, 2010):

$$\cos \theta = \frac{R_{\text{tube}}}{(1 + 2\sqrt{\pi G})F(\theta, G)} \kappa_H, \quad (3.5)$$

where κ_H is the mean curvature, measured by the surface fitting and the level-set method, G is the shape factor defined as $G = A/O^2$, where A and O are the tube cross-sectional area and perimeter length, respectively. The function $F(\theta, G)$ is dependent on the pore shape and is set 1.0 as suggested by Ramstad, Øren, and Bakke (2010). As can be seen from Figure 3.7, the case of $R_{\text{tube}} = 20.0 \text{ l.u.}$ serves as the outline of the contact angle data (excluding the case of $R_{\text{tube}} = 1.5 \text{ l.u.}$), and for the same model parameter, the contact angle becomes smaller as the tube size decreases. This is due to the presence of a finite-thickness W phase layer which increases the mean curvature by a larger fraction for a smaller tube size. For SC model, the variations in the contact angle results for $R_{\text{tube}} = 2.0 \sim 4.0 \text{ l.u.}$ is not as big as those in RK model.

3.4.2 Tilted Tube Case

In the tilted tube test, since a staircase shape along the tube interior walls is introduced, it is more representative of a real pore than the flat walls of the untilted tube in the previous section. First, the capillary pressure - mean curvature measurements is shown in Figure 3.8. The results of mean curvature measured by the level-set method can be found in Appendix F. For $\bar{R}_{\text{tilted}} = \{1.44, 1.85\}$, data interpolation is needed to provide adequate statistics to estimate curvature using the surface fitting method. The staircase structure means that this interpolation is performed on an irregular and

non-convex domain, so an unstructured-grid linear interpolation scheme that implements the Quickhull algorithm (Barber, Dobkin, and Huhdanpaa, 1996) is used via the SciPy library (Jones, Oliphant, and Peterson, 2001). However, for $\bar{R}_{\text{tilted}} = 1.44$, due to the large variation in density between neighbouring voxels, the interpolation scheme did not handle the concave features well and exaggerated the density of dissolved fluid near the solid surface. This results in biased segmented input data for the surface fitting method and decreasing the accuracy of the curvature estimates. Therefore, although visual inspection of the fluid configurations demonstrates that there is no catastrophic breakdown at $\bar{R}_{\text{tilted}} = 1.44$ for both models, we were unable to accurately determine the curvature at this resolution limit. Curvature results for $\bar{R}_{\text{tilted}} = 1.44$ are therefore not shown. However, in Figure 3.9(a) and (c), examples of 3D contour plots (in red) of the zero phase field for SC and RK models are shown, respectively, with $G_{\text{ads},\text{nw}} = 0.50$ for SC model, and $\Phi_{\text{wall}} = -0.63$ for RK model. The phase field is calculated according to 2.61 and the zero phase field indicates the fluid-fluid interface. Also, Figure 3.9(b) and (d) show the corresponding non-wetting fluid phase field projected to the diagonal cross-section of the simulation domain.

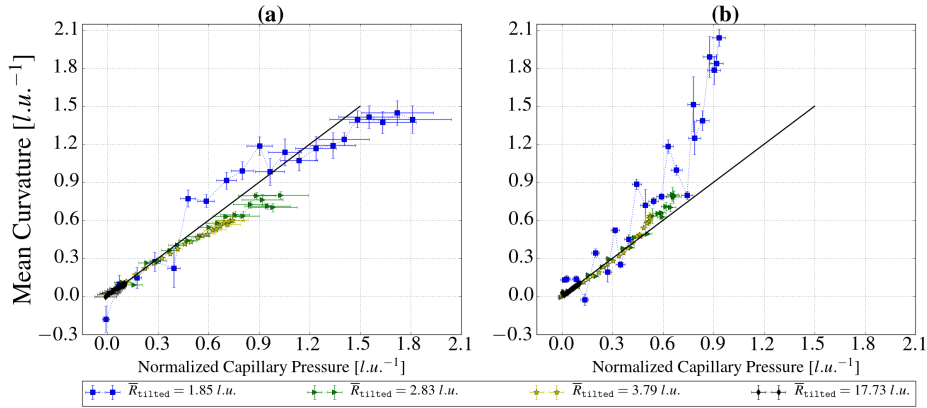


FIGURE 3.8: The mean curvature-capillary pressure measurements of the tilted tube test for (a) SC model, and (b) RK model. The black line in each sub-plot corresponds to the Young-Laplace law (i.e. a one-to-one correspondence between the mean curvature and the normalised capillary pressure). The error bar in the mean curvature is due to statistical variability from point sampled on the interface. The error bar in the capillary pressure is due to the calculation of a volume-averaged pressure. Note that for $\bar{R}_{\text{tube}} = 1.85 \text{ L.u.}$, the surface fitting method uses linearly interpolated density data.

From Figure 3.8, it can be seen that for both capillary pressure and the measured curvature, the standard deviation error bars are larger than those in the flat tube, indicating that the voxelisation of the tilted walls plays a more significant role. In the flat tube case, the standard deviations in the capillary pressure for both models are negligible since the pressure along the tube centreline was uniform. In contrast, for the titled tube, the SC model pressure shows significant variation, much greater than that in the RK model. This low pressure variation in the RK model indicates that the

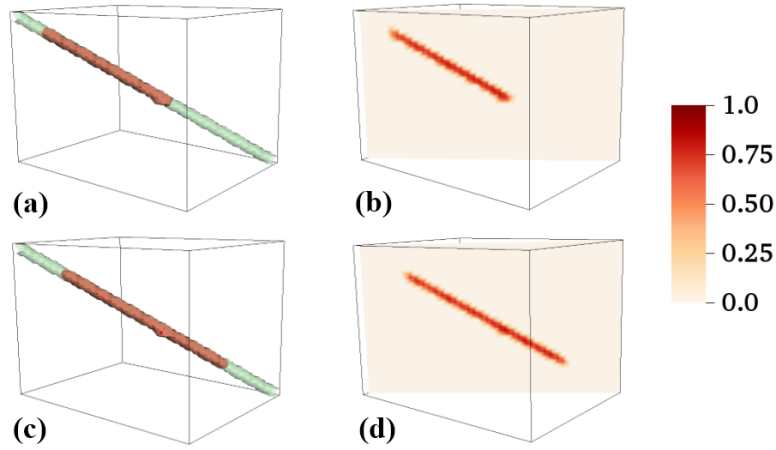


FIGURE 3.9: Three-dimensional non-wetting fluid configurations at $\bar{R}_{\text{tilted}} = 1.44 \text{ l.u.}$ in the tilted tube test. The non-wetting phase is highlighted by the surface contour of the zero phase field in red for (a) SC model, and (c) RK model, where the light green depicts the boundary of the tilted tube. The phase field in diagonal cross-section is also shown for (b) SC model, and (d) RK model. Since the diagonal cross-section is not orthogonal to any of the axis planes, the pixel rendering is needed. The phase field is calculated according to equation 2.61, and the zero phase field indicates the fluid-fluid interface.

"zigzag" effect of the staircase walls is averaged out into an equivalent smooth wall, whereas for the SC model the crevices of the staircase strongly affect the density distribution throughout the tube. Figure 3.10 qualitatively shows the different responses of SC and RK models to the zigzag solid surface, where the surface contours of the non-wetting phase pressure for both models are presented, at $\bar{R}_{\text{tilted}} = 1.85 \text{ l.u.}$ with a mean curvature $\kappa_H \approx 0.9$. Also, to highlight the spatial variations of the phase pressure, several 2D contour plots which cut the y - z plane of the domain are added at the centre and the ends of the surface contours. It can be seen that for RK model, the morphology of the surface contour along the axis of the tilted tube presents a periodic pattern, whereas in SC model, the pattern of the surface contour is more irregular. For RK model, the three 2D contour plots at different locations along tilted tube show a consistent pattern of the contour lines; however in SC model, the contour lines of the 2D contour plots all present different patterns.

From Figure 3.8, it can be also seen that, for RK model in particular, the measured mean curvature at $\bar{R}_{\text{tilted}} = 1.85 \text{ l.u.}$ shows a much larger deviation from the prediction line than that at $R_{\text{tube}} = 2.0 \text{ l.u.}$ in the flat tube test. This is again due to the different response of RK and SC models to the 'zigzag' solid boundaries: RK model sees the staircase as being averaged out such that the effective solid surface point is up at the outer edge of the staircase (i.e. an effective $\bar{R}_{\text{tilted}} < 1.85 \text{ l.u.}$). Thus higher mean curvatures ensue. Moreover, the curvature data exhibits significant variation for both models for $\bar{R}_{\text{tilted}} = 1.85 \text{ l.u.}$. We believe that it is the longitudinal variation (i.e. in the direction of the axis of the tilted tube) in the location of the interface relative to the staircase wall that gives rise to the fluctuations in the

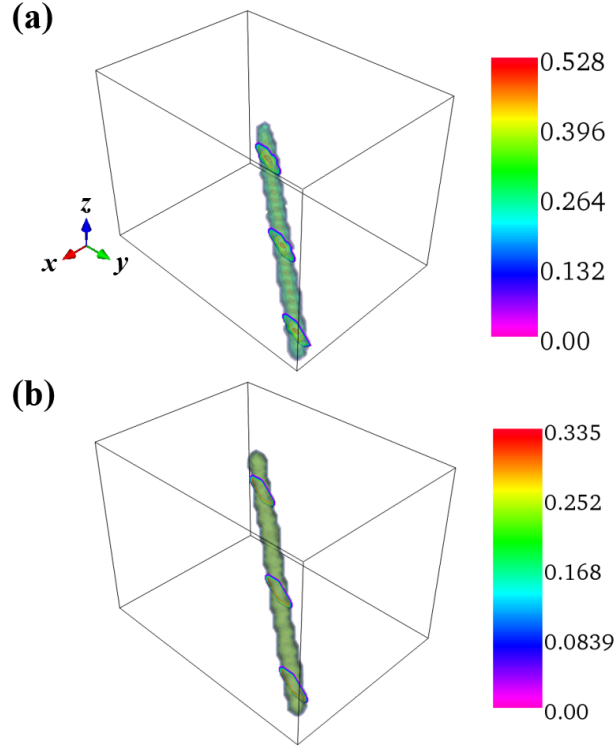


FIGURE 3.10: Three-dimensional surface contour plots of the non-wetting phase pressure profiles in the tilted tube test for (a) SC model, and (b) RK model. To highlight the spatial variations in the pressure profiles, the individual colour bar is used for each sub-plot. Alongside the iso-surface plots, 2D cut-plane contour plots are also added at the centre as well as the ends of the surface contours, where the cut-plane is in the y - z plane.

measured curvatures.

In Figure 3.11, we show how the measured curvature values are affected by shifting the NW/W phase interface by only a few voxels. We use RK model in a tilted tube of $\bar{R}_{\text{tilted}} = 1.85 \text{ l.u.}$ as an example. By adjusting the initial NW phase density at the NW/W phase interface, the fluid phase saturation will change as the NW or W phase will expand or shrink, such that the pinning locations of the NW/W phase interface at equilibrium can be manipulated. As a reference, setting $\rho_{\text{nw},\text{major}} = 1.0$ and $\rho_{\text{w},\text{minor}} = 0.0$ at the NW/W phase interface (on the side of the NW phase), as specified in Table 3.3, is called the original configuration. Other initial configurations are obtained by setting $\rho_{\text{nw},\text{major}} = \{0.75, 0.50, 0.25, 0.00\}$ and $\rho_{\text{w},\text{minor}} = \{0.00, 0.25, 0.50, 0.75\}$. Once the system reaches the equilibrium, we calculate the wetting phase saturation S_w for each configuration and measure the mean curvature. It is noted that the direct control of S_w prior to the simulation is challenging due to the limited lattice size and associated discretisation effects. For simplicity, we test a few RK wetting parameters Φ_{wall} to generate a representative range of mean curvature and contact angle. Different configurations by setting $\rho_{\text{nw},\text{major}} = \{0.75, 0.50, 0.25, 0.00\}$ result in the change of W phase saturation as $\Delta S_w = \{0.78\%, 1.57\%, 2.35\%, 3.14\%\}$. The

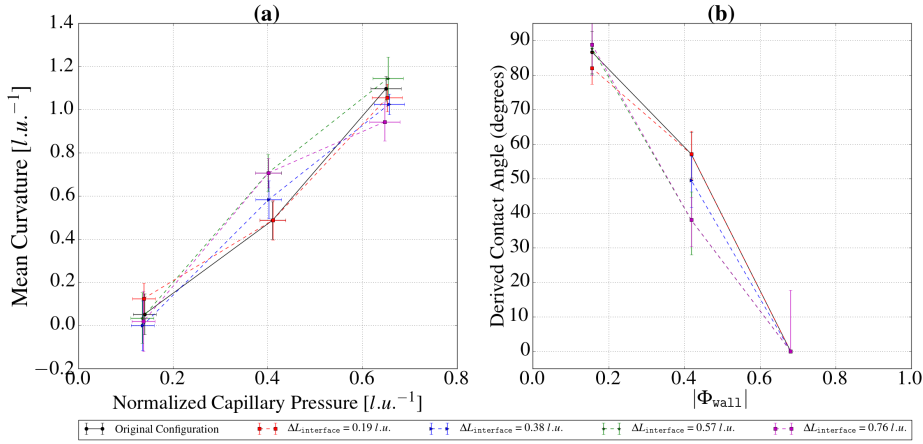


FIGURE 3.11: (a) The mean curvature - capillary pressure measured for RK model in a tilted tube of $\bar{R}_{\text{tilted}} = 1.85 l.u.$. There are five configurations by setting $\rho_{nw, \text{major}} = \{1.00, 0.75, 0.50, 0.25, 0.00\}$ and $\rho_{w, \text{minor}} = \{0.00, 0.25, 0.50, 0.75, 1.00\}$ as the initial conditions, at the NW/W phase interface (on the side of the NW phase). The original configuration refers to the case of $\rho_{nw, \text{major}} = 1.0$ with $\rho_{w, \text{minor}} = 0.0$. (b) The derived contact angle for these five configurations. The effective shift of the NW/W phase interface $\Delta L_{\text{interface}}$ is calculated with respect to the original configuration. Setting $\rho_{nw, \text{major}} = \{0.75, 0.50, 0.25, 0.00\}$ at NW/W interface leads to $\Delta L_{\text{interface}} = \{0.19, 0.38, 0.57, 0.76\} l.u.$

effective shift (in the lattice size) of the NW/W phase interface can then be calculated as $\Delta L_{\text{interface}} = 0.5 \times \Delta S_w V_{\text{tilted}} / (4\bar{R}_{\text{tilted}}^2)$, where V_{tilted} and $4\bar{R}_{\text{tilted}}^2$ are the total volume and the average cross-sectional size of the tilted tube, respectively, and the factor of 0.5 accounts for the fact that there are two spherical NW/W interfaces in the tube test. The effective shift are $\Delta L_{\text{interface}} = \{0.19, 0.38, 0.57, 0.76\} l.u.$

It can be seen from Figure 3.11 that at the resolution limit there is an apparent sensitivity of the curvature measurement to the tiny movement of the phase interface. For example, for the case of $\Phi_{wall} = -0.42$ at $\bar{R}_{\text{tilted}} = 1.85 l.u.$, which gives a normalised capillary pressure of $\sim 0.4 l.u.^{-1}$, the measured mean curvature changes by $\sim 19.5\%$ if shifting the NW phase interface by only $0.38 l.u.$ from the configuration that gives the measurement results in Figure 3.8. This implies that, for RK model, the shift of the NW/W phase interface for every consecutive data points (at the same \bar{R}_{tilted}) in Figure 3.8 potentially ranges from ~ 0.02 to $\sim 0.4 l.u.$. Therefore, when there are only a few voxels across the tube with roughened surface, even a tiny shift of the interface will lead to apparent variation in the curvature measurement. Overall, neither RK nor SC model derive an advantage from this test, since it is not clear whether a staircase-type surface should be interpreted as a planar one, however for practical purposes and given that the variations in the pressure profile are smaller in RK model, it is advantageous to average out single-voxel features and so the RK model's behaviour is slightly preferable.

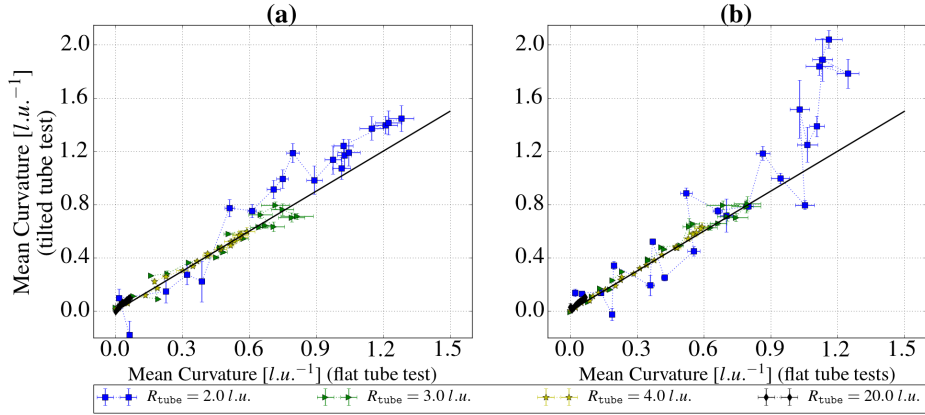


FIGURE 3.12: The mean curvature measured from the flat tube and the tilted tube tests for (a) SC model, and (b) RK model. The black line in each sub-plot is the one-to-one reference line. The legend shows the tube size in the flat tube test. Flat tube sizes of $R_{\text{tube}} = \{2.0, 3.0, 4.0, 20.0\} \text{ l.u.}$ correspond to tilted tubes of $\bar{R}_{\text{tilted}} = \{1.85, 2.83, 3.79, 17.73\} \text{ l.u.}$ respectively.

Figure 3.12 shows the mean curvatures of tilted tubes compared to those of flat tubes of comparable size, at the same model wetting parameters. It can be seen that for $R_{\text{tube}} \geq 3.0$ there is a good agreement between the flat and tilted tube cases, although the actual averaged tilted tube size is slightly smaller than the flat tube size (because it is not possible to create tilted tubes with radii of exact integer values). This indicates that the discretisation effect is negligible down to a pore throat size (i.e. a diameter) of $\sim 6 \text{ l.u.}$. For $R_{\text{tube}} = 2.0 \text{ l.u.}$ (corresponding to $\bar{R}_{\text{tilted}} = 1.85 \text{ l.u.}$), both the RK and SC models give larger curvature values in the tilted tube, suggesting that the prominence in the staircase boundaries significantly affects the interfacial shape.

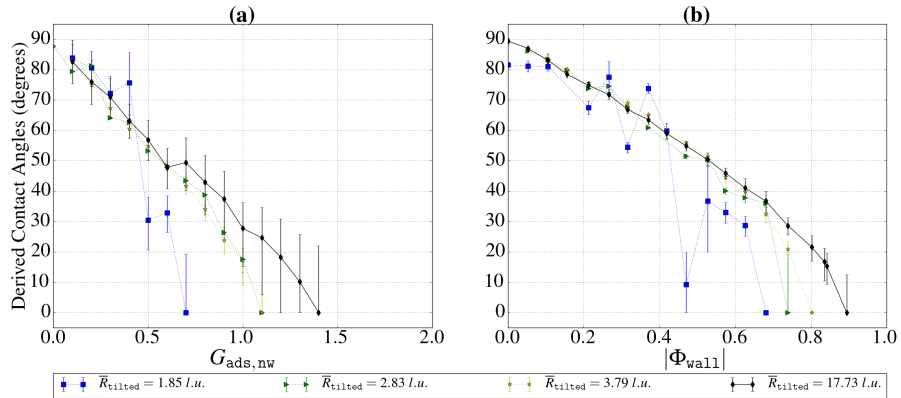


FIGURE 3.13: The derived contact angle of the tilted tube test plotted against model parameters for (a) SC model, and (b) RK model.

Lastly, the derived contact angle for the tilted tube test is shown in Figure 3.13. For

$\bar{R}_{\text{tilted}} = \{1.85, 2.83, 3.79, 17.73\}$, there is little difference in the contact angle results between the flat and tilted tube cases for both models. But the large fluctuations in the mean curvature are reflected in the contact angle data for $\bar{R}_{\text{tilted}} = 1.85 \text{ l.u.}$. Overall, the tilted tube analysis further demonstrates the effectiveness of both RK and SC models at very high levels of discretisation.

3.4.3 Correlation with Unit Conversion

In practice, the simulated LB capillary pressure P_{LB}^c needs to be converted to its counterpart P_{phys}^c in the physical unit, which is given by (Schaap et al., 2007):

$$P_{\text{phys}}^c = \gamma_{\text{phys}} h^{-1} P_{\text{LB}}^c \gamma_{\text{LB}}^{-1} = \gamma_{\text{phys}} h^{-1} \kappa_{\text{LB}}, \quad (3.6)$$

where γ_{phys} is the physical interfacial tension in N/m, h is the resolution of the simulation domain, in the unit of for example $\mu\text{m}/\text{l.u.}$, and P_{LB}^c and γ_{LB} are the lattice capillary pressure and lattice interfacial tension, respectively. If the Young-Laplace relation $P_{\text{LB}}^c \gamma_{\text{LB}}^{-1} = \kappa_{\text{LB}}$ holds, using either κ_{LB} or $P_{\text{LB}}^c \gamma_{\text{LB}}^{-1}$ to do the unit conversion is equivalent. However, Figure 3.6 and 3.8 show that $\kappa_{\text{LB}} < P_{\text{LB}}^c / \gamma_{\text{LB}}$ for SC model and $\kappa_{\text{LB}} > P_{\text{LB}}^c / \gamma_{\text{LB}}$ for RK model, especially when the mean curvature is large (Note it assumes that κ_{LB} and P_{LB}^c can be measured independently). A potential positive side is that one might utilise this deviation of the Laplace relation to offset the requirement of the image resolution: for RK model if κ_{LB} ($> P_{\text{LB}}^c \gamma_{\text{LB}}^{-1}$) is used to convert to P_{phys}^c , one can in fact use a lower resolution image to still achieve the given P_{phys}^c ; similarly, in SC model, one can use P_{LB}^c ($> \gamma_{\text{LB}} \kappa_{\text{LB}}$) information to convert to P_{phys}^c in a low-resolution image.

The physical time can be derived from equation 2.48:

$$\delta t_{\text{phys}} = \sqrt{3} \nu_{\text{LB}} \nu_{\text{phys}}^{-1} h^2, \quad (3.7)$$

where δt_{phys} is in the unit of second per lattice time, and the lattice time in this work is the iteration time step equal to 1 *l.t.*. ν_{phys} and ν_{LB} are physical and lattice kinematic viscosities. When the range of the physical pressure to be simulated is given, and considering the deviations from the Laplace relation for both models, it is important to increase the resolution (i.e. a smaller h) to maintain accurate simulation results, because the relation $\kappa_{\text{LB}} = P_{\text{LB}}^c \gamma_{\text{LB}}^{-1}$ is only maintained when κ_{LB} is small, and higher resolution will ensure the given P_{phys}^c can be obtained with a relatively small κ_{LB} . An obvious side effect of a higher resolution is that δt_{phys} decreases significantly since $\delta t_{\text{phys}} \sim \mathcal{O}(h^2)$, thus a much longer simulation time is needed to achieve the given physical time. Also, a higher resolution image means longer μCT image acquisition time, therefore in most cases it is possible to simply up-sample the image to circumvent the problem.

3.5 Primary Drainage in Square Capillary Tubes

The bubble test and static capillary tube tests in the previous sections are of more fundamental characterisation value, in which the boundary conditions only involve simple periodic or solid-wall boundaries. In practice, we are more interested in models' behaviours in dynamic numerical tests such as drainage and imbibition, where pressure or velocity are specified at the boundaries. In this section, primary drainage (PD) simulations are performed in a square capillary tube with fixed pressure boundary conditions.

Fluid displacement simulations in a square capillary tube are of particular value since the physical behaviour is known analytically: for a square tube, the saturation-capillary pressure relation of the wetting phase beyond the entry pressure can be calculated from the simple geometry as (e.g. see Pan, Hilpert, and Miller (2004)):

$$S_w = \frac{4(1 - \pi/4)R^2}{A_P}, \quad (3.8)$$

where A_P is the cross-sectional area of the pore, and $R = R(P_c)$ is the radius of the cylindrical meniscus in the cross section of the tube, which is related to P_c by the Laplace's law as $P_c = \gamma_{wn}(\frac{1}{R} + \frac{1}{\infty}) = \frac{\gamma_{wn}}{R}$. Therefore by comparing the measured primary drainage curves against the analytical relation equation (3.8), the validity and accuracy of two models can be investigated.

The simulation set-up for the primary drainage test is shown in Figure 3.14, which is mainly adapted from Pan, Hilpert, and Miller (2004). A NW phase reservoir (NWR) and a W phase reservoir (WR) are placed at the entry and exit of the capillary tube respectively. Each reservoir consists of a certain number of layers of the fluid phase. An extra porous plate is inserted between the WR and the capillary tube, which serves as a barrier to prevent the NW phase from exiting the tube beyond the entry pressure. This porous plate includes at least one square-shaped tube of smaller diameter than the primary tube.

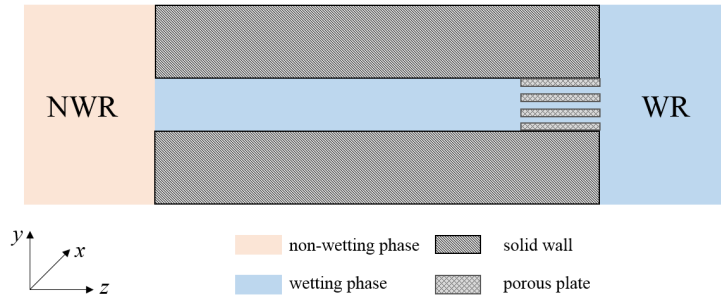


FIGURE 3.14: Set-up of the primary drainage test. A square capillary tube is sandwiched by a non-wetting phase reservoir (NWR) and a wetting phase reservoir (WR). Between the capillary tube and WR, there is a porous plate, acting as a barrier to prevent NW phase from entering WR. In our set-up, this porous plate is simply a narrower capillary tube than the primary tube in the flow medium domain.

For NWR and WR, periodic boundary conditions are applied in the transverse directions (i.e. x and y), and pressure boundary conditions are applied longitudinally, to the first layer of NWR and the last layer of WR, respectively. To simulate the primary drainage (PD) process, the capillary tube, void space of the porous plate, and WR are initially saturated with the wetting fluid, and NWR is filled with non-wetting fluid, as shown in Figure 3.14. The simulation starts from a condition of zero capillary pressure between NWR and WR. Then the capillary pressure is increased progressively, by decreasing the WR boundary pressure while keeping the NWR boundary pressure constant. The pressure gradient causes a capillary pressure and thus a curved interface, driving the NW phase into the capillary tube and displacing the W phase. For each capillary pressure P_c , we let the system evolve until it reaches the equilibrium condition of equation (3.2), i.e. there is no more change in the W phase saturation S_w in the capillary tube. At each capillary pressure, the resulting S_w is recorded, giving a P_c - S_w primary drainage curve.

Our results show that for small R_{tube} , the drainage experiment is affected by several parameters whose influence can be neglected when the resolution is not a limiting factor. These include:

1. how W phase saturation S_w is calculated;
2. for SC model, the peculiarity of the pressure boundary condition on the NWR/WR boundaries;
3. for RK model, where the capillary pressure P_c is measured.
4. the inscribed radius R_{pore} of the single pore in the porous plate, and the thickness of the porous plate L_{pore} (both in the units of $l.u.$);
5. the size of the capillary tube: R_{tube} (in $l.u.$);

3.5.1 Effect of Phase Saturation

First, we consider the effect of how W phase saturation S_w is calculated. We calculate S_w using four methods: (i) threshold of NW phase density (Pan, Hilpert, and Miller, 2004), (ii) threshold of W phase density, (iii) threshold of the difference between NW and W phase densities (Schaap et al., 2007), and (iv) proportional to the the scaled difference of NW and W phase densities. For example, for RK model, method (i) defines a lattice node as being occupied by W phase if the NW phase density on that node is less than half the prescribed NW phase density on the NWR boundary. For method (ii), a lattice node is occupied by W phase if the W phase density on that node is larger than half of the prescribed W phase density on the WR boundary. Method (iii) defines a lattice node as occupied by W phase if the W phase density is greater than the NW phase density. In method (iv), targeted at tubes only a few nodes across, we allow nodes to be partially occupied by both phases, computing the

local W phase saturation $S_w(\mathbf{x})$ as follows:

$$f_{nw}(\mathbf{x}) = \frac{\rho_{nw}(\mathbf{x}) - \rho_{nw,minor}}{\rho_{nw,major} - \rho_{nw,minor}}, \quad (3.9a)$$

$$f_w(\mathbf{x}) = \frac{\rho_w(\mathbf{x}) - \rho_{w,minor}}{\rho_{w,major} - \rho_{w,minor}}, \quad (3.9b)$$

$$S_w(\mathbf{x}) = \frac{f_w(\mathbf{x})}{f_{nw}(\mathbf{x}) + f_w(\mathbf{x})}, \quad (3.9c)$$

$$S_w = \frac{\sum_{\mathbf{x}} S_w(\mathbf{x})}{V_{tube}}, \quad (3.9d)$$

where $\rho_{nw,major}$, $\rho_{w,minor}$, $\rho_{w,major}$, and $\rho_{nw,minor}$ are the prescribed densities of each fluid component at the NWR and WR boundaries. The overall W phase saturation S_w is obtained by averaging $S_w(\mathbf{x})$ over the interior of the capillary tube. There is no a-priori reason to favour one of these methods over another. For simplicity, only the grey-scale method (method (iv)) is used in the rest of the section. Here an example primary drainage (PD) test is used to illustrate the difference of four methods, where a PD simulation is performed at $R_{tube} = 4.0 \text{ l.u.}$, using a porous plate with a pore size $R_{pore} = 1.5 \text{ l.u.}$ for SC and RK models. The PD curves are shown in Figure 3.15.

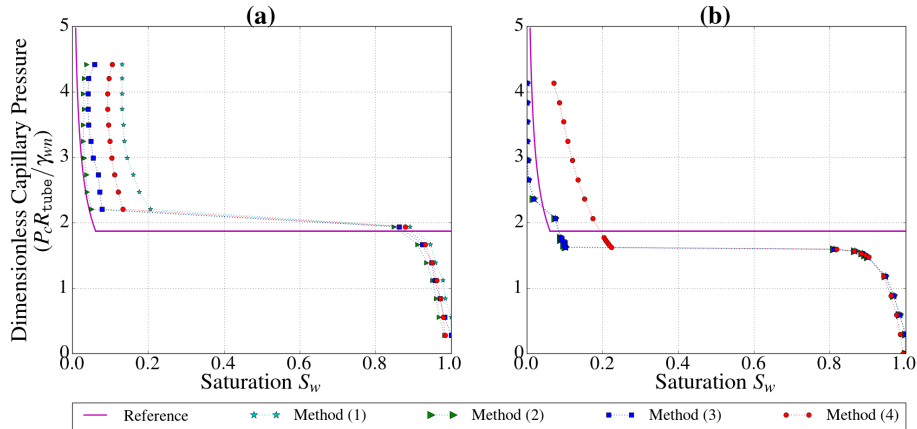


FIGURE 3.15: Primary drainage curves for (a) SC model, and (b) RK model, at a capillary tube size $R_{tube} = 4.0 \text{ l.u.}$ with a porous plate of the pore size $R_{pore} = 1.5 \text{ l.u.}$. It assumes a zero contact angle in the primary drainage process by using $G_{ads,nw} = 1.0$ and $G_{ads,w} = 0.0$ for SC model and $\Phi_{wall} = -0.835$ for RK model, based on the curvature measurement in the flat tube test. The W phase saturation S_w is calculated with four different methods. The entry pressure of the reference line is obtained from the flat tube test of $R_{tube} = 20.0 \text{ l.u.}$ of SC and RK models, respectively. The S_w beyond the entry pressure in the reference line is calculated according to equation (3.8).

For RK model, it is found that the difference in S_w calculated by method (i), (ii) and (iii), is negligible, and in fact the data points of method (i) - (iii) overlap as shown in Figure 3.15. Whereas for SC model, there is apparent difference especially when P_c^d is above the entry pressure. Method (i) to (iii) are closely related to each other:

for a fluid node \mathbf{x}_0 being considered as occupied by W phase, method (i) requires $\rho_{\text{nw}}(\mathbf{x}_0) < \rho_{\text{nw}}(\mathbf{x}_{\text{NWR}})/2$, method (ii) requires $\rho_{\text{w}}(\mathbf{x}_0) > \rho_{\text{w}}(\mathbf{x}_{\text{WR}})/2$, and method (iii) requires $\rho_{\text{nw}}(\mathbf{x}_0) < \rho_{\text{w}}(\mathbf{x}_0)$, where $\rho_{\text{nw}}(\mathbf{x}_{\text{NWR}})$ and $\rho_{\text{w}}(\mathbf{x}_{\text{WR}})$ are densities at NWR and the WR boundaries, respectively. In RK model, for a fluid node where $\rho_{\text{nw}}(\mathbf{x}_0) < \rho_{\text{w}}(\mathbf{x}_0)$, it also naturally leads to $\rho_{\text{nw}}(\mathbf{x}_0) < \rho_{\text{nw}}(\mathbf{x}_{\text{NWR}})/2$ as well as $\rho_{\text{w}}(\mathbf{x}_0) > \rho_{\text{w}}(\mathbf{x}_{\text{WR}})/2$, due to RK model's good immiscibility, so that all three methods regard the node \mathbf{x}_0 being occupied by W phase.

On the other hand, in SC model when there is $\rho_{\text{nw}}(\mathbf{x}_0) < \rho_{\text{w}}(\mathbf{x}_0)$, it is likely that both $\rho_{\text{nw}}(\mathbf{x}_0)$ and $\rho_{\text{w}}(\mathbf{x}_0)$ are small in magnitude because of SC model's partial miscibility, leading to $\rho_{\text{nw}}(\mathbf{x}_0) < \rho_{\text{nw}}(\mathbf{x}_{\text{NWR}})/2$ and also $\rho_{\text{w}}(\mathbf{x}_0) < \rho_{\text{w}}(\mathbf{x}_{\text{WR}})/2$, such that method (ii) gives an opposite answer to what method (i) and (iii) give. For SC model, since method (i) only examines NW phase density, method (ii) only examines W phase density, while method (iii) considers both, it can be seen that method (iii) gives S_w (beyond entry pressure) somewhat in between what method (i) and (ii) give. Comparing method (iii) to method (iv) (since both methods consider NW and W density components), it can be seen that beyond the entry pressure, S_w by method (iv) is larger than that by method (iii) for RK and SC models. This is because the criterion in method (iii), $\rho_{\text{nw}}(\mathbf{x}) < \rho_{\text{w}}(\mathbf{x})$, is after all an abrupt method: the contribution of each fluid node to S_w is either 1 or 0, which is independent of $\rho_{\text{w}}(\mathbf{x})$ or $\rho_{\text{nw}}(\mathbf{x})$ itself, and if $\rho_{\text{w}}(\mathbf{x}) < \rho_{\text{nw}}(\mathbf{x})$ its contribution to S_w is zero. Whereas the method (iv) collects the contributions to S_w from all fluid nodes as long as $\rho_{\text{w}}(\mathbf{x}) > 0.0$ on that node, despite that there might be $\rho_{\text{w}}(\mathbf{x}) < \rho_{\text{nw}}(\mathbf{x})$. In addition, for SC model when the dimensionless capillary pressure becomes greater than 4.0, it can be seen there is a minor increase in S_w , which is due to the boundary conditions and is a type II breakdown.

3.5.2 Effect of Pressure Boundary Condition

We now consider the effect of the pressure boundary condition, which is a particular problem for SC model. Pressure boundary conditions are implemented for SC and RK models by prescribing certain pressure values, which is equivalent to prescribe the densities, i.e. $\rho_{\text{nw},\text{major}}$ and $\rho_{\text{w},\text{minor}}$ on the NWR boundary, and $\rho_{\text{w},\text{major}}$ and $\rho_{\text{nw},\text{minor}}$ on the WR boundary. For RK model, simply setting $\rho_{\text{nw},\text{major}} = \rho_{\text{w},\text{major}} = 1.0$ and $\rho_{\text{nw},\text{minor}} = \rho_{\text{w},\text{minor}} = 0.0$ will give a zero capillary pressure condition, and decreasing $\rho_{\text{w},\text{major}}$ progressively while keeping all other densities fixed gives an increasing capillary pressure. For SC model, there is an extra concern, that changing average density due to the pressure boundary condition will change the value of $G_{\text{coh}}\rho_{\text{total}}$ and thus change the surface tension of the system. Schaap et al. (2007) proposed that the boundary densities be determined from the flat tube test that uses simple periodic boundary conditions, as shown in Figure 3.3. Here we could use densities extracted from the $R_{\text{tube}} = 1.5 \text{ l.u.}$ flat tube test to specify the boundary conditions, as the small tube gives the widest range of curvature values for different contact angles. However, using these densities, we find that the NW phase cannot be driven into a

capillary tube of $R_{\text{tube}} = 2.0 \text{ l.u.}$, no matter how high the capillary pressure is set. A similar phenomenon is also observed when trying a PD test for $R_{\text{tube}} = 1.5 \text{ l.u.}$. Further discussion can be found in Appendix C. In short, as the capillary pressure becomes very high, the density components of for example $R_{\text{tube}} = 1.5 \text{ l.u.}$ no longer retain a well-behaved trend as for the larger tube shown in Figure 3.3 (see Figure C.1 in Appendix C), which leads to erroneously high entry pressure that stops NW phase from breaking through. The example PD curves indicating the breakdown at $R_{\text{tube}} = \{1.5, 2.0\} \text{ l.u.}$ can also be found in Figure C.2 in Appendix C.

In addition, if $\rho_{w,\text{minor}}$ is fixed at a much smaller value than that extracted from the tube test, the NW phase can be driven into the tube for $R_{\text{tube}} \leq 2.0 \text{ l.u.}$. However, at such case the system non-physically reaches several equilibrium states for $0.5 < S_w < 0.8$, with an example PD curve shown in Figure C.3 in Appendix C, where the invading NW phase stops halfway along the tube, indicating the surface tension of the system is constantly changed along the length of the tube (i.e. type II breakdown). Hence it is concluded that for SC model it is very challenging to maintain a constant surface tension, and meanwhile to perform a fluid displacement process for $R_{\text{tube}} \leq 2.0 \text{ l.u.}$. All primary drainage simulations for SC model in this section are for $R_{\text{tube}} \geq 3.0 \text{ l.u.}$, using the density information extracted from the tube test of $R_{\text{tube}} = 3.0 \text{ l.u.}$ as the boundary conditions. Overall, the issue associated with the pressure boundary in SC model originates from the severe miscibility of the density components which represents an exaggerated Kelvin relation (equation (3.3)) as discussed in the section 3.3. This is a long standing issue (Schaap et al., 2007; Huang, Sukop, and Lu, 2015), and if the surface tension can be decoupled from the densities and can be chosen arbitrarily like in the RK model, it is easier to maintain approximately a constant surface tension, as well as maintaining low density compressibility. In practice, a porous medium has various pore throat sizes within it, but in order for SC model to give stable fluid displacement simulations, the use of calibrated pressure boundary conditions from a square tube of $R_{\text{tube}} = 3.0 \text{ l.u.}$ means pores with effective pore radii smaller than 3.0 l.u. will not be invaded by the NW phase within the numerically stable range of capillary pressure.

A side effect of using densities from the flat tube test as the boundary conditions is the snap-off of the invading NW phase after the entry of the capillary tube. An example of such snap-off process is shown in Appendix G. The snap-off usually occurs when the capillary pressure is high, and the exact onset pressure can be found in Table 3.4. The cause of such snap-off can be seen as an collapse of solubility in SC model at very high capillary pressure: since we impose the boundary conditions according to the densities such as shown in Figure 3.3 and Figure C.1 (in Appendix C), as the pressure becomes higher, $\rho_{w,\text{minor}}$ starts to increase (i.e. Figure C.1), as opposed to the normal trend shown in Figure 3.3 for small capillary pressure. Such a boundary density for $\rho_{w,\text{minor}}$ at NWR boundary will eventually cause the invaded NW phase near the inlet of the capillary tube becomes supersaturated and so the W phase ‘condenses out’. By the same token, $\rho_{nw,\text{minor}}$ is also large when the capillary pressure is very high

(e.g. the case of $R_{\text{tube}} = 1.5 \text{ l.u.}$ in Figure C.1), and we observed the NW phase can also ‘condenses out’ inside the W phase reservoir (not shown in this work). The ‘condensation’ of the dissolved phase also brings numerical instability (i.e. type III breakdown). A consequence of this collapse of solubility in SC model is that, if the pressure boundary conditions calibrated from the tube test are used in a real porous medium (which is useful to maintain an approximately constant surface tension), when the capillary pressure is very high, significant errors in the phase saturation will be introduced due to anomalously changed dissolved components of NW and W phases.

Incidentally, it should be noted that the snap-off of the NW phase, although being triggered by the pressure boundary in our particular case, is fundamentally caused by the severe inter-phase dissolution of SC model, and is independent of how the driving force of the flow is implemented; for example, the use of body force to drive the flow will also lead to snap-off, provided that a large pressure gradient is built up where the minor dissolved phase tends to condense out.

3.5.3 Effect of Various Radius Tube

We now consider the effect of how capillary pressure P_c is measured. In the PD test, it is observed that the NW phase pressure at the entry of the capillary tube differs from that at the boundary of NWR (the W phase pressure is always measured at the boundary of WR due to the presence of the porous plate), most prominently in the RK model. Figure 3.16 shows the measured PD curves for the RK model at $R_{\text{tube}} = \{2.0, 3.0, 4.0\}$, with P_c measured at both the tube entrance and the NWR boundary. To put the capillary pressure at different R_{tube} under the same scale, Figure 3.16 plots dimensionless capillary pressure $P_c^d = P_c R_{\text{tube}} / \gamma_{wn}$ against S_w . Figure 3.16 shows that the major difference in P_c^d occurs after the NW phase percolates through the tube, and P_c^d values based on NWR/WR boundary are less than those measured at the tube entrance.

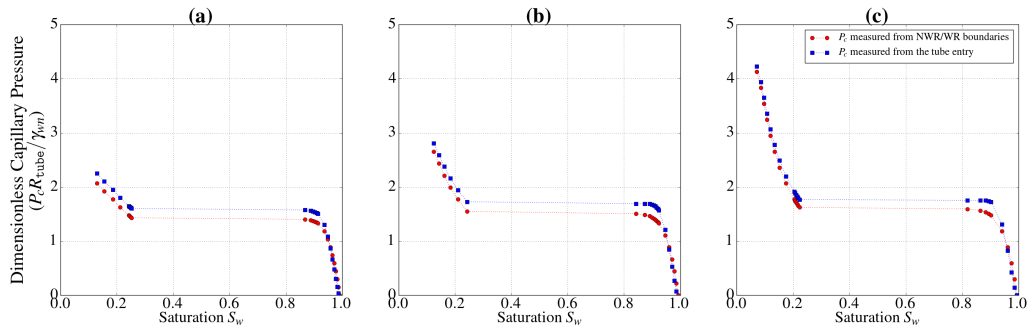


FIGURE 3.16: Primary drainage curves of RK model, at (a) $R_{\text{tube}} = 2.0 \text{ l.u.}$, (b) $R_{\text{tube}} = 3.0 \text{ l.u.}$, and (c) $R_{\text{tube}} = 4.0 \text{ l.u.}$. The NW phase pressure is measured from the entry of the tube (blue), or is directly extracted from the NWR boundary (red). The size of the porous plate is $R_{\text{pore}} = 1.5 \text{ l.u.}$ with $L_{\text{pore}} = 10 \text{ l.u.}$. The maximal P_c is limited by the breakthrough of NW into the porous plate.

To screen out the potential influence due to the pressure boundary condition, we implement a special flat tube test as shown in Figure 3.17(a). Simple periodic boundary conditions are applied to the open boundaries of NWR and WR. Figure 3.17(b) and (c) show the longitudinal pressure profile for SC and RK models respectively, at a 45° contact angle and $R_{\text{tube}} = 4.0 \text{ l.u.}$. At equilibrium, the pressure throughout each phase should be uniform, but the pressure is clearly distorted by proximity to the solid phase, as the pressure is lower in the reservoir than in the tube.

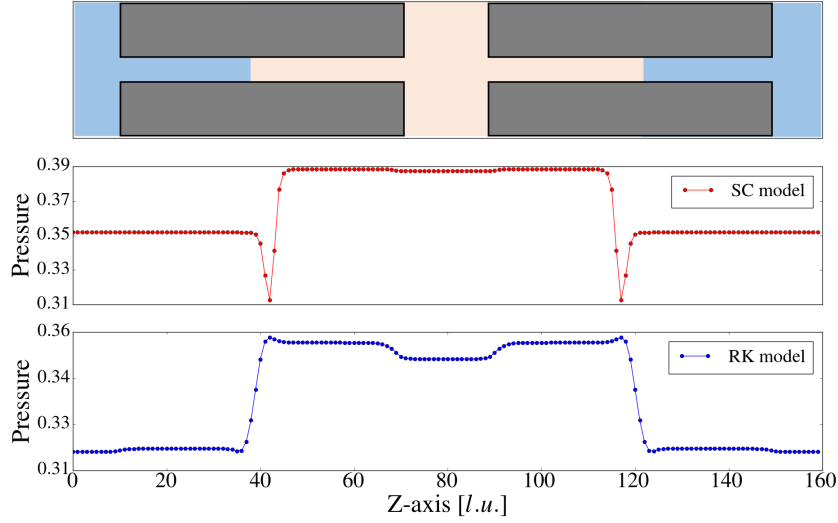


FIGURE 3.17: Top: Schematic showing the set-up for the special tube test. Centre and Bottom: longitudinal fluid pressure profile in the middle of the tube with $R_{\text{tube}} = 4.0 \text{ l.u.}$, for the SC and RK models, at a 45° contact angle (i.e. $G_{\text{ads}, \text{nw}} = 0.7$ for the SC model and $\Phi_{\text{wall}} = -0.63$ for the RK model). To generate similar fluid pressures, $G_{\text{coh}} = 2.0$ is used for SC model and $A_{\text{R}, \text{B}} = 0.225$ is used for RK model such that the lattice surface tension γ_{wn} for both models is ~ 0.1 . Note the non-physical pressure shifts at $Z = 10, 70, 90$ and 150 l.u. . At 45° contact angle, the pressure shift in SC model is smaller than that in RK model and see more details in Figure 3.18

The difference between capillary pressures measured in the open reservoirs to those measured within the tube is shown in Figure 3.18 for a range of R_{tube} for SC and RK models. In order to compare SC model to RK model on a relatively equal footing, $G_{\text{coh}} = 2.0$ for SC model and $A_{\text{R}, \text{B}} = 0.225$ are used so that the resultant lattice surface tensions of two models are of the same order of magnitude. For all cases, we find that capillary pressure measured in the open reservoirs is less than when measured in the tube. There are two features in Figure 3.18: first, as the tube size becomes larger, the deviations in capillary pressure decrease for both models. This is expected since it is the proximity to walls in all directions that causes the distortion in the pressure distributions, which is why near the walls in a bigger tube there is not such a problem as at the centre of the a smaller tube. Second, for more strongly wetting conditions (i.e. lower contact angles), for SC model the deviation becomes larger, and for RK model

the deviations looks almost independent of the wetting condition for $|\Phi_{\text{wall}}| > 0.2$. Overall, both the SC and RK models present similar trends and magnitudes in the deviations. This implies that, for a realistic porous medium simulation, the capillary pressure measured at the inlet and outlet reservoirs will differ from the local capillary pressures in pores of radii $\leq 6.0 \text{ l.u.}$, by up to 17%. The results in Figure 3.18 are consistent with observed discrepancies in P_c^d in the PD test for the RK model with the relative deviation of P_c^d being $\sim 15\%$ for smaller tube sizes. The deviation in the measured P_c^d in the PD test for RK model is a type II breakdown behaviour, and it should be noted that the discontinuity in the local pressure between open and confined space is limited to the multicomponent LB models and is not observed when only a single component is present.

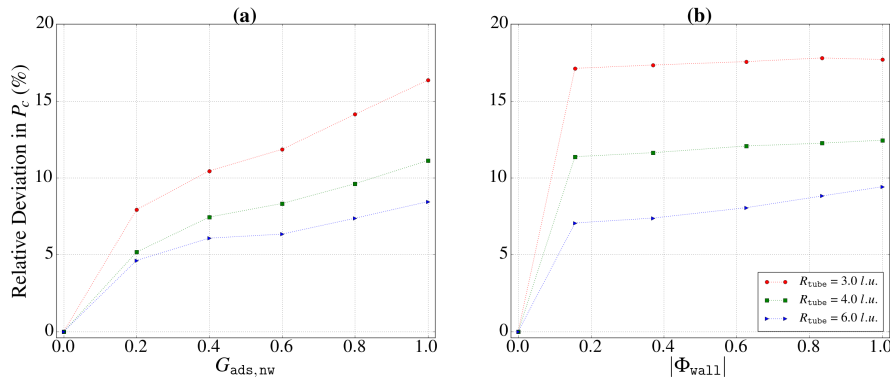


FIGURE 3.18: Relative deviations in the capillary pressure for (a) SC model, and (b) RK model between open reservoir and capillary tube, using the set-up shown in Figure 3.17. The inscribed tube radius R_{tube} in the special tube test is varied from 3.0 to 6.0 l.u. , and the lattice surface tension γ_{LB} for both model is fixed at ~ 0.1 , by setting $G_{\text{coh}} = 2.0$ for SC model and $A_{\text{R,B}} = 0.225$ for RK model. For both models, the deviation in P_c decreases as the tube size becomes larger. This is expected since the boundary phase layer at the solid surface is effectively thinner for a larger tube.

In addition, an extended study on the influence of the surface tension on the deviations in the capillary pressure is shown in Figure 3.19, where a tube of $R_{\text{tube}} = 4.0 \text{ l.u.}$ is used for this study. For SC model, G_{coh} is varied from 1.8 to 2.8 (the initial $\rho_{\text{total}} = 1.0$), which corresponds to the surface tension of $0.1 \sim 0.175$ according to the bubble test. For RK model, $A_{\text{R,B}}$ is varied from 0.001 to 0.8, corresponding to the surface tension of $4.44 \times 10^{-4} \sim 0.36$ according to equation 2.65.

It can be seen from Figure 3.19 that SC and RK models generate about the same levels of the relative deviations. SC model's surface tension is in a much narrower range, so the corresponding deviations is at the same magnitude as for RK model at $A_{\text{R,B}} = 0.225$. Also, it indicates that a larger surface tension gives a smaller relative deviation, which implies that a larger surface tension is preferred to reduce the non-uniformity effect in the pressure fields. However, for a larger surface tension the associated compressibility in the phase density is also increased, as a requirement to generate larger pressures. In practice, in a dynamic fluid displacement simulation

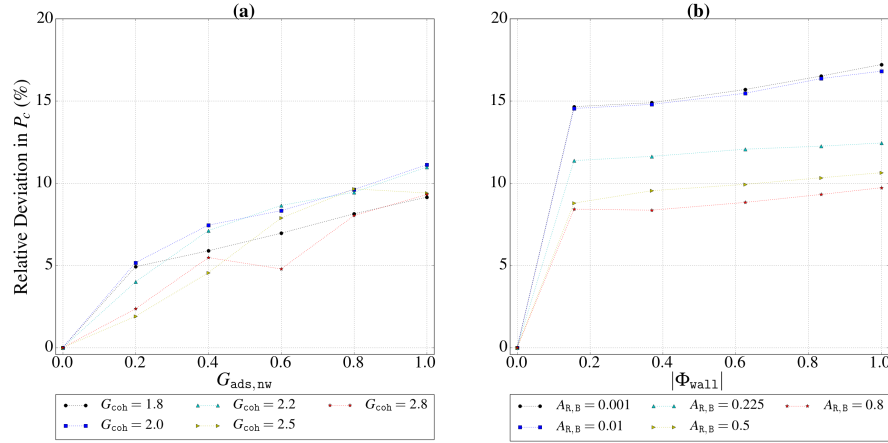


FIGURE 3.19: Relative deviations in capillary pressure for (a) SC model, and (b) RK model by comparing the results measured from NWR/WR to those measured from within the tube. The inscribed tube radius R_{tube} is 4.0 l.u. . The SC model parameter G_{coh} is varied from $1.8 \sim 2.8$, giving the lattice surface tension of $0.1 \sim 0.175$; the RK model parameter $A_{\text{R,B}}$ is varied from $0.001 \sim 0.8$, giving the surface tension of $4.44 \times 10^{-4} \sim 0.36$.

where the pressure boundary condition is usually used, low compressibility in phase densities is desired, since we want the pressure gradient developed between NWR and WR due to the compressibility is just big enough to drive the flow, but is also small enough to avoid the numerical instability and to not violate the incompressible limit of LB models. Hence, as a compromise, for both SC and RK models, an intermediate surface tension should be considered. Overall, it is found that for SC model the deviation is almost independent of the surface tension, whereas for RK model an increased surface tension leads to a decreased deviation. It is noted that the surface tension of RK model used in the PD test is one order of magnitude higher than that of SC model, so the deviation in capillary pressure in SC model is generally lower, and reflected in the $P_c^d - S_w$ curve, the deviation in P_c^d is not as apparent as in RK model.

3.5.4 Effect of Porous Barrier

We have found that the porous plate plays an important role which can be studied by varying its size. The dimensions of the porous plate are characterised by (a) the inscribed radius R_{pore} of the tube through the plate and (b) the thickness L_{pore} of the plate. To examine the models' behaviour at the resolution limit, porous plates with channels of $R_{\text{pore}} = \{0.5, 1.0, 1.5\} \text{ l.u.}$ and two different thickness $L_{\text{pore}} = 3.0$ and 10.0 l.u. are tested for a capillary tube of $R_{\text{tube}} = 4.0 \text{ l.u.}$. The thin porous plate is comparable to the phase interface thickness of two models, and the thick porous plate refers to $L_{\text{pore}} = 10.0 \text{ l.u.}$, which is much greater than the phase interface thickness. The SC and RK models are then used to simulate primary drainage for these 6 porous

plate configurations, with P_c^d varied from 0.0 to the entry pressure of the porous plate. These simulations result in several non-physical behaviour.

First, for both SC and RK models, before the breakthrough of the NW phase into the capillary tube, the NW phase accumulates inside the porous plate, with higher NW saturation in the smaller porous plate channels, which is a type II breakdown behaviour. The average NW phase fractions in the porous plate are summarised in Table 3.4. It can be seen that for both models, as R_{pore} becomes larger, the non-physical NW fluid accumulation decreases without ever reaching zero. This is not due to a non-conservation of NW phase but is transported from the NWR through the main capillary tube: as the simulation begins, the NW fluid is first attracted to the walls at the tube entry, and gradually propagates along the surface of the walls (especially the corners) to the porous plate. For $R_{\text{pore}} \leq 1.0 \text{ l.u.}$, the surface-to-volume ratio of the porous plate channel is very high, which provides perfect accommodation to trap the dissolved NW fluid, as is discussed in Chapter 4.

TABLE 3.4: Summary of Breakdown Due to Size of Porous Plate

R_{pore}	L_{pore}	Average percentage $\rho_{\text{nw, minor}}$ in porous plate before breakthrough		Onset pressure of snap-off	Onset pressure of leak through	Reference entry pressure of the porous plate (RK model)
		SC model	RK model	SC model	RK model	
0.5 l.u.	3.0 l.u.	7.0%	5.0%	$P_c^d = 4.62$	$P_c^d = 1.77$	$P_c^d = 14.16$
	10.0 l.u.	8.0%	3.0%	$P_c^d = 4.62$	$P_c^d = 1.77$	
1.0 l.u.	3.0 l.u.	4.5%	1.0%	$P_c^d = 4.79$	$P_c^d = 4.13$	$P_c^d = 7.08$
	10.0 l.u.	5.0%	1.0%	$P_c^d = 4.79$	$P_c^d = 1.77$	
1.5 l.u.	3.0 l.u.	3.8%	0.5%	$P_c^d = 4.79$	$P_c^d = 3.83$	$P_c^d = 4.72$
	10.0 l.u.	4.1%	0.6%	$P_c^d = 4.79$	$P_c^d = 4.42$	

Second, for RK model after the entry of NW phase into the capillary tube, the invaded NW phase leaks through the porous plate at relative low capillary pressure, which is a type II breakdown behaviour. For example, as shown in Table 3.4, for the porous plate of $R_{\text{pore}} = 0.5 \text{ l.u.}$, the leak-through occurs at $P_c^d = 1.77$, whereas the breakthrough of such porous plate is supposed not to occur until $P_c^d \sim 14.16$ (the actual entry pressure for $R_{\text{tube}} = 4.0 \text{ l.u.}$ is $P_c^d = 1.77$, so the corresponding entry pressure for a porous plate of $R_{\text{pore}} = 0.5 \text{ l.u.}$ should be 8 times higher, which is $P_c^d = 14.16$). Figure 3.20 captures the moments of before and after the leak-through of the porous plate with $R_{\text{pore}} = 0.5 \text{ l.u.}$ for both $L_{\text{pore}} = 3.0$ and 10.0 l.u. , which rules out the possibility that this non-physical behaviour is due to the finite interfacial thickness. It is the dissolved NW fluid trapped on the walls of the porous plate that behaves as a conduction layer and leads to the non-physical transport of NW fluid. For $R_{\text{pore}} = \{0.5, 1.0\} \text{ l.u.}$, all of fluid nodes inside the porous plate are corner fluid nodes, on which the NW phase forms a conduction layer to facilitate the leak-through, hence giving a much lower entry pressure of the porous plate than reality. Only when R_{pore} increases to 1.5 l.u. , where there are non-boundary fluid nodes and a reduced surface-to-volume ratio, the NW phase flux within the porous plate that flows towards WR decreases, and the entry pressure of the porous plate is comparable to the theoretical value. Also shown in Table 3.4, the case of $R_{\text{pore}} = 1.0 \text{ l.u.}$ with $L_{\text{pore}} = 3.0 \text{ l.u.}$ is an outlier with a much higher breakthrough pressure. We found no clear pattern

for leak-through pressure at such low resolution and simply recommend avoiding such small channels in all simulations. The leak-through behaviour raises the concern that, in real porous media simulations, the RK model cannot sustain two disconnected NW ganglia at different pressures if they are separated via a narrow throat filled with W fluid, since conducting layers of NW phase will form on the walls of the throat allowing the ganglia pressure to equalise. An example of the leak-through of the porous plate for RK model with $R_{\text{pore}} = 0.5 \text{ l.u.}$ and $L_{\text{pore}} = 3.0 \text{ l.u.}$ is shown in Appendix G. Later in the section 3.6, this NW phase attraction and the associated non-physical fluid transport will be revisited with a realistic porous medium, and some consequences are explored.

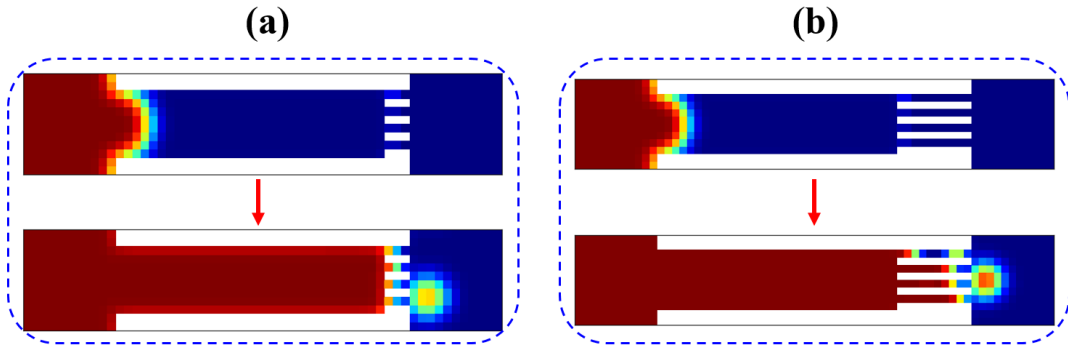


FIGURE 3.20: Snapshots of RK model's breakdown behaviour during the drainage test before and after the entry of the NW phase into the main capillary tube, with the porous plate of (a) $L_{\text{pore}} = 3.0 \text{ l.u.}$, and (b) $L_{\text{pore}} = 10.0 \text{ l.u.}$. The inscribed radii of the main capillary tube and the porous plate are $R_{\text{tube}} = 4.0 \text{ l.u.}$ and $R_{\text{pore}} = 0.5 \text{ l.u.}$, respectively. The 2D plots are extracted from the central plane ($x = 5$). Due to high surface-to-volume ratio of the porous plate, the dissolved NW phase that accumulates inside the porous plate forms a conduction layer and leads to the breakthrough.

Third, for SC model, even with the presence of the NW conduction layer, another instability issue - the snap-off of the NW phase occurs earlier before a possible porous-plate leak-through can be observed for all sizes of the porous plate. The dimensionless capillary pressure at which the snap-off occurs is summarised in Table 3.4. Although the snap-off masks any possible leak-through in this work, Porter, Schaap, and Wildenschild (2009) reported non-physical leakage through a porous plate of $R_{\text{pore}} = 0.5 \text{ l.u.}$ and $L_{\text{pore}} = 1.0 \text{ l.u.}$ when simulating drainage in glass beads with a velocity boundary condition. The leak-through occurred at dimensionless capillary pressure (if translated into our context) of $P_c^d \approx 1.58$. Study of the breakdown behaviour of the SC and RK models when velocity boundary conditions are used is a topic for future research. The pressure boundary condition was also implemented in Porter, Schaap, and Wildenschild (2009), but the highest capillary pressure applied in simulations was (converted into our context) $P_c^d \approx 1.85$, hence no non-physical leak-through or snap-off behaviour was reported. Incidentally, the wetting boundary condition of SC model is more often set by $G_{\text{ads,nw}} = -G_{\text{ads,w}}$ in the literature, which is different from our setting, i.e. varying $G_{\text{ads,nw}}$ from 0.0 to 1.0 while $G_{\text{ads,w}} = 0.0$; however, it

should be noted that the more common setting of $G_{\text{ads,nw}} = -G_{\text{ads,w}}$ will not mitigate the nonphysical mass transport of dissolved NW phase near solid surface. This will become clear in section 4.1.

Fourth, readers are noted that both snap-off and leakage capillary pressure summarised in Table 3.4 are specific to our square tube drainage tests. In applications to real porous media, taking RK model as an example, there is no such “leak-off” threshold pressure above which the nonphysical leakage happens, since the nonphysical mass transport of NW phase occurs and evolves right as the simulation begins (see more discussion in Chapter 4 and see Figure 4.8). Therefore, the erroneous “snap-off” and “leak-off” behaviours are indeed concerns as they are somewhat unpredictable in real porous medium applications.

Overall, the results of Table 3.4, suggest that a larger ($R_{\text{pore}} > 1.0 \text{ l.u.}$) and a thicker porous plate is preferable, to suppress early NW phase leak-through in the RK model. On the other hand, snap-off in the SC model occurs regardless of what the size of the porous plate is used, and is mainly due to the anomalously high $\rho_{\text{w,minor}}$ values at the NWR boundary.

3.5.5 Effect of Capillary Tube Size

The last factor affecting the PD curve is the resolution of the capillary tube. To solely investigate the effect of R_{tube} , we performed PD simulations for $R_{\text{tube}} = \{2.0, 3.0, 4.0\} \text{ l.u.}$, all with a porous plate of $R_{\text{pore}} = 1.5 \text{ l.u.}$ and $L_{\text{pore}} = 10.0 \text{ l.u.}$, to avoid NW phase leak-through. As a result, the case of $R_{\text{tube}} = 1.5 \text{ l.u.}$ is not examined, as this requires that the porous plate has $R_{\text{pore}} < 1.5 \text{ l.u.}$. Moreover, for SC model the case of $R_{\text{tube}} = 2.0 \text{ l.u.}$ is not studied, since as discussed before, a numerically stable simulation with a conserved surface tension cannot be conducted for $R_{\text{tube}} \leq 2.0 \text{ l.u.}$. The density components extracted from the flat tube test of $R_{\text{tube}} = 3.0 \text{ l.u.}$ are used as the boundary conditions for the SC model. A zero-contact-angle condition is assumed, in which, according to Figure 3.7, $G_{\text{nw,ads}} = 1.0$ and $|\Phi_{\text{wall}}| = 0.83$ are used for SC and RK models, respectively. All PD curves are summarised in Figure 3.21. For RK model the measurement of the PD curves stop when the breakthrough of the porous plate occurs; for SC model the snap-off of the invading NW phase has an earlier onset so the PD curves stop when the snap-off occurs. In addition, the theoretical PD curve after NW phase entry is shown on both plots, where $S_w(P_c^d)$ is calculated according to equation (3.8). The entry pressure of the theoretical PD curve for each model is calculated by averaging the individual entry pressure of different R_{tube} , since for both models there is little difference in the entry pressure for different R_{tube} .

From Figure 3.21, we make several observations. First, for both models, it can be seen that the irreducible W phase is larger than the theoretical line. This is partly because the reference line assumes an ideal cylindrical meniscus NW phase filling the capillary tube after the entry, whereas near the porous plate the actual NW phase forms a spherical shape. Moreover, by examining the cross-sectional W phase saturation of the tube (we checked several locations along the tube, i.e. near the

inlet, at the middle of the tube, and near the porous plate), the offset still remains, which indicates that at the low resolution the effect of the measurement error in our density-based S_w calculation method (i.e. equation (3.9)) is not negligible. Regardless of the offset, for both models at $R_{\text{tube}} \geq 3.0$ l.u., the patterns of P_c^d - S_w curves are well-behaved and look similar to the theoretical line.

Second, for RK model at $R_{\text{tube}} = 2.0$ l.u., the simulated P_c^d - S_w curve deviates from the theoretical line, where S_w decreases faster as the capillary pressure increases, indicating that the interfacial curvature may be larger than Young-Laplace law predicts. This is consistent with the deviation from the Young-Laplace law found in the flat tube test whose result is shown in Figure 3.6.

Third, for SC model after the entry of the NW phase, it can be seen that W phase saturation increases with decreasing lattice sizes. This dependence is expected since for most of the diffused interface based models, at a lower resolution it becomes harder to represent the meniscus at the fluid-solid interface with finite numbers of voxels. Compared to the RK model, the W phase layer thickness in SC model seems to be more dependent on the lattice size.

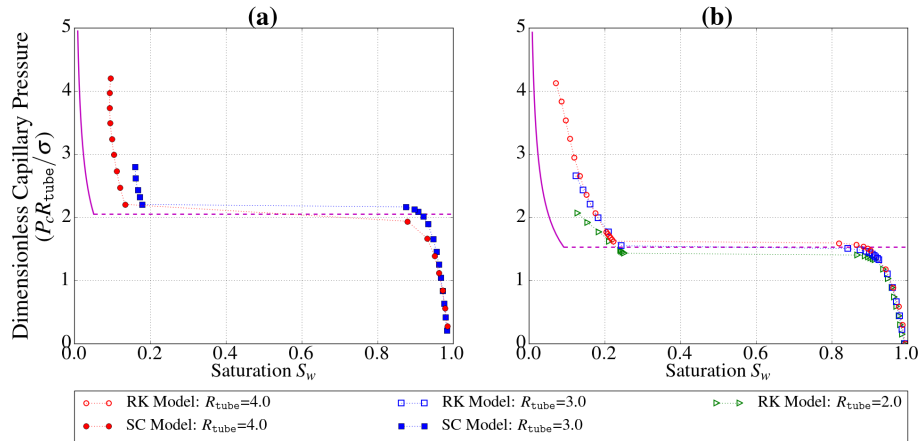


FIGURE 3.21: Primary drainage curves at various R_{tube} for (a) SC model, and (b) RK model. The size of the porous plate used in the simulation is $R_{\text{pore}} = 1.5$ l.u. with $L_{\text{pore}} = 10.0$ l.u.. γ_{wn} is the surface tension. The wetting phase saturation is calculated using the grey-scale method. The wetting parameters of $G_{\text{nw, ads}} = 1.0$ and $|\Phi_{\text{wall}}| = 0.83$ are used for SC and RK models, respectively, which assumes a zero-contact-angle condition according to Figure 3.7. The measured data points in the PD curves stop when the breakthrough of the porous plate occurs for the RK model, and when the snap-off occurs for the SC model. A reference line is plotted for each model, in order to show the theoretical P_c^d - S_w relation beyond the entry, where S_w after the entry is calculated according to equation (3.9). The entry pressure of the reference line is simply an average of the individual entry pressure at different R_{tube} for each model.

Overall, both models can handle well the displacement processes as small as $R_{\text{tube}} = 3.0$ l.u., and the size of the tubes do not play significant roles in the displacement processes, with $P_c^d(S_w)$ relation in SC model having slightly more resolution

dependence after the entry. At the low resolution limit, the systematic error in the S_w measurement is inevitable for diffused interface based model, even if a grey-scale based S_w calculation method (i.e. equation (3.9)) is adopted.

3.6 Primary Drainage in Porous Medium

This section is a test for the more promising RK method in a realistic but challenging porous medium, attempting to correlate our breakdown analysis in simple geometries in the previous sections with real-world simulations. The simulations in this section are performed using a graphics processing unit (GPU)-based implementation of the adaptive MRT RK model that is introduced in section 2.4 (McClure, Prins, and Miller, 2014), and the wetting boundary condition between the fluid and solid interface is implemented according to equation (2.66).

As will be shown in the rest of this section, almost all of breakdown issues encountered in the simple-geometry characterisations from section 3.3 to 3.5⁴, have their reminiscence in the realistic porous medium simulations. An exception is that, since only the RK model is used, the severe inter-phase dissolution and miscibility issue (see equation 3.3 and Figure 3.3) are no longer a concern as those issues particularly pertain to the SC model. For the consequence of inter-phase dissolution of SC model in real porous media applications, please see the discussion at the end of the conclusion section 3.7. In addition, the reminiscence of two key breakdown issues found previously, namely the nonphysical mass transport of dissolved phase near solid surface and the interfacial spurious currents, are not examined in this section, but in Chapter 4 and in section 5.2 of Chapter 5), respectively, because their importance is worthy of dedicated discussions. A zero contact angle condition is implemented by setting the phase field of solid nodes as $\phi_s = -1.0$; although this is only a ‘makeshift’, it technically rules out the influence of nonphysical transport of dissolved NW phase⁵.

The simulations in an X-ray μ CT image of Bentheimer sandstone mimic primary drainage experiments performed on the same sample as in Herring et al. (2017), for a fluid pair of n-decane (non-wetting) and brine (wetting). More details of the experimental set-up and properties of materials can be found in (Herring et al., 2017). The voxel size of the μ CT image is $4.95 \mu\text{m}/l.u.$, and a sub-domain of $256^3 l.u.^3$ is used in this work. The porosity of the sub-domain is 0.22. For simplicity, both the density and viscosity ratios of n-decane - brine system are taken as 1.0. For the lattice-Boltzmann simulation, the relaxation time is $\tau_{R,B} = 0.7$, and the surface tension parameter $A_{R,B} = 0.01$. Both the non-wetting phase reservoir (NWR) and the wetting phase reservoir (WR) consist of 10 layers at the inlet and outlet, respectively. Between the WR and the porous medium, a porous plate with L_{pore} of 3 $l.u.$ and R_{pore} of 1.5 $l.u.$ is inserted. We use R_{pore} of 1.5 $l.u.$ since this is large enough to prevent the non-physical

⁴A summary of all key breakdown issues is in section 3.7.

⁵See section 4.2 for why this would circumvent the nonphysical mass transport near solid surface.

NW fluid transport through the porous plate (see section 3.5.4) and small enough to prevent NW fluid entry in our simulations.

We also performed characterisation on the Bentheimer sub-sample based on the watershed partitioning and network statistical analysis: the distribution of the pore and throat radii can be found in Figure D.1 in Appendix D, which shows that over 70% of the throats have a radius less than 3 $l.u.$, and 50% of the pores have pore radii less than 3 $l.u.$. The maximum square/circular throat radius at the percolation threshold is ~ 4 $l.u.$. Based on the tilted tube tests for RK model (see Figure 3.8), a mean curvature of 0.48 $l.u.^{-1}$ (corresponding to a circular throat radius of ~ 4.17 $l.u.$) is at about the onset of the type I behaviour, where the simulated Young-Laplace relation starts to deviate. This implies that, given the current image resolution, there will be some loss of accuracy beyond percolation due to the gradual onset of type I errors.

To check the results of the bubble and flat/tilted tube tests, we performed drainage simulations using a constant pressure boundary condition and 0° contact angle (i.e. $\Phi(\mathbf{x}_{wall}) = -1.0$). The pressure gradient applied to the medium, if converted to the equivalent mean curvature, is 0.403 $l.u.^{-1}$, slightly less than the percolation threshold. The simulation was run until steady state which was judged to have occurred at 800,000 time steps, when the interface-averaged mean curvature κ_{wn} is changing less than 10^{-6} $l.u.^{-1}$ per 1000 iterations as shown in Figure 3.22(a). A snapshot of the fluid configuration at steady state is shown in Figure 3.22(b). The spatial averaging of physical and geometrical quantities are based on the multi-scale averaging theory (McClure et al., 2016). The initial fluctuations in κ_{wn} and $p_n - p_w$ that are visible in Figure 3.22(a) are due to (1) the fact that an abrupt large pressure gradient is applied across the medium at the beginning, and (2) Haines jumps occur during drainage. However, it is the steady state that is of interest here for drawing correlation with previous simple geometry tests.

Figure 3.22(a) shows that, at steady state, the type I error is observed by comparing κ_{wn} to $p_n - p_w / \gamma_{wn}$, where γ_{wn} is the interfacial tension. The difference between the pressure and the mean curvature during the drainage and at steady state is mainly due to the breakdown behaviour shown in Figure 3.17 and Figure 3.18 where NW phase pressure is reduced in confined spaces less than 6 $l.u.$ in radius. This will cause an error since pressure averaging will include both larger and smaller pores. It is uncertain that whether this deviation is also related to the breakdown behaviour shown in Figure 3.6(b) and Figure 3.8(b) where the Young-Laplace relation is gradually violated when the mean curvature is large: we tested the Young-Laplace relation at the steady state (i.e. at 800,000 time steps) in a small region (50 $l.u.^3$) highlighted in the red circle in Figure 3.22(b), which contains abundant non-wetting and wetting phase. Averaged over just this domain, the mean curvature and the pressure difference agree well with the Young-Laplace equation.

At steady state, it can be also seen that the boundary applied $p_n^\Gamma - p_w^\Gamma$ slightly deviates from the volume averaged $p_n - p_w$, when all the invaded non-wetting phase

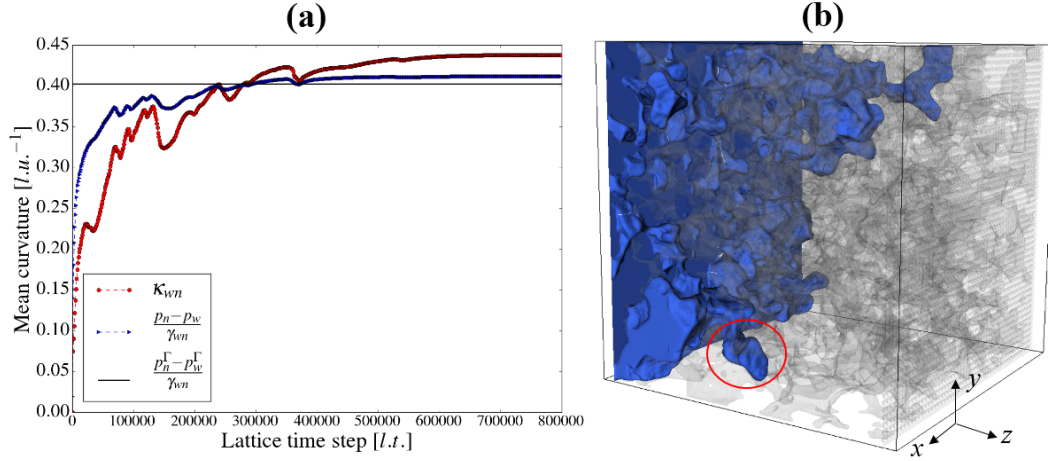


FIGURE 3.22: Primary drainage simulation in a μ CT image of Bentheimer sandstone with a constant pressure difference applied between the inlet and outlet boundaries. (a) Evolution of the interface-averaged mean curvature κ_{wn} , the mean curvature converted from the pressure difference, $p_n^\Gamma - p_w^\Gamma$, measured from the pressure boundary condition, and the mean curvature converted from the volume-averaged pressure difference $p_n - p_w$. (b) The corresponding non-wetting fluid configuration when the system reaches the steady state at 800,000 time steps. For visual clarity, the wetting phase is not shown. The light grey phase indicates the pore matrix of the Bentheimer sandstone.

branches are still connected to the reservoir. This again correlates with the results of the special flat tube test (i.e. Figure 3.17 and Figure 3.18(b)). Based on the results in Figure 3.18(b), for a 0° contact angle (i.e. $|\Phi(\mathbf{x}_{wall})| = 1.0$), the deviation in the capillary pressure is $\sim 9\%$ for $R_{tube} = 6.0 \text{ } l.u.$, whereas the deviation here in Figure 3.22(a) is only $\sim 2\%$, which means that many pores of radius greater than $6.0 \text{ } l.u.$ contribute to the volume average.

Overall, as a counterpart of the primary drainage process in single square tube (section 3.5), the drainage in a realistic porous medium shares some of breakdown issues (although to a less extent). The pressure variation within one fluid due to local solid confinement (see Figures 3.17, 3.18 and 3.19) clearly leads to some errors as evident in Figure 3.22 showing disagreement in system's capillary pressure measured by different means. For the breakdown issue of inaccurate discrete representation of curved interface (see Figures 3.2, 3.6, and 3.8) however, it is not certain that whether this is the cause of the deviation between the interface-averaged mean curvature κ_{wn} and the volume-averaged phase difference (normalised by the interfacial tension) $\gamma_{wn}^{-1}(p_n - p_w)$, which is observed in Figure 3.22(a), or the deviation might also be due to numerical artefact in both mean curvature and phase pressure measurements. The reminiscence of the other two issues encountered in the simple-geometry tests, the non-physical attraction of dissolved NW phase near solid surface and the speed of interfacial current, will be discussed in detail in Chapter 4 and section 5.2, respectively.

3.7 Conclusions

In this chapter, we have characterised the breakdown behaviours of two commonly used multicomponent lattice-Boltzmann models: Shan-Chen model and Rothman-Keller model, by performing a series of small-scale, artificial-geometry tests, with the feature size of the domain being pushed down to the discrete unit size. Both models display quite reasonable basic accuracy (i.e. compared to Young-Laplace law) to mean curvatures approaching $\sim 1.0 \text{ l.u.}^{-1}$, meaning that the models can potentially simulate drainage of tubes down to radius of $\sim 2.0 \text{ l.u.}$. However the inherent miscibility of the SC model causes great problems with constant pressure boundary conditions, resulting in severe instabilities in smaller tubes unless the boundary conditions are carefully tuned. Recently there have been much work on improving the stability of SC model, such as the work by Sbragaglia et al. (2007), where a secondary fluid-fluid cohesion coefficient is introduced such that the equation of state and the surface tension can be tuned independently to enhance numerical stability, or the work by Porter et al. (2012), where an explicit forcing scheme is proposed to demonstrate enhanced stability and capacity to simulate wider range of viscosity ratio; however, to the author's knowledge, the severe inter-phase dissolution still remains as one of the most challenging issue for Shan-Chen-type multicomponent model, and certainly more work is needed in the future.

The RK model is generally more stable, but the current implementation of wetting boundary conditions causes layers of dissolved non-wetting phase to accumulate at the solid surface, thus pressure gradients eventually drive the non-wetting phase into the tube at non-physically low entry pressure. To correlate our knowledge from the simple-geometry characterisations with the real-world simulations, we also implemented the Rothman-Keller based model in a sub-domain of a Bentheimer sandstone μ CT image. The standard test results were largely confirmed in the porous medium, with discrepancies in pressures in the porous medium consistent with predictions from special geometries.

At the resolution limit, the behaviours of the two models are categorised into different breakdown types. There are several key issues arising from various tests, which can be summarised as follows, where the onsets of these issues have been highlighted either by the individual model parameters or the related geometric measures:

1. Inaccurate discrete representation of curved interface due to the finite width of fluid-fluid interface.
 - *Feature tests*: (1) bubble test, (2) flat tube test, and (3) tilted tube test (see sections 3.3, 3.4.1, and 3.4.2).
 - *Onset of the issue*: **SC model**: (1) Not observed (masked by dissolution that has earlier onset); (2) $\kappa_H = 1.0 \text{ l.u.}^{-1}$; (3) $\kappa_H = 0.4 \text{ l.u.}^{-1}$. **RK model**: (1) $\kappa_H = 0.65 \text{ l.u.}^{-1}$; (2) $\kappa_H = 1.2 \text{ l.u.}^{-1}$; (3) $\kappa_H = 0.5 \text{ l.u.}^{-1}$.

- *Consequences*: For both SC and RK models, the simulated Young-Laplace relation ($P_c - \kappa_H$ relation) is not accurate, which will introduce errors in estimating the fluid volume fraction such as S_w .
 - *Error types*: Type I.
2. Inter-phase dissolution due to capillary pressure.
- *Feature tests*: (1) bubble test, and (2) flat tube primary drainage test (see sections 3.3 and 3.5).
 - *Onset of the issue*: **SC model**: (1) It depends on G_{coh} and initial phase volume ratio; (2) All R_{tube} , G_{coh} and G_{ads} . **RK model**: Not observed.
 - *Consequences*: **SC model**: (1) The behaviour of NW ganglia depends on initial conditions and there is potential transport of dissolved fluid between disconnected ganglia; (2) Pressure boundary conditions need empirical calibrations, which would otherwise lead to changing surface tension, snap-off of the non-wetting phase, or erroneously high entry pressure. **RK model**: N/A.
 - *Error types*: **SC model**: (1) Type II; (2) Type II and III. **RK model**: N/A.
3. Speed of interfacial spurious currents approaching the lattice speed of sound.
- *Feature tests*: bubble test (see section 3.3).
 - *Onset of the issue*: **SC model**: $G_{\text{coh}} \geq 3.0$. **RK model**: $A_{\text{R,B}} > 0.5$.
 - *Consequences*: This issues introduces numerical instability and program failure, and it also renders the interfacial velocity indistinguishable from large spurious currents.
 - *Error types*: Type I and III.
4. Accumulation of dissolved non-wetting phase at solid surface.
- *Feature tests*: (1) flat tube test, and (2) flat tube primary drainage test (see sections 3.4.1 and 3.5).
 - *Onset of the issue*: **SC model**: (1) $G_{\text{ads}} \geq 0.0$; (2) Not observed (masked by snap-off that has earlier onset). **RK model**: (1) $|\Phi_{\text{wall}}| \geq 0.0$; (2) Depending on R_{pore} (see Table 3.4).
 - *Consequences*: **SC model**: (1) Errors in estimating fluid volume fraction (e.g. S_w); (2) N/A. **RK model**: (1) Errors in estimating fluid volume fraction (e.g. S_w); (2) Transport of non-wetting phase through capillary barrier prior to the capillary entry; Inability to reach high capillary pressure; and potential transport of non-wetting phase between isolated ganglia.
 - *Error types*: **SC model**: (1) Type I and II; (2) N/A. **RK model**: (1) Type I and II; (2) Type II.

5. Pressure variation within one fluid due to local solid confinement.

- *Feature test*: special tube test (see section 3.5.3)
- *Onset of the issue*: It depends on R_{tube} and G_{coh} (for SC model) and $A_{\text{R,B}}$ (for RK model) (see Figure 3.18 and Figure 3.19).
- *Consequences*: It introduces errors in measuring capillary pressure. Also, non-equilibrium interfacial curvature due to pressure depends on the local neighbouring solid nodes.
- *Error type*: Type II.

It should be noted that, while the issues 1 and 5 can be partially alleviated by increasing the image resolution or applying image up-sampling, to fix issues 2, 3 and 4, more advanced models are needed. For both issues 1 and 5, it is shown in section 3.6 that type I error occurs in the globally averaged pressure difference; this is due to the fine features in the porous media (i.e. characteristic throat size $\leq 8 \text{ l.u.}$); on the other hand, for some local region (e.g. red circle in Figure 3.22) the type I error diminishes. In real porous media applications, where there are always fine features, the type I error is bound to happen due to issues 1 and 5.

For issue 2, this exaggerated tendency of small bubbles dissolving into the ambient fluid makes the SC model unsuitable for immiscible flow (unless an improved model is developed.): Figure 3.3 shows that larger the capillary pressure, greater the solubility will be; hence when two initially separate NW bubbles are trapped at different capillary pressure, the system will not reach an equilibrium state until the bubble at higher capillary pressure completely dissolves. Hence the issue 2 clearly will cause type II error in real porous media simulations, and also considering the breakdown behaviour in capillary tube (Figure G.1), the issue 2 also leads to type III error. In fact, the inter-phase dissolution problem in the multicomponent SC model (not the *single-component multiphase* SC model) has long been overlooked by the LB community, and many observations based on such multicomponent SC model are thus biased: in McClure (2011), the author has pointed out that the (non-physical) inter-phase dissolution “explains the apparent absence of disconnected phase from the simulations reported by Porter, Schaap, and Wildenschild (2009)”; and “the existence of disconnected phases observed in Pan, Hilpert, and Miller (2004) is due to termination prior to equilibrium as a consequence of the termination criteria”. Incidentally, the severe inter-phase dissolution turns out to be a problem for the free-energy LB multicomponent model as well, as pointed out by Liu et al. (2016). On the other hand, for modelling single-component multiphase phenomena, a tuneable miscibility feature in SC model is desirable; the recent work such as Yuan and Schaefer (2006), Sbragaglia et al. (2007) and Porter et al. (2012) have largely improved the original single-component multiphase SC model with enhanced numerical stability and wider coverage of density and viscosity ratios.

For issue 3, the large interfacial spurious current might hinder the accurate measurement of the actual velocity field of the fluids, and this effect becomes more significant at low capillary number. To address issue 3 for SC model, several improved models have been proposed such as Lee and Fischer (2006) and Kuzmin and Mohamad (2010). For RK model implemented in section 3.6, the phase field, being the direct solution of LBM, is used to solve for the level-set equation, thus the evolution of the interface can be accurately determined (McClure et al., 2016).

For issue 4, which is also resolution independent, several improved wetting boundary conditions have been proposed to address the issue for the SC model (Jansen and Harting, 2011; Chen et al., 2015) and for the RK model (Wang, Huang, and Lu, 2013; Liu et al., 2015; Leclaire et al., 2016; Leclaire et al., 2017; Xu, Liu, and Valocchi, 2017). Additionally, the issue 4 is also a problem for other commonly used multi-component LB models, such as free-energy and phase-field LB models (Liang et al., 2019). Readers are referred to the work by Lee and Liu (2010), Wiklund, Lindström, and Uesaka (2011), Lou, Yang, and Xu (2018), and Liang et al. (2019), to name but a few, for the potential resolution of nonphysical mass transport in free-energy and phase-field LB models.

In terms of the future work, first, more thorough resolution dependence simulations are needed to investigate the impact of the under-resolved features of a complex porous medium on the overall fluid interfacial movement. This can be tested by firstly running up-sampled simulations, and then running progressively down-sampled simulations until the behaviour of the fluid phase front changes significantly. These tests serve as a guidance for the so-called minimal numerical resolution that can be applied to most of diffused interface based models, in comparison with the μ CT image resolution.

Second, in some cases, the entire simulation domain can be described as under-resolved; to study the two-phase flow in such condition requires the development of Shan-Chen-type or Rothman-Keller-type greyscale lattice-Boltzmann models, which utilise the sub-resolution porosity and effective permeability as input parameters. The greyscale LB models can well compliment the study when the μ CT images are under-resolved, and they are Darcy-scale modelling techniques, which are different from the pore-scale LB models studied in this thesis. The hybrid approach (i.e. normal LB model plus greyscale LB model) is therefore a future direction for the up-scaling study of multiphase flow in porous media.

Chapter 4

Wetting Boundary in Lattice-Boltzmann Models

In section 3.4.1 where a static flat tube simulations were performed, it has been shown in Figure 3.5 that in the bulk wetting phase, the dissolved non-wetting phase is attracted near the solid surface (especially the corner nodes) for both SC and RK models. More seriously, when it comes to the dynamic simulation where the primary drainage simulation was performed in square tube, the dissolved NW phase that accumulates at the solid surface in RK model leads to significant breakdown such that once the NW phase front approaches the porous plate, the NW front can break through the porous plate at a much smaller entry pressure than that required by the Laplace's law. The similar breakthrough (of the porous plate) in SC model, under the constant pressure boundary condition, was not observed in our study, since the potential leakage is masked by an earlier breakdown behaviour, the snap-off of the NW phase (see section 3.5.2 and Appendix G). However, using the velocity boundary condition, the non-physical leakage through the porous plate is indeed observed, reported by Porter, Schaap, and Wildenschild (2009). The issue of non-physical attraction (of dissolved NW phase) is not limited to SRT-LB models, since it is only related to the treatment of the boundary phase field gradient between the fluid and solid phases; it is shown in section 4.3 that our current MRT-LB model also suffers the same non-physical error.

In this section the cause of the attraction of the dissolved NW fluid to solid surface is discussed in detail. In fact, researchers have been well aware of such non-physical behaviour and have proposed several improved wettability models attempting to eliminate the NW phase attraction. Generally speaking, there are two major branches of LB wettability models, the surface-energy based approach and the geometry-based approach, with our current implementation falling into the former branch. Thus we also have a detailed review of state-of-the-art geometric method in section 4.4. In practice, however, the surface-energy based method is more often used because of its very simple algorithm and more sound physics it models, hence we propose a new energy-based approach and briefly introduce its conceptual implementation in section 4.5. Since this proposed wetting model has not been validated through tests, more future work is needed to implement the model, to compare against the geometric based method, and to evaluate the pros and cons of the two methods.

4.1 Wetting Boundary in Shan-Chen Model

For SC model, such non-physical behaviour of dissolved NW phase in the bulk W phase is due to the imbalance between fluid-fluid cohesion force and fluid-solid adhesion force, which has been discussed in detail in (Chen et al., 2015). Ideally we expect that near the solid surface, W phase is attracted and NW phase is repelled for non-zero adhesion forces \mathbf{F}_{nw}^{ads} and \mathbf{F}_w^{ads} for NW and W fluids, respectively. However, even for $\mathbf{F}_{nw}^{ads} = \mathbf{F}_w^{ads} = 0$, which supposedly gives a neutral wetting condition with a 90° contact angle, both fluids have a significant attraction to the surface which overcomes the immiscibility and attracts significant non-physical minor fluid density, which is illustrated in Figure 4.1 as adapted from Chen et al. (2015). For the sake of continuity with later discussions, we still use the naming of NW and W fluids when explaining Figure 4.1 (and Figure 4.3 for RK model), although at neutral wetting condition there is no NW or W fluid, but simply two immiscible fluids.

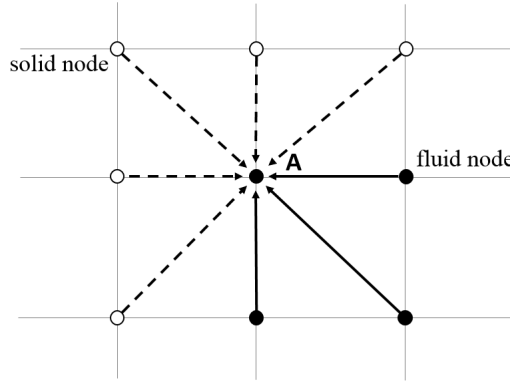


FIGURE 4.1: A two-dimensional schematic illustrating the fluid-solid boundary at the corner of a square capillary tube. The arrows of solid lines indicate the fluid-fluid cohesion forces exerting on the fluid node A, and arrows of broken lines indicate the fluid-solid adhesion forces experienced by node A. The actual tube test is in three dimensions, so there are more cohesive and adhesive forces coming from the adjacent planes which are parallel to the plane of the paper. At the neutral wetting condition, the adhesion force is exactly zero. (Adapted from Chen et al. (2015))

In Figure 4.1, node A is a fluid node at the corner of a square tube. The NW fluid particles on node A experience repulsive cohesion forces from W fluid particles on the neighbouring fluid nodes, as well as repulsive adhesion forces from surrounding solid nodes. Therefore, if there is no adhesion forces, such as at the neutral wetting condition, the NW fluid will accumulate at the solid surface since it experiences a net force pointing towards the solid phase. For dissolved NW phase near the solid surface, it is the competition between \mathbf{F}_{nw}^{ads} and \mathbf{F}_{nw}^{coh} that determines how much NW fluid will be attracted.

Figure 4.2 shows how dissolved NW density distributions in the bulk W phase change with an increasing \mathbf{F}_{nw}^{ads} , extracted from the flat tube test. According to our analysis, the density attraction due to an imbalance of \mathbf{F}_{nw}^{ads} and \mathbf{F}_{nw}^{coh} should be

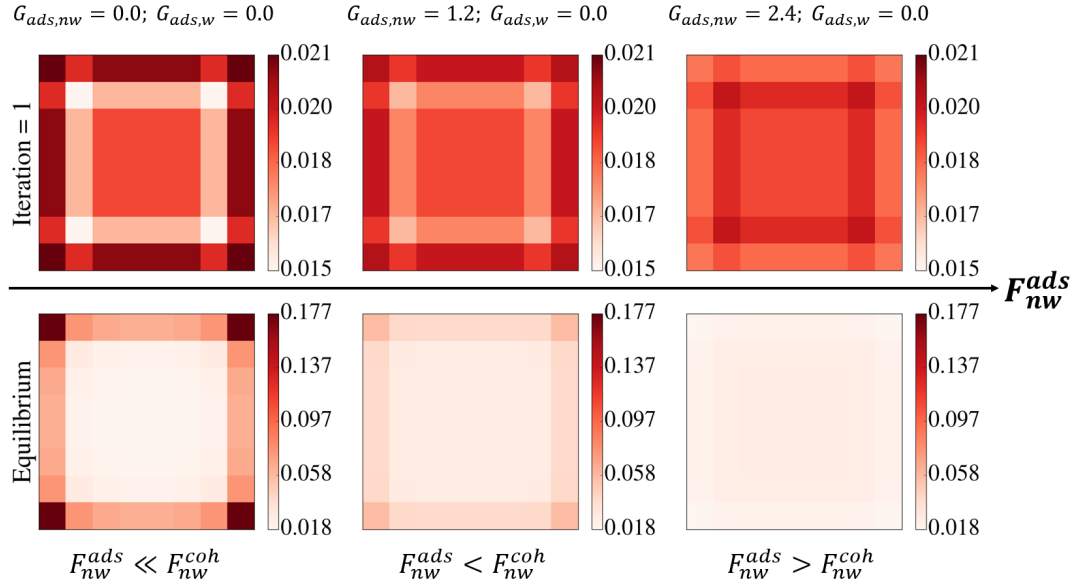


FIGURE 4.2: Cross-sectional density profiles of dissolved NW phase in the bulk W phase are extracted from the end of the capillary tube, at different wetting conditions for SC model. The inscribed radius of the capillary tube is $4.0 \text{ } l.u.$. The adhesive force \mathbf{F}_{nw}^{ads} exerting on the NW fluid increases along the direction of the arrow of \mathbf{F}_{nw}^{ads} . \mathbf{F}_{nw}^{coh} is the cohesion force that W phase exerts on the NW phase.

reflected immediately as the system evolves, thus the NW density profiles just after one iteration are also presented. The adhesion force \mathbf{F}_{nw}^{ads} is increased by adjusting $G_{ads,nw}$, where $G_{ads,w}$ is fixed at 0.0. It can be seen from Figure 4.2 that for $0.0 \leq G_{ads,nw} \leq 1.2$, after one iteration NW fluid is already attracted to the solid surface, and the case of $G_{ads,nw} = 1.2$ has less NW fluid attracted compared to that of $G_{ads,nw} = 0.0$ since \mathbf{F}_{nw}^{ads} is increased. Eventually, at $G_{ads,nw} = 2.4$ we have $\mathbf{F}_{nw}^{ads} > \mathbf{F}_{nw}^{coh}$ so that NW fluid is repelled from the solid surface. Nevertheless, our contact angle measurement indicates that $G_{ads,nw} = 1.2$ already gives a 0° contact angle, but at $G_{ads,nw} = 1.2$ a significant amount of NW phase density accumulates near the solid surface. This essentially indicates that in a normal range of contact angles $0^\circ \sim 90^\circ$, the issue of the non-physical accumulation of dissolved NW phase near solid surface is parasitic. This issue can be reduced (but not completely eliminated) by the use of an unrealistically high $G_{ads,nw}$, or applying a new wetting model: Jansen and Harting (2011) and Chen et al. (2015) have resolved the problem for SC model by introducing virtual fluid on the solid nodes to compensate for the imbalance between cohesive and adhesive forces near the solid surface. In a real porous medium, different amount of dissolved NW fluid will be trapped at various irregular-shaped corners where the net force of \mathbf{F}_{nw}^{ads} and \mathbf{F}_{nw}^{coh} can be pointing to any directions. Furthermore, even if an improved wetting boundary condition is implemented, the non-physical miscibility (discussed in sections 3.3 and 3.5.2) in the SC model still makes it unsuitable for most studies of immiscible flow.

4.2 Wetting Boundary in Rothman-Keller Model

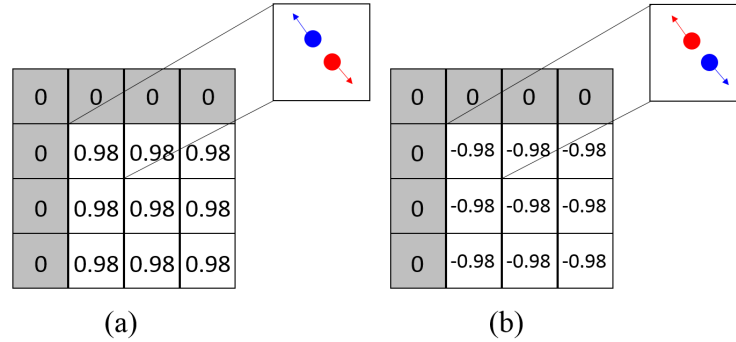


FIGURE 4.3: (a) A two-dimensional schematic of the phase field near the corner of a square capillary tube, extracted from the centre of tube, and (b) the ends of the tube. $\rho_{\text{wall, red}} = \rho_{\text{wall, blue}} = 0.1$ is set, so the phase field values on wall nodes are zeros. At the centre of the tube, the initial conditions are $\rho_{\text{red}} = 1.0$ and $\rho_{\text{blue}} = 0.02$, and at the ends of the tube the initial conditions are $\rho_{\text{red}} = 0.02$ and $\rho_{\text{blue}} = 1.0$.

For RK model, different wetting conditions are realised through the gradient of the phase field $\Phi(\mathbf{x})$ between solid nodes and adjacent fluid nodes (i.e. colour gradient $\mathbf{G}(\mathbf{x})$ at the solid surface). According to the recolouring step in equation (2.63) and the way we define the phase field, red fluid particles tend to move to where $\mathbf{G}(\mathbf{x}) > 0$ and blue fluid particles tend to move to where $\mathbf{G}(\mathbf{x}) < 0$. More specifically, at the solid surface, if the phase field on wall nodes is less than that on adjacent fluid nodes, blue fluid particles will be attracted towards wall nodes and red fluid particles will tend to move away from these wall nodes, thereby the red fluid being the NW phase and blue fluid being the W phase. Similar to SC model, even at neutral wetting condition, the fluids still have ‘preference’ towards the solid surface. To explain this, the initial phase fields near the corner of the tube are shown in Figure 4.3, where $\Phi_{\text{wall}}(\mathbf{x}) = 0.0$ is set, which is expected to give a 90° contact angle. Again, for the sake of continuity with rest of the discussion in this chapter, we still use the naming of NW and W phases at contact angle of 90° , even though there is no NW and W fluids at neutral wetting condition. Figure 4.3(a) shows the initial phase field in the bulk NW phase (e.g. the centre of the tube in a flat tube test). Because of the phase field gradient between solid nodes and fluid nodes, the red and blue fluid particles would adjust their distributions according to this gradient, which makes the wetting boundary ‘less neutral’. By the same token, Figure 4.3(b) shows that in the bulk W phase (e.g. the end of the tube in a flat tube test), the dissolved NW fluid particles are attracted to the solid surface in response to the local phase field gradient. At the neutral wetting condition, to eliminate the phase density attraction/repulsion for example at the centre of the tube (i.e. Figure 4.3(a)), we can remove the phase field gradient between boundary fluid nodes and solid nodes by setting $\Phi_{\text{wall}}(\mathbf{x}) = 0.98$, but this would not change the fact that dissolved NW phase is still attracted to the solid phase at the ends of the tube (i.e. Figure 4.3(b)). As the $\Phi_{\text{wall}}(\mathbf{x})$ is changed

from 0.0 to negative values (i.e. from neutral wetting to strong wetting), less dissolved NW phase will be attracted to solid surface.

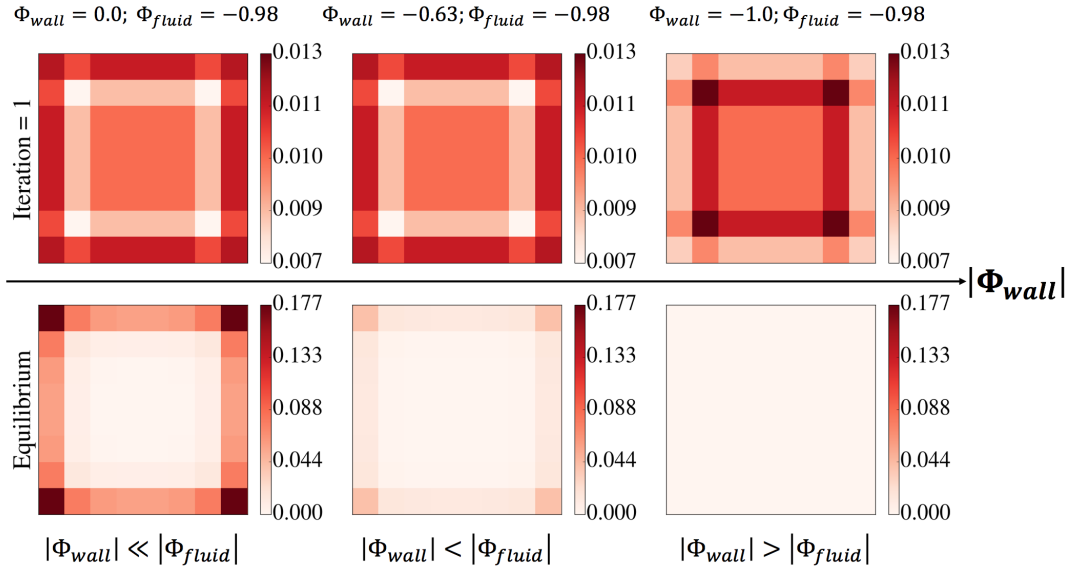


FIGURE 4.4: Cross-sectional density profiles of dissolved NW phase in the bulk W phase are extracted from the end of the capillary tube, at different wetting conditions for RK model. The inscribed radius of the capillary tube is 4.0 $l.u.$. The absolute values of the phase field on wall nodes $|\Phi_{wall}|$ increase along the direction of the arrow of $|\Phi_{wall}|$.

Figure 4.4 shows how dissolved NW phase distributions in the bulk W phase change with a decreased phase field on wall nodes. According to the analysis as shown in Figure 4.3, the attraction of dissolved NW phase near solid surface should be reflected immediately after one iteration for $-0.63 \leq \Phi_{wall} \leq 0.0$, and compared to the case of $\Phi_{wall} = 0.0$, less amount of NW phase is attracted for $\Phi_{wall} = -0.63$. Lastly, when Φ_{wall} becomes smaller than Φ_{fluid} , NW phase is repelled from solid surface. However, when Φ_{wall} is around -0.63, a 0° contact angle is reached already, and $\Phi_{wall} = -1.0$ gives rise to a thick film of W phase near the wall. Hence, similar to what is found in SC model, for a normal range of contact angle $0^\circ \sim 90^\circ$, the non-physical surface attraction of dissolved NW phase is parasitic. To overcome the non-physical issue in the current RK wetting boundary condition, an alternative approach, geometric formulation, has been recently proposed by several works such as Wang, Huang, and Lu (2013), Liu et al. (2015), Leclaire et al. (2016), and Xu, Liu, and Valocchi (2017). The geometric approach is briefly reviewed in section 4.4.

The pressure of the models is directly linked to the phase densities: for RK model, it is simply the sum of NW and W densities weighted by the lattice speed of sound, but for SC model, besides the sum there is an extra non-linear term $G_{coh}\rho_{nw}\rho_w/3$ in the pressure equation (2.58), which arises due to the presence of the cohesion force and the requirement of correctly recovering the macroscopic momentum equation (Huang, Sukop, and Lu, 2015). The cross-sectional pressure profiles from the tube test at a contact angle of $\sim 45^\circ$ and an inscribed tube radius of 4.0 $l.u.$ are shown in Figure

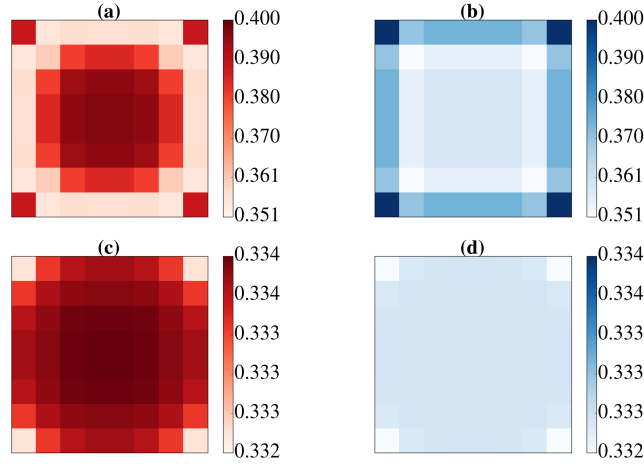


FIGURE 4.5: For SC model, the cross-sectional pressure profiles are shown, at (a) the centre of the tube, and (b) the end of the tube. For RK model, the cross-sectional pressure profiles are shown, at (c) the centre of the tube, and (d) the end of the tube. The contact angle for both models is $\sim 45^\circ$. The inscribed tube radius is 4.0 l.u. . For each model, the same colour bar for the pressure distribution is used.

4.5 for both models. Figure 4.5(a) and (c) show the profiles at the centre of the tube (i.e. the bulk NW region) for SC and RK models, respectively. RK model's profile looks as is expected: the pressure is higher in the centre of the tube and is the lowest at corners. On the contrary, the high pressure at corners in SC model is non-physical, which is essentially due to SC model's partial miscibility such that the major and minor fluid densities are comparable at the corner, and thus the non-linear term $G_{\text{coh}}\rho_{\text{nw}}\rho_{\text{w}}/3$ also plays a significant role. More specifically, on the corner nodes where the W phase film arises, the NW phase does not vanish completely - in fact they are about the same order of magnitude, which makes $\rho_{\text{nw}}\rho_{\text{w}}$ at corners much greater than $\rho_{\text{nw}}\rho_{\text{w}}$ in the centre where ρ_{w} is very small. Thus, it also should be noted, given that SC model's partial miscibility which leads to comparable NW and W phase densities at corner nodes, some errors in the curvature and contact angle measurement will be introduced due to erroneous phase field at corners which is needed as input for these measurements. If the pressure were calculated the same way as in RK model, there is no such peculiar distribution. Figure 4.5(b) and (d) show the profiles at the end of the tube (i.e. the bulk W region), which ideally should present a uniform pressure distribution. However both models show non-uniform distributions, with the SC model showing a stronger pressure variations near the solid surfaces.

4.3 Consequence in Porous Media Simulation

In section 3.5.4 where the primary drainage simulation was taken in a single square tube, the consequence of problematic wetting boundary (for RK model) has been

investigated and it shows that due to accumulated dissolved NW phase near and inside the porous barrier, the invading NW phase in the tube can easily break into the porous barrier below the required entry pressure. This can certainly lead to numerical instability as it blows NW bubbles inside the W phase reservoir and might give erroneous phase distributions due to non-physical fluid transport. For SC model, such non-physical breakthrough of porous barrier is not observed with pressure boundary condition, because it is masked by another breakdown, the snap-off of NW phase during invasion (see section 3.5.2 and Figure G.1), which has an earlier onset. Therefore, in this section our extended study of the problematic wetting boundary will exclusively focus on the RK model.

The leakage of NW phase through porous barrier shown in section 3.5.4 seemingly makes the impression that non-physical attraction of NW phase only becomes problematic when the surface-to-volume ratio of the medium is large (e.g. surface-to-volume ratio of 4 for a porous plate of $R_{\text{pore}} = 0.5 \text{ l.u.}$ and $L_{\text{pore}} = 10 \text{ l.u.}$), or one might think by smoothing the image, the consequence could be mitigated. However, based on the discussion in section 4.2, it is clear that this non-physical attraction of NW phase is essentially a problem of colour-gradient LB model and is image resolution independent. In the following, we will show that accumulation of dissolved NW phase leads to erroneous NW fluid distribution where numerous small NW phase bubbles ($\leq 15 \text{ l.u.}^3$) were “generated”, none of which were due to known physical processes such as snap-off during Haines jumps. Where those ‘fake’ NW phase bubbles are generated, does not necessarily need a high surface-to-volume ratio.

Following the set-up in section 3.6, here we use a combined boundary condition to more realistically mimic drainage experiment in reality: a constant flux boundary (see more in section 5.1.2) is applied at the inlet, and a constant pressure boundary is applied at the outlet. A mid-contact angle of 50° was used (i.e. $\Phi(\mathbf{x}_{\text{wall}}) = -0.55$ according to the calibration in (McClure, Prins, and Miller, 2014)). The advantage of flux boundary condition is that the Capillary number (Ca) can be easily specified in advance, and more details about this boundary condition can be found in section 5.1.2. The capillary number with respect to the invading phase in drainage can be calculated as $Ca = \nu u / \gamma_{\text{wn}}$, where ν is the kinematic viscosity, and u is the Darcy non-wetting phase velocity given by $u = q / \epsilon$, where ϵ is the porosity, and the flux q can be specified by the flux boundary condition.

Figure 4.6 shows non-wetting fluid configurations at three capillary numbers at a wetting phase saturation of $S_w \sim 0.98$ (i.e. early in drainage). In Figure 4.6(a), where $Ca = 2 \times 10^{-5}$, numerous non-wetting phase bubbles are visible, with 90% of the bubbles having volumes of 15 l.u.^3 or smaller, equivalent to a sphere of radius $\leq 1.5 \text{ l.u.}$. A close examination of the displacement process shows that a non-physical film of dissolved non-wetting fluid forms on the solid surface in advance of the main NW phase front (see Figure 4.8). This film gradually migrates along the surface towards the interior of the domain and agglomerates into NW phase droplets near crevices. This is essentially also the cause of the breakdown behaviour observed in single square

tube drainage test (see Figure 3.20(b)). Figure 4.7 illustrates the “growth” process of a non-physical NW ganglion (in the red circle) that is never connected to the main NW phase, due to the non-physical transport of the dissolved non-wetting phase.

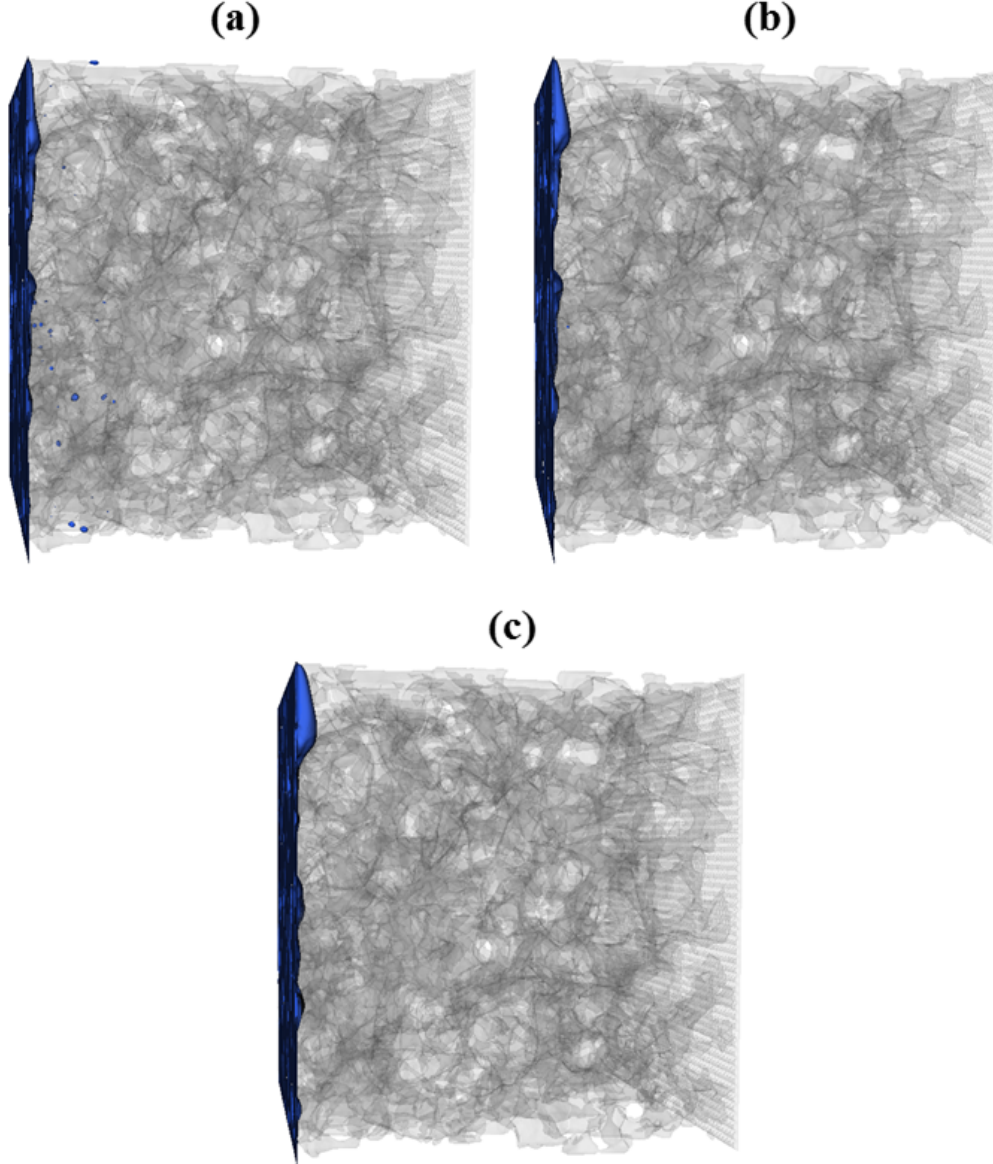


FIGURE 4.6: Primary drainage simulations in the Bentheimer sandstone sample using flux boundary conditions with capillary numbers of (a) 2×10^{-5} , (b) 3×10^{-4} , and (c) 3×10^{-3} . The wetting phase saturation for all three configurations is around 0.98. The non-wetting phase is in blue, and for visual clarity, the wetting phase is not shown. The light grey phase indicates the pore matrix of the Bentheimer sandstone sample.

Due to the slow migration of the dissolved NW fluid films, we expect the growth of these small non-physical bubbles to depend on the flow rate. This is confirmed in Figures 4.6 and 4.8, where the extent and thickness of dissolved films and the number of non-physical bubbles are significantly decreased at higher flow rates. It can be also

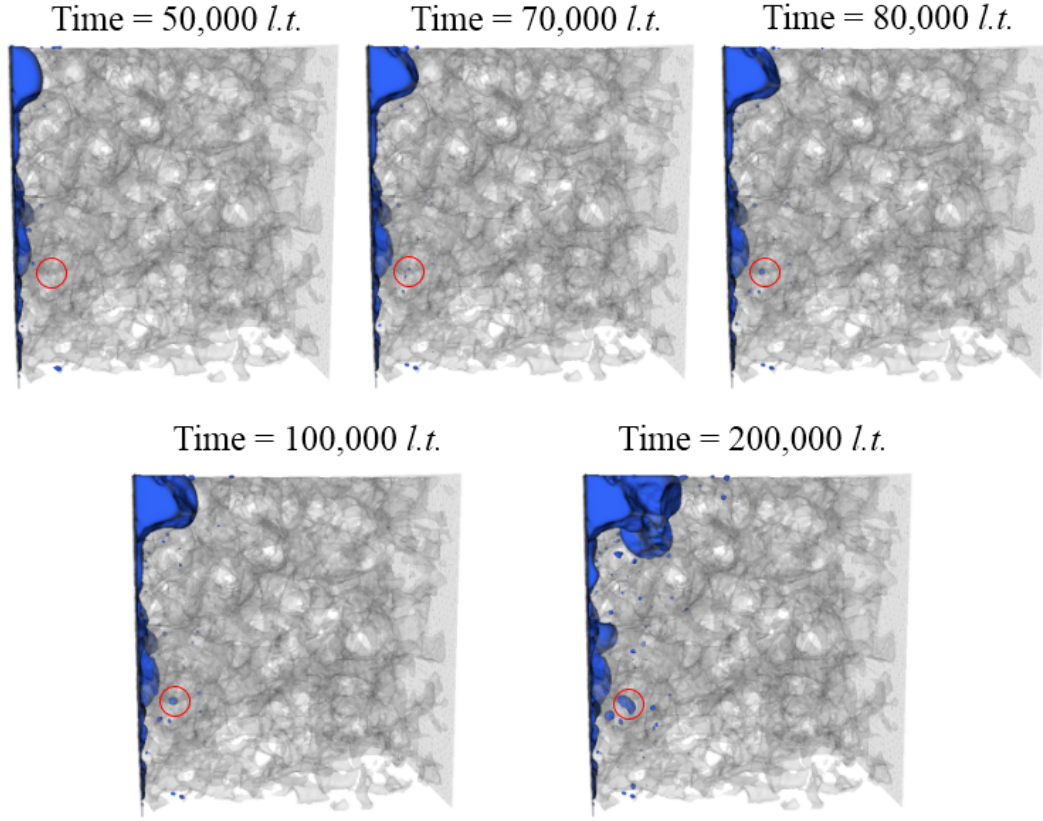


FIGURE 4.7: A illustration of the growth of a non-physical non-wetting phase ganglion during the drainage process in the Bentheimer sandstone sample. The non-physical ganglion is highlighted in the red circle.

shown that this phenomenon is independent of boundary conditions: using constant pressure boundary conditions with a capillary pressure smaller than the capillary entry pressure, we observed numerous small non-wetting phase bubbles present before an apparent non-wetting phase invasion happens, as shown in Figure 4.9(c) and (d).

Furthermore, in section 4.2 we also show that at smaller contact angles, less dissolved non-wetting phase is attracted to the solid surface (see Figure 4.4). Therefore, here we also performed the drainage simulation at 0° contact angle for both pressure and flux boundary conditions (Figure 4.9 (b) and (d)), and it can be seen that the amount of small non-wetting droplets is drastically decreased, comparing to Figure 4.9 (a) and (c).

Lastly, it is noted that this propagation and accumulation of the dissolved non-wetting phase cannot be reduced with higher image resolution. In Figure E.1 (Appendix E), we show that the amount of dissolved non-wetting phase density attracted at corner nodes and normal fluid boundary nodes in fact becomes larger with increased tube size¹. Also, same simulations as shown in Figure 4.6 were preformed using a smaller sub-domain (64^3 l.u.^3) and a refined sub-domain where the image resolution is double (the refining is performed based on linearly interpolating the correspond signed distance map of the sub-domain). We still observe the generation of

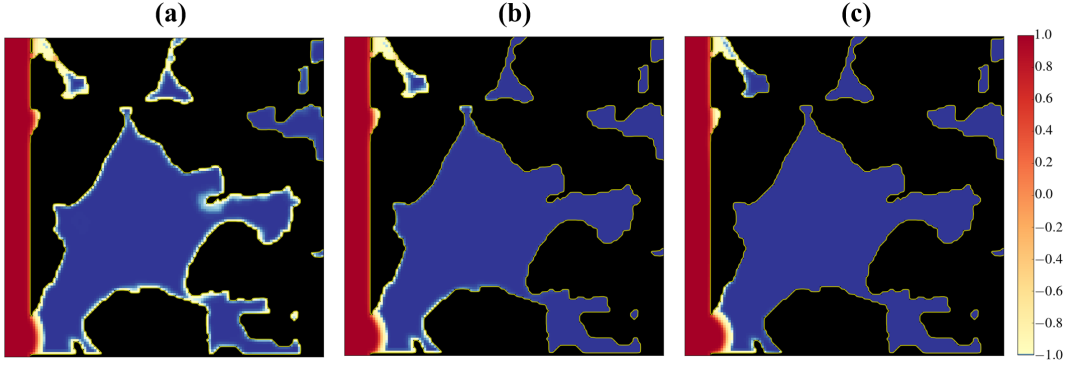


FIGURE 4.8: Illustrations of the propagation of the transport of dissolved non-wetting phase along the solid surface, where the 2D views (i.e. y - z plane) of a sub-domain of $125 \times 125 \text{ l.u.}^2$ of the phase field are shown, with the capillary number of (a) 2×10^{-5} , (b) 3×10^{-4} and (c) 3×10^{-3} . It can be seen that there are less surface that is “coated” with dissolved NW phase at higher flow rates. The $125 \times 125 \text{ l.u.}^2$ sub-domain is extracted from $x = 7$. A non-linear colour scale is used for the phase field to highlight the distribution of the dissolved non-wetting phase near the solid surface. The yellow solid line delineates the pore-solid boundary, and the solid phase is in black. The contact angle is 50° .

‘fake’ NW bubbles inside the sub-domain (not shown in the thesis), before the major NW phase front enters the medium.

4.4 Introduction to Geometric Formulation

In the previous sections, the problematic wetting boundary conditions in SC and RK model have been reviewed, and we have explored the consequence of such wettability model in realistic porous medium simulations for RK model, which causes significant non-physical ganglia generation that could potential render the modelling meaningless. We are not the first to notice this phenomenon: for SC model, based on SC’s original wetting model (Martys and Chen, 1996), Jansen and Harting (2011) and Chen et al. (2015) have made improvement by introducing virtual density to the solid boundary nodes, which equivalently reinforces the (fluid-solid) adhesive force to ‘offset’ the unbalanced (fluid-fluid) cohesive forces. More details of the implementation can be found in their works. For RK model, to the author’s knowledge, there has not been any improved wettability model being proposed based on the commonly adopted fictitious-density model, which is also being used in this thesis, and is proposed by Latva-Kokko and Rothman (2005b). The fictitious-density model introduced in section 4.2, assigns a fictitious density to solid nodes, which sets up a colour-gradient such that NW and W fluid particles are redistributed near the solid boundary. Since this model essentially follows the assumption that the solid boundary is a mixture of NW and W fluids by Rowlinson and Widom (1982) and is based on the Young’s

¹It is also noted that in such case, the total mass fraction of dissolved NW phase decreases due to the decrease in the ratio of the volume of fluid boundary nodes to the total volume of fluid nodes.

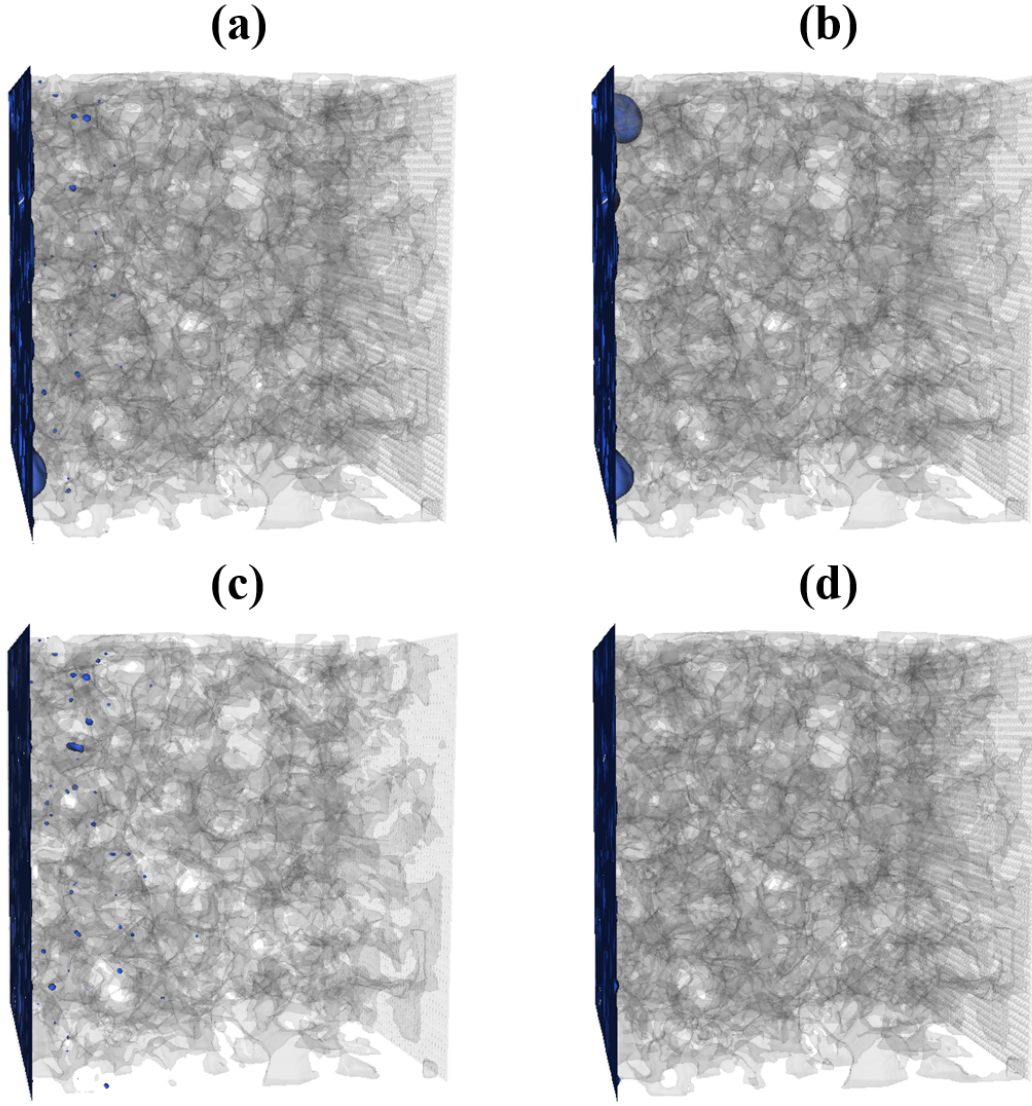


FIGURE 4.9: The drainage simulations in the Bentheimer sandstone sample using (a) the flux boundary condition at 50° contact angle, (b) the flux boundary condition at 0° contact angle, (c) the pressure boundary condition at 50° contact angle, and (d) the pressure boundary condition at 0° contact angle.

equation of surface tension (Latva-Kokko and Rothman, 2005b), it is also called the surface-energy formulation (Jacqmin, 2000; Briant, 2002; Khatavkar, Anderson, and Meijer, 2007; Yu et al., 2018). On the other hand, an alternative wettability model, the so-called geometric formulation, has been proposed for RK model for fixing the non-physical behaviour. This approach was initially proposed for the diffuse interface method by Ding and Spelt (2007), and was extended to be implemented in RK model in 2D by Wang, Huang, and Lu (2013), Ba et al. (2013), Liu et al. (2015), Liu and Zhang (2015), Leclaire et al. (2016), and Xu, Liu, and Valocchi (2017) and in 3D by Ba et al. (2015), Leclaire et al. (2017), and Akai, Bijeljic, and Blunt (2018). Incidentally, the similar geometric formulation has also been proposed for SC model by Li, Zhou, and Yan (2016). However, some of these reported approaches are either limited

to flat surface (Wang, Huang, and Lu, 2013; Ba et al., 2013; Ba et al., 2015; Liu et al., 2015; Liu and Zhang, 2015; Li, Zhou, and Yan, 2016; Yu et al., 2018) or may lead to non-symmetric results for a physically symmetric problem such as in Leclaire et al. (2016), as pointed out by Xu, Liu, and Valocchi (2017). This leaves us with the approach by Xu, Liu, and Valocchi (2017) in 2D, which is then extended by Akai, Bijeljic, and Blunt (2018) to 3D case, and the approach by Leclaire et al. (2017), both of which are algorithmically feasible to handle arbitrary surface.

For the rest of this section, the approach by Leclaire et al. (2016) and Leclaire et al. (2017), referred as *Leclaire's method* hereafter, and the approach by Akai, Bijeljic, and Blunt (2018), referred as *Akai's method* hereafter will be introduced. These two methods following the same methodology of geometric formulation, but are different in the computation of the unit vector normal to the fluid-fluid interface. The basic idea of geometric method is to artificially modify the orientation of the colour gradient \mathbf{G} on the fluid boundary nodes such that the prescribed contact angle θ is matched². First of all, we group the lattice sites into several categories as follows (Leclaire et al., 2016; Xu, Liu, and Valocchi, 2017; Akai, Bijeljic, and Blunt, 2018):

1. C_{FB} : a list of lattice nodes that belong to the fluid domain and are in contact with at least one lattice node in the solid domain.
2. C_{FI} : a list of lattice nodes that belong to the fluid domain but are not in contact with any lattice nodes in the solid domain.
3. C_{SB} : a list of lattice nodes that belong to the solid domain and are in contact with at least one lattice node in the fluid domain.
4. C_{SI} : a list of lattice nodes that belong to the solid domain but are not in contact with any lattice nodes in the fluid domain.

To satisfy a certain contact angle at the contact line, the following simple relation must be respected for nodes belonging to C_{FB} :

$$\mathbf{n} \cdot \mathbf{n}_s = \cos \theta, \quad (4.1)$$

where \mathbf{n}_s is the unit normal vector of the solid boundary. \mathbf{n}_s is purely a characteristic of the porous medium that can be obtained prior to the LB simulations, hence it can be assumed known and the calculation of \mathbf{n}_s will be introduced in the end. \mathbf{n} is the orientation of the colour gradient \mathbf{G} , namely the unit vector normal to the fluid interface, and can be calculated as:

$$\mathbf{n}(\mathbf{x}) = \frac{\mathbf{G}}{|\mathbf{G}|}. \quad \mathbf{x} \in C_{\text{FB}} \quad (4.2)$$

²It should be noted that, in reality even for a homogeneously wet porous medium, the local contact angle (measured from μCT images based on various image processing algorithms) can vary significantly. Therefore, it is still debatable whether this methodology of setting prescribed contact angle artificially has a sound physics foundation.

Therefore, in the context of geometric formulation, the contact angle θ is the input (which is known), \mathbf{n}_s is also known, and obviously the key is to compute \mathbf{n} . However, equation (4.1) is a degenerate system with one equation but three unknowns (i.e. three components of a 3D vector \mathbf{n}). To overcome this difficulty, Leclaire et al. (2016) proposed the prediction-correction methodology: an initial guess \mathbf{n}^* is first calculated on each node ($\mathbf{x} \in C_{\text{FB}}$) based on the colour gradient information in the current iteration, and such prediction is then corrected after considering the prescribed contact angle.

The *Leclaire's method* and *Akai's method* are different in how \mathbf{n}^* is corrected. In terms of obtaining \mathbf{n}^* for $\mathbf{x} \in C_{\text{FB}}$, which is equivalently to obtain the (guessed) colour gradient \mathbf{G}^* for $\mathbf{x} \in C_{\text{FB}}$, the information of the phase field Φ for $\mathbf{x} \in C_{\text{SB}}$ is needed, which is not known. Hence, the phase field Φ for $\mathbf{x} \in C_{\text{SB}}$ is extrapolated based on a weighted average of its nearest $\Phi \in C_{\text{FB}}$ as follows (Xu, Liu, and Valocchi, 2017):

$$\Phi(\mathbf{x}) = \frac{\sum_{i: \mathbf{x} + \mathbf{e}_i \delta_t \in C_{\text{FB}}} \omega_i \Phi(\mathbf{x} + \mathbf{e}_i \delta_t)}{\sum_{i: \mathbf{x} + \mathbf{e}_i \delta_t \in C_{\text{FB}}} \omega_i}, \quad \mathbf{x} \in C_{\text{SB}} \quad (4.3)$$

where ω_i is the weighting coefficient of LB lattice. Once Φ for $\mathbf{x} \in C_{\text{SB}}$ is obtained, the guessed colour gradient \mathbf{G}^* for $\mathbf{x} \in C_{\text{FB}}$ can be calculated, and the guessed unit normal vector \mathbf{n}^* can be determined by $\mathbf{n}^* = \frac{\mathbf{G}^*}{|\mathbf{G}^*|}$.

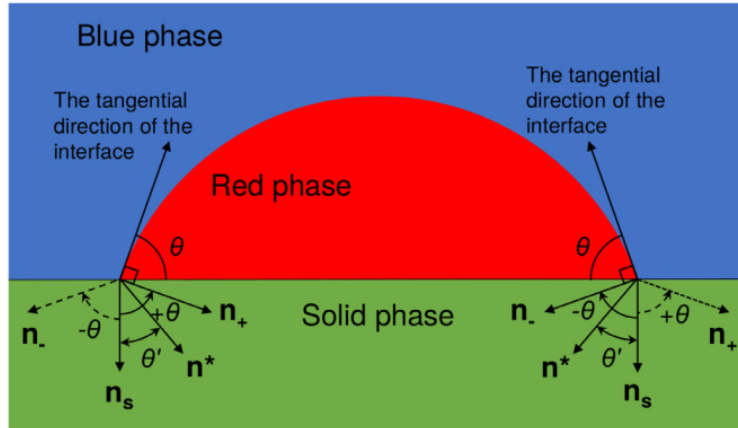


FIGURE 4.10: (Figure copied from Akai, Bijeljic, and Blunt (2018)) Schematic of the wetting boundary condition of *Akai's method*. \mathbf{n}_s is the unit normal vector of the solid nodes for $\mathbf{x} \in C_{\text{SB}}$. \mathbf{n}_+ and \mathbf{n}_- are the two possible unit vectors which have an angle θ from \mathbf{n}_s in a counter-clockwise and clockwise direction, respectively. The unit vectors \mathbf{n}_{\pm} are obtained by the linear combination of \mathbf{n}_s and the guessed unit normal vector \mathbf{n}^* through equation (4.4). Then the guessed vector \mathbf{n}^* is replaced with either \mathbf{n}_+ or \mathbf{n}_- according to equation (4.6).

The next step is to correct the direction of \mathbf{G}^* to match the prescribed contact angle, while still keeping the magnitude $|\mathbf{G}|$ unchanged. The *Akai's method* borrowed the idea from the OpenFOAM finite volume library, an open source CFD toolbox, to go through a vector transform that rotates \mathbf{n}_s to obtain the corrected \mathbf{n} . An

illustration of the wetting boundary condition in *Akai's method* is shown in Figure 4.10, which is directly adopted from Akai, Bijeljic, and Blunt (2018). In Figure 4.10, it can be seen that there are two contact lines, each of which makes an angle θ with \mathbf{n}_s in two possible directions (i.e. the unit vectors \mathbf{n}_+ and \mathbf{n}_-). The two unit vectors \mathbf{n}_+ and \mathbf{n}_- can be calculated via the linear combination of \mathbf{n}_s and \mathbf{n}^* as follows:

$$\mathbf{n}_{\pm} = \left(\cos(\pm\theta) - \frac{\sin(\pm\theta) \cos \theta'}{\sin \theta'} \right) \mathbf{n}_s + \frac{\sin(\pm\theta)}{\sin \theta'} \mathbf{n}^*, \quad (4.4)$$

where $\theta' = \arccos(\mathbf{n}_s \cdot \mathbf{n}^*)$. To choose the appropriate unit normal vector to interface, the Euclidean distances D_{\pm} between \mathbf{n}_{\pm} and \mathbf{n}^* are evaluated as follows:

$$D_+ = |\mathbf{n}_+ - \mathbf{n}^*|, \quad (4.5a)$$

$$D_- = |\mathbf{n}_- - \mathbf{n}^*|. \quad (4.5b)$$

Then the corrected unit normal vector of the fluid-fluid interface \mathbf{n} is selected by:

$$\mathbf{n} = \begin{cases} \mathbf{n}_+ & D_+ \leq D_- \\ \mathbf{n}_- & D_+ > D_- \end{cases} \quad (4.6)$$

Lastly, the corrected colour gradient \mathbf{G} that matches desired contact angle can be calculated as:

$$\mathbf{G} = |\mathbf{G}^*| \mathbf{n} \quad (4.7)$$

For the correction step in *Leclaire's method*, instead of dealing with complicated 3D vector transformation, the numerical method of secant is used, with the guess \mathbf{n}^* being the initial condition, and a solution \mathbf{n} is obtained via recurrence relation with iterative index n as follows:

$$\mathbf{n}^{(0)} = \mathbf{n}^*, \quad (4.8a)$$

$$\mathbf{n}^{(1)} = \mathbf{n}^* - \lambda(\mathbf{n}^* + \mathbf{n}_s), \quad (4.8b)$$

$$\mathbf{n}^{(n)} = \frac{\mathbf{n}^{(n-2)} f(\mathbf{n}^{(n-1)}) - \mathbf{n}^{(n-1)} f(\mathbf{n}^{(n-2)})}{f(\mathbf{n}^{(n-1)}) - f(\mathbf{n}^{(n-2)})}, \quad (4.8c)$$

where $f(\mathbf{n})$ is simply the condition 4.1 but with an arbitrary vector:

$$f(\mathbf{n}^{(n)}) = \mathbf{n}^{(n)} \cdot \mathbf{n}_s - |\mathbf{n}^{(n)}| \cos \theta, \quad (4.9)$$

where θ is the prescribed contact angle.

In *Leclaire's method*, due to the special choice of first two order approximations $\mathbf{n}^{(0)}$ and $\mathbf{n}^{(1)}$, the final iterative solution \mathbf{n} will be situated in the plane spanned by \mathbf{n}^* and \mathbf{n}_s . For simplicity, λ of 0.5 is adopted in *Leclaire's method* and the iteration stops at $n = 2$ to avoid too much computational cost. The recurrence equation (4.8) does not guarantee the norm of $\mathbf{n}^{(n)}$ is unity, thus the normalisation is taken before

it is used to calculate the corrected colour gradient as:

$$\mathbf{G} = |\mathbf{G}^*| \mathbf{n}^{(2)}. \quad (4.10)$$

Incidentally, Tölke, Prisco, and Mu (2013) also proposed similar wettability model based on the idea of geometric formulation, but instead of making a initial guess \mathbf{n}^* and then performing the correction, Tölke, Prisco, and Mu (2013) directly solved the condition (4.1), together with two extra constraint equations, which, in total, constituted five non-linear equations with five unknowns. Those equations were numerically solved by Newton-Raphson method, which is more computationally expensive compared to the approach proposed by Leclaire et al. (2017).

For the unit normal vector of the solid boundary \mathbf{n}_s , there are at least two methods: either directly performing the gradient operation on the binary solid matrix of μ CT image using eighth-order isotropic discretisation (Xu, Liu, and Valocchi, 2017), or smoothing the μ CT image first and then performing gradient operation using a lower-order discretisation (e.g. fourth-order isotropic discretisation as in equation 2.62) (Leclaire et al., 2017). If directly performing the gradient operation using eighth-order isotropic discretisation, \mathbf{n}_s can be calculated as follows (Xu, Liu, and Valocchi, 2017):

$$\mathbf{n}_s(\mathbf{x}) = \frac{\sum_l \omega(|\mathbf{c}_l|^2) s(\mathbf{x} + \mathbf{c}_l \delta_t) \mathbf{c}_l}{|\sum_l \omega(|\mathbf{c}_l|^2) s(\mathbf{x} + \mathbf{c}_l \delta_t) \mathbf{c}_l|}, \quad \mathbf{x} \in C_{\text{FB}}, \quad (4.11)$$

where $s(\mathbf{x})$ is the indicator function that is 0 for $\mathbf{x} \in C_{\text{FI}} \cup C_{\text{FB}}$, and 1 for $\mathbf{x} \in C_{\text{SI}} \cup C_{\text{SB}}$. $\omega(|\mathbf{c}_l|^2)$ is the eighth-order weight function which is given by Sbragaglia et al. (2007):

$$\omega(|\mathbf{c}_l|^2) = \begin{cases} 4/21 & |\mathbf{c}_l|^2 = 1 \\ 4/45 & |\mathbf{c}_l|^2 = 2 \\ 1/60 & |\mathbf{c}_l|^2 = 4 \\ 2/315 & |\mathbf{c}_l|^2 = 5 \\ 1/5040 & |\mathbf{c}_l|^2 = 8 \end{cases} \quad (4.12)$$

where \mathbf{c}_l is the l th mesoscopic velocity associated with eighth-order isotropic discretisation, which can also be found in Sbragaglia et al. (2007).

Alternatively, the μ CT binary image can be first smoothed iteratively proposed by Leclaire et al. (2017) as follows:

$$s(\alpha, \beta, \gamma)^{(n)} = \sum_{k=-1}^{k=1} \sum_{j=-1}^{j=1} \sum_{i=-1}^{i=1} \omega(i^2 + j^2 + k^2) s(\alpha + i, \beta + j, \gamma + k)^{(n-1)}, \quad (4.13)$$

where n is the iterative index, and $\omega(i^2 + j^2 + k^2)$ are the weighting coefficients for D3Q27 lattice with $\omega(0) = 8/27$, $\omega(1) = 2/27$, $\omega(2) = 1/54$, and $\omega(3) = 1/216$. Then \mathbf{n}_s can be calculated based on the smoothed indicator function $s(\mathbf{x})^{(n)}$ for example

by forth-order isotropic discretisation:

$$\mathbf{n}_s = \frac{1}{c_s^2} \sum_i \omega_i s(\mathbf{x} + \mathbf{e}_i \delta_t)^{(n)} \mathbf{e}_i, \quad \mathbf{x} \in C_{\text{FB}}, \quad (4.14)$$

where ω_i here is the weighting coefficient for D3Q19 lattice.

Overall, it can be seen that the geometric formulation heavily relies on the calculations of local unit normal vectors \mathbf{n} and \mathbf{n}_s , which can be potentially disadvantageous in the highly complex porous media or the media at low resolution. Furthermore, in the mixed wet situation, it might be very difficult to set the unit normal vectors appropriately at the boundary of different minerals where different contact angles are prescribed, especially when the solid geometry is highly irregular, which might cause the fluid interface being pinned at certain point.

4.5 Proposed Wetting Boundary for RK Model

In the previous section, the wettability model based on the geometric formulation has been reviewed. Compared to the surface-energy formulation (or fictitious-density approach) used in section 4.3, the ideology between geometric and surface-energy methods are fundamentally different: in the geometric method, the contact angle is an input parameter and different wetting condition is implemented through artificial manipulation of the unit normal vectors of interface; whereas in surface energy method, contact angle is an outcome of pseudo-interaction between fluid density on pore nodes and fictitious density on solid nodes, which is more consistent with the original idea of surface free energy. Although the obvious shortcoming of the current surface-energy approach is its non-physical behaviour in the dissolved NW phase as reviewed in section 4.2 and 4.3, the surface-energy formulation can handle arbitrarily complex geometries of porous media with great ease and its ideology is perfectly suitable for the mixed wetting condition. In this section, the preliminary work of an alternative surface-energy model, which just took place recently before the writing of this thesis, is introduced. With the intention of hopefully fixing the non-physical attraction of dissolved NW phase near the solid surface, more future work is needed to implement our proposed algorithm and validate the approach.

As is illustrated in section 4.2, for the conventional surface-energy formulation, it is the manipulation of local colour gradient between fluid boundary nodes and solid nodes that redistributes the NW and W fluids, in which a single phase field value Φ_s is assigned to the solid nodes. For example, to realise a mid-contact angle of $\sim 50^\circ$, a $\Phi_s = -0.55$ is used for solid nodes. Figure 4.11(a) and (b) show the initial phase field distribution at the centre and the end of a square tube (near the corner), respectively. At the centre of the tube where the bulk NW phase is assumed to reside, the local phase field decreases as it moves from fluid nodes towards solid nodes, thereby leading to repulsion of NW phase and attraction of W phase, which is expected and correct. However at the end of the tube where resides the bulk W phase, the local phase field

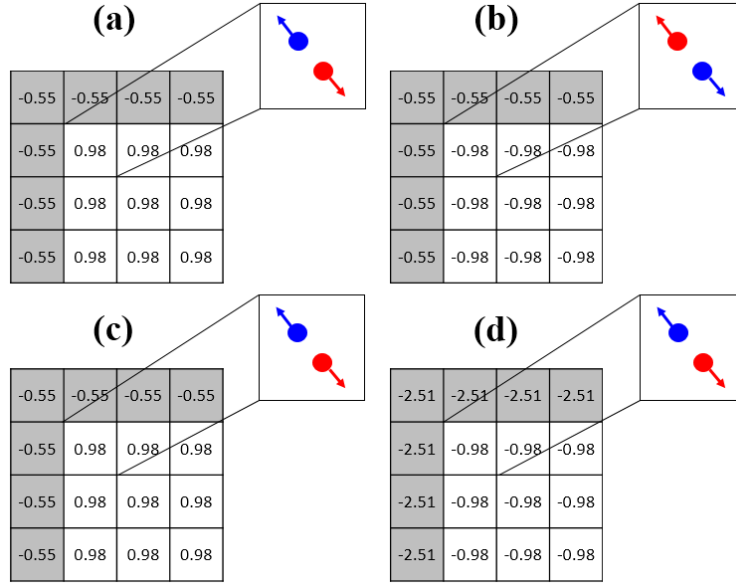


FIGURE 4.11: A two-dimensional schematic of the phase field near the corner of a square capillary tube, at the centre of tube, where the solid phase field is calculated with (a) the conventional wetting boundary condition, and (c) the proposed wetting boundary condition. Similarly, the phase field at the end of the tube is shown with solid phase field calculated based on (b) the conventional wetting boundary condition, and (d) the proposed wetting boundary condition.

increases as it moves from fluid nodes towards solid nodes, which leads to attraction of non-physical NW phase and repulsion of W phase.

Inspired by the works of Chen et al. (2015) and Jansen and Harting (2011), we propose a new way of calculating the phase field on solid nodes such that the colour gradient between fluid and solid nodes in the bulk W phase region can be reversed to avoid non-physical attraction of dissolved NW phase:

$$\Phi_s^{\text{avg}}(\mathbf{x}, t) = \frac{1}{N_{C_{\text{FB}}}} \sum_{i: \mathbf{x} + \mathbf{e}_i \delta_t \in C_{\text{FB}}} \Phi(\mathbf{x} + \mathbf{e}_i \delta_t, t), \quad \mathbf{x} \in C_{\text{SB}}, \quad (4.15)$$

where C_{SB} and C_{FB} are sub-sets of the simulation nodes which are introduced in section 4.4, and $N_{C_{\text{FB}}}$ is the total number of nodes for $\mathbf{x} \in C_{\text{FB}}$. In doing so, the local phase field gradient vanishes for the contact angle of 90° : for example in Figure 4.3(a) in section 4.2, equation (4.15) gives for all solid nodes $\Phi_s^{\text{avg}} = 0.98$ in the bulk NW phase, and $\Phi_s^{\text{avg}} = -0.98$ in the bulk W phase in Figure 4.3(b), such that a true neutral wetting condition is achieved. For contact angle other than 90° , an extra amount of solid phase field is added:

$$\Phi_s(\mathbf{x}, t) = \Phi_s^{\text{avg}}(\mathbf{x}, t) - \Delta\Phi_s(\mathbf{x}), \quad \mathbf{x} \in C_{\text{SB}}, \quad (4.16)$$

where $\Delta\Phi_s(\mathbf{x})$ is a positive spatial variable to account for the mixed wetting condition, and if the medium consists of only one kind of mineral, it can simply be a constant. For instance, to achieve about the same contact of 50° as in Figure 4.11(a) and (b),

we might use $\Delta\Phi_s = 1.53$ so that $\Phi_s(\mathbf{x}, 0) = -0.55$ in the bulk NW phase as shown in Figure 4.11(c). More importantly, in the bulk W phase in Figure 4.11(d), the initial phase field is $\Phi_s(\mathbf{x}, 0) = -2.51$, so that the local colour gradient correctly lead to repulsion of NW phase and attraction of W phase. This new wetting boundary scheme is still preliminary, thus to achieve a contact angle of 50° in reality, the actual $\Delta\Phi_s$ value might be different. The essence of the proposed approach is to dynamically adapt the solid phase field value in every LB iteration, by considering the phase field of all its neighbouring fluid-boundary nodes, such that the colour gradient between fluid and solid can always be maximally suppressed. The full development and numerical validation of this new wetting boundary condition is, however, beyond the scope of this thesis.

Overall, for surface-energy formulation, the contact angle is an outcome not an input parameter, thus a calibration is needed beforehand to map $\Delta\Phi_s$ to certain contact angle; on the contrary, in the geometric formulation a contact angle is prescribed *a priori*, but it also involves heavy computations on the local unit normal vectors and it might be challenging to implement in a mixed wet condition. Conceptually, the idea of contact angle comes out as a result of pseudo-interaction between fluid nodes and solid boundary nodes in the fictitious method is more consistent with the original idea of surface free energy, but practically more future work is needed to implement our proposed method and to validate if the fix will work or not.

Chapter 5

Two-fluid Flow in Porous Medium and Haines Jump Dynamics

In the previous two chapters, we have taken a thorough characterisation of two commonly used multicomponent LB models, examined these models' numerical behaviour and how well the multiphase physics is recovered, and had concluded that the colour-gradient based Rothman-Keller (RK) model is a more suitable candidate for modelling immiscible two-fluid flow in porous media. In this chapter, based exclusively on the MRT-RK model (section 2.4), we perform preliminary study on the Haines jump dynamics and the associated snap-off through primary drainage simulations. Haines jumps, which were named after Haines (1930), is an irreversible event during drainage when the NW phase front invades a wider pore body through a narrow throat. As the NW phase front first reaches the entry of the throat, the local capillary pressure is high as the NW phase needs to overcome the entry pressure; once the entry pressure is surpassed, the front rapidly enters the pore body with large local velocity, during which the mean curvature of the phase front suddenly becomes smaller, corresponding to a sudden drop in the local capillary pressure, thus the name of Haines jumps. Also, because of the sudden pressure drop, the W phase quickly enters the narrow throat, which, depending on the local pore geometry and fluid properties, may snap off the remaining NW fluid in the throat. The entire process (from Haines jump to snap-off) happens so fast (in milliseconds) that it is still challenging to capture such phenomenon experimentally (Armstrong and Berg, 2013; Berg et al., 2013; Singh et al., 2019). However, it is important to resolve the detailed dynamics of Haines jumps and snap-off so to better understand their potential impact on the macroscopic flow. LB modelling is a good candidate for studying Haines jumps since its temporal resolution (i.e. the physical time per LB iteration step) can be flexibly manipulated to achieve the required time-scale for Haines jumps.

In this chapter, to advance our knowledge of understanding the fundamental mechanism during Haines jumps and snap-off, we perform a series of primary drainage simulations in a Bentheimer sandstone μ CT image under a range of viscosity ratios and capillary numbers, with the focus specifically on the Haines jumps that leads to snap-off. The rest of this chapter is organised as follows. Before presenting the simulation results, we first introduce two extra features being implemented in our MRT-RK

model that enable us to more realistically mimic the experimental condition and perform the simulations with non-unitary viscosity ratio. Then the influence of the large spurious velocity present at fluid-fluid and fluid-solid interfaces on the two-phase flow is discussed, since it is critical to know how well the physics of the interface movement is captured by the LB model before the simulation results can be seriously studied. Lastly the results of all drainage simulations, the Haines jumps, and the associated snap-off are presented and discussed.

5.1 Methods

In this section, the calibrations of two important features that are implemented in our MRT-RK model are introduced. The capability of coping with non-unitary viscosity ratios and mimicking the volumetric flow condition at the inlet boundary are the prerequisites for performing practical drainage simulations. Thus it is important to validate our RK model in some common calibration tests with known theoretical answers.

5.1.1 Non-unity Viscosity Test

The details of how the non-unitary viscosity feature is implemented in the MRT-RK model has been introduced in section 2.4. Here we present the calibration results of a 3D parallel plate test, in which the theoretical velocity profiles are known. The viscosity ratio M^1 , by definition, is given by the ratio of NW phase dynamic viscosity to that of W phase (i.e. $M = \frac{\mu_{nw}}{\mu_w}$), where the dynamic viscosity is defined, for example for NW phase, as $\mu_{nw} = \rho_{nw}\nu_{nw}$, where ν_{nw} is the NW phase kinematic viscosity. Therefore, the change of viscosity ratio is due to an interplay of both fluid density and kinematic viscosity. In this thesis, we limit the testing case to only varying the kinematic viscosity, while keeping the density of both fluids unity, although the variation of the density ratio is also available in our model. Hence $M = \nu_{nw}/\nu_w$. There are two testing cases: one with NW phase more viscous than W phase of $M = 2.5$, and the other one with W phase more viscous than NW phase of $M = 0.2$. If the density ratio is also varied, a much wider range of viscosity ratio can be achieved.

For immiscible two-fluid flow in porous media at a strong water-wet condition, the W phase attaches and moves along the solid surface, while the NW phase flows in the centre of the pores. The momentum exchange between two phases leads to viscous coupling and lubrication. Hence the viscosity ratio plays an important role, which influences the relative velocity between phases, and is also closely linked to the relative permeability of the flow system (Huang and Lu, 2009; Ramstad, Øren, and Bakke, 2010).

Here we study two-fluid co-current flow through two parallel plates, which is illustrated in Figure 5.1. The flow direction is along z -axis, and the periodic boundary condition is applied to all four side boundaries. The normal bounce-back boundary

¹The viscosity ratio is also known as mobility ratio, thus the abbreviation M .

condition is applied in the upper and lower plates. The same body force is applied to both fluids along z -axis to drive the flow. The initial thickness of NW and W phase layers is set $a = b = 25 \text{ l.u.}$, and a body force of $10^{-6} \text{ kg} \cdot \text{l.u.} \cdot \text{l.t.}^{-2}$ is used. For the case of $M = 2.5$, $\tau_{\text{nw}} = 1.0$ and $\tau_{\text{w}} = 0.7$ are used; and for $M = 0.2$, $\tau_{\text{nw}} = 0.7$ and $\tau_{\text{w}} = 1.5$ are used.

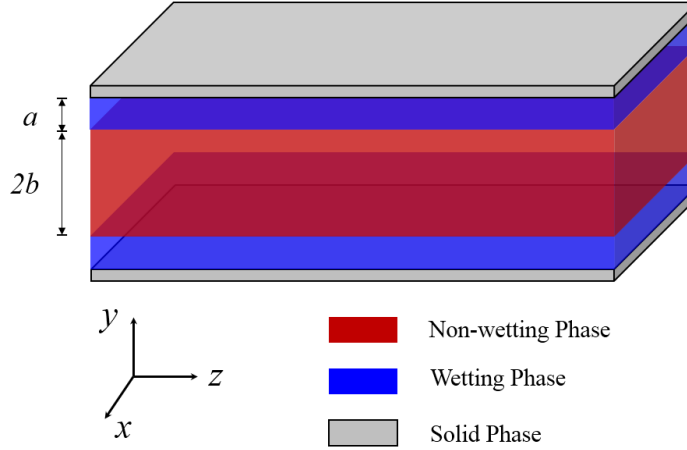


FIGURE 5.1: Schematic of three-dimensional two-fluid co-current flow through parallel plate. The flow direction is along z -axis. Note that the diagram is not drawn to scale.

The velocity profiles for $M = 0.2$ and $M = 2.5$ are shown in Figure 5.2. The velocity is measured along the central line ($x = 51$) in the central plane ($z = 51$), and is compared to the analytical solution for the layered multiphase flow between the parallel plates. The corresponding derivation of analytical solutions can be found in Huang and Lu (2009). It can be seen that for both cases, the velocity profiles computed from the LB model agree well with the analytical solutions, which demonstrates the capability of our MRT-RK model to simulate two-phase flow with non-unitary viscosity ratios.

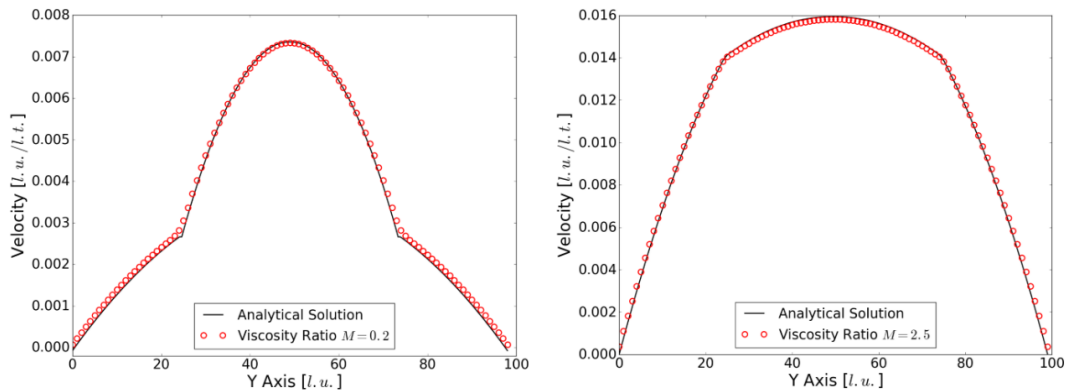


FIGURE 5.2: Velocity profiles along the central line ($x = 51 \text{ l.u.}$) in the central plane ($z = 51 \text{ l.u.}$) of three-dimensional parallel plate system, at viscosity ratios of $M = 0.2$ and $M = 2.5$, respectively. The relaxation-time parameters for $M = 0.2$ are $\tau_{\text{nw}} = 0.7$ and $\tau_{\text{w}} = 1.5$, and for $M = 2.5$ are $\tau_{\text{nw}} = 1.0$ and $\tau_{\text{w}} = 0.7$

5.1.2 Total Flux Boundary Condition

The capacity to deliver (numerically stable) multiphase simulations mimicking experimental volumetric flow boundary condition is of strong interest, since as shown in this thesis and elsewhere, instability is a problem for LBM in many situations. The details of the implementation of our adaptive volumetric flux boundary condition, however, will not be repeated here as it can be found in McClure et al. (2018). The flux boundary condition is different from the commonly used velocity boundary condition as it allows the velocity to vary over the boundary region, provided that the total flux through the boundary satisfies a prescribed constraint. In this section, we test the boundary condition with both single- and two-phase simulations in a square tube and a Bentheimer sandstone μ CT image. Results can also be found in McClure et al. (2018).

First of all, the single-phase Poiseuille flow in a 3D square tube is performed, in order to verify the accuracy of the flux boundary condition. A square tube of size $(L_x, L_y, L_z) = (40, 40, 80)$ *l.u.* is used, where the flow direction is along z -axis. The 3D Poiseuille flow in a square tube, driven by the pressure gradient over the flow direction, has an analytical steady-state solution, which can be derived from solving the Navier-Stokes equation with non-slip boundary condition (Zhang, Shi, and Wang, 2015). For our set-up, if the Cartesian origin is at the centre of the plane normal to the flow axis, and the flow region is: $-w \leq x \leq w$ and $-w \leq y \leq w$, the 3D Poiseuille flow is known to have a steady-state solution given by:

$$u_z(x, y) = \frac{16a^2}{\nu\pi^3} \left(-\frac{dp}{dz} \right) \sum_{k=1,3,5,\dots}^{\infty} (-1)^{(k-1)/2} \left\{ 1 - \frac{\cosh[k\pi x/(2w)]}{\cosh(k\pi/2)} \right\} \frac{\cos[k\pi y/(2w)]}{k^3}, \quad (5.1)$$

where w is half of the width of the square tube, dp/dz is the pressure gradient along the flow axis of the tube, and ν is the kinematic viscosity of the fluid. The infinite series in equation (5.1) was truncated at $k = 200$ to allow for a good approximation of the theoretical values. For the numerical simulations, the criterion used to determine steady state flow is:

$$\frac{\sum_{\mathbf{x}} |\mathbf{u}(\mathbf{x}, t) - \mathbf{u}(\mathbf{x}, t - 1000)|}{\sum_{\mathbf{x}} |\mathbf{u}(\mathbf{x}, t)|} \leq 10^{-6}. \quad (5.2)$$

The relaxation time for the single-phase simulation is $\tau = 1.0$. Three cases of inlet fluid velocity u_z were applied to the boundary (a constant pressure boundary condition is applied at the outlet), and Figure 5.3 shows that the simulation results are in close agreement with the analytical solutions given in equation (5.1), which validates the implementation of the flux boundary condition for single-phase flow.

After the validation of single-phase test, we then performed primary drainage tests with unitary density and viscosity ratios in a square tube and a sub-domain of a Bentheimer sandstone μ CT image. Typically when performing two-phase simulations to match experiment, the inlet volumetric flow rate Q_z (e.g. in $\mu\text{L/hr}$) is assumed

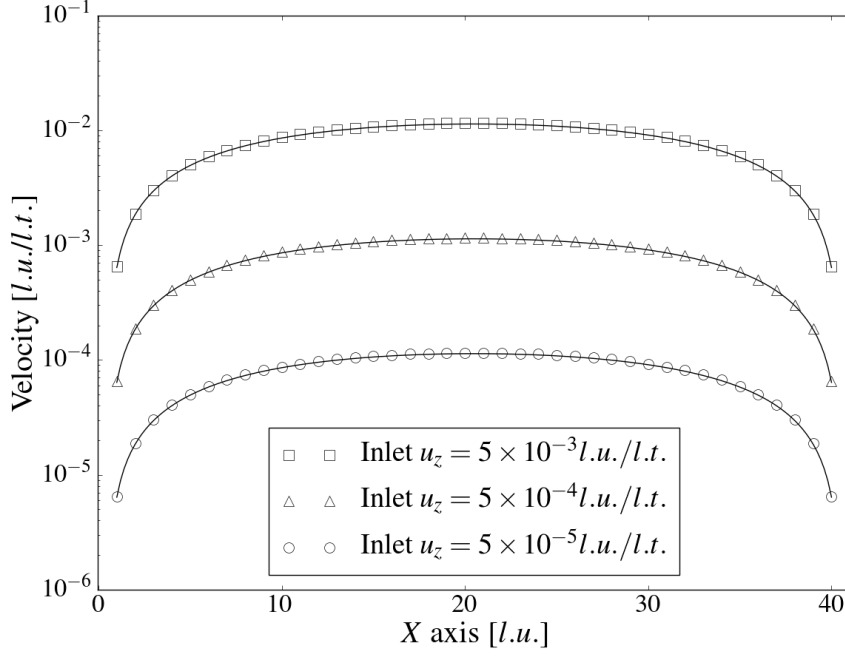


FIGURE 5.3: Velocity profiles for Poiseuille flow along the central line $y = 20 \text{ l.u.}$ at the middle plane of the square tube ($z = 40 \text{ l.u.}$). The solid line indicates the theoretical solution given by equation (5.1).

known, and the flow rate for each phase satisfy (McClure et al., 2016):

$$\frac{\partial S_w}{\partial t} = \frac{Q_z}{\epsilon V}, \quad (5.3)$$

where S_w is the W phase saturation, ϵ is the porosity of the rock sample, and V is the total volume of the sample. The commonly used capillary number (Ca), for a drainage process in which NW phase displaces W phase, can be calculated as:

$$Ca = \frac{\mu_{nw} Q_z}{\gamma_{wn} \epsilon A}, \quad (5.4)$$

where A is the cross-sectional area of the inlet boundary.

To match the experimental capillary number, the input parameter of simulation, the LB volumetric flow rate Q_z^{LB} (in $\text{l.u.}^3 \cdot \text{l.t.}^{-1}$), can be calculated as:

$$Q_z^{\text{LB}} = \epsilon A_{\text{LB}} \frac{\gamma_{wn}^{\text{LB}}}{\mu_{nw}^{\text{LB}}} Ca. \quad (5.5)$$

The primary drainage tests were first performed in the square tube with the same size as in the single-phase test. More specifically, the computation domain consists of a capillary tube sandwiched by a NW phase reservoir (NWR) and a W phase reservoir (WR), each with six layers of pure fluid nodes, which is similar to the set-up shown in Figure 3.14 in Chapter 3. Three cases of lattice volumetric flow rate, $Q_z^{\text{LB}} = \{0.02, 0.2, 2.0\} \text{ l.u.}^3/\text{l.t.}$, were simulated. The time rate change of the saturation, $\partial S_w / \partial t$, multiplied by the pore volume of the tube (ϵV), is plotted (in blue) against

different Q_z^{LB} , as shown in Figure 5.4. The colour of the data points (from light to dark) indicates the temporal evolution, with the time scale normalised by the total simulation time. It can be seen that, as time evolves, the time rate change of the saturation approaches the prescribed Q_z^{LB} once the steady state displacement is reached. The consistency between the prescribed injection rate and the actual displacement rate thus validates the total flux boundary condition.

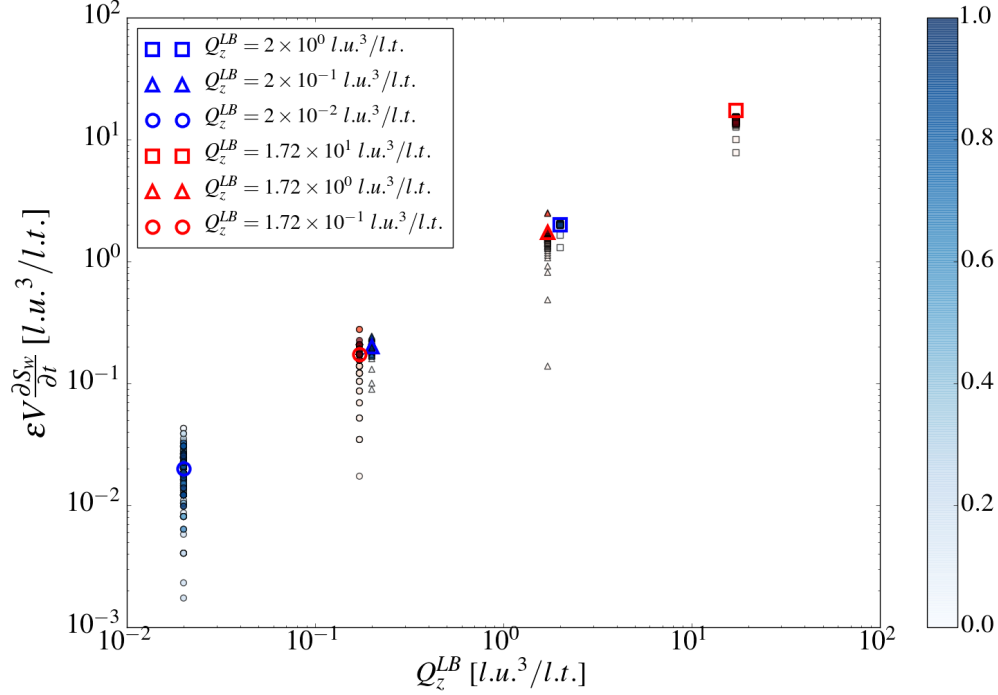


FIGURE 5.4: The time rate change of the saturation (scaled by the pore volume of the media) in the primary drainage simulations, is plotted against the volumetric flow rate Q_z^{LB} specified at the inlet, for the case of the square tube in blue, and for the case of the Bentheimer sandstone in red. The colour of the data points indicates the temporal evolution, and the time scale is normalised by the total simulation time. For visual clarity only the colour bar (in blue) for the square tube case is presented. The blank symbols are used to highlight the exact values of Q_z^{LB} . The LB surface tension parameter α is 10^{-5} . The phase density ρ_i^{LB} is 1.0, and the phase kinematic viscosity ν_i^{LB} is $1/6$ (i.e. $\tau_i = 1.0$), where $i \in \{nw, w\}$.

It is also noted that, at the initial stage $\partial S_w / \partial t$ deviates from Q_z^{LB} , but eventually stabilises to match the boundary flux. The fluctuations in initial $\partial S_w / \partial t$ are possible due to fluid compressibility and the rearrangement of the diffuse interface in the RK model. At low-flow rates the presence of spurious currents may also influence the accuracy of the boundary condition, which is a known limitation as is identified in Chapter 3 (see section 3.7). This can be mitigated by using larger fluid reservoirs such that spurious currents do not arise in proximity to the boundary.

The primary drainage tests were then performed in an X-ray μCT image of Bentheimer sandstone sample, which is the same sample used in sections 3.6, 4.3 and 5.4. The resolution of the image is $4.95 \mu\text{m}/l.u.$. A sub-domain of $256^3 l.u.^3$ was used,

which corresponds to a cube with side lengths 1.27mm. The sub-domain was again sandwiched by six layers of NWR and WR. Three cases of lattice volumetric flow rate, $Q_z^{\text{LB}} = \{0.172, 1.72, 17.2\} \text{ l.u.}^3/\text{l.t.}$ were set such that the capillary numbers were the same as in the square tube case.

The time rate change of saturation is also shown in Figure 5.4 in red. Due to the initial capillary entry effect, the time rate change gradually approaches the prescribed Q_z^{LB} as the steady-state displacement is reached. Moreover, to illustrate the capability of the proposed flux boundary to locally adjust the inlet flux, a two-dimensional $u_z(x, y)$ profile at the inlet boundary of NWR, for the case of $Q_z^{\text{LB}} = 1.72 \text{ l.u.}^3/\text{l.t.}$ is shown in Figure 5.5. Since the NWR consists of pure fluid nodes, a contour line in white delineating the fluid-solid boundary of the first layer of the porous medium is also shown. It can be seen that the proposed boundary condition only directs positive flux towards the pore space of the medium, while maintaining zero flux for where the solid phase is present. This demonstrates that the boundary condition allows the local flow rate to adapt itself across the boundary region based on the interior structure of the flow, while maintaining control over the volumetric flow rate for fluid injected into the system.

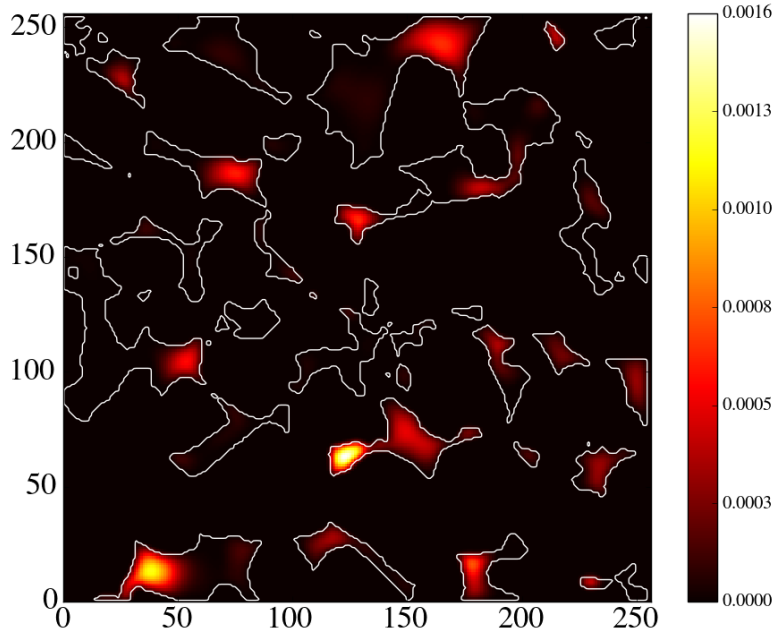


FIGURE 5.5: The cross-sectional view of the velocity field $u_z(x, y)$ at the inlet boundary of NWR in Bentheimer sandstone primary drainage simulation for the case of $Q_z^{\text{LB}} = 1.72 \text{ l.u.}^3/\text{l.t.}$. The white contour line depicts the fluid-solid boundary of the first layer of the medium. The velocity field was extracted at time step 250,000 l.t. when the steady state displacement was reached.

Overall, the results of the velocity profiles for single-phase Poiseuille flow demonstrate the accuracy of our flux boundary implementation as a consistent alternative

LB boundary condition. The results of two-phase flow further demonstrates the capacity of the flux boundary condition to match experiment conditions based on the resolution, volumetric flow rate and capillary number. However, it is also noted that, for two-fluid simulations, spurious currents associated with the interfacial tensions can reduce the accuracy of the approach, although the method is sufficient to set the capillary number to match experimental conditions in practice. In fact, our numerical examination covers a much wider range of capillary number, up to $Ca \sim 10^0$.

5.2 Influence of Interfacial Spurious Currents

Before we study the Haines jump dynamics using LBM, there is another important issue that might render the simulation results less meaningful, which is the spurious currents that are present at the fluid-fluid and fluid-solid interface. In static simulations such as the bubble test in section 3.3, large spurious currents may prevent the system from reaching a true equilibrium state and thus lead to numerical instability; in dynamic simulations, large spurious currents render the actual velocity field indistinguishable from the interfacial spurious current (McClure et al., 2016; Zacharoudiou and Boek, 2016). As we have shown in the bubble test (Figure 3.4), the magnitude of the LB spurious current is proportional to the LB surface tension, which implies that, if not using an improved LB model with a special treatment on spurious current, a smaller LB surface tension might be an appropriate option to alleviate the problem. In this section however, it will be demonstrated that, for any practical applications, the manipulation of LB surface tension is not helpful, since other LB parameters need to be scaled to match the same physical system. This leaves us the only viable option, i.e. implementing an improved multicomponent LB model. In fact, the battle against the spurious current started almost the same time as various multicomponent LB models were born - as long as the model is based on a diffused interface deployed on a finite number of spatial grid points, there will be imbalanced discretised interfacial tension forces, and the spurious current ensues. Over the past two decades, researchers have proposed all kinds of treatments for Shan-Chen model, e.g. (Shan, 2006; Yuan and Schaefer, 2006; Sbragaglia et al., 2007), for colour-gradient based model, e.g. (Lishchuk, Care, and Halliday, 2003; Halliday et al., 2017), for free-energy model, e.g. (Pooley and Furtado, 2008; Connington and Lee, 2012), and for phase-field based model, e.g. (Liu et al., 2014a), to name but a few. However, it should be noted that the reduction or even elimination of the spurious currents achieved by these methods typically occurs long after equilibrium has been reached, and none of them work effectively to eliminate the spurious current during the transient part of simulation. It is beyond the scope of this thesis, however, to propose any improved multicomponent LB model for spurious current reduction. Instead, we explore the consequences of the spurious current in the dynamic simulations and provide the research community with the guideline of what the appropriate LB surface tension parameters are to be used, and what the associated trade-off would be in practical LB simulations

Generally, the magnitude of the spurious current is proportional to the LB surface tension, and inversely proportional to the LB viscosity (Shan, 2006). However, in a practical porous medium simulation given by a set of μ CT images with known image resolution and fluid properties, the LB surface tension and viscosity are always coupled and cannot be adjusted independently (see more in section 2.2). More specifically, for a given two-fluid displacement experiment, we aim at matching two key dimensionless numbers: the viscosity ratio (or the mobility ratio, M) and the capillary number (Ca), which together characterise the experiment. One can choose to first match the physical surface tension γ_{phys} (or physical viscosity $\nu_{\text{nw,phys}}$) by selecting an appropriate surface tension parameter α (or viscosity parameter τ_i for $i \in \{\text{nw}, \text{w}\}$), from which the time converting factor δt_{phys} can be calculated; then the viscosity parameter τ for $i \in \{\text{nw}, \text{w}\}$ which satisfies the prescribed viscosity ratio (or surface tension parameter α) is automatically determined.

Based on McClure, Prins, and Miller (2014), an appropriate range of the surface tension parameter α for our MRT-RK model is $10^{-5} \sim 10^{-2}$, and the viscosity parameter should be $\tau_i > 0.5$ for $i \in \{\text{nw}, \text{w}\}$. In practice, it is more convenient to first match the physical surface tension by selecting a proper α and calculate the resultant LB viscosity parameters. For the following characterisation tests, we choose two representative $\alpha = \{10^{-4}, 10^{-2}\}$. Given the relation $\gamma_{\text{phys}} = m_0 n_0 \delta t_{\text{phys}}^{-2} \gamma_{\text{LB}}$, for the same γ_{phys} , the time converting factor δt_{phys} of $\alpha = 10^{-2}$ is 10 times larger than that of $\alpha = 10^{-4}$. In other words, every LB iteration step in $\alpha = 10^{-2}$ is equal to 10 steps in $\alpha = 10^{-4}$, i.e. the case of $\alpha = 10^{-4}$ has a higher temporal resolution. On the other hand, according to the relation $\nu_{\text{phys}} = h^2 \delta t_{\text{phys}}^{-1} \nu_{\text{LB}}$, a smaller δt_{phys} leads to a smaller LB viscosity (to match the same physical viscosity). Since the LB viscosity is directly linear to the relaxation parameter τ as $\nu_{\text{LB}} = (\tau - 0.5)/3$, a τ too close to 0.5 will also trigger numerical instability. Therefore, we choose $\tau_{\text{nw}} = \tau_{\text{w}} = 1.0$ for $\alpha = 10^{-2}$, so that according to the unit conversion restriction the relaxation parameters are $\tau_{\text{nw}} = \tau_{\text{w}} = 0.55$ for $\alpha = 10^{-4}$. Overall, there is an obvious trade-off in the practical simulations, because the use of a smaller α gives a higher temporal resolution which could have a better account on the initial transient part of the simulation, but it also requires significantly longer computation time.

We use the same water-oil system as in Chapter 3 with an interfacial tension of 32 mN/m, and the same μ CT image resolution of $h = 4.95 \mu\text{m}/l.u.$. For $\alpha = \{10^{-4}, 10^{-2}\}$, we perform spontaneous imbibition test and drainage test in a square tube with various tube sizes, and drainage test in a small sub-domain ($64^3 l.u.$) of the Bentheimer sample, same as the one used in the previous section 5.1.2. The advantage of using simple geometry such as a square tube is that the measured velocity field can be directly examined by comparing to the known theoretical relation (e.g. Hagen-Poiseuille relation). The results in the square tube are discussed in this section, and simulations in the Bentheimer sandstone sample is presented in the next section.

5.2.1 Capillary Filling in Square Tube

In this sub-section, the capillary filling, i.e. spontaneous imbibition, in a square tube using periodic boundary condition is discussed. A 2D schematic of the simulation set-up is shown in Figure 5.6. The domain again consists of a square tube, sandwiched by a NW phase and a W phase reservoir. The periodic boundary condition is applied to all boundaries of the reservoirs. By using the periodic boundary condition we can examine the spontaneous evolution of the phase field subject to the spurious current, without the influence of any external dynamic boundary conditions (e.g. constant pressure or flux boundary conditions). As the W phase invades the capillary tube, the interface between NWR and WR (connected by the periodic boundary condition) is allowed to spontaneously shift from the very left end of the simulation domain. Three tube sizes are tested: $R_{\text{tube}} = \{3.0, 5.0, 10.0\} \text{ l.u.}$, and the corresponding domain sizes, (L_x, L_y, L_z) , are $(18, 18, 280)$, $(30, 30, 280)$ and $(60, 60, 280)$, respectively, in order to keep the ratio R_1/h constant. Also, three different contact angles are used, which is realised by setting fluid-solid phase field parameter $\phi_s = \{-0.4, -0.7, -1.0\}$. According to the calibration in McClure, Prins, and Miller (2014), at high resolution², for $\phi_s = \{-0.4, -0.7\}$ it gives the static contact angle of $\{63^\circ, 41^\circ\}$; and for $\phi_s = -1.0$ it gives complete water-wet condition, i.e. the solid is coated with wetting phase film. Although $\phi_s = -1.0$ might be considered as an overshoot especially at high resolution, it is used previously in the drainage simulations in Chapters 3 and 4 to eliminate the non-physical transport of dissolved NW phase and prevent the fake bubble generation, and thus it is also of interest to investigate the kinematics of the phase field at such a value.

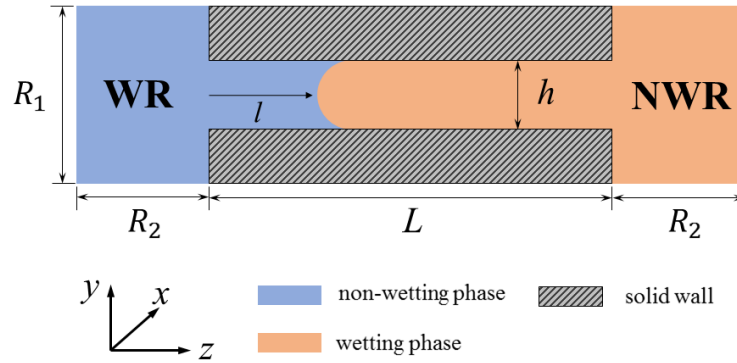


FIGURE 5.6: Schematic of the capillary filling in a square tube. The length of the tube L and the length of the reservoir R_2 are kept as constant of 100 l.u. and 90 l.u. , respectively. Three tube sizes are tested: $R_{\text{tube}} = h/2 = \{3.0, 5.0, 10.0\} \text{ l.u.}$, and accordingly the widths of the reservoir are $R_1 = \{18, 30, 60\} \text{ l.u.}$, where the ratio h/R_1 is a constant for different tube sizes. The periodic boundary condition is applied to all boundaries of the reservoirs.

²The calibration was taken in a large cylindrical tube with $R_{\text{tube}} = 16 \text{ l.u.}$. However, according to the low resolution study in Chapter 3, in different tube sizes the actual contact angles given by these ϕ_s values can vary significantly.

As is mentioned before, in order to model the same physical system, the LB viscosity parameter must be adjusted according to different α : for $\alpha = 10^{-2}$, $\tau_{nw} = \tau_w = 1.0$; and for $\alpha = 10^{-4}$, $\tau_{nw} = \tau_w = 0.55$. Given the unitary viscosity ratio, it is expected that the fluid advancement occurs at a constant speed, i.e. the filling length l scales linearly with time (Washburn, 1921; Zacharoudiou and Boek, 2016). Figure 5.7 shows the W phase saturation S_w within the tube during the capillary filling, as a function of LB time step. Neglecting the data points during the initial transition, it indicates that the filling length indeed scales linearly with time for both α^3 . By fitting to the slope of the steady-state part of the data in Figure 5.7, an average advancing speed of the W phase can be obtained, and this speed is a ‘genuine’ reflection of how the interface moves given the existence of spurious currents. This interface speed and its relation to the dynamic contact angle will be studied together with the data from the drainage in the next sub-section.

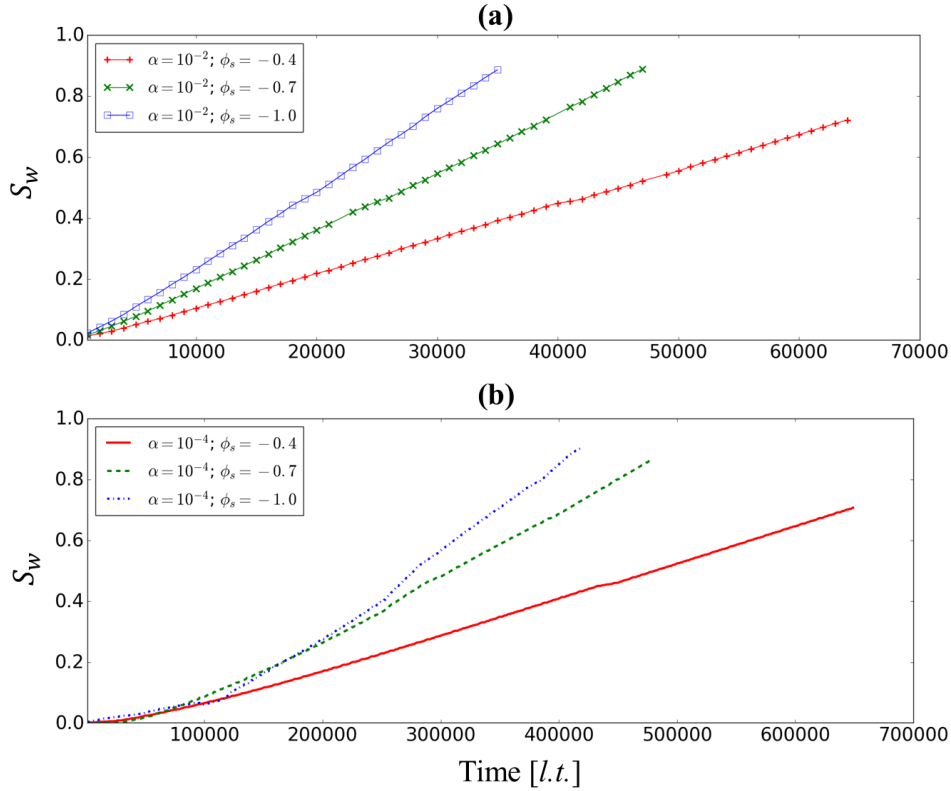


FIGURE 5.7: The wetting phase saturation as a function of simulation time for the capillary filling in a square tube of $R_{\text{tube}} = 5 \text{ l.u.}$, for (a) $\alpha = 10^{-2}$, and (b) $\alpha = 10^{-4}$.

³It is noted that, due to different LB temporal resolution given by different α , the case of $\alpha = 10^{-4}$ generates much more data points than the case of $\alpha = 10^{-2}$, such that the initial nonlinearity is highlighted in $\alpha = 10^{-4}$. If only the data points at the same physical time steps were extracted for both cases (i.e. only plot the saturation at 10,000, 20,000, etc. for $\alpha = 10^{-4}$, in line with the data points of 1000, 2000, etc. for $\alpha = 10^{-2}$), the data curve of $\alpha = 10^{-4}$ will appear less nonlinear. Overall, linearity during the initial transition is not expected because LB method is an explicit numerical method and it takes finite amount of time steps to form a well-defined fluid-fluid and fluid-solid interfaces, and mean-while the system is subject to an external flow field.

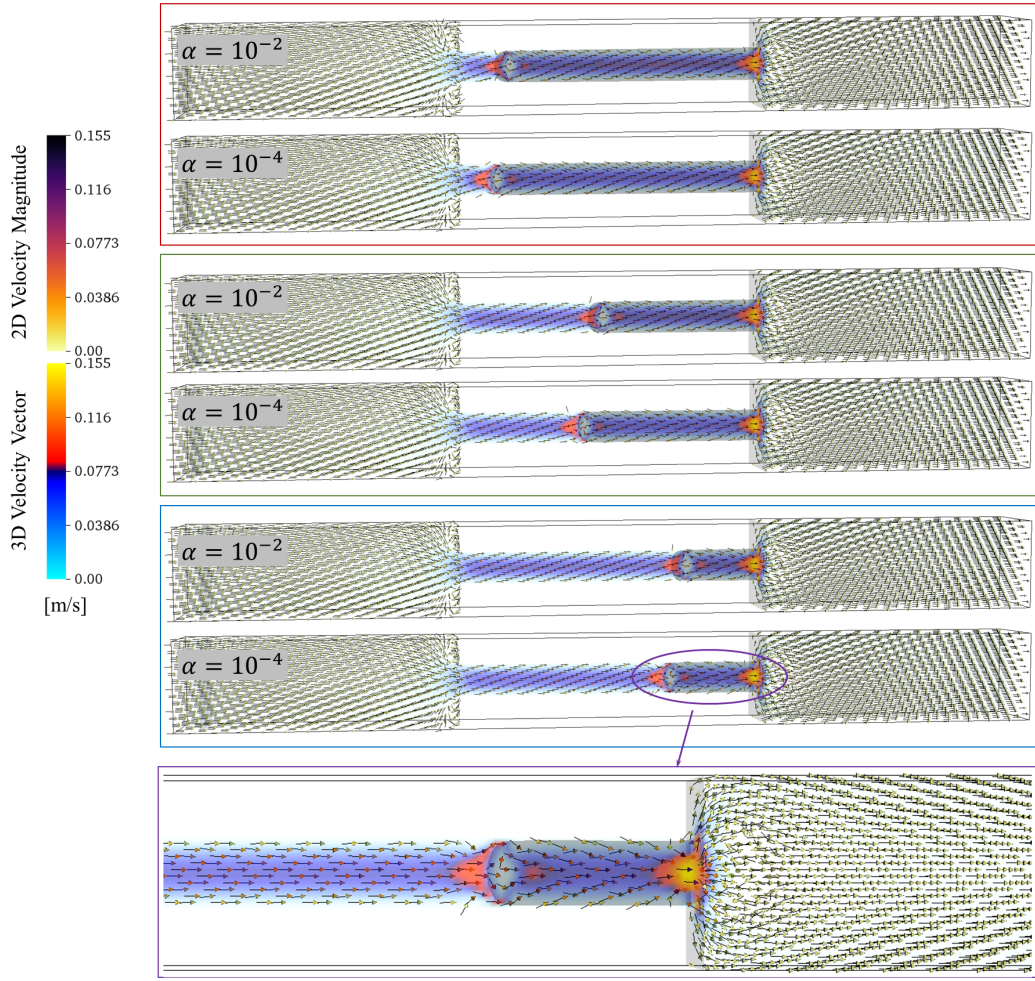


FIGURE 5.8: Three-dimensional vector plot of the velocity field for the capillary filling process in a square tube of $R_{\text{tube}} = 5.0 \text{ l.u.}$ with $\phi_s = -0.7$, with the two-dimensional cross-sectional view of the magnitude of the velocity field at the central plane of the domain. The velocity fields are extracted from the same physical time step for each α . The colour of the velocity vectors represents the magnitude of the velocity. The zero-level contour of the phase field in light grey is also included to highlight the NW/W interface, which from the top to the bottom figures, indicates the advancement of the W phase.

Figure 5.8 shows three groups of 3D vector plots of the velocity field (in the physical unit m/s) during the capillary filling process, with each group being extracted at the same physical time for both α ; the magnitude of the velocity (i.e. $\sqrt{u_x^2 + u_y^2 + u_z^2}$) at the central plane of the domain is also included to highlight the spurious current disruption; the zero-level contour of the phase field in light grey is used to indicate the actual interface. Here the velocity is presented in physical units instead of in LB units, such that the extent to which the spurious currents disrupt the bulk velocity field for different α can be compared on equal footing. It is redundant to show velocity in LB units as it has been demonstrated that by using a smaller LB surface tension the entire magnitude of the LB velocity field is scaled down, which is shown in the bubble test in Figure 3.4 of section 3.3.

Figure 5.8 shows that the major spurious current disruption appears at the fluid-fluid interface within the tube, and at the interface between WR and the tube, i.e. the tube exit, whose order of magnitude is much larger than the major flow field within the bulk NW and W phases inside the tube. This is expected since these places are where the most unbalanced discretised interfacial forces (either fluid-fluid or fluid-solid forces) are present. The use of a smaller α does not mitigate the physical spurious currents, because, to comply with the unit conversion restriction and to match the capillary number, the LB viscosity must be scaled to the LB surface tension, i.e. a big α is always paired with a big τ . This means that for a large α that gives a stronger interfacial tension, the fluid is also more viscous, thus more viscous damping ensues which can offset the supposedly high spurious current to a level that is about the same as the case with a weaker interfacial tension⁴.

Given the spurious current present at the interface, it is important to check to what extent the spurious current disrupts the major flow field within each fluid phase. Figures 5.9 and 5.10 compare the measured velocity components in the cross-section within each bulk phase to the theoretical Poiseuille profile for two α at $R_{\text{tube}} = 5.0 \text{ l.u.}$ and $\phi_s = -0.7$: the sub-plot on top shows the 2D z -components of the velocity in the central plane of the domain, where the W phase is half-way through as indicated by the apparent interruption at NW/W interface; the slice-by-slice averaged LB pressure along the flow axis is shown below, from which the pressure gradient within each bulk phase can be extracted and is used as input to calculate the Poiseuille flow profile, according to the theoretical solution, equation 5.1; the measured z -component of the velocity is shown against the theoretical profile in the bottom sub-plots, together with the x - and y -components of the velocity, all of which are extracted from the middle line of the tube cross-section within the bulk phase⁵.

Excellent agreement between u_z and the theoretical profile are obtained within the bulk NW and W phases for both α , and similar results are also seen for all other tube sizes and ϕ_s values. Theoretically, u_x and u_y should be zero in such flow condition, but this is only observed within the bulk W phase, because the phase field here (≈ -1.0) is close to that of the solid wall ($\phi_s = -0.7$); on the other hand, apparent disturbance in u_x and u_y is seen within the bulk NW phase ($\phi_{\text{nw}} \approx 1.0$), due to the spurious current at the NW-solid interface caused by the large phase field gradient. Nevertheless, the disruption in the u_x and u_y does not seem to affect the major flow field of u_z . Incidentally, we observed no apparent dependency of the magnitude of spurious currents on tube size. Overall, for both α , it seems that the influence of the spurious current is quite limited and does not extend to the major flow field, i.e. the

⁴The fluid with a smaller LB surface tension is also less viscous. Hence an alternative view is that a weaker interfacial tension is supposed to generate less spurious current, but the fluid is also less viscous, i.e. less viscous dissipation, such that the resultant spurious current is as bad as that in the case of a stronger interfacial tension.

⁵In the 2D central plane view of the z -component of the velocity in Figures 5.9 and 5.10, it can be seen that u_z is uniform within the bulk phase, thus it gives essentially the same 1D u_z profile at any slice normal to z -axis.

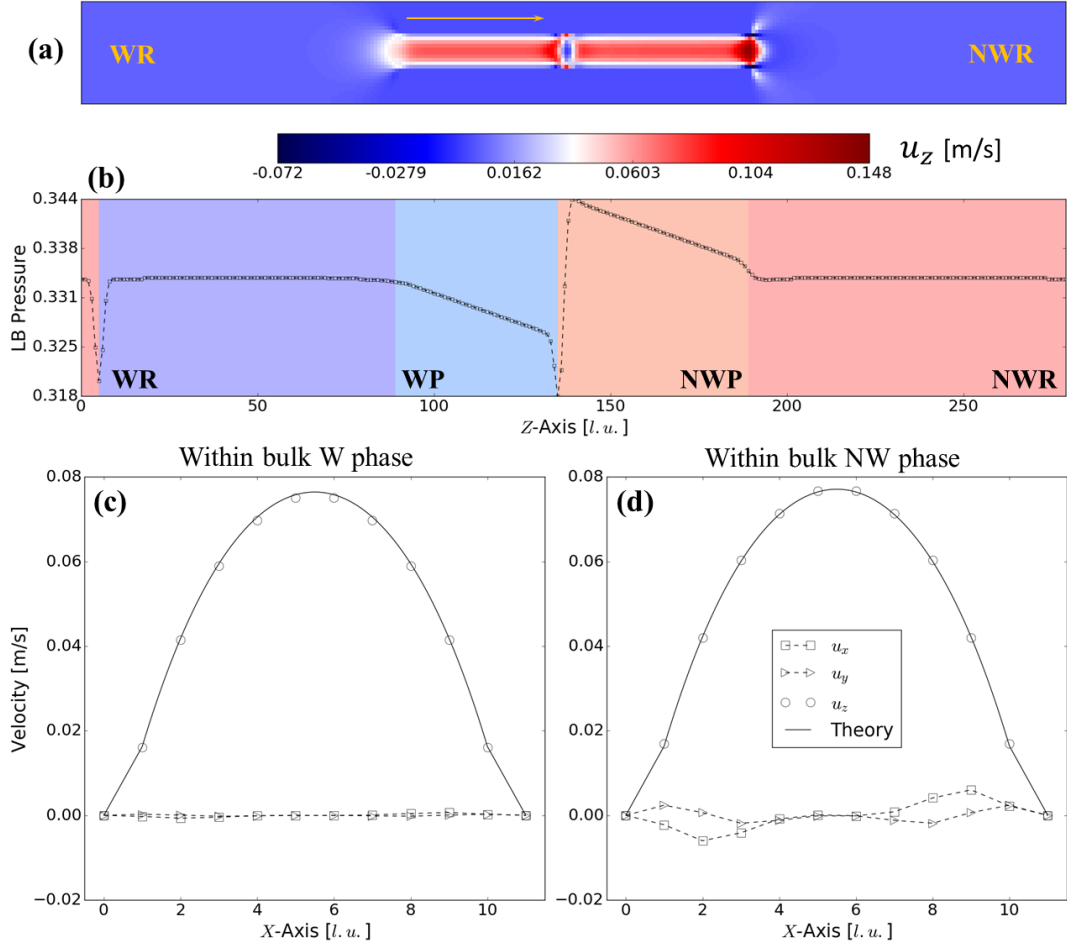


FIGURE 5.9: For $\alpha = 10^{-2}$: (a) Two-dimensional cross-sectional view of the z -component of the velocity for the capillary filling in a square tube of $R_{\text{tube}} = 5.0$ l.u. at $\phi_s = -0.7$, when the advancing W phase is halfway through the tube. (b) The corresponding slice-by-slice averaged LB pressure field along the flow direction. Different colours are filled to highlight different regions of the domain, with WR denoting the W phase reservoir, WP denoting the W phase inside the tube, NWP denoting the NW phase inside the tube, and NWR denoting the NW phase reservoir. Because of the periodic boundary condition, it can be seen that part of NWR is shifted to the left-end of the domain where was initially occupied by the W phase. The velocity components across the middle line of the tube cross-section extracted within (c) the W phase, and (d) the NW phase, are plotted against the theoretical Poiseuille profile, which is calculated according to the viscous pressure gradient measured within each phase in the sub-plot (b). Note that due to the LB half-way bounce back boundary condition, the actual location of the wall nodes should have been 0.5 voxels shifted towards the centre of the tube, thus there would not have been any ‘kink’ in the theoretical Poiseuille profiles near the wall.

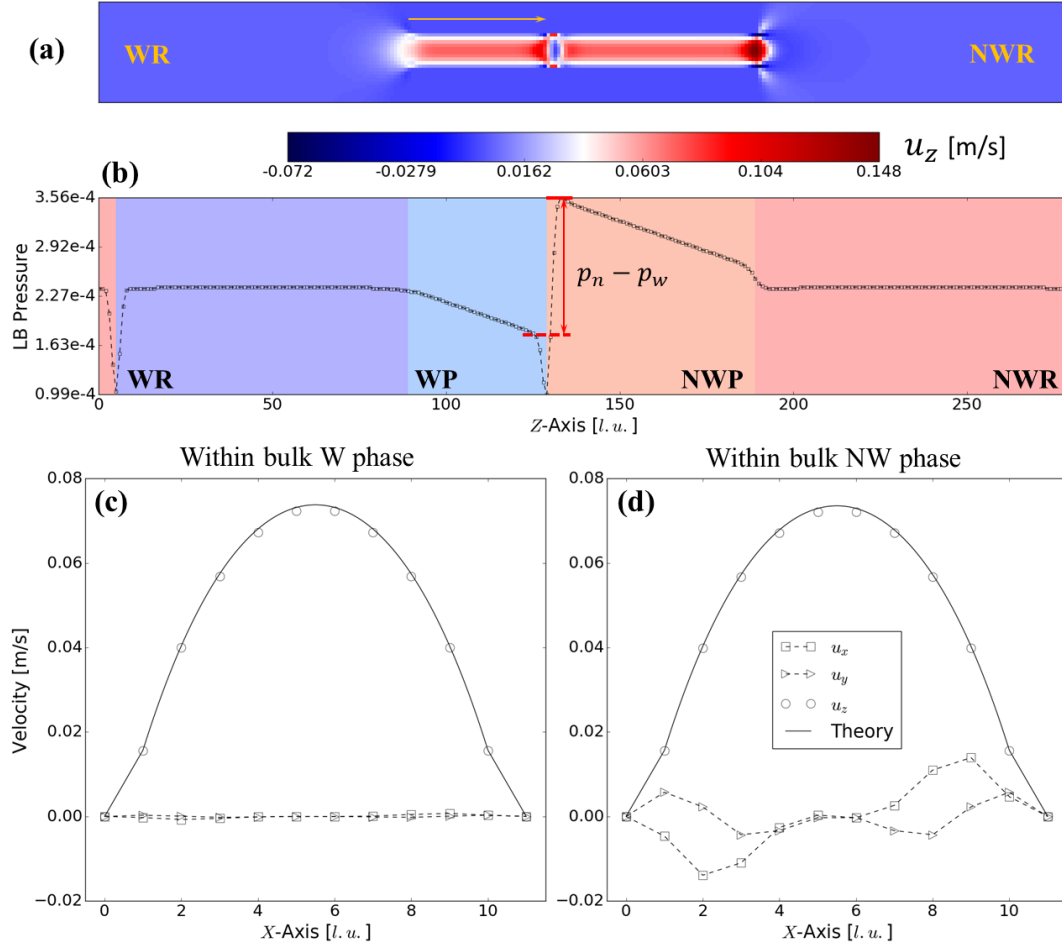


FIGURE 5.10: For $\alpha = 10^{-4}$: (a) Two-dimensional cross-sectional view of the z -component of the velocity for the capillary filling in a square tube of $R_{\text{tube}} = 5.0 \text{ l.u.}$ at $\phi_s = -0.7$, when the advancing W phase is halfway through the tube. (b) The corresponding slice-by-slice averaged LB pressure field along the flow direction. Different colours are filled to highlight different regions of the domain, with WR denoting the W phase reservoir, WP denoting the W phase inside the tube, NWP denoting the NW phase inside the tube, and NWR denoting the NW phase reservoir. Because of the periodic boundary condition, it can be seen that part of NWR is shifted to the left-end of the domain where was initially occupied by the W phase. The velocity components across the middle line of the tube cross-section extracted within (c) the W phase, and (d) the NW phase, are plotted against the theoretical Poiseuille profile, which is calculated according to the viscous pressure gradient measured within each phase in the sub-plot (b). Note that due to the LB half-way bounce back boundary condition, the actual location of the wall nodes should have been 0.5 voxels shifted towards the centre of the tube, thus there would not have been any ‘kink’ in the theoretical Poiseuille profiles near the wall.

axial velocity, and the LB model is still able to capture the right physics law even under the disruption of the spurious current.

Lastly, we examine the Young-Laplace relation during the capillary filling, by plotting the phase pressure difference across the fluid interface, $p_n - p_w$ (normalised by LB surface tension), against the measured mean curvature of NW-W interface, as shown in Figure 5.11. An example of how the pressure difference near the interface is measured is illustrated in Figure 5.10(b) for which the invading W phase is half-way through; the pressure difference is measured for all of the time steps within the steady-state part of the simulation, and the average is calculated, thereby giving the horizontal coordinate of a data point in Figure 5.11. The mean curvature is measured by the *in-situ* analysis facility of the LB code based on the porous media marching cube (PMMC) algorithm by McClure et al. (2007), and similarly only the steady-state part of the simulation is used for calculating the average of the mean curvature, giving the vertical coordinate of a data point in Figure 5.11. It can be seen that a qualitatively good linear relation between mean curvature and phase pressure difference is obtained for both α . The *in-situ* measured interfacial mean curvatures for all cases are slightly greater than the derived curvatures from the phase pressure difference. This deviation is likely due to: (i) the particular (mean curvature measurement) algorithms implemented in the LB code, since the curvature values measured by the surface fitting method give better one-to-one correspondence, see Appendix I; (ii) the effect of the confined space on the pressure which is explored in section 3.5.3, and (iii) the limited resolution of the narrow tube, especially for the case of $R_{\text{tube}} = 3.0$ *l.u.*. Overall, given that both the mean curvature and the phase pressure difference are measured near the interface, the presence of the spurious current does not appear to play a disruptive role, and the correct Young-Laplace relation is captured by our LB model throughout the dynamics filling of the tube.

5.2.2 Drainage in Square Tube

In this section, another type of dynamic simulation, drainage, is studied in square tube, with the external flux boundary condition added (see section 5.1.2). The layout of the domain is the same as the case of capillary filling, except that the length of the reservoir R_2 is shortened to 10 *l.u.* since it no longer needs large space to accommodate the shifted phase from the other side due to the periodic boundary condition. The boundary of NWR is applied with the flux boundary (section 5.1.2) and a constant pressure boundary condition is applied to the boundary of WR. Again there are three tube sizes: $R_{\text{tube}} = \{3.0, 5.0, 10.0\}$ *l.u.*, and for each R_{tube} , three contact angles with $\phi_s = \{-0.4, -0.7, -1.0\}$ are tested. For each testing case, three boundary flux values are applied to generate a wide enough span of the advancing velocity of the NW phase, with the objective to cover the range of the peak speed during Haines jumps in the sandstone studied in the later section 5.4. For more experimentally relevant conditions at low Ca , readers are referred to the work by Latva-Kokko and Rothman (2007) and McClure et al. (2016). The boundary flux values are different for different

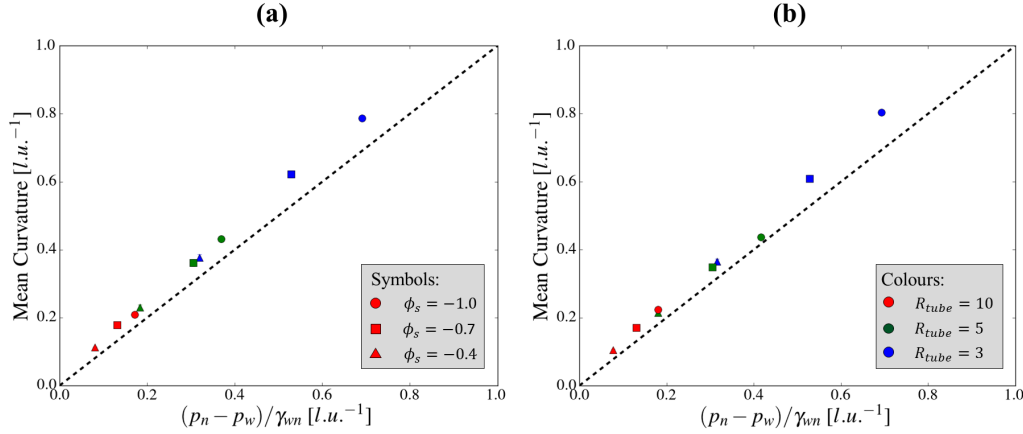


FIGURE 5.11: Young-Laplace test where the interfacial mean curvature is plotted against the phase pressure difference normalised by the LB surface tension, for capillary filling in a square tube, for (a) $\alpha = 10^{-2}$, and (b) $\alpha = 10^{-4}$. Both the mean curvature and the pressure difference are measured from the steady-state part of the simulation, and the mean values are calculated and presented in the figure, with the error bars indicating the standard deviations of the mean (it may be too small to see).

tube sizes, which give the prescribed global capillary numbers (see equation 5.5) of $Ca = \{4.5 \times 10^{-3}, 9 \times 10^{-3}, 4.5 \times 10^{-2}\}$.

Figure 5.12 shows several snapshots of the 3D vector plots of the velocity field during the drainage, at the equivalent physical time for both α . Again to highlight the spurious current disruption, the magnitude of the velocity in the central plane of the domain is also included. The zero-level contour of the phase field is shown in light grey to indicate the NW/W interface. The spurious current primarily appears at the phase interface within the tube, and at the interface between NWR and the tube, i.e. the tube entrance, where the most unbalanced fluid-fluid or fluid-solid forces are present.

With the spurious currents present at the interface, we again examine whether or not their influence significantly affects the overall flow. First, for the case of the lowest prescribed global $Ca = 4.5 \times 10^{-3}$, Figures 5.13 and 5.14 compare the measured velocity components to the theoretical Poiseuille profiles in the tube of $R_{tube} = 5.0$ $l.u.$ with $\phi_s = -0.7$, for α of 10^{-2} and 10^{-4} , respectively: the 2D z -component of the velocity in the central plane of the domain in the top sub-plot highlights the uniformity of u_z within each bulk phase; the slice-by-slice averaged LB pressure shown in the middle is again used as input to calculate the theoretical Poiseuille profiles given by equation 5.1, and the comparison is shown at the bottom. Very good agreement between u_z and the theory is obtained, despite the spurious current present at the NW/solid interface which disrupts the x - and y -components of the velocity, primarily within the bulk NW phase due to the large phase field gradient (i.e. $\phi_{nw} \approx 1.0$ and $\phi_s = -0.7$). Similar good agreement in u_z is obtained for the case of mediate $Ca = 9 \times 10^{-2}$ as well.

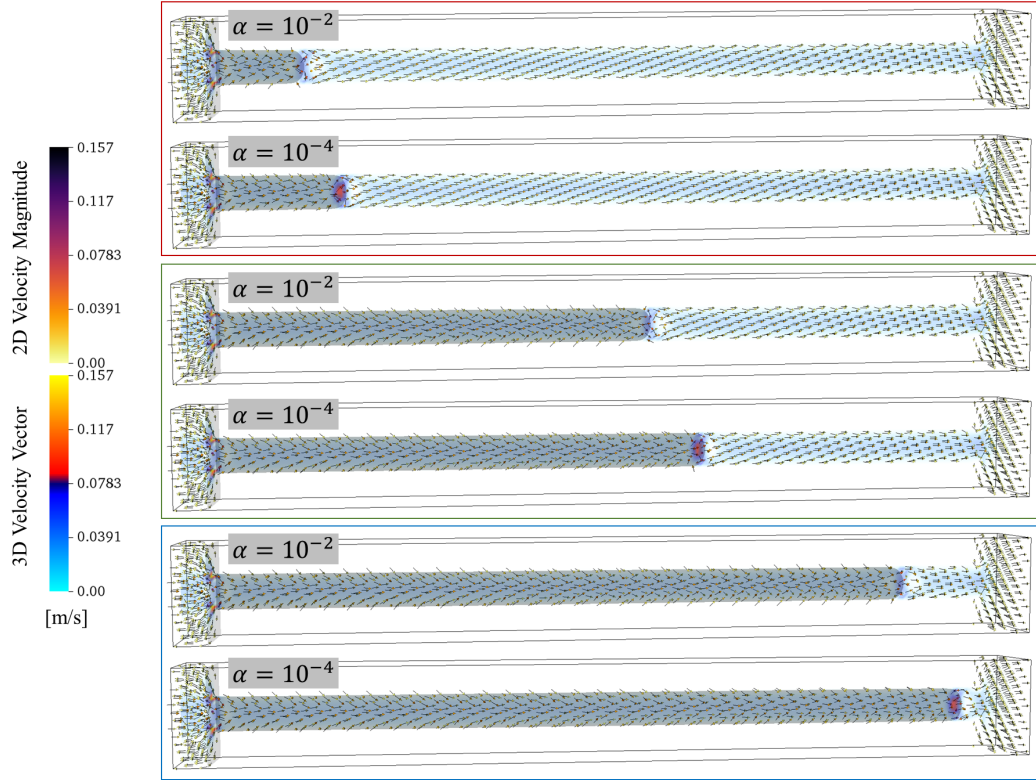


FIGURE 5.12: Three-dimensional vector plot of the velocity field for the drainage process in a square tube of $R_{\text{tube}} = 5.0 \text{ l.u.}$, with the two-dimensional cross-sectional view of the magnitude of the velocity field at the central plane of the domain. The data are from the case of the prescribed global $Ca = 5 \times 10^{-4}$ with $\phi_s = -0.7$, and for each α , the velocity field is extracted at the same physical step. The colour of the velocity vectors represents the magnitude of the velocity. The zero-level contour of the phase field in light grey is also included to highlight the NW/W interface, which from the top to the bottom of the figure, indicates the intrusion process of the NW phase.

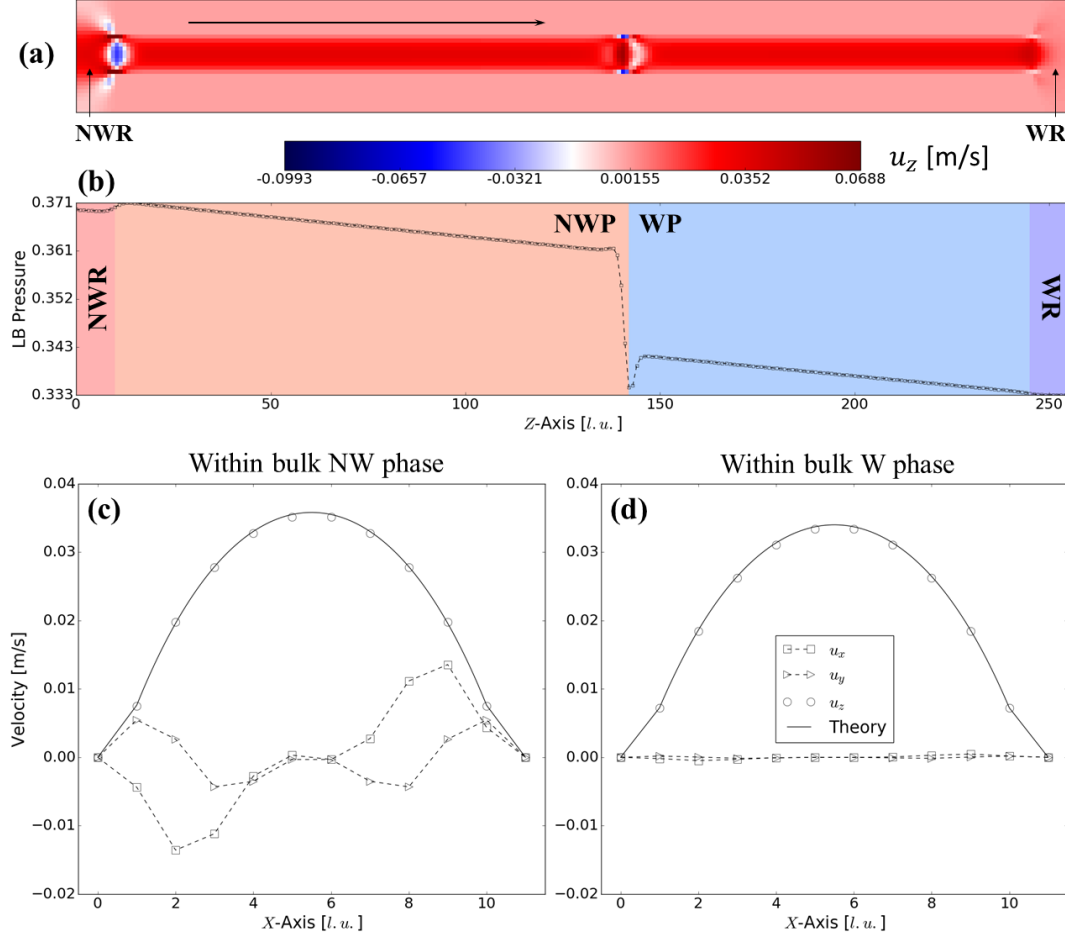


FIGURE 5.13: For $\alpha = 10^{-2}$: (a) Two-dimensional cross-sectional view of the z -component of the velocity for the drainage in a square tube of $R_{\text{tube}} = 5.0 \text{ l.u.}$ at $\phi_s = -0.7$, when the advancing NW phase is halfway through the tube. (b) The corresponding slice-by-slice averaged LB pressure field along the flow direction. Different colours are filled to highlight different parts of the domain, with WR denoting the W phase reservoir, WP denoting the W phase inside the tube, NWP denoting the NW phase inside the tube, and NWR denoting the NW phase reservoir. The velocity components across the middle line of the tube cross-section extracted within (c) the NW phase, and (d) the W phase, are plotted against the theoretical Poiseuille profile, which is calculated according to the viscous pressure gradient measured within each phase in the sub-plot (b). Note that due to the LB half-way bounce back boundary condition, the actual location of the wall nodes should have been 0.5 voxels shifted towards the centre of the tube, thus there would not have been any ‘kink’ in the theoretical Poiseuille profiles near the wall. .

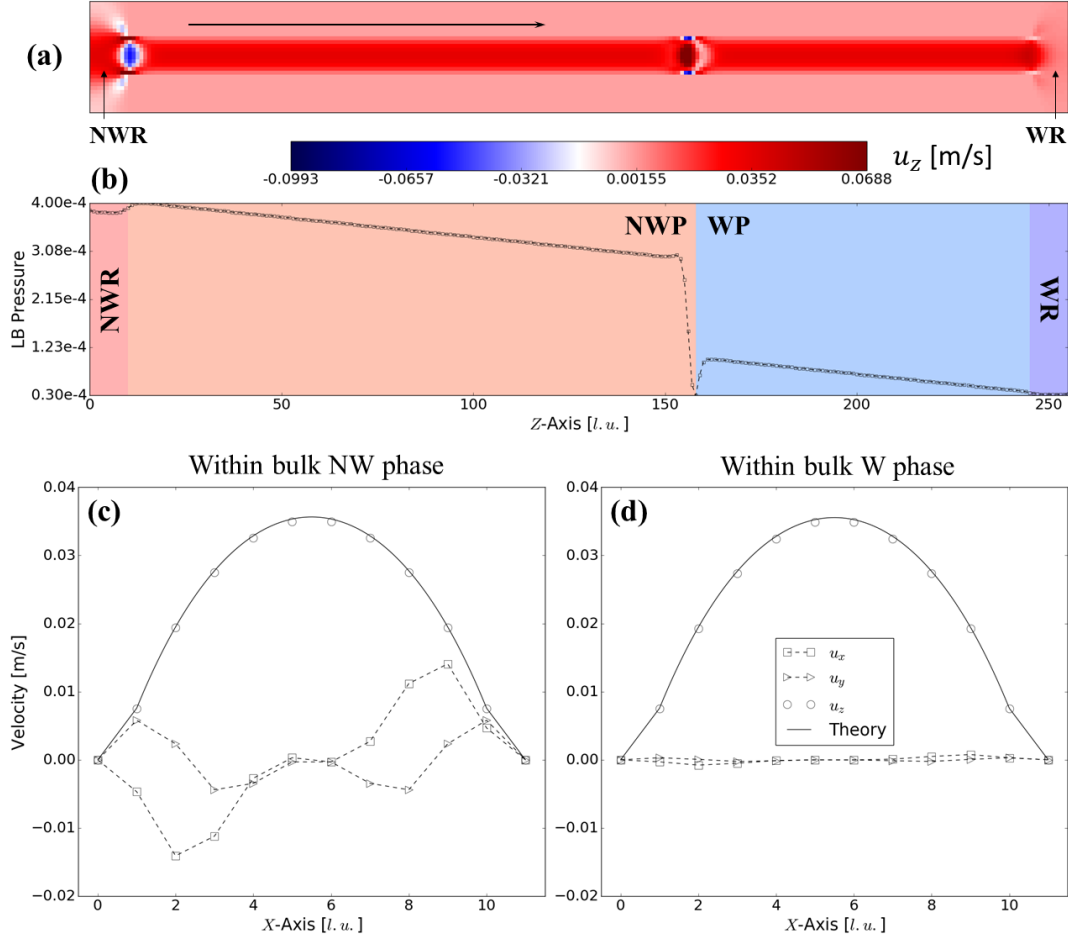


FIGURE 5.14: For $\alpha = 10^{-4}$: (a) Two-dimensional cross-sectional view of the z -component of the velocity for the drainage in a square tube of $R_{\text{tube}} = 5.0 \text{ l.u.}$ at $\phi_s = -0.7$, when the advancing NW phase is halfway through the tube. (b) The corresponding slice-by-slice averaged LB pressure field along the flow direction. Different colours are filled to highlight different parts of the domain, with WR denoting the W phase reservoir, WP denoting the W phase inside the tube, NWP denoting the NW phase inside the tube, and NWR denoting the NW phase reservoir. The velocity components across the middle line of the tube cross-section extracted within (c) the NW phase, and (d) the W phase, are plotted against the theoretical Poiseuille profile, which is calculated according to the viscous pressure gradient measured within each phase in the sub-plot (b). Note that due to the LB half-way bounce back boundary condition, the actual location of the wall nodes should have been 0.5 voxels shifted towards the centre of the tube, thus there would not have been any ‘kink’ in the theoretical Poiseuille profiles near the wall. .

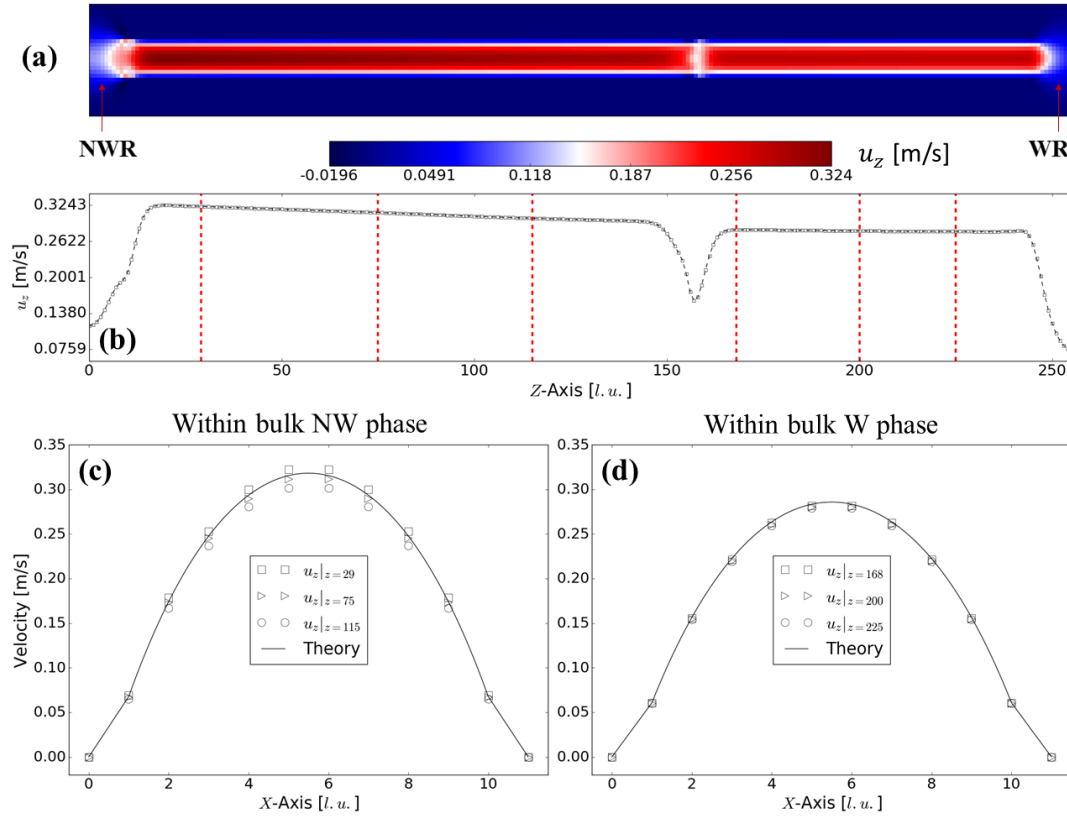


FIGURE 5.15: For $\alpha = 10^{-2}$: (a) Two-dimensional cross-sectional view of the z -component of the velocity at the central plane of the domain for the drainage test at $R_{\text{tube}} = 5.0$ l.u. and $\phi_s = -0.7$ with the largest prescribed global $Ca = 5 \times 10^{-3}$. The NW phase is halfway through the tube. (b) The corresponding one-dimensional z -component of the velocity along the central line in the central plane of the domain. The z -component of the velocity across the middle line of the tube cross-section, which are extracted at several locations within (c) the NW phase, and (d) the W phase, are plotted against the theoretical Poiseuille profile. The Poiseuille profile is calculated according to the viscous pressure gradient within each bulk phase. The red dash lines in sub-plot (b) highlight the locations from which the z -components of the velocity are extracted. Note that due to the LB half-way bounce back boundary condition, the actual location of the wall nodes should have been 0.5 voxels shifted towards the centre of the tube, thus there would not have been any ‘kink’ in the theoretical Poiseuille profiles near the wall. .

However, for the case of the largest global $Ca = 4.5 \times 10^{-2}$, u_z is not uniform within each bulk phase for the case of $\alpha = 10^{-2}$, which is illustrated in Figure 5.15: on top the sub-plot shows the 2D view of u_z at the central plane of the domain; in the middle the 1D profile of u_z along the central line in the central plane is shown, where an apparent variation of u_z along the flow direction can be seen, especially within the bulk NW phase; we extract 1D u_z profiles (across the middle line of the tube cross-section) at several locations as highlighted in the red dash lines and compare them to the theoretical Poiseuille profiles, which are shown in the bottom sub-plots

(c) and (d). The deviation on average from the theory, primarily within the bulk NW phase, is of only 5% of the maximal value of u_z . Since it has been demonstrated from Figures 5.9, 5.10, 5.13 and 5.14 that the influence of the spurious current is limited near the fluid-fluid and fluid-solid interfaces, the deviations seen here are more likely due to the low temporal resolution brought by a large α , which prevents the system from operating in a quasi-equilibrium manner, especially when being applied with a large boundary Q_z value. This is also proved by checking the u_z field at the same R_{tube} , ϕ_s and prescribed global $Ca = 4.5 \times 10^{-2}$ for $\alpha = 10^{-4}$ (not shown here), where an uniform u_z within each bulk phase is obtained, which looks similar to the top sub-plot (a) in Figures 5.14. The issue of the LB temporal resolutions given by different α will be revisited in section 5.3.

Next, the Young-Laplace relation during the drainage processes is examined. Figure 5.16(a) and (b) show the interfacial mean curvature against the phase pressure difference (normalised by LB surface tension) for α of 10^{-2} and 10^{-4} , respectively. Again, both the curvature and pressure data are measured from the steady-state part of the simulation. The phase pressure difference is measured across the NW-W interface the same way as in the capillary filling process exemplified in Figure 5.10(b), and the mean curvature is measured by the *in-situ* analysis facility of the LB code. For each R_{tube} case, the colour of the symbol, from dark to light, corresponds to the prescribed global Ca from low to high. It can be seen that with $Ca = \{4.5 \times 10^{-3}, 9.0 \times 10^{-2}\}$, for both α , a good linear relation is obtained for all R_{tube} and ϕ_s values; moreover, at the same R_{tube} and ϕ_s , both the directly measured interfacial curvature and the derived one from the pressure difference barely varies for different Ca , since it is only the boundary flux rate Q_z that is changed, and the capillary pressure across the NW-W interface should remain the same. However, for the case of prescribed global $Ca = 4.5 \times 10^{-2}$, there are apparent deviations in the phase pressure difference, especially for $\alpha = 10^{-4}$ at $R_{\text{tube}} = 3.0 \text{ l.u.}$, although the directly measured interfacial mean curvature remains largely unaffected. The large deviations is caused by the very high-flow condition, at which the system is being constantly driven out of a quasi-equilibrium process; also, it is further exacerbated by the very narrow tube size, with which it is challenging to accurately obtain the pressure profile. It should also be noted that, the less severe deviation for $\alpha = 10^{-2}$ at $Ca = 4.5 \times 10^{-2}$ and $R_{\text{tube}} = 3.0 \text{ l.u.}$, does not necessarily mean that $\alpha = 10^{-2}$ has a better performance: the instantaneous Ca for $\alpha = 10^{-2}$, which is calculated by directly measuring the interface advancing speed, is in fact much smaller than that of $\alpha = 10^{-4}$; thus the case of $\alpha = 10^{-2}$ is subject to a slower flow field, and the requirement of quasi-equilibrium process is less compromised, giving a smaller deviation⁶. Overall, similar to the observation in the capillary filling, the spurious current does not appear to play a disruptive role for the drainage process, and the correct Young-Laplace relation is captured for both α with the flow condition of global Ca

⁶In other words, the case of $\alpha = 10^{-2}$ fails to achieve the required flow condition given by the prescribed global Ca . See more in Figure 5.17

as large as $\sim 10^{-2}$. The phase pressure difference across the fluid interface starts to deviate from the theory when an even larger Ca is imposed; nevertheless, it should be noted that, for $Ca \sim 5 \times 10^{-2}$, at which the breakdown of the Young-Laplace relation is observed, it is about one order of magnitude greater than the equivalent peak Ca during the Haines jumps, from both reported experiment (Berg et al., 2013; Armstrong and Berg, 2013) and simulation (Zacharoudiou and Boek, 2016), and it is also much larger than the peak Ca in our results (which can be directly converted from the velocity data in Figures 5.39 and 5.41). Therefore, our LB model should still be capable of capturing the fast phenomena such as Haines jumps with an accurate Young-Laplace relation.

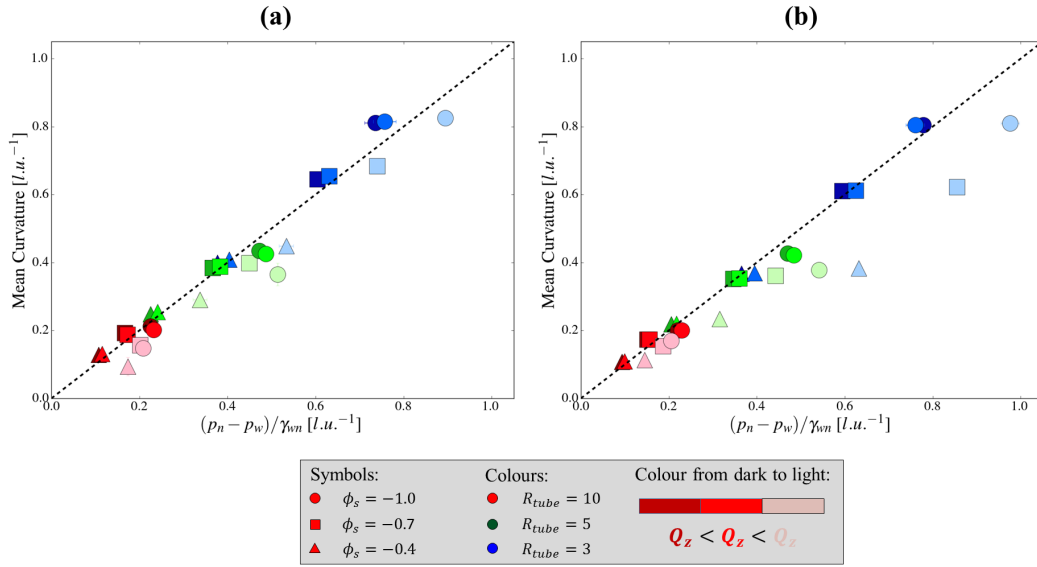


FIGURE 5.16: Young-Laplace test, where the interfacial mean curvature is plotted against the phase pressure difference normalised by the LB surface tension, for drainage in a square tube, for (a) $\alpha = 10^{-2}$, and (b) $\alpha = 10^{-4}$. Both the mean curvature and the pressure difference are measured from the steady-state part of the simulation, where the mean values are calculated and presented in the figure, with the error bars indicating the standard deviations of the mean. For each R_{tube} case, the colour of the symbol, from dark to light, corresponds to the prescribed global Ca from low to high.

Lastly, we examine whether or not the spurious current influences the movement of the NW-W fluid interface, for both capillary filling and drainage processes. Figure 5.17 shows the directly measured interfacial mean curvature versus the instantaneous Ca , which characterises the evolution of the interface and is calculated as: (McClure et al., 2018)

$$Ca = L \frac{\partial S_{nw}}{\partial t} \frac{\nu_{LB} \rho_{LB}}{\gamma_{wn}^{LB}}, \quad (5.6)$$

where L is the total length of the tube, and the NW phase saturation S_{nw} is calculated based on the local phase field such that a voxel of $\phi(\mathbf{x}) > 0$ is considered as being occupied by the NW phase. The value of $\partial S_{nw}/\partial t$ is obtained by fitting to the slope

of the steady-state part of S_{nw} v.s. time profile (e.g. Figure 5.7), and for both capillary filling and drainage a linear relation between S_{nw} and time is obtained. In the capillary filling, the NW phase is retreating from the tube, thus the corresponding instantaneous Ca is considered as negative. As a reference, a so-called static mean curvature at $Ca = 0$ is also presented, which is obtained by performing the square tube tests with periodic boundary condition (see section 3.4.1) at the same R_{tube} and ϕ_s as each of the dynamic case. For both capillary filling and drainage, it is expected that the interfacial mean curvature should well retain the same value as in the static case⁷, independent of the flow condition. This is indeed observed for $\alpha = 10^{-4}$: Figure 5.17(b) shows the flat lines for almost all of combinations of R_{tube} and ϕ_s ; and furthermore, for the drainage process, the measured instantaneous Ca agrees well with the prescribed Ca , even for the case of the largest prescribed Ca . For $\alpha = 10^{-2}$, as shown in Figure 5.17(a), some discrepancy is seen for the largest instantaneous Ca , and only for the biggest tube size $R_{tube} = 10.0$, the instantaneous Ca agrees with the prescribed flow condition. Nonetheless, as we mentioned previously, the case of largest prescribed Ca is much more than enough to cover the normal range of Haines jumps, hence we consider that both α are competent to deliver accurate simulations, so long as the imposed global flow condition follows $Ca < 10^{-2}$, which is common in the pore-scale two-phase flow experiments.

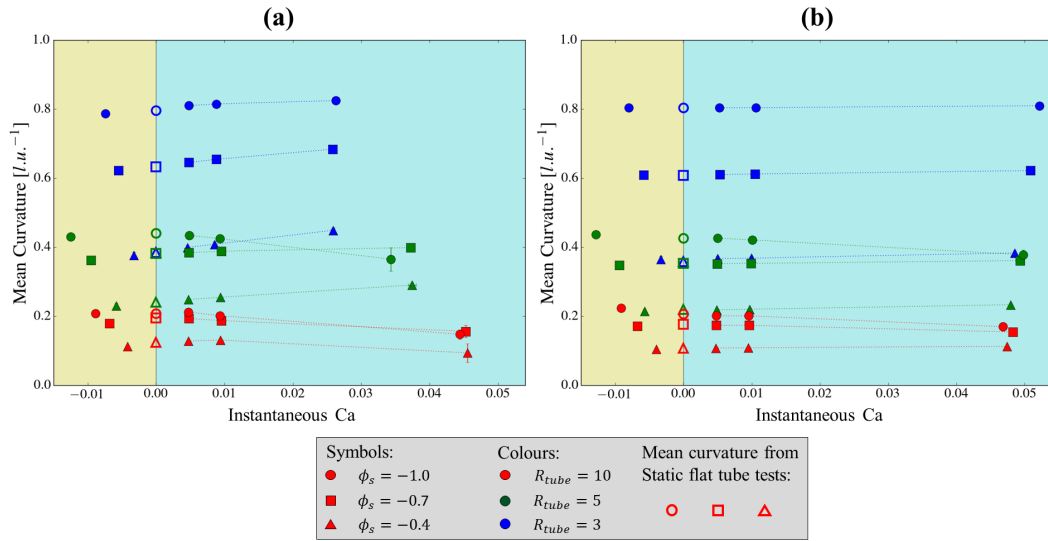


FIGURE 5.17: Mean curvature as a function of instantaneous capillary number calculated for the same physical system with (a) $\alpha = 10^{-2}$ and (b) 10^{-4} . The instantaneous Ca is calculated based on the evolution of the phase field, i.e. by fitting to the slope of S_{nw} vs. time profile. Positive and negative Ca in the filled symbols indicate the drainage and capillary filling processes, respectively. The mean curvature at $Ca = 0$ in the empty symbols is obtained by performing the square tube test (similar to the tests in section 3.4.1) at the same R_{tube} and ϕ_s values.

⁷The mean curvature is averaged over the fluid-fluid interface; instead, if it is the contact angle that is compared here, the dynamic contact angle is expected to be smaller than the static one.

In summary, based on all the characterisations at different resolution and wettability, it indicates that our MRT colour-gradient based model gives accurate simulation results, despite large spurious currents near the interface: the bulk velocity field is preserved and complies well with the Hagen-Poiseuille relation; the phase field evolves correctly according to the imposed global flow condition; and the interface does not significantly deform and does not give derailed mean curvature values. The range of the flow condition well covers the peak Haines jump velocity, and hence we conclude that both small and large α are potentially suitable for dynamic simulations for studying fast pore-scale phenomena such as Haines jumps and snap-off.

5.3 Influence of LB Temporal Resolution

Based on the characterisations in the previous section, we see that for a wide range of interfacial velocity, the colour-gradient based model can still capture the right physics during dynamic processes despite the spurious current disruption at interfaces; choosing a different LB surface tension parameter α cannot mitigate the spurious currents, which can be ultimately resolved only by implementing an improved multicomponent LB models. However, what different α does bring are different temporal resolutions, which turns out to play an important role in how the system copes with the initial transient part of the simulation. The lattice-Boltzmann method is an explicit numerical method, meaning that information takes a finite number of iteration steps to propagate through the domain. For a large α that gives a poor temporal resolution, the time scale such as the one that takes to develop a well-defined fluid-fluid interface, is competing against the time scale given by the characteristic flow field subject to the external boundary condition or the body force; on the other hand, for a smaller α the former time scale is better resolved, and is generally finer than the latter one.

In the previous section of square tube tests, because the geometry of the medium is simple, the different responses to the initial transition given by different α do not manifest themselves clearly. However, in Figures 5.8 and 5.12 where the 3D snapshots of the NW phase distributions for both α are shown, it can already be seen the saturation of both α does not match exactly for the equivalent physical system at the equivalent physical time step.

In this section, we perform a series of drainage tests in a small sub-domain (64^3 l.u.³) of a Bentheimer sandstone sample (the same one as in section 5.1.2), to demonstrate the consequence of different temporal resolutions due to different α . Three LB surface tension parameters $\alpha = \{10^{-4}, 10^{-3}, 10^{-2}\}$ are used, and the flux boundary condition is applied with two global $Ca = \{10^{-4}, 10^{-3}\}$ ⁸. For each α , the LB viscosity parameter τ_i for $i \in \{\text{nw}, \text{w}\}$, as well as the injection flux at the inlet are adjusted accordingly to retain the same physical surface tension, physical viscosity, and capillary number. In other words, the physical systems being modelled by different α are exactly same. For simplicity only the case of unitary viscosity ratio is investigated.

The wetting parameter $\phi_s = -1.0$ is used to eliminate the non-physical transport of the dissolved NW phase.

For the case of global $Ca = 10^{-3}$, Figure 5.18 shows the NW phase distribution for three α extracted at the equivalent physical time, where it can be seen that the fluid configurations are very different, and the saturations are $S_w = \{0.897, 0.821, 0.803\}$ for $\alpha = \{10^{-2}, 10^{-3}, 10^{-4}\}$, respectively. The discrepancy between each α in this more complicated geometry is much larger than that in the square tube case (see Figures 5.8 and 5.12). Furthermore, for all three cases of α the local fluid morphologies in the narrow throat (highlighted by the black arrows) present slightly different mean curvatures.

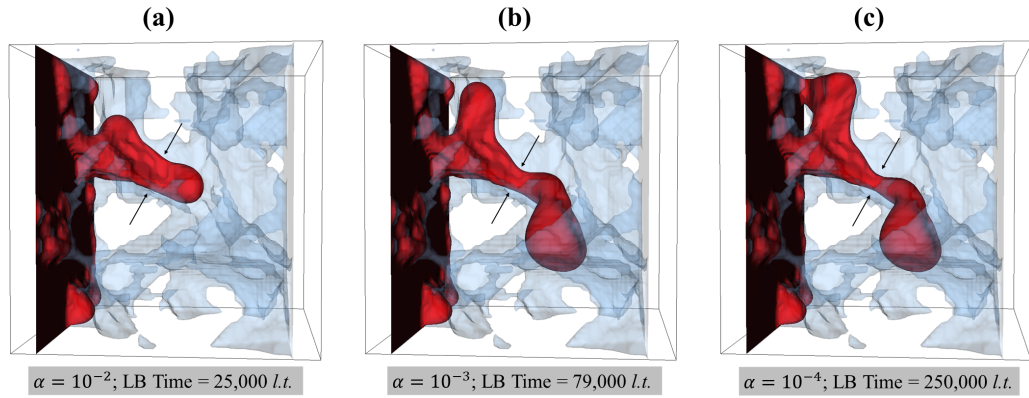


FIGURE 5.18: For prescribed global $Ca = 10^{-3}$: NW phase distributions during drainage with different LB surface tension parameter α but at the same physical time. The NW phase is in red, the solid matrix is in light grey, and for visual clarity the W phase is not shown. It can be seen the portion of NW fluid highlighted between the black arrows presents slightly different curvature for three α .

Instead of extracting the data at the equivalent physical time step, we continue to examine the phase distribution at the same saturation⁹, which is shown in Figure 5.19: from the top row to the middle row, for which the saturation S_w goes down from 0.803 to 0.799, not only are the fluid configurations different, a snap-off event occurs in $\alpha = 10^{-4}$ but not in the other two cases. We ran the simulations of $\alpha = \{10^{-3}, 10^{-2}\}$ for longer time until the most advanced NW phase front breaks into the W phase reservoir, but still did not observe any snap-off events, as shown by the bottom row.

For the case of prescribed global $Ca = 10^{-4}$, we again examine the evolution of the phase field at the same saturation, as shown in Figure 5.20: with a smaller global Ca , thus a larger time scale of the characteristic flow field, the phase distributions of three α show much better resemblance as indicated by the first two rows. At $S_w = 0.810$,

⁸The objective of this section is to examine the two competing time scales, namely, the time of information propagation and the time scale associated with the external flow field (imposed by either body force or dynamic boundary conditions). Therefore, two relatively large Ca cases have been chosen; for smaller Ca the time scale of the external field is relaxed, and thus it is less relevant to the objective of this section.

⁹The saturation S_w is calculated based on the phase field: a voxel of $\phi(\mathbf{x}) > 0.0$ is considered as being occupied by the NW phase, and $\phi(\mathbf{x}) < 0.0$ is considered as being occupied by the W phase.

both α of 10^{-4} and 10^{-3} show snap-off, whereas for $\alpha = 10^{-2}$, it is not until $S_w = 0.80$ the snap-off occurs.

Overall, based on the above characterisations, it indicates that, when the domain geometry is complex and the characteristic flow field is large, the influence of the temporal resolution given by different α becomes critical. Even though different pairs of α and τ_{LB} are set such that the equivalent physical system is modelled, the simulated drainage displacement pattern can become different. The obvious cost of using a smaller α is the prolonged computation time, hence considering the balance between computational efficiency and accuracy, a moderate alpha such as 10^{-3} could be an appropriate choice.

5.4 Results and Discussion

5.4.1 Overview of All Cases

After reviewing the capacity of our MRT-RK model to model various viscosity ratios and to match experimental condition with the flux boundary condition, as well as validating the minor influence of spurious current disruption on the interfacial kinematics, we now apply the model to study the dynamics of Haines jumps and associated snap-off phenomena. Based on the investigation of the LB surface tension parameter α , it is now known that the choice of α , which gives different LB temporal resolutions, strongly affects the computation time and can present different flow patterns under certain circumstances¹⁰. Therefore, we perform the drainage simulations in a realistic porous medium using two sets of LB surface tension parameter $\alpha = \{3.57 \times 10^{-2}, 1 \times 10^{-4}\}$ to explore the consequences in a larger-scale practical applications.

The medium used is the same 256^3 l.u.³ sub-domain (~ 1.3 mm³) of the Bentheimer sandstone μ CT image that is also used in sections 3.6, 4.3 and 5.1.2. The drainage tests are performed for a range of capillary numbers (Ca) and viscosity ratios (M). The flux boundary condition introduced in section 5.1.2 is applied to achieve the prescribed capillary numbers, and a constant pressure is applied at the outlet based on the implementation of Hecht and Harting (2010). A range of inlet volumetric flow rate and the LB viscous parameters are assigned which in total give five testing cases for each α . All key parameters (and parts of key results) are summarised in Table 5.1 and 5.2, for α of 3.57×10^{-2} and 10^{-4} , respectively. Incidentally, the strongly wetting boundary condition ($\phi_s = -1.0$) is used to avoid the potential non-physical attraction of dissolved NW phase and the generation of ‘fake’ NW bubbles.

Among these cases, we in fact choose the case 3 as the baseline case, which matches the high flow-rate case (i.e. the inlet pump rate $Q_z = 435 \mu\text{L/hr}$) of the n-decane/water system in the experiment of Herring et al. (2018): in order to match the n-decane/water interfacial tension of 32 mN/m, the density of n-decane (i.e. 729.88

¹⁰It is also one of the key advantages in LB method that the temporal resolution can be flexibly manipulated, and a higher temporal resolution than that can be achieved experimentally can be set.

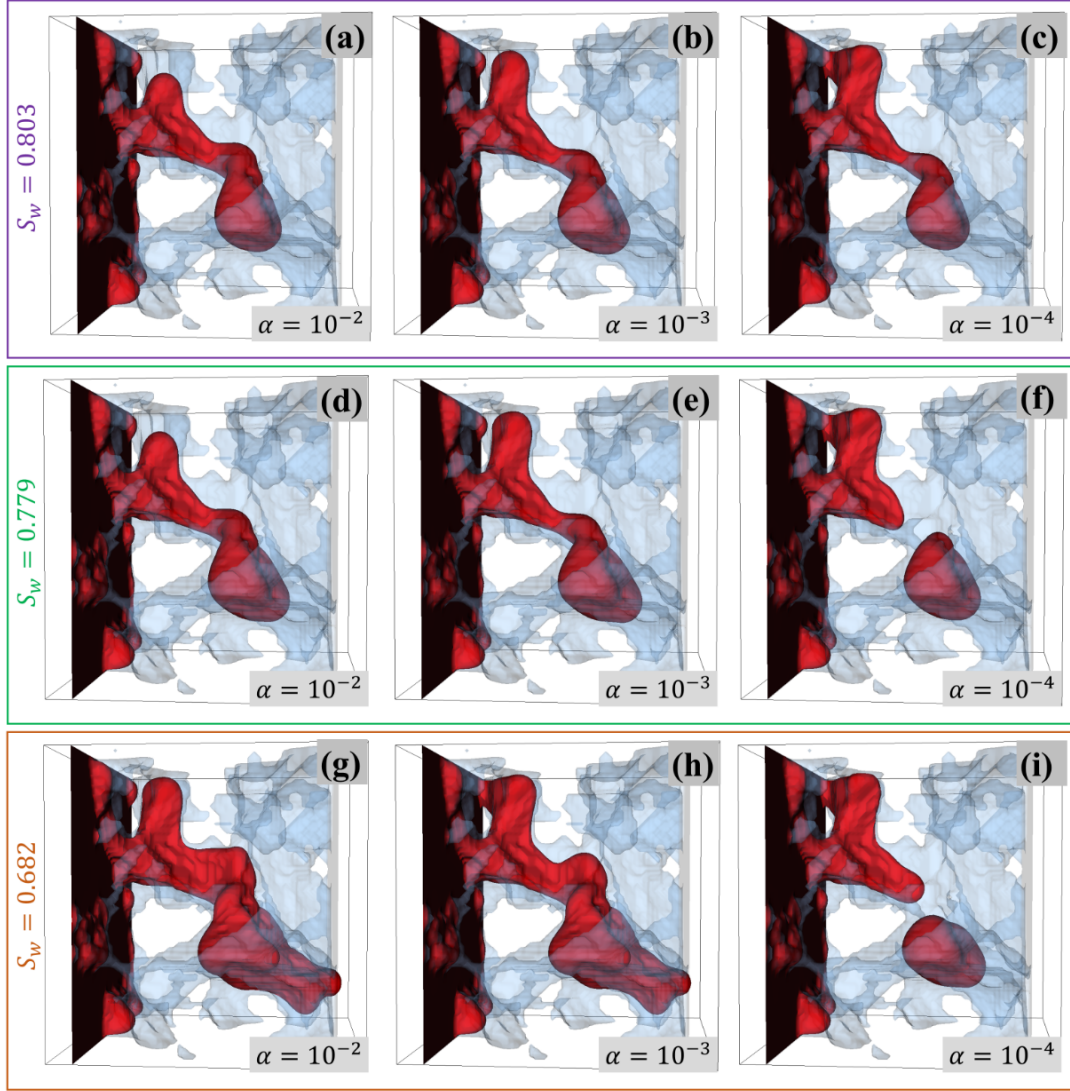


FIGURE 5.19: For prescribed global $Ca = 10^{-3}$: NW phase distributions during drainage at same S_w (in each row) for the equivalent physical system, but with different LB surface tension parameter α .

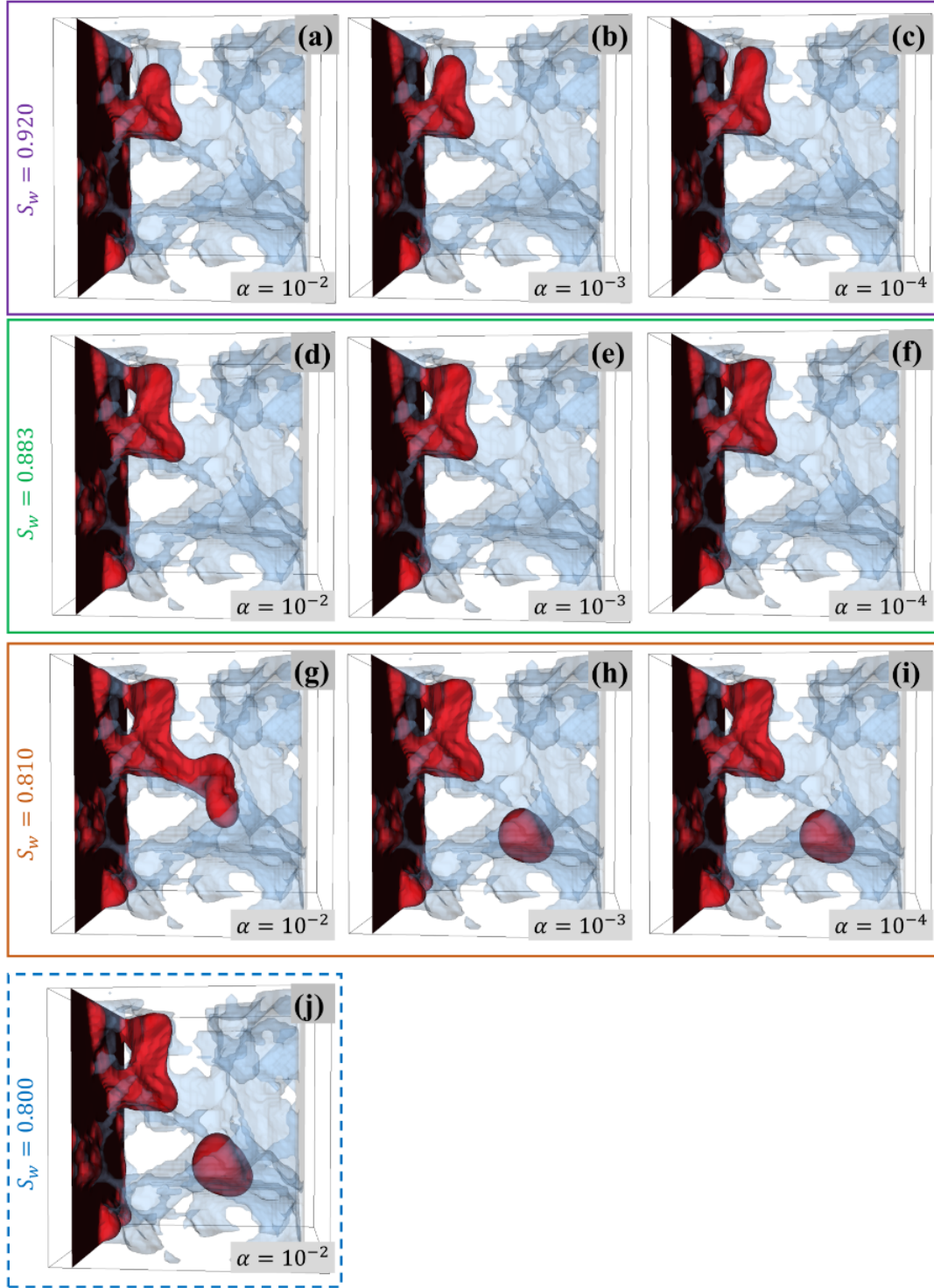


FIGURE 5.20: For prescribed global $Ca = 10^{-4}$: NW phase distributions during drainage at same S_w (in each row) for the equivalent physical system, but with different LB surface tension parameter α . The last row indicates the drainage and associated snap-off occur at a slightly lower W saturation for $\alpha = 10^{-2}$.

kg/m³) which is less than that of water, is approximated as 1000 kg/m³ to give a unitary density ratio. Given the image resolution of 4.95 μm/*l.u.*, and considering the time conversion relation between LB and physical units (equation 2.49), the LB simulation has temporal resolution δt_{phys} of 8.86×10^{-7} s/*l.t.* and 4.69×10^{-8} s/*l.t.*, for α of 3.57×10^{-2} and 10^{-4} , respectively. The *in-situ* analysis module of our LB code reports physically and morphologically averaged quantities every 1000 *l.t.* (i.e. 0.89 ms and 0.047 ms, for α of 3.57×10^{-2} and 10^{-4} , respectively). The fluid phase, pressure and velocity field data are also saved in every 1000 *l.t.* for $\alpha = 3.57 \times 10^{-2}$, and in every 10,000 *l.t.* (i.e. 0.47 ms) for $\alpha = 10^{-4}$ for post-analysis¹¹. Once δt_{phys} is determined, the LB kinematic viscosities ν_{LB} for NW and W phases can be calculated accordingly, to match the n-decane dynamic viscosity of 0.922 mPa·s. Then using the parameters in case 3 as a baseline, we varied the NW and W phase viscosities and the inlet pump rate to generate all other cases. It is noted that physical system modelled by the other testing cases might be largely artificial, whose significance of guiding the experiment may be limited. In this work, the capillary number is defined in terms of the more viscous fluid, thus denoted as Ca^* , which may be different from the usual one that is defined in terms of the invading fluid.

It should be noted that only the case 3 is equivalent for both α , as all of the macroscopic physical parameters (i.e. surface tension and viscosity etc.) are exactly the same. For the cases 1, 2, 4, and 5, although the physical surface tension, capillary number, and viscosity ratio are the same for both α , the dynamic viscosity used in $\alpha = 10^{-4}$ is on average one order of magnitude higher¹² than that in $\alpha = 3.57 \times 10^{-2}$. Therefore, in terms of other dimensionless number, e.g. the Ohnesorge number ($Oh = \mu / \sqrt{\rho \gamma_{wn} L}$), which relates the viscous forces to inertial and surface tension forces, the cases 1, 2, 4 and 5 between two α are apparently not equivalent. In $\alpha = 10^{-4}$, more viscous fluids are used because too small viscosity would lead to the relaxation parameter τ being very close to the critical value of 0.5, which could potentially cause numerical instability.

During the drainage processes, the Haines jumps constantly happen as the NW phase tries to enter a large pore body via a narrow throat, and some of them lead to (Roof-type) snap-off (Roof, 1970). To better trace the individual snap-off event, we partitioned the pore space of the μCT image into numbered labels based on a novel geometry-topology analysis via persistent homology (Robins et al., 2015; Herring, Robins, and Sheppard, 2019) (see section 5.4.4 for more discussion), so that we can designate an identifier for each of the snap-off events as follows:

Case number/pore body labels/throat labels

where the throat labels indicate the throat through which the NW phase invades and snaps off, and pore body labels indicate where the ganglion resides after snap-off;

¹¹The data access frequencies of 0.89 ms and 0.47 ms for α of 3.57×10^{-2} and 10^{-4} , respectively, are good enough to capture the rapid drainage events such as Haines jumps (Armstrong and Berg, 2013; Zacharoudiou and Boek, 2016).

¹²Such situation is achieved by manipulating the inlet pumping rate.

TABLE 5.1: Simulation Parameters of Primary Drainage for Haines Jumps and Snap-off Study with $\alpha = 3.57 \times 10^{-2}$

Case	Ca^*	M	μ_{nw}	μ_w	Snap-off Time [‡]	Snap-off Pore Bodies [†]	Invading Throats [†]	Snap-off Identifier [†]
1	5×10^{-4}	0.2	0.922 mPa.s	4.610 mPa.s	134 ms	5; 8	752	1/(5; 8)/752
					220 ms	5; 49; 55	752	1/(5; 49; 55)/752
					229 ms	5; 49; 55	752	1/(5; 49; 55)/752
2	5×10^{-5}	0.2	0.922 mPa.s	4.610 mPa.s	N/A	N/A	N/A	N/A
					1,575 ms	5; 8	752	3/(5; 8)/752
					1,579 ms	5; 8	752	3/(5; 8)/752
3	1.25×10^{-5}	0.8	0.922 mPa.s	1.153 mPa.s	1,611 ms	5; 8; 49; 55	752	3/(5; 8; 49; 55)/752
					1,655 ms	5; 8; 49; 55	752	3/(5; 8; 49; 55)/752
					1,689 ms	5; 8; 49; 55	752	3/(5; 8; 49; 55)/752
					1,733 ms	5; 8; 49; 55	752	3/(5; 8; 49; 55)/752
					1,767 ms	5; 8; 49; 55	752	3/(5; 8; 49; 55)/752
					175 ms	15; 16	832	4/(15; 16)/832
4	5×10^{-4}	10	4.610 mPa.s	0.461 mPa.s	190 ms	8	752	4/8/752
					520 ms	2	627	5/2/627
					1,394 ms	15; 16	646	5/(15; 16)/646
5	5×10^{-5}	10	4.610 mPa.s	0.461 mPa.s	1,408 ms	15; 16	646	5/(15; 16)/646
					1,422 ms	4; 262	646	5/(4; 262)/646
					1,422 ms	15; 16	646	5/(15; 16)/646
					1,435 ms	4; 15; 16; 262	646	5/(4; 15; 16; 262)/646

[‡] The total simulation time (at which the NW phase breaks into the W phase reservoir) for case 1 to 5 are: 240ms, 1,648ms, 1,608ms, 204ms, and 1,435ms, respectively.

[†] The pore bodies and throats, as well as the combined ‘snap-off identifier’, are classified into the numbered labels by the geometry-topology analysis via persistent homology (Herring, Robins, and Sheppard, 2019). See more in section 5.4.4.

together with the case number, a snap-off event can be uniquely identified¹³. All snap-off events are summarised in Tables 5.1 and 5.2.

To obtain qualitative understanding of the two-phase flow regime that different testing cases might involve, the commonly used (M, Ca^*) phase diagram, originally proposed by Lenormand, Touboul, and Zarcone (1988), is shown in Figure 5.21. The displacement pattern classified by the more recent work of Zhang et al. (2011) is also drawn in dash lines for reference. However, it is noted that such a classification is based on the experimental 2D micromodels, and we include a few representative 2D examples to illustrate each flow pattern shown in Figure 5.22. More recently, Tsuji, Jiang, and Christensen (2016) performed LB drainage simulations on a 3D sample of Berea sandstone μ CT image with various Ca and M and obtained the flow pattern classification very different from the 2D micromodels: the most pronounced observation is that capillary fingering occurs even at high Ca and high M , for which is deemed as the stable displacement regime according to the experiments in micromodels.

¹³As can be seen in Tables 5.1 and 5.2, there are some repeated snap-off events in the same pore body via the same throat for the same testing case. In such situation our identifier does have some degeneracy. More future work is needed to further explore the geometric significance of these pore bodies and throats.

TABLE 5.2: Simulation Parameters of Primary Drainage for Haines Jumps and Snap-off Study with $\alpha = 10^{-4}$

Case	Ca^*	M	μ_{nw}	μ_w	Snap-off Time [‡]	Snap-off Pore Bodies [†]	Invading Throats [†]	Snap-off Identifier [†]
1	5×10^{-4}	0.2	17.4 mPa.s	87.1 mPa.s	449 ms	12*	836	1/12/836
					502 ms	12*	836	1/12/836
					671 ms	60	909	1/60/909
					736 ms	60	909	1/60/909
					901 ms	60; 334	909	1/(60; 334)/909
					901 ms	5; 8; 49; 55	786	1/(5; 8; 49; 55)/786
					948 ms	5; 8; 49; 55	786	1/(5; 8; 49; 55)/786
2	5×10^{-5}	0.2	17.4 mPa.s	87.1 mPa.s	490 ms	57; 86	775	2/(57; 86)/775
					831 ms	12	836	2/12/836
					872 ms	12	836	2/12/836
					1,184 ms	60	909	2/60/909
					1,318 ms	60	909	2/60/909
3	1.25×10^{-5}	0.8	0.922 mPa.s	1.153 mPa.s	285 ms	2	627	3/2/627
					990 ms	15; 16	646	3/(15; 16)/646
					996 ms	4; 15; 16	646	3/(4; 15; 16)/646
					1,011 ms	4; 15; 16; 29; 97; 262	646	3/(4; 15; 16; 29; 97; 262)/646
4	5×10^{-4}	10	87.1 mPa.s	8.71 mPa.s	381 ms	12	836	4/12/836
					414 ms	12	836	4/12/836
					677 ms	60	909	4/60/909
					724 ms	60	909	4/60/909
					1,024 ms	24; 39	728	4/(24; 39)/728
					1,054 ms	71	1315	4/71/1315
					1,093 ms	71	1315	4/71/1315
5	5×10^{-5}	10	87.1 mPa.s	8.71 mPa.s	1,241 ms	5	786	4/5/786
					584 ms	12	836	5/12/836
					869 ms	12	836	5/12/836
					1,269 ms	60	909	5/60/909
					1,546 ms	24; 39	728	5/(24; 39)/728

[‡] The total simulation time (at which the NW phase breaks into the W phase reservoir) for case 1 to 5 are: 956ms, 1,547ms, 1,125ms, 1,294ms, and 1,715ms, respectively.

[†] See the same footnotes in Table 5.1.

* The repeated pore body labels indicate that the snap-off occurs repeatedly in the same pore bodies. The detailed snap-off processes of all cases for $\alpha = 10^{-4}$ have been made into videos and can be accessed upon request.

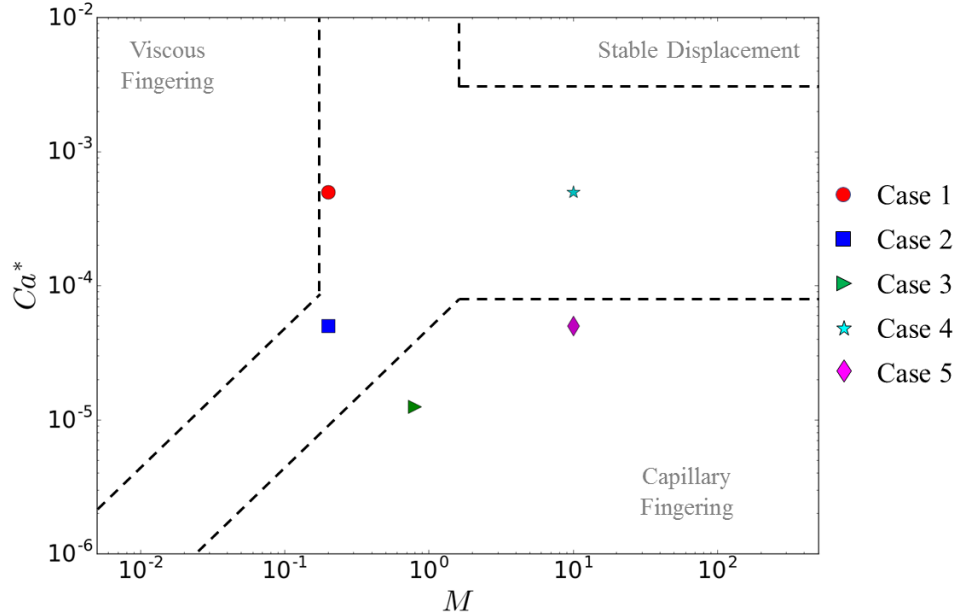


FIGURE 5.21: Classification of drainage flow patterns based on the capillary number Ca and viscosity ratio M for all the primary drainage simulations. The dash lines depict the flow regime boundaries according to Zhang et al. (2011).

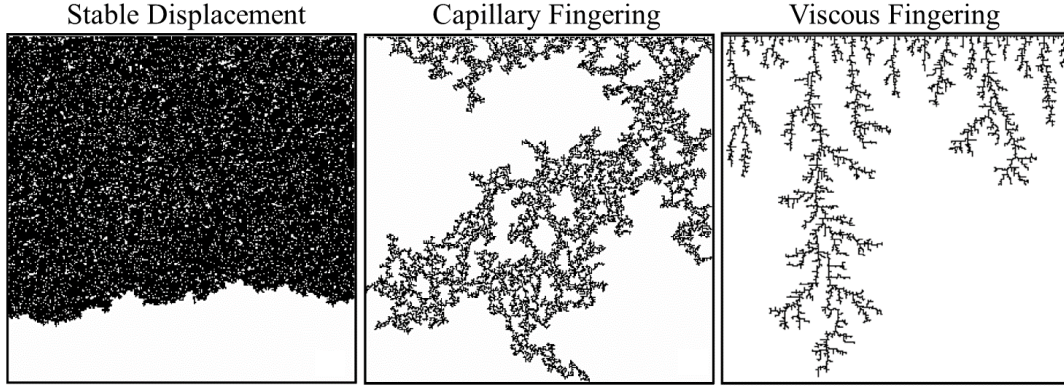


FIGURE 5.22: Schematic illustration of the flow patterns based on the 2D micromodels. The figure is adapted from Ewing and Berkowitz (2001).

Figures 5.23 and 5.24 show the corresponding ‘end-state’ NW phase distributions for α of 3.57×10^{-2} and 10^{-4} , respectively, where the most advanced NW phase front reaches the W phase reservoir. According to the classification of Zhang et al. (2011), both case 1 and 2 are in the crossover regime close to viscous fingering; case 3 and 5 are in the capillary fingering regime, and case 4 is in the crossover regime. However, for $\alpha = 3.57 \times 10^{-2}$, all of the end states shown in Figure 5.23 exhibits capillary fingering feature, in the sense that the finger front moves not only in the injection direction, but also presents some backward movement, i.e. against the injection direction towards the inlet. Although we use a different rock type, our observation largely agrees with the work by Tsuji, Jiang, and Christensen (2016), that is, based on the range of Ca and M , all cases are in capillary fingering regime. Likewise, for the case of $\alpha = 10^{-4}$, case 2, 3, 4 and 5 all present capillary fingering patterns; however the case 1 resembles more closely a viscous fingering pattern. Overall, although our observation on the end-state of the NW phase distributions seems to agree more with the recent work by Tsuji et al., which may highlight the difference in fluid behaviour between 3D natural rocks and 2D homogeneous models (potentially due to the heterogeneity of the complex 3D pore geometry and connectivity), it should be noted that our current domain size is still too small to make any definite conclusion, since the classification of the flow pattern is indeed length-scale dependent, and future work with much larger domain size is needed.

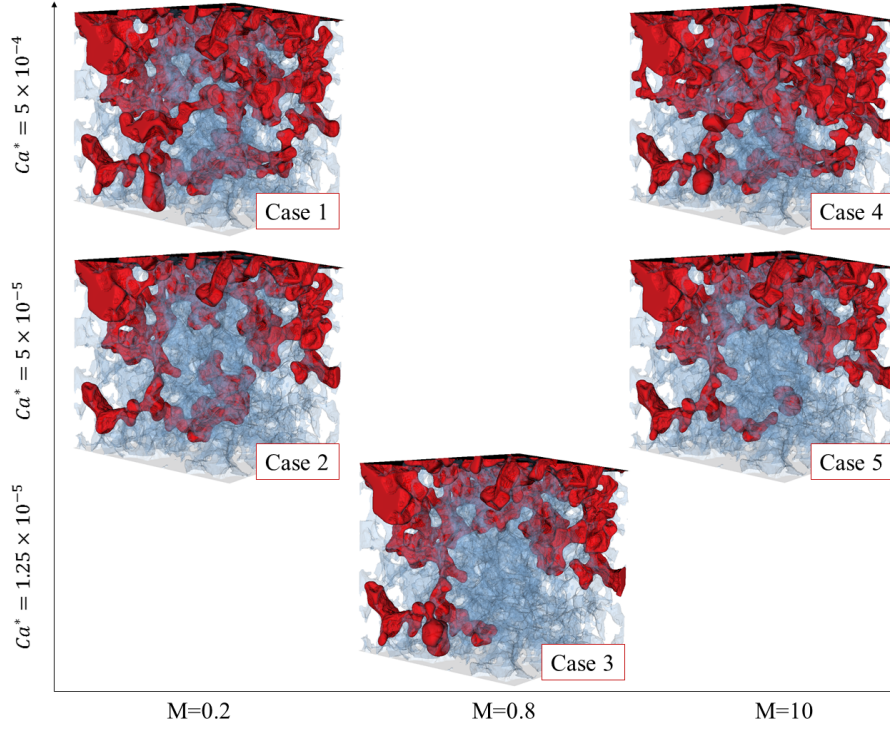


FIGURE 5.23: The end-states of NW phase configurations of $\alpha = 3.57 \times 10^{-2}$. The capillary number Ca^* is redefined in terms of the more viscous fluid.

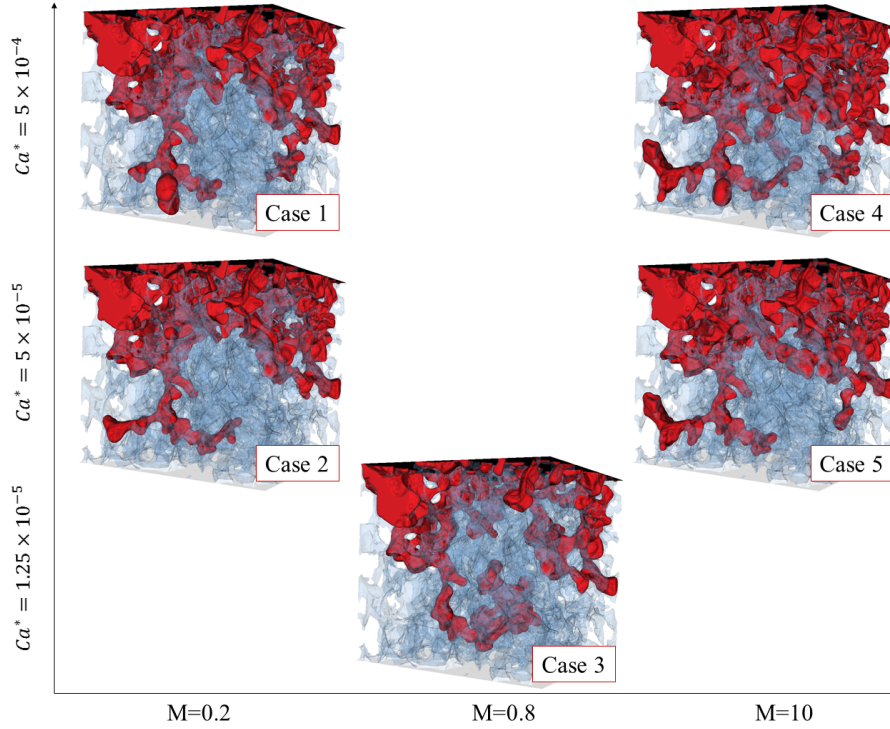


FIGURE 5.24: The end-states of NW phase configurations with the same layout as in Figure 5.23, but for $\alpha = 10^{-4}$.

5.4.2 Drainage Displacement Patterns

In this subsection, we primarily investigate the capillary pressure-saturation relationships as well as the NW phase distributions along the drainage process at several saturations. As is mentioned in the previous sub-section, only for case 3, the exactly same physical system is modelled by $\alpha = \{3.57 \times 10^{-2}, 10^{-4}\}$. Therefore, the P_c - S_{nw} relations and the NW phase configurations of case 3 will be firstly compared. Then the results and discussion for case 1, 2, 4 and 5 are presented, for which it is noted that although both α model the same physical surface tension, capillary number and viscosity ratio, the NW and W phase viscosities in $\alpha = 10^{-4}$ are on average one order of magnitude higher than those in $\alpha = 3.57 \times 10^{-2}$.

Results

First, for case 3 of both α , the capillary pressure normalised by the surface tension is plotted against the NW phase saturation in Figure 5.25. Both the saturation and the capillary pressure are obtained from the *in-situ* analysis module of the LB code, where the normalised capillary pressure is simply the interface-averaged mean curvature data. For each P_c - S_{nw} curve, the data points of which the snap-off occurs are highlighted in different colours. Snap-off events are grouped according to different invading throat labels. The vertical dash lines along the curves highlight four NW phase saturation at which the corresponding 3D NW phase configurations are shown in Figure 5.26, together with the ‘end-state’ configurations when the NW phase front breaks into the W phase reservoir.

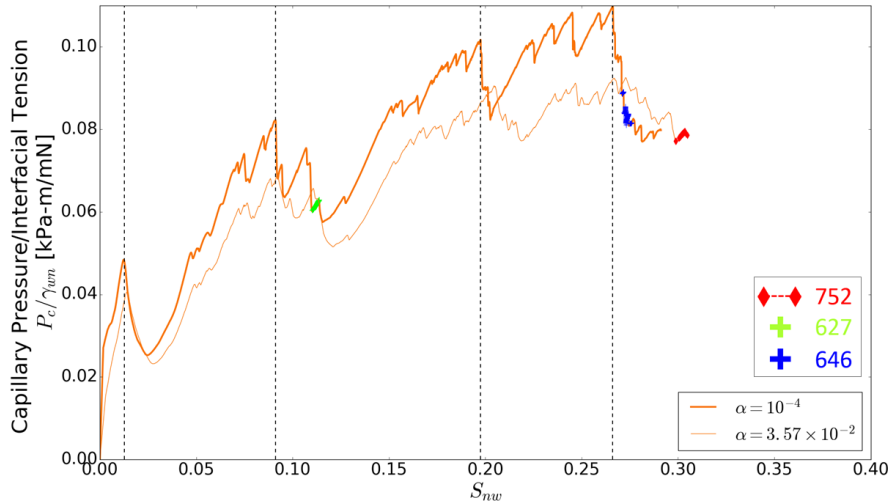


FIGURE 5.25: The Capillary pressure (normalised by surface tension) is plotted against the saturation for the primary drainage simulations of case 3. Parts of the P_c/γ_{wn} - S_{nw} curves are plotted in diamond and plus symbols in different colours, showing the time period when a disconnected NW phase component exists associated with a Roof-type snap-off. Each symbol colour corresponds to a particular invading throat through which the snap-off happens (see more in Table 5.1 and 5.2). The black dash lines indicate the saturation at which the corresponding 3D NW fluid distributions are drawn in Figure 5.26.

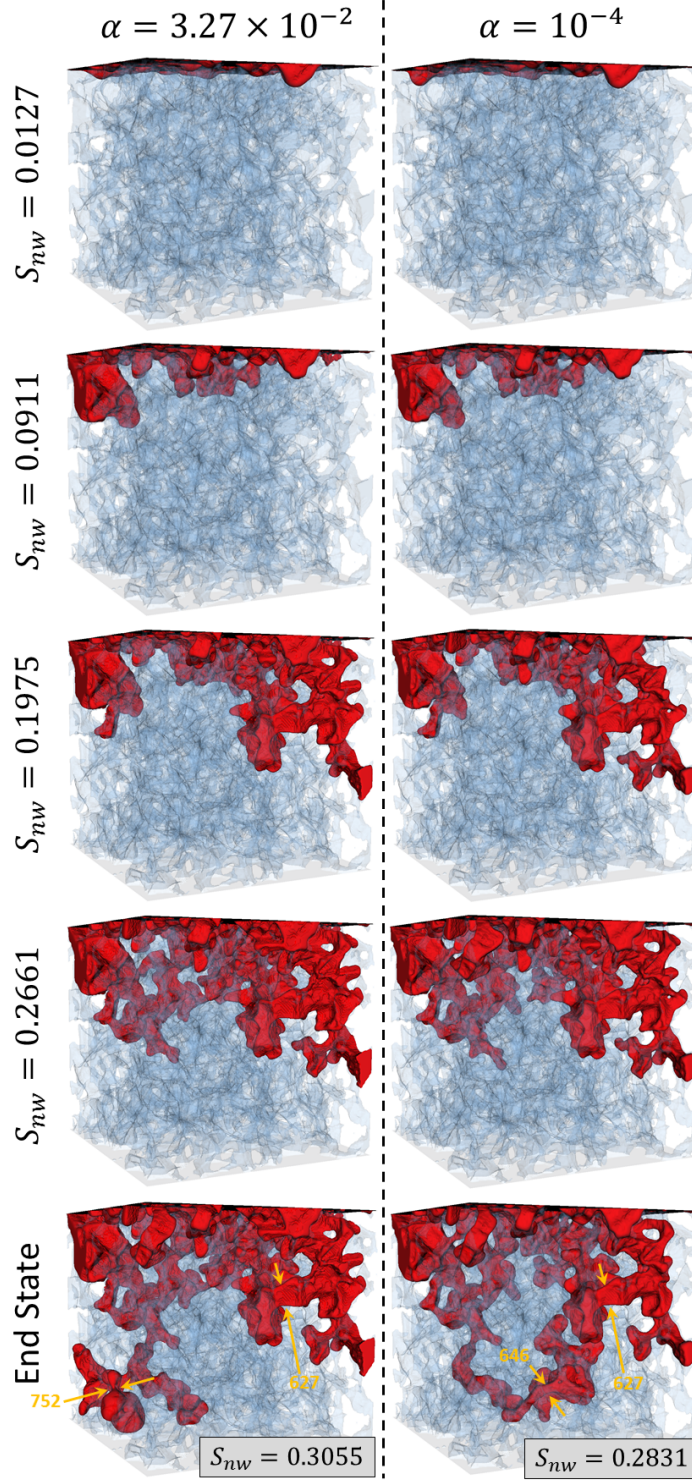


FIGURE 5.26: Three-dimensional non-wetting fluid distributions of case 3 for $\alpha = \{3.57 \times 10^{-2}, 10^{-4}\}$, at a series of non-wetting phase saturations. The solid matrix is in light blue and the wetting phase is made transparent. The first four saturations correspond to the dash lines in Figure 5.25. The ‘End State’ refers to the state where the most advanced NW phase front reaches the W phase reservoir. The numbers in the end-states are the throat labels identified by the persistent homology analysis.

Moreover, Figure 5.27 illustrates some of Haines jump events that occur during drainage for the case of $\alpha = 3.57 \times 10^{-2}$, which are captured as sudden P_c drop in the P_c - S_w curve. The same P_c - S_{nw} curve is shown in Figure 5.27(a)¹⁴, with five Haines jumps being labelled by the titles of the rest sub-plots. Figure 5.27(b) to (f) shows the corresponding 3D NW phase distributions, each of which represents the difference in NW fluid distribution between the beginning and the end states of the Haines jump. The colour convention for the NW fluid at different states follows Helland et al. (2017), in which gold indicates fluid that is present for both “before” and “after” states; cyan indicates the fluid advancement, whereas the portion in red is an indication of retraction. Overall, it can be seen that Haines jumps are non-local phenomena, which agrees with the experimental observation of 2D micromodel in Armstrong and Berg (2013): the Haines jump (highlighted in cyan) is accompanied by temporary imbibition nearby or a few pores away (highlighted in red).

For case 1, 2, 4, and 5, the P_c - S_{nw} relationships are shown in Figure 5.28 for both α , with the snap-off events being highlighted in different colours as per invading throat labels. Again, the vertical dash lines locate several NW phase saturations, and the corresponding 3D NW phase configurations are shown in Figure 5.29 to 5.36.

¹⁴Note that the ending S_{nw} point here is greater than that in Figure 5.25. The simulation was running for a longer time after the NW phase front reaches the W phase reservoir, in order to collect more Haines jump data.

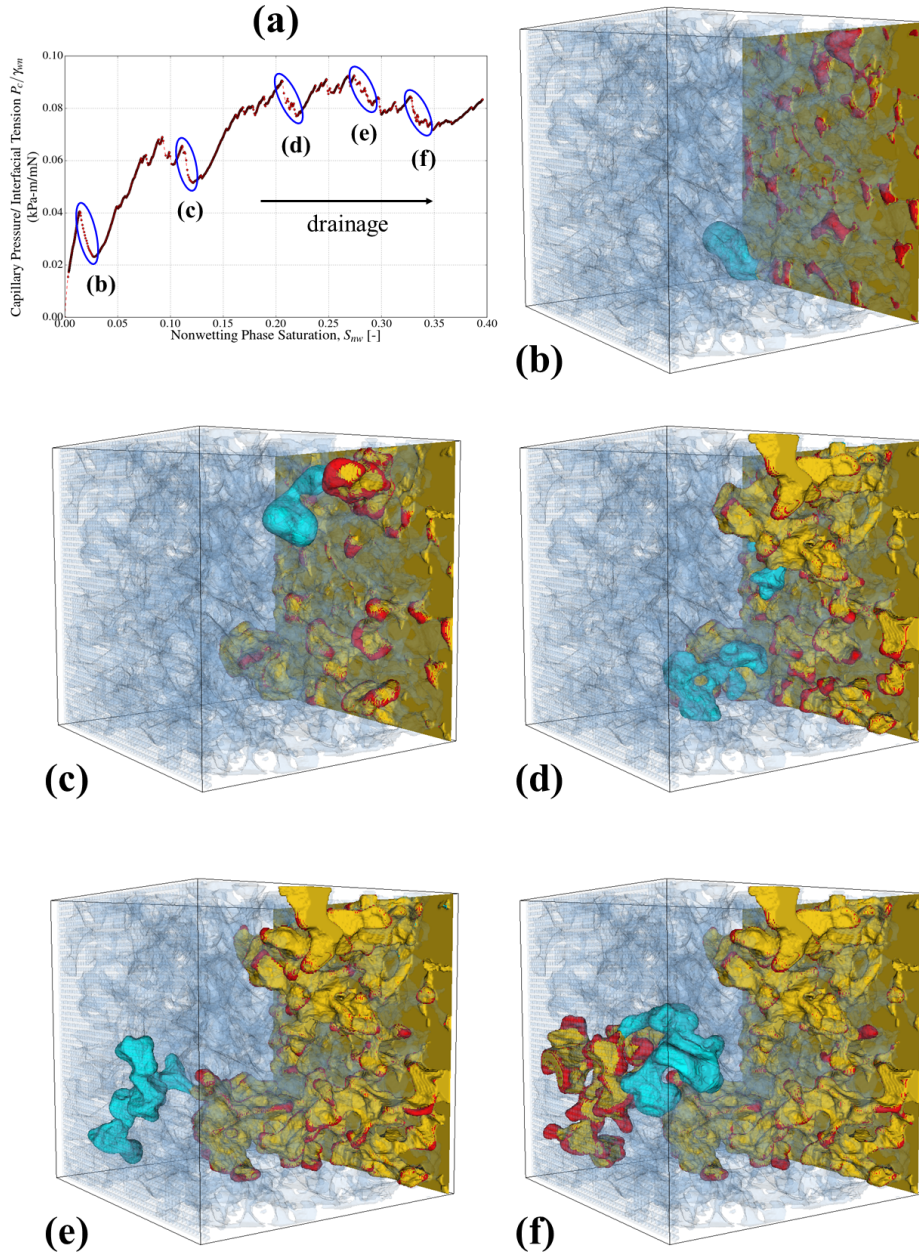


FIGURE 5.27: Visualisation of Haines jumps during drainage from LB simulation. (a) shows the (normalised) capillary pressure as a function of NW phase saturation (S_{nw}), with P_c drops indicating Haines jumps highlighted in blue ellipse, and the corresponding three-dimensional NW fluid distribution for each event can be identified by the title of each sub-plot. For sub-plots (b) to (f), the evolution of the NW phase fluid occupancy is shown: gold, cyan and red indicate the unchanged part, advancement, and retraction of the NW fluid throughout the P_c drop, respectively. The W phase is made transparent, and the rock matrix is in light grey.

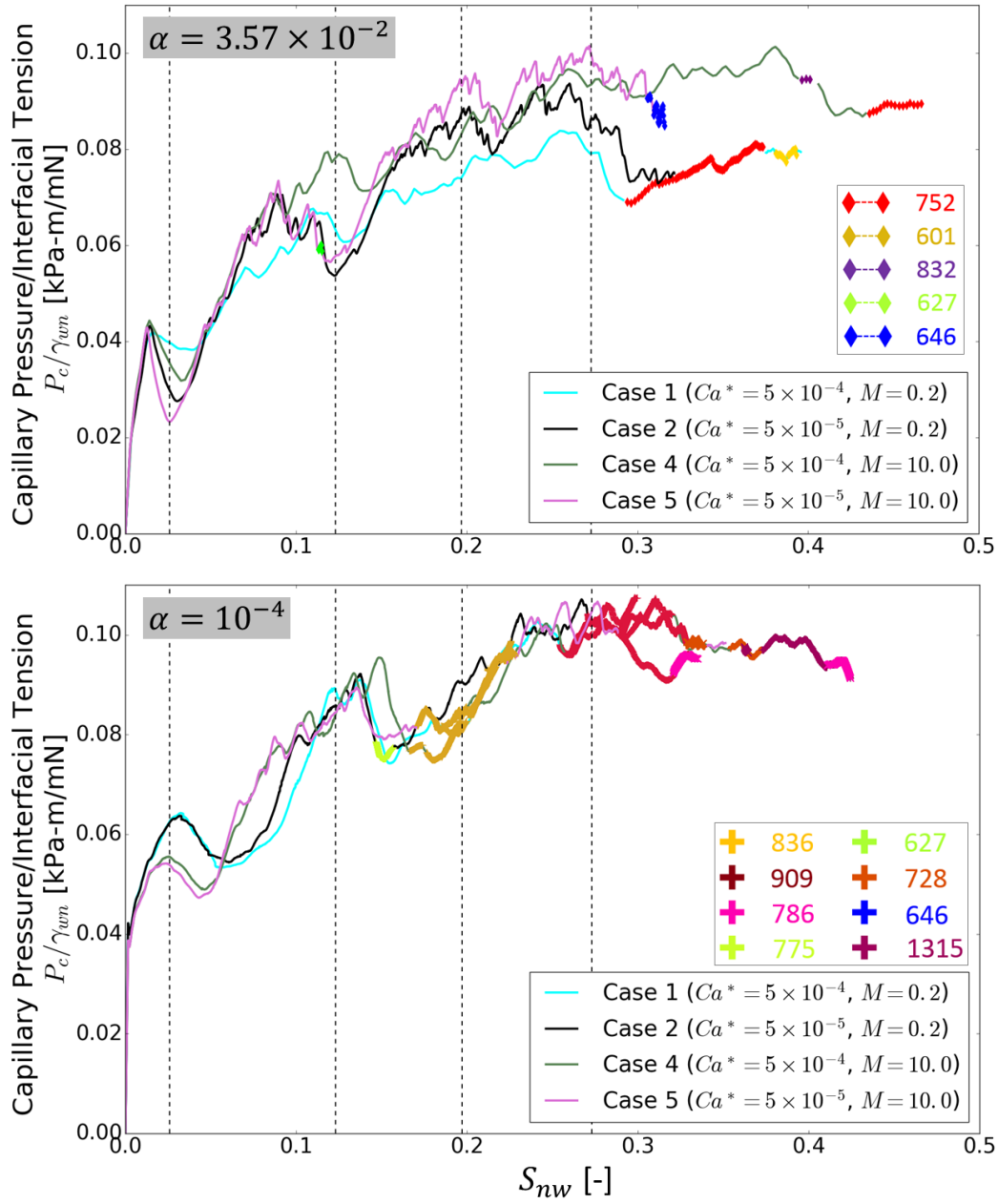


FIGURE 5.28: The Capillary pressure (normalised by surface tension) is plotted against the saturation for the primary drainage simulations of case 1, 2, 4 and 5. Parts of the P_c/γ_{wn} - S_{nw} curves are plotted in diamond and plus symbols in different colours for α of 3.57×10^{-2} and 10^{-4} , respectively, to highlight the snap-off events. Each symbol colour corresponds to a particular invading throat through which the snap-off happens (see more in Table 5.1 and 5.2). The black dash lines indicate the saturation at which the corresponding 3D NW fluid distributions are drawn for visual inspection.

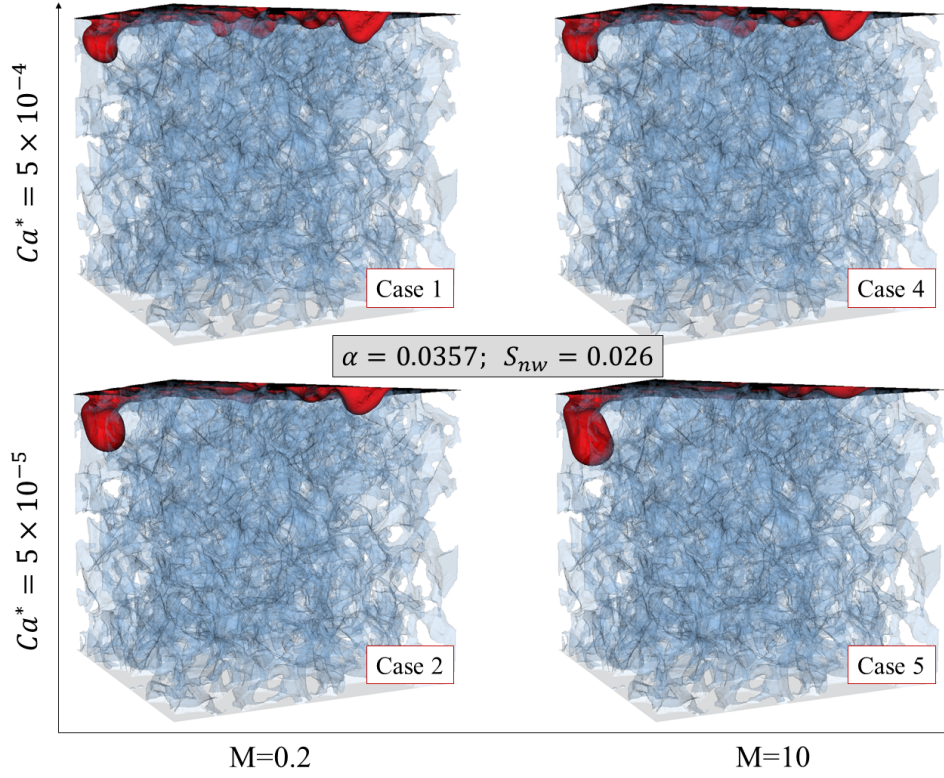


FIGURE 5.29: NW fluid distributions for $\alpha = 3.57 \times 10^{-2}$, at $S_{nw} = 0.026$.

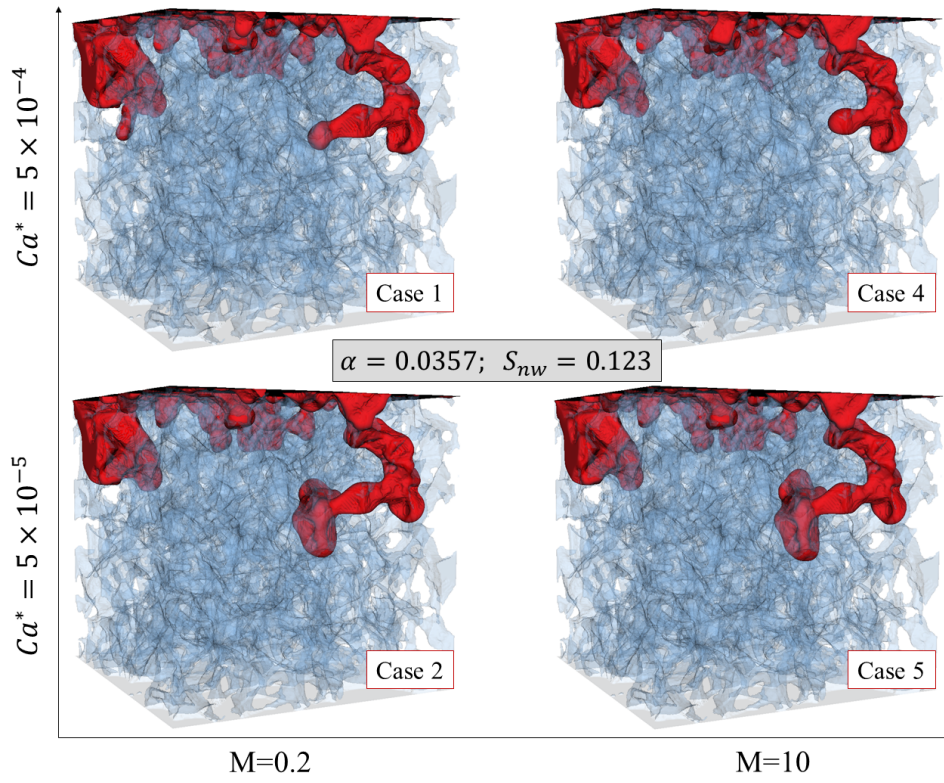


FIGURE 5.30: NW fluid distributions for $\alpha = 3.57 \times 10^{-2}$ at $S_{nw} = 0.123$.

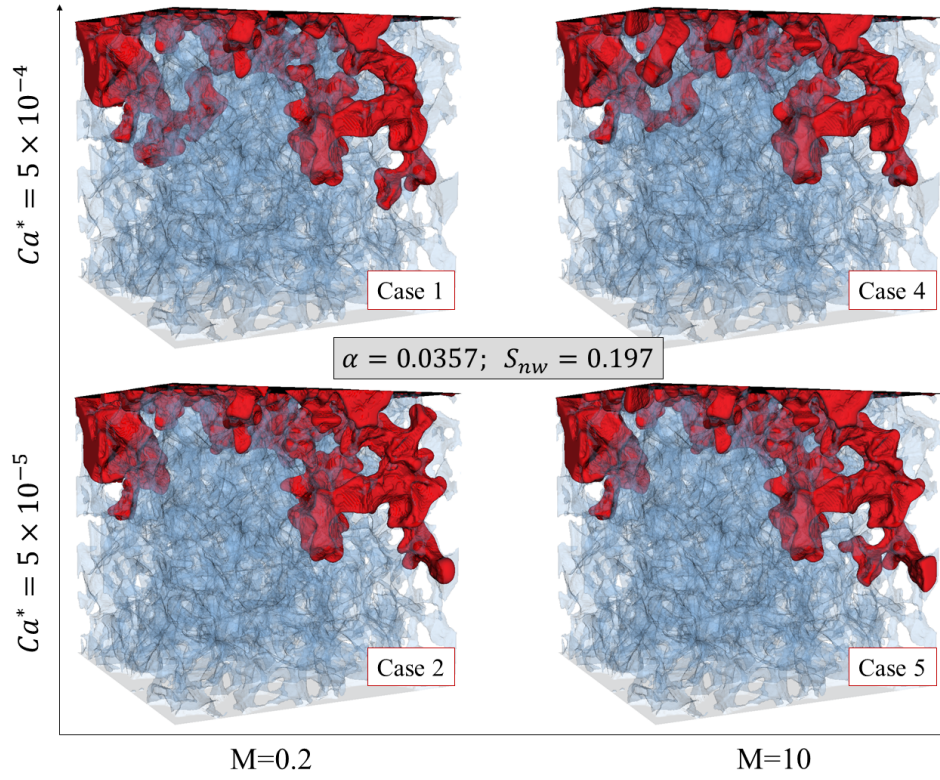


FIGURE 5.31: NW fluid distributions for $\alpha = 3.57 \times 10^{-2}$ at $S_{nw} = 0.197$.

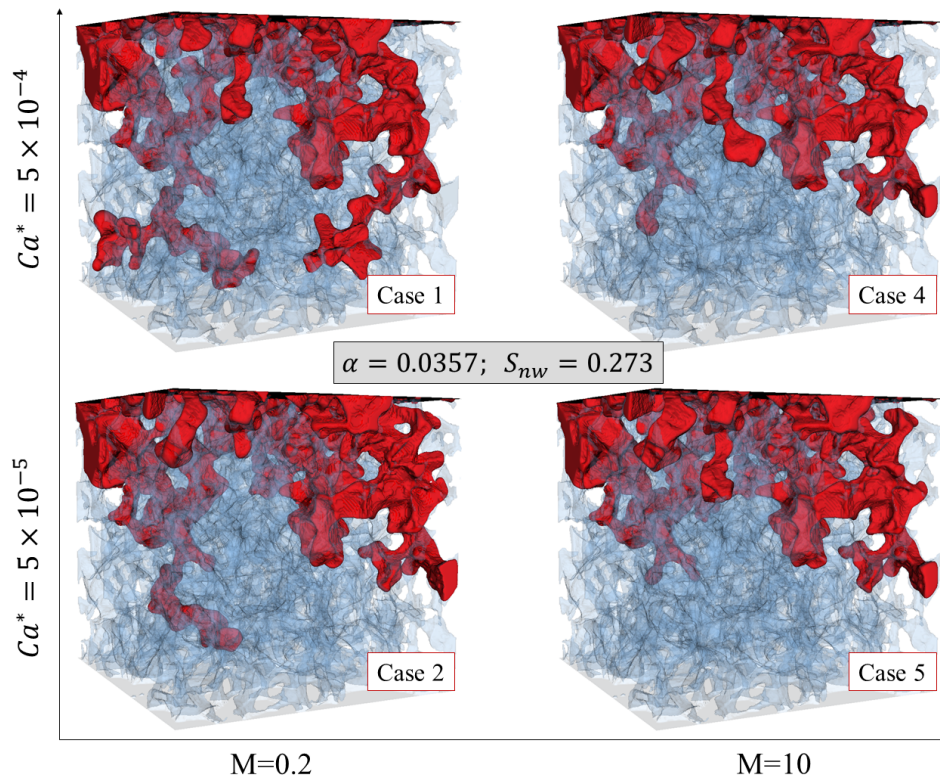
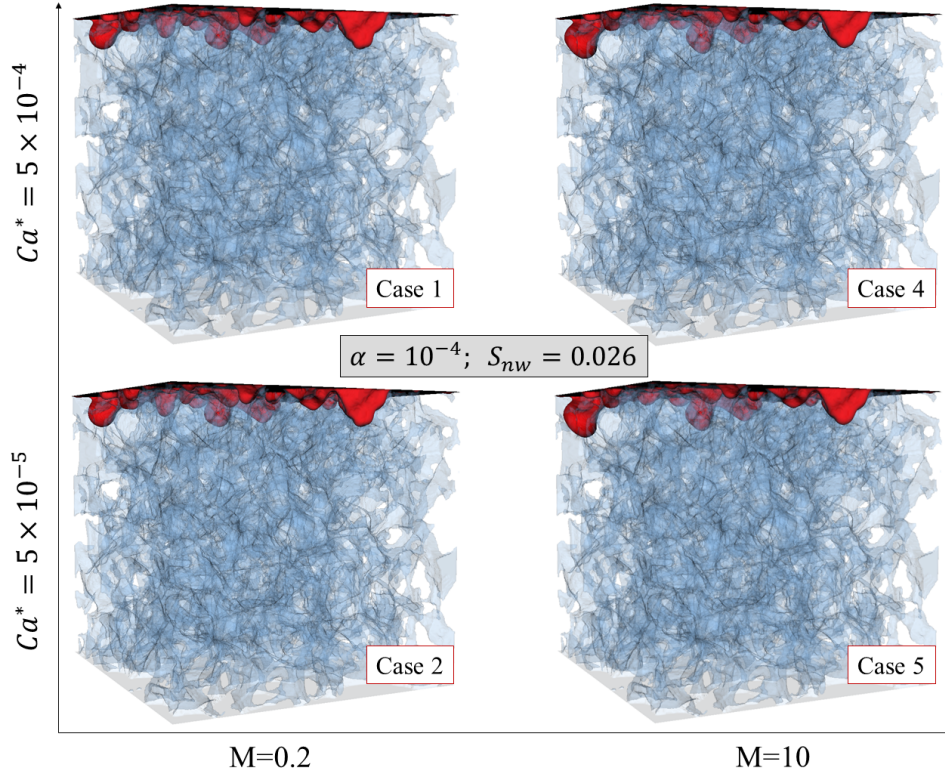
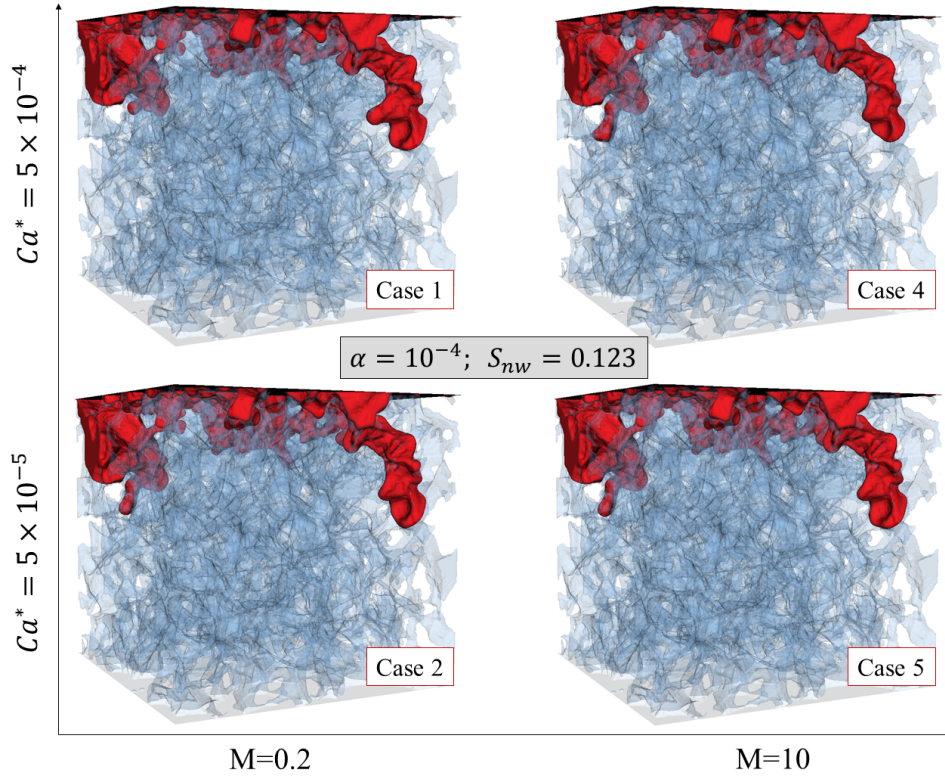
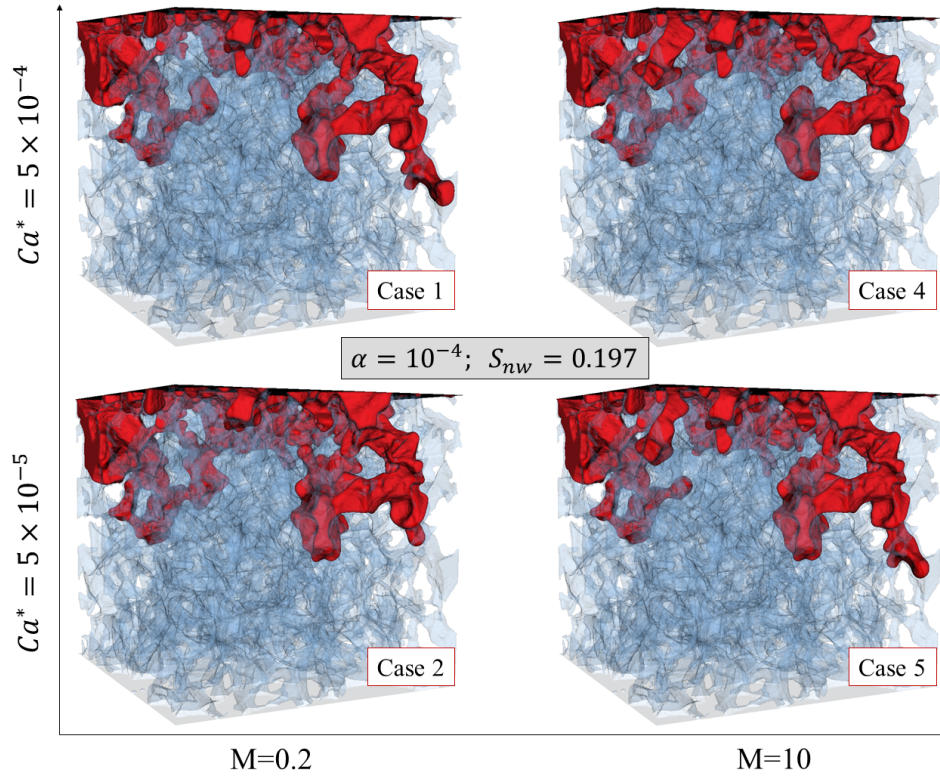
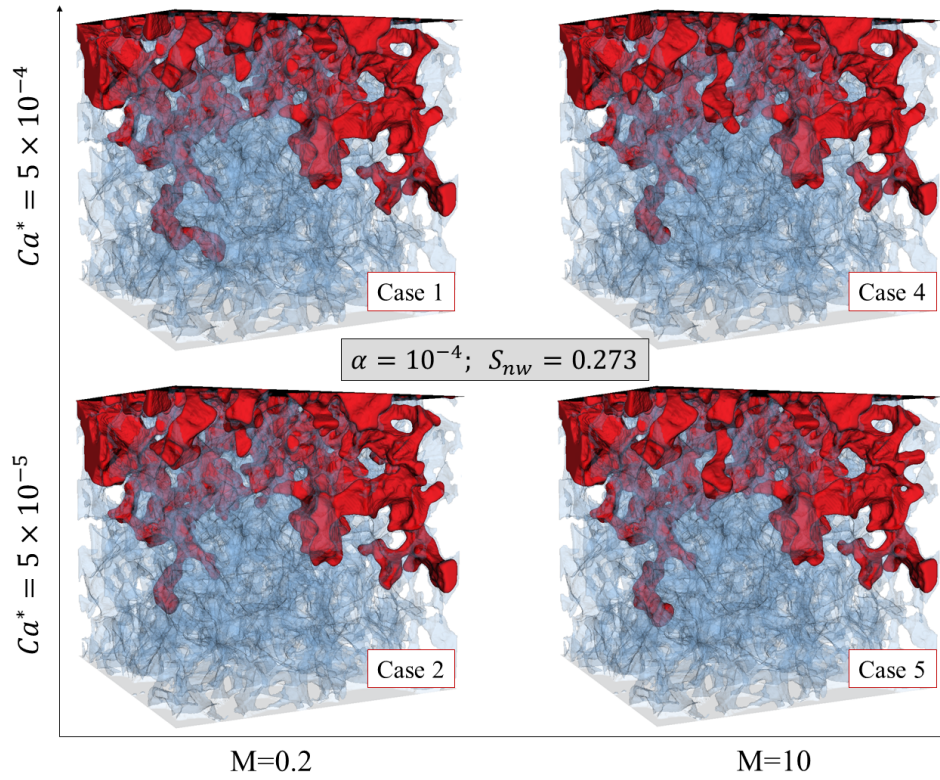


FIGURE 5.32: NW fluid distributions for $\alpha = 3.57 \times 10^{-2}$ at $S_{nw} = 0.273$.

FIGURE 5.33: NW fluid distributions for $\alpha = 10^{-4}$ at $S_{nw} = 0.026$.FIGURE 5.34: NW fluid distributions for $\alpha = 10^{-4}$ at $S_{nw} = 0.123$.

FIGURE 5.35: NW fluid distributions for $\alpha = 10^{-4}$ at $S_{nw} = 0.197$.FIGURE 5.36: NW fluid distributions for $\alpha = 10^{-4}$ at $S_{nw} = 0.273$.

Discussion

As is mentioned previously, the case 3 is the only truly equivalent case modelled by both α , characterised by the same dimensionless numbers (i.e. Ca and M) as well as the same physical surface tension and viscosity. Such condition is achieved by adjusting the LB relaxation time parameters of each α accordingly. Hence the case 3 modelled by both α is only different in terms of the temporal resolution. Comparing the P_c - S_{nw} relationship between two α in Figure 5.25, the discrepancy exists at the very beginning of the displacement, and the case of $\alpha = 10^{-4}$ presents on average higher mean curvature than the case of $\alpha = 3.57 \times 10^{-2}$. This can be explained by the accompanying 3D NW phase distributions in Figure 5.26, where it can be seen the flow path starts to deviate as early as $S_{nw} = 0.0127$, at which on the top left there is a pore that is invaded in $\alpha = 10^{-4}$ but not in $\alpha = 3.57 \times 10^{-2}$. As the draining goes on, the overall flow patterns of both α still look qualitatively similar until $S_{nw} = 0.2661$, after which one of the NW phase branch chooses different sets of pores to invade, giving different end-state configurations. Furthermore, the snap-off sites are completely different: for the snap-off 3/(5; 8)/752 in $\alpha = 3.57 \times 10^{-2}$, and the snap-off 3/(15; 16)/646 in $\alpha = 10^{-4}$, both of which only occur in one case but not in the other, we can see from the end-states of Figure 5.26 that due to the completely different flow path, throat #752 is not invaded in $\alpha = 10^{-4}$ and throat #646 is not invaded in $\alpha = 3.57 \times 10^{-2}$. Although throat #627 is invaded in both α , only in $\alpha = 10^{-4}$ there is a snap-off event 3/2/627.

Overall, considering also the discussion in section 5.3, we can see that once the medium geometry becomes complicated, despite the (relatively) low global flow field, the flow paths can be influenced significantly at different LB temporal resolutions. The lower temporal resolution brought by a larger α does not mean that it could be ‘overcome’ by saving the phase field data more frequently, since the low temporal resolution issue starts to affect the interfacial evolution right at the initial transient part of the simulation. More future work is needed to systematically explore the influence of the different temporal resolution with a larger domain size and different medium types.

Although the use of different α will affect the flow patterns and even the accuracy, the dynamics of the Haines jumps are still well captured by both α . For example, Figure 5.27 shows a good correspondence between the capillary pressure drop and the Haines jump for $\alpha = 3.57 \times 10^{-2}$. Not all of the Haines jumps lead to snap-off events; here in this case only the Haines jump (e) gives rise to a snap-off 3/(5; 8)/752 (see also Figure 5.25); however all Haines jumps share the similar P_c increase-decrease process: P_c first increases as the NW fluid is pushed into the narrow throat, until the NW phase front passes through the throat where peak P_c is reached; the meniscus is unstable at this stage and it rapidly enters the wider pore body, where the curvature of meniscus decreases suddenly corresponding to a P_c drop.

For the case 1, 2, 4 and 5, the two α model the system with the same Ca and M , but the viscosity in $\alpha = 10^{-4}$ is around one order of magnitude larger than those in

$\alpha = 3.57 \times 10^{-2}$. Figure 5.28 shows P_c - S_{nw} curves for both α . In $\alpha = 10^{-4}$, case 1 and 2 with the same M shows much resemblance qualitatively, and so do case 4 and 5, which is also reflected in the 3D NW phase configurations in Figure 5.33 to 5.36; whereas for $\alpha = 3.57 \times 10^{-2}$, each case presents a distinctive trend in the P_c - S_{nw} relation. It is also interesting to note that, the distribution of the snap-off sites is more uniform in $\alpha = 10^{-4}$: the snap-off events occurring through the throats #836 and #909 are seen in all four cases; on the other hand, in $\alpha = 3.57 \times 10^{-2}$, only the snap-off through the throat #752 is shared by case 1 and 4 (as well as case 3). Moreover, the case 2 in $\alpha = 3.57 \times 10^{-2}$ does not show any snap-off events, which might again be linked to the flow path discrepancy caused by LB model's different initial transient behaviour due to different temporal resolutions. Overall, irrespective of resemblance of P_c - S_{nw} trend (or not) among different testing cases, the displacement patterns can vary, which is to some extent expected, due to the sensitivity of local displacement to small changes in fluid properties for an arguably homogeneous porous medium. The P_c - S_{nw} curve alone is of course insufficient to characterise the flow behaviour, and it is currently under extensive research to include more measures to better characterise the fluid topology and the pore-scale flow (Herring et al., 2013; Schlüter et al., 2016; McClure et al., 2018; Armstrong et al., 2018).

5.4.3 Preliminary Study: Haines Jump Velocity

In this sub-section, we study the interfacial velocity of the Haines jumps that lead to snap-off as reported in Tables 5.1 and 5.2. To author's knowledge, there is only few work on investigating the detailed dynamics in 3D natural rocks using LB modelling, e.g. (Zacharoudiou, Boek, and Crawshaw, 2018), and none for the detailed evaluation of the Haines jump velocity profiles. Nevertheless, it is important to know such velocity since it can serve as a validation of the LB model (e.g. given the fast dynamic μ CT imaging techniques, the experimental fluid velocity field is possibly back-calculated and can be compared against the LB results), and also allows exploration of the influence of geometry on snap-off. The current interfacial velocity results are still preliminary, which are measured by two methods that will be introduced as followings. Future work is needed to give more in-depth discussion and more comprehensive conclusions.

Most straightforwardly, we could simply rely on the saved velocity data as an estimation of the Haines jump velocity (though it needs some extra calculation to get from phase velocity to interfacial velocity), which can be called a direct method. However, due to the complex medium geometry and fluid-fluid interface distributions, the spurious currents significantly disrupts the velocity near both fluid-fluid and fluid-solid interfaces. Figure 5.37 shows examples of the saved 2D-sliced velocity fields of both α at the end state of case 3, whose full NW fluid distributions can be found in Figure 5.23 and Figure 5.24 for $\alpha = 3.57 \times 10^{-2}$ and 10^{-4} , respectively. Noting that the fluid properties and the reservoir conditions in case 3 are exactly same for two α , the physical magnitude of the spurious current, concentrated at the inlet (i.e. the

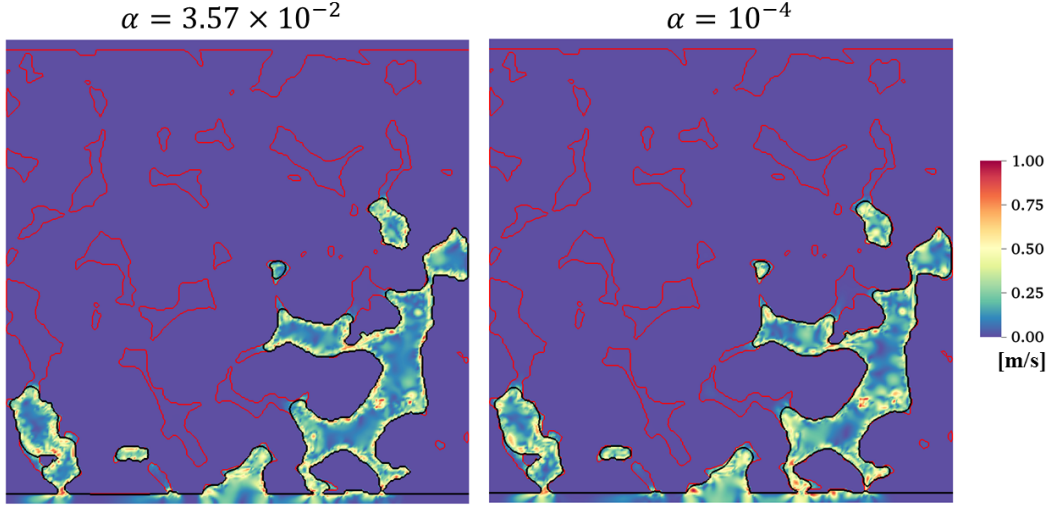


FIGURE 5.37: 2D sliced velocity field in physical units for case 3 of $\alpha = \{3.57 \times 10^{-2}, 10^{-4}\}$, where spurious velocity can be seen concentrated at the entrance, the NW-W phase interface as well as the NW-solid interface. The 2D slice in x - z plane is extracted from $y = 220$ l.u., of the end states (where the most advanced phase front reaches the W phase reservoir). The red line highlights the pore space-solid boundary, and the black line indicates the boundary of NW phase.

bottom of the figures), the NW-solid interface as well as the NW-W phase interface, are the same as well, despite the fact that LB spurious current scales with different α . Given the disruption of interfacial spurious currents, at this stage it is very challenging to use the existing velocity field to calculate the Haines jump velocity. Therefore, an indirect method is needed to measure the interfacial movement. In this work, the local interface velocity is measured by rearranging the level-set equation (Osher and Sethian, 1988; McClure et al., 2016):

$$\partial_t \phi + \zeta |\nabla \phi| = 0, \quad (5.7)$$

where ϕ is the phase field, and ζ is the interface velocity in the direction normal to the interface. The temporal gradient of the phase field is evaluated by the central difference approximation:

$$\partial_t \phi \approx \frac{\phi(t + \delta t) - \phi(t - \delta t)}{2\delta t}, \quad (5.8)$$

where δt is 1000 and 10,000 LB time steps for α of 3.57×10^{-2} and 10^{-4} , respectively, which is the frequency of which the phase field data is saved. The spatial gradient of the phase field is also calculated based on the central difference algorithm using Python-Numpy library (Oliphant, 2015). For this method to work most effectively, the region of the pore-filling event (and the following snap-off event) is manually selected and isolated from the rest of simulation domain¹⁵. The isolated region is cropped to

¹⁵The isolated local regions for all of snap-off events are illustrated in Appendix H, where the detailed processes of snap-off events are shown for the case of $\alpha = 3.57 \times 10^{-2}$.

an ‘irreducible minimum’ such that over the consecutive time steps (i.e. δt) the most interfacial movement primarily happens around the phase front of interest.

Given the finite-difference nature of this indirect method as shown in equation 5.8, the essential prerequisite for this method to work accurately is that the overall movement of the relevant interface should be around or less than 1 voxel per δt ¹⁶, otherwise this method tends to underestimate the actual interface movement. This condition is satisfied by the cases 1, 2, 4, and 5 of $\alpha = 10^{-4}$ because of the relatively higher LB temporal resolution and the use of more viscous fluids. For the case 3 of $\alpha = 10^{-4}$, where much less viscous fluids are used, and for all cases of $\alpha = 10^{-2}$, it is found (by simply the visual inspection) that the interface of interest usually moves more than 1 voxel per δt increment during the Haines jump, and the indirect method fails to give accurate estimation on the actual jump velocity. To overcome such difficulty, we also manually track the interfacial movement and measure the velocity. An example of the manual measurement of a Haines jump is illustrated in Figure 5.38. As shown in Figure 5.38(c) and (d), a 2D slice oriented normal to the advancing direction of the NW phase front is manually set; as the NW fluid moves, the interception of the slice with one of the orthogonal axes is recorded, which in this case is the y -axis; then the phase front advancement d can be calculated based on simple trigonometry, such as $d = \Delta y \cos \theta$ as shown in Figure 5.38(b).

In the future work, the manual selection of the local region where the Haines jump happens could be automated by monitoring the temporal change of local saturation in the partitioned μ CT image: the pore bodies of the porous medium is first partitioned by either the conventional water-shed segmentation method or the recently developed persistent homology method (Herring, Robins, and Sheppard, 2019); then the temporal evolution of the phase field in each labelled pore body can be monitored and the pore-filling rates can be calculated. This automated method is still under development during the writing of the thesis.

Figure 5.39 shows the interfacial velocity data measured by the manual method for all cases of $\alpha = 3.57 \times 10^{-2}$ and the case 3 of $\alpha = 10^{-4}$, where the colour codes are consistent with what is shown in P_c - S_{nw} curve in Figure 5.28, i.e. the same colour indicates the snap-off occurs via the same throat¹⁷. The Haines jump velocity of the snap-off event 1/(5; 49; 55)/752 is not measured, because prior to this event, the pore body #5 has been filled by the previous snap-off event 1/(5; 8)/752 (for more details see the footnote under Table 5.1). Figure 5.39(a) shows the interfacial velocities through the throat #752 for case 1, 3 and 4 of $\alpha = 3.57 \times 10^{-2}$. For case 1 and 3, given the same NW phase viscosity, the peak Haines jump velocity agrees quite well, despite the different global Ca and viscosity ratio; in case 4 where the NW phase is more viscous, the peak Haines jump velocity is smaller. Figure 5.39(b) shows

¹⁶This is because the assumption of the level-set method is that the local image difference is related to the interface movement, i.e. assuming that the phase field gradient is constant.

¹⁷ Again, note that the reason of including the results of case 3 of $\alpha = 10^{-4}$ in Figure 5.39, is not only that it models the same physical surface tension as in $\alpha = 3.57 \times 10^{-2}$, but also because the physical viscosity of case 3 of $\alpha = 10^{-4}$ is around the same order of magnitude as the cases of $\alpha = 3.57 \times 10^{-2}$. Thus the comparison is on an equal footing.

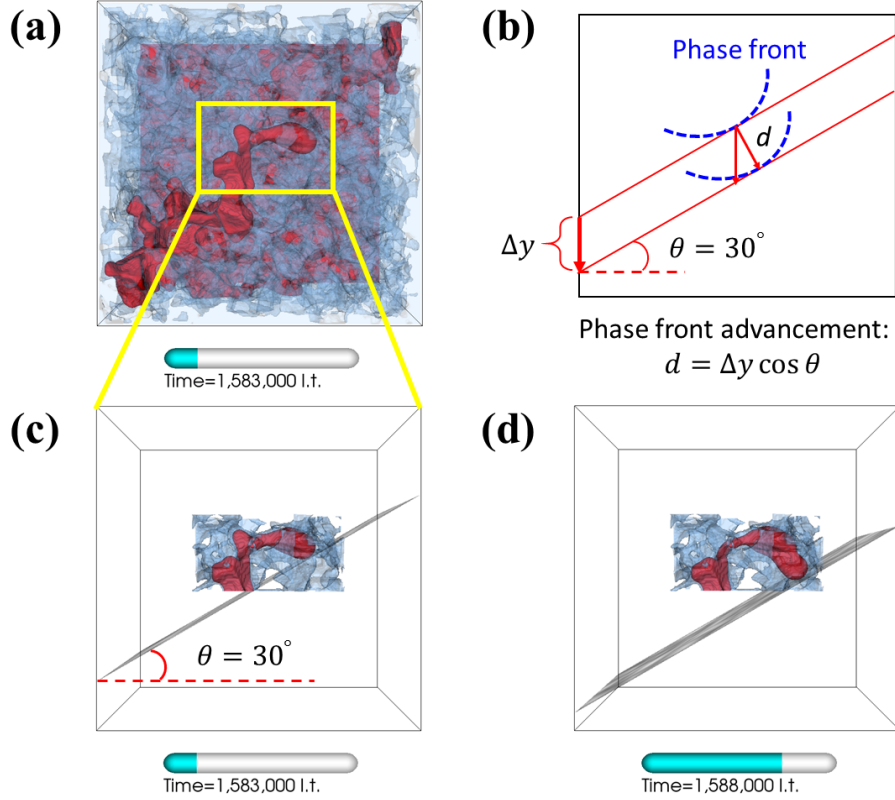


FIGURE 5.38: Illustration of manual measurement of local interfacial velocity for the Haines jump followed by the snap-off event 5/(15; 16)/646 occurring at 1408 ms (i.e. LB time of 1,589,000 *l.t.*) in $\alpha = 3.57 \times 10^{-2}$ (see Table 5.1). (a) The overall NW fluid distribution (in red) at LB time step of 1,583,000 *l.t.* prior to snap-off. The rock matrix is in light grey and W fluid is not shown. (c) and (d) show the beginning and the (almost) end of the Haines jump, respectively. A 2D plane which is in the normal direction to the phase front advancement is used for the manual measurement. (b) illustrates the simple geometry of how the manual measurement is performed and how the phase advancement d can be calculated based on simple trigonometry.

the interfacial velocity for two consecutive Haines jumps in case 5 of $\alpha = 3.57 \times 10^{-2}$ via the same throat #646¹⁸, and a Haines jump from the case 3 of $\alpha = 10^{-4}$. Because the NW fluid viscosity in the case 3 of $\alpha = 10^{-4}$ ($\mu_n = 0.922$ mPa-s) is much smaller than that in the case 5 of $\alpha = 3.57 \times 10^{-2}$ ($\mu_n = 4.610$ mPa-s), the peak Haines jump velocity is higher correspondingly. Figure 5.39(c) shows un-grouped Haines jumps through the throats #832 and #627, and for the latter one, the result of case 3 of $\alpha = 10^{-4}$ is also presented. For the two Haines jumps via throat #627, again due to the lower viscosity in $\alpha = 10^{-4}$ ($\mu_n = 0.922$ mPa-s), the peak Haines jump velocity is greater than the counterpart of $\alpha = 3.57 \times 10^{-2}$ ($\mu_n = 4.610$ mPa-s). For the Haines jump via throat #832, a distinctive feature is that there are two peaks during the event. If checking the detailed process of the jump in Figure H.5 in Appendix H, it

¹⁸More specifically, for the two Haines jumps of case 5, the circles correspond to the Haines jump happens from LB time 1,567,000 *l.t.* to 1,573,000 *l.t.* (i.e. the physical time from 1,388 ms to 1,393 ms), and the squares correspond to the Haines jump happens between LB time of 1,583,000 *l.t.* and 1,588,000 *l.t.* (i.e. the physical time from 1,402 ms to 1,407 ms).

suggests that these two peaks are real and well captured by the manual measurement. Lastly, Figure 5.39(d) shows all of the data for a direct comparison. The peak Haines jump velocity in this work is also (qualitatively) compared to the experimental data in 2D micromodel by Armstrong and Berg (2013), and the order of magnitude of the Haines jump velocity data agrees well with the published work.

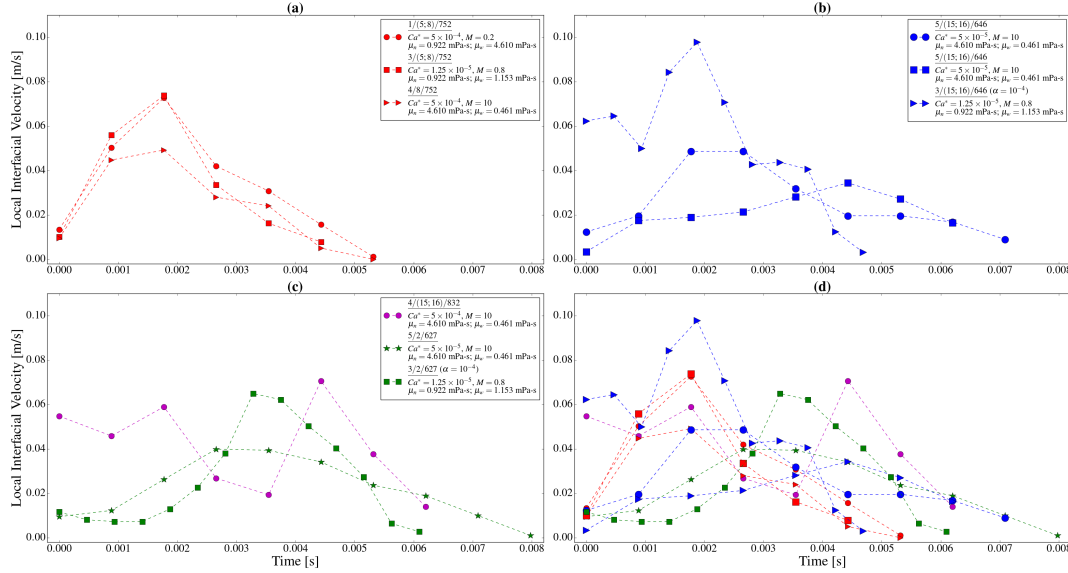


FIGURE 5.39: Local interfacial velocity of Haines jumps followed by the snap-off events in $\alpha = 10^{-2}$. The data is presented according to the labels of pore bodies and invading throats, which can be identified by the snap-off identifiers (see Table 5.1). Grouped data with same filling pore bodies and same invading throats is shown in (a) and (b). Un-grouped data with different pore bodies and throats is shown in (c). For direct visual comparison, all data are plotted together in (d). The estimated error in the manual measurement is 0.1 voxel per 1000 LB steps, which is equivalent to 5.6×10^{-4} m/s.

Overall, all results in Figure 5.39 are quite straightforward: the viscosity of the invading phase (i.e. the NW phase) plays a predominant role in determining the peak Haines velocity, and less viscous the invading phase is, the higher the peak Haines jump velocity could be. However, at this stage, without more data on numerous other Haines jumps that do not give rise to snap-off, it is hard to tell whether or not the presented interfacial velocity data is statistically distinguishable or in fact falls into the same class, and of course future work is needed to include as much local interfacial velocity data as possible, before any in-depth and comprehensive conclusion can be drawn.

Moreover, as a direct comparison, Figure 5.40 shows the full evolution of the 2D sliced velocity field for the Haines jump 3/(5; 8)/752 against the indirectly measured velocity profiles (shown in Figure 5.39(a)). The most prominent feature is that the peak velocity field in the throat indeed dominates the flow field during the jump, and has a reasonable correspondence to the indirectly measured interface velocity profile; but the magnitude of such peak velocity field is much greater than the (indirectly

measured) peak Haines jump velocity. The supplementary vector presentation of the velocity field again shows highly irregular pointing directions near interfaces. The fact that spurious currents dominate the flow field in dynamic simulations is generally overlooked by literature, and here it is important for us to point this out. To author's best knowledge, there are so far no effective means of reducing spurious currents during dynamic processes for any of the multicomponent LB models, and future work is definitely needed to resolve this problem.

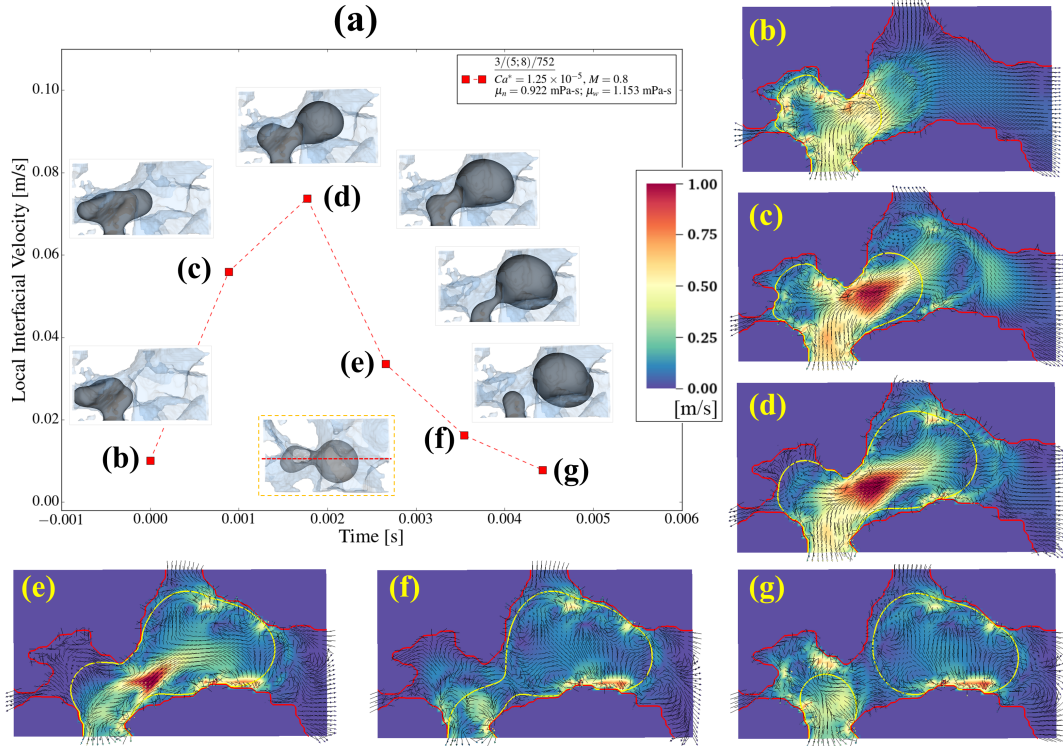


FIGURE 5.40: Direct comparison between indirectly measured interfacial velocity and the LB velocity field for the Haines jump 3/(5; 8)/752 of case 3 of $\alpha = 3.57 \times 10^{-3}$. (a) the Haines jump velocity profile same as the one in Figure 5.39(a), which is measured by the manual front tracking, with 3D NW fluid configurations showing the jump process and the associated snap-off. At the bottom is a top view of the NW fluid, with the red dash line highlighting the position of the extracted 2D velocity field. From (b) to (g), the 2D velocity field together with the vector presentation is shown for the Haines jump. The red line indicates the pore space-solid boundary, and the yellow line highlights the NW phase boundary.

Figure 5.41 shows the Haines jump velocity data measured by the automated level-set method for all cases of $\alpha = 10^{-4}$. Again the same colour of the plots indicates the Haines jumps via the same throat. Because of the use of more viscous fluids, it can be seen that, compared to Figure 5.39, the overall time scale is one order of magnitude longer, and the velocity is one order of magnitude smaller. Furthermore, the results shown in Figure 5.41(a) and (b) seem to some extent counter-intuitive: about the same peak Haines jump velocity is achieved for different cases, irrespective of the viscosity of the invading NW phase. To confirm that it is not the automated

level-set method giving the misleading results, we selected two Haines jump events, 1/12/836 and 4/12/836 from Figure 5.41(a) which shows about the same peak Haines jump velocity, although μ_n in case 1 is smaller than that in case 4, and performed the manual interfacial velocity measurement. The manual measurement confirms the assumption of the automated level-set method is not violated, i.e. the average interfacial movement is less than 1 voxel per δt (i.e. 10,000 LB steps), and gives very close results as the automated one does¹⁹. It suggests that the viscosity of the defending phase may also play a role in determining the peak interfacial velocity. Again, since what is presented so far is still a preliminary study, more work is needed to analyse as many Haines jumps (including the ones not giving snap-off) as possible to give more comprehensive conclusion on what fluid properties play a more bottle-neck role under what circumstances. Nonetheless, the (measurement) methods used in this work serve as the basis for the future larger-scale study and can be extended potentially to other more advanced and efficient measuring techniques.

5.4.4 Preliminary Study: Impact of Medium Geometry

In this section we present a preliminary study exploring the potential geometric causes for the snap-off events listed in Tables 5.1 and 5.2. This geometric impact is characterised by a novel method, persistent homology, which provides some insightful correlation of the pore space geometry of the medium with the snap-off sites. The investigation is still preliminary because in order to achieve any statistically meaningful conclusion, a large amount of snap-off events from much larger domains are needed, which is the future work that not only the LB simulations, but also the experimental snap-off data extracted from various reservoir rock types will be examined.

To better characterise the porous media, there have been numerous methods of partitioning the pore space of the porous medium into pore bodies and throats. For example, the watershed partition is one of the commonly used methods, from which the pore body and throat size distributions and body-throat aspect ratios can be derived from the corresponding pore-network statistics (Beucher and Lantu  joul, 1979; Sheppard, Sok, and Averdunk, 2004; Thompson and Reed, 2005). Recently, persistent homology provides an alternative approach to correlate the length scale of the features of porous media to the topological features (Robins, 1999; Edelsbrunner, Letscher, and Zomorodian, 2002; Delgado-Friedrichs, Robins, and Sheppard, 2015). For details of how persistent homology is applied to the pore-space topological characterisation, readers are referred to Robins et al. (2015) and Herring, Robins, and Sheppard (2019), and here only the necessary details of the method are introduced.

The persistent homology approach of characterising the pore space of media is closely related to a topological quantity, Euler characteristic, which is defined as the alternating sum of the first three Betti numbers (β): $\chi = \beta_0 - \beta_1 + \beta_2$, where β_0 is the number of individual objects present in the volume, β_1 is the number of redundant

¹⁹The manual and level-set measurements agree both in the peak Haines jump velocity and the trend of the velocity profile, i.e. at which time step the peak velocity is reached.

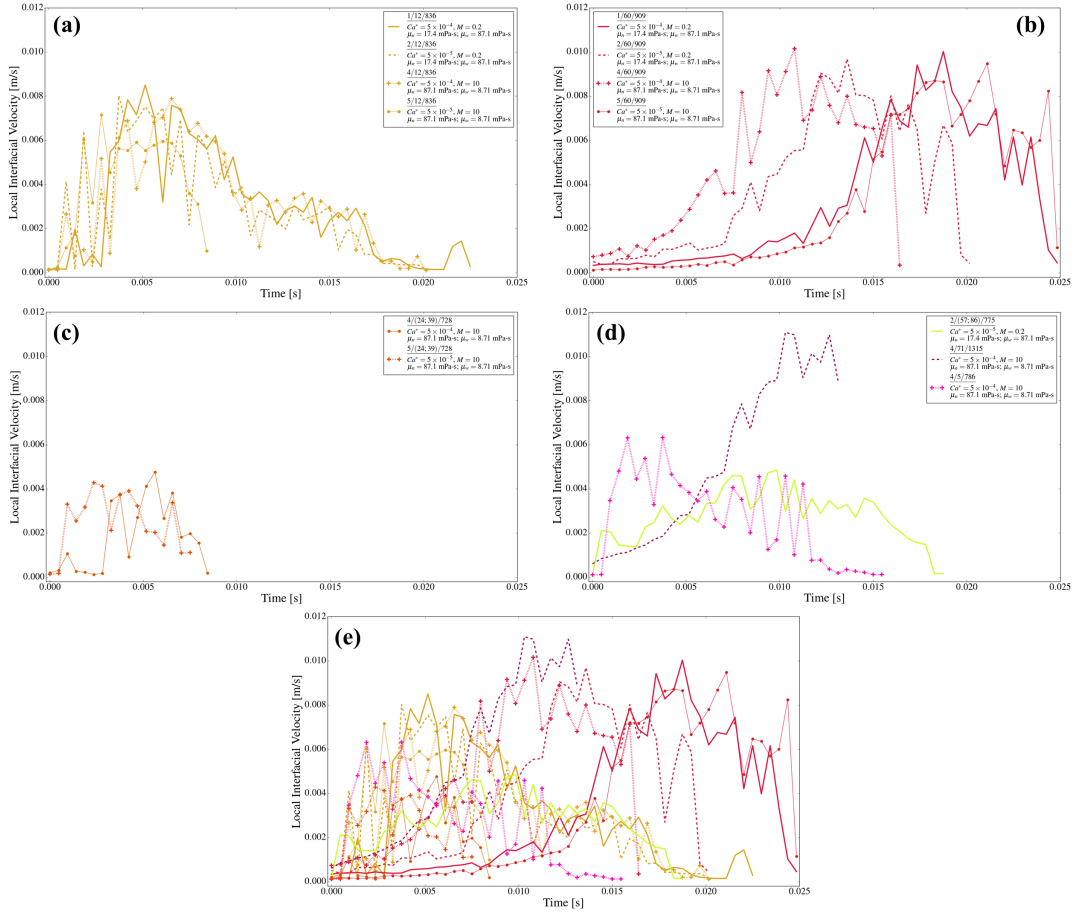


FIGURE 5.41: Local interfacial velocity of Haines jumps followed by snap-off events for $\alpha = 10^{-4}$. The data is presented according to the labels of pore bodies and invading throats, which can be identified by the snap-off identifiers (see Table 5.1). Grouped data with same filling pore bodies and same invading throats is shown in (a), (b) and (c). Un-grouped data with different pore bodies and throats is shown in (d). For direct visual comparison, all data are plotted together in (e).

loops within the objects, and β_2 is the number of cavities within the object (Mecke and Wagner, 1991; Vogel and Kretzschmar, 1996; Wildenschild and Sheppard, 2013; Herring et al., 2013). Here in this section, β_0 is the most relevant quantity for characterising the topology of the pore space of the medium. The persistent homology analysis is implemented as following: (Herring, Robins, and Sheppard, 2019) given a segmented two-phase μ CT image (i.e. pore phase and grain phase), a signed Euclidean distance map (SEDM) of the image is computed, where the value on each grid point represents the Euclidean distance from the point to the solid-pore space boundary, with the convention that negative distance value representing the pore space and the positive representing the grain phase. Then the changes in the topology of the level sets (i.e. the contours of the signed distance values in both phases) can be monitored, by scanning from the largest negative values (i.e. the largest pore body centres) progressively to the largest positive values (i.e. the largest grain centres). The appearance of a new topological feature is termed as ‘birth’, the disappearance of the feature is

termed as ‘death’, and the difference between the two values is the ‘persistence’ of the topological feature (Robins et al., 2015; Herring, Robins, and Sheppard, 2019). Using these three measures, namely recording the level-set threshold values when certain features are born, die, as well as their persistence, the pore space of the medium can be partitioned.

Commonly, the results of performing persistent homology analysis are presented in a so-called persistence diagram, where the counts of topological features in each Betti number are plotted as a function of birth and death level-set threshold values. In our analysis herein, only the pore phase β_0 features are of interest, which all have negative birth values since they are born in the pore space. When a pore phase β_0 feature dies, it can have either negative or positive death value: if such β_0 feature is born in connected pore bodies, its death value is also negative because it will merge with other β_0 features in the pore body; alternatively, if such β_0 feature is born in the disconnected pore bodies, it will die in the grain phase with a positive death value. In short, for connected pore bodies, the birth value characterises the maximal inscribed sphere radii (which also gives an estimation of the size of the pore bodies), whereas the death value measures the largest pore throat size, of which throat connects to the pore body. Overall, the ensemble of β_0 features that are identified in the persistent homology analysis corresponds to the partitioned pore bodies, each of which is labelled with a number, e.g. the labels in Tables 5.1 and 5.2.

One of the key advantages of using persistent homology to do the pore space partitioning, as was reported in the recent work by Herring, Robins, and Sheppard (2019), is that topological features with very low persistence (i.e. features with very similar birth and death level-set distance values) can be easily identified and thus removed²⁰, in contrast to the conventional watershed partitioning method which usually tends to over-partition the pore space if without fine tuning of the input parameters or without extra region-merging filters. The process of removing the low-persistence feature is termed ‘simplification’: an one-voxel simplification was applied in this work, which means any β_0 features with death minus birth values smaller than one voxel (i.e. 1 *l.u.*) has been removed from analysis.

Figure 5.42 shows the (*birth*, *death*) pairs for all of partitioned pore bodies of the 256^3 *l.u.*³ sub-domain, where each data point corresponds to a labelled pore body. The pore bodies in which snap-off occurs are also highlighted in bold and red colour (and some other colours for highlight) using the snap-off identifiers in Tables 5.1 and 5.2. The snap-off identifiers of $\alpha = 10^{-4}$ starts with the double-dagger. Note that to maximise the visual clarity, the identifiers of repeated snap-off in the same pore bodies within the same testing case is not shown, unless such snap-off reoccurs via a different throat. In Figure 5.42 on the left it also shows three two-dimensional slices of the partitioned porous medium along the *z*-axis.

The most pronounced feature of this persistence diagram is that snap-off occurs in all of the three most ‘persistent’ pore bodies, namely the pore body #2, #4 and #5

²⁰In this context, ‘remove’ means merging pore bodies and removing the throat between them.

for both α . These pore bodies are most persistent because their birth values are the three largest (i.e. their β_0 features were born at the very beginning), while their death values are very small (i.e. their β_0 features die only in the end). This indicates that these pore bodies have the largest (effective) sizes, but connect to other neighbouring pore bodies via narrow throats. Second, for all of the snap-off pore-bodies found in $\alpha = 3.57 \times 10^{-2}$, snap-off also happens for $\alpha = 10^{-4}$, but not vice versa: for example, there are some pore bodies, #12, #60, (#24; #39), (#57; #86), and #71 are unique to the case of $\alpha = 10^{-4}$, although these pore bodies present less prominent persistence features. Note that a major difference between the cases (i.e. case 1, 2, 4 and 5) of $\alpha = 3.57 \times 10^{-2}$ and $\alpha = 10^{-4}$ is that the viscosity in $\alpha = 10^{-4}$ is about one order of magnitude higher, though the viscosity ratios are the same between two α . At this stage, however, it is beyond the scope of this work to draw a definite correlation between the fluid properties and the potential speciality of these pores, without using larger domain sizes and more snap-off data (from both simulations and experiments).

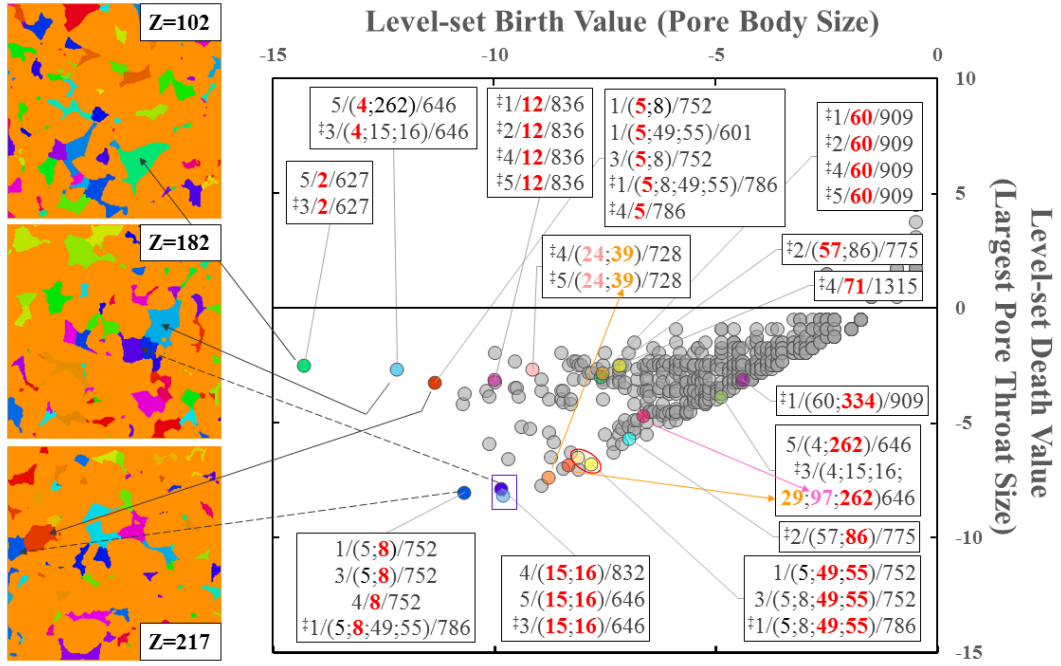


FIGURE 5.42: Persistent homology diagram of β_0 topological feature in the LB sub-domain, with partitioned two-dimensional slices of μ CT image highlighting the labelled pore bodies in which the snap-off events for $\alpha = \{3.57 \times 10^{-2}, 10^{-4}\}$ take place. Each data point in the persistence diagram corresponds to a labelled pore body. The snap-off identifiers from Tables 5.1 and 5.2 are used to highlight the relevant pore bodies in bold and red (and some other colours), with the case of $\alpha = 10^{-4}$ beginning with a double-dagger.

Among the identified pore bodies, pore body #2 is the most persistent pore body of the current sub-domain and there are two snap-off events from different cases of different α . Pore body #4 is the second most persistent pore body and there are in total four snap-off events involving this pore, two for each α , and the snap-off usually occurs not only in this single pore body, but within a group of interconnected pore

bodies, e.g. in the pore-body group (#4; #15; #16; #262) in $\alpha = 3.57 \times 10^{-2}$, or in an even larger conglomerate of (#4; #15; #16; #29; #97; #262) in $\alpha = 10^{-4}$, where the neighbour pore bodies #15 and #16 are in direct contact with pore body #4 as shown in the 2D labelled porous medium at $z = 182$ of Figure 5.42 (left column, second row). The pore-body group (#15; #16) itself also contributes several snap-off events for both α . Pore body #5 is the third most persistent pore body, which is in direct contact with pore body #8, #49 and #55 (pore bodies #49 and #55 are not shown in the 2D slice in Figure 5.42; they are located at farther end of the medium close to the W phase reservoir). There are in total 10 and 2 snap-off events, for α of 3.57×10^{-2} and 10^{-4} , respectively, involving pore bodies #5, #8, #49, and #55, which clearly indicates the important geometric signature of this pore-body group, noticing the pore body #5 being the third most persistent pore body.

Overall, based on these preliminary results, it can be seen that most of the snapped-off ganglia reside in the most highly persistent pores or their directly neighbouring pores, and it also suggests that potentially the persistent homology analysis can be an effective approach to characterise the snap-off phenomena in the multiphase flow in porous media. In the recent experiments by Herring et al. (2018) (our case 3 for both α matches the high flow-rate condition of this work), significant and prevalent snap-off of NW phase during drainage were observed in a much larger domain with more geometric heterogeneity; though the discussion of the experimental results is beyond the scope of this thesis, more future work is needed to include more simulation data (and possibly the simulations in a larger domain at lower resolution, which can also partly determine if lower resolution simulations than what were performed here are plausible) and experimental data into the persistence diagram.

5.5 Conclusions and Future Work

The two-phase fluid drainage process in a 3D Bentheimer sandstone sample were studied under various reservoir conditions. The main results are summarised as the followings, with future work being also proposed wherever relevant.

1. Based on a series of careful characterisations, from the non-unitary viscosity test, the implementation of flux boundary condition that mimics realistic experimental setup, to the examination of the impact of large interfacial spurious velocity on the fluid kinematics, it suggests that our current multicomponent Lattice-Boltzmann model is a potentially suitable candidate for investigating the key pore-scale dynamics such as the Haines jump and snap-off phenomena, at various viscosity ratios and capillary numbers. One of the advantages of performing LB simulations is it can provide a much higher temporal resolution than that can currently be extracted from experiments, so that a more detailed physical process can be resolved and more insights can be obtained, despite the large interfacial spurious velocity reported in the next item.

2. The zone of influence of the spurious velocity is confined only near the interface, and the bulk velocity field is still preserved and complies well with the Hagen-Poiseuille relation, according to our characterisations in the simple geometry such as square tube. However, in a much more complex porous medium, there can be numerous narrow throats and small pore bodies (further exacerbated by the low-resolution μ CT image), and the fluid-fluid and fluid-solid interfaces can be everywhere, the widespread spurious currents really dominate the real velocity and make the velocity field near-meaningless; for our current Haines jump velocity measurement this only has minor effect since the interfacial velocity is a separate quantity different from the bulk velocity; however, the severe spurious currents become more of a hindrance during the steady-state relative permeability calculation where the bulk velocity field is directly used. Moreover, although LB interfacial spurious velocity scales with the LB surface tension parameter α , due to the coupled LB-to-physical unit conversion relation, the corresponding physical spurious velocity does not change by different α . Therefore, future work is needed to revise the multicomponent LB model in order to truly reduce the spurious velocity.
3. Different LB surface tension parameter α , however, does give different temporal resolution, i.e. the physical time per LB iteration step, and the smaller the α , the higher the temporal resolution. Different temporal resolutions will significantly influence the initial transient behaviour of the LB simulation. For simulations in 3D heterogeneous rock, this could lead to very different displacement patterns, even if different α is set such that the equivalent physical system is modelled. A potential downside of using a smaller α is it is computationally more expensive, but such issue is gradually mitigated by the growing computer power and more efficient LB algorithms.
4. The drainage simulations are performed on a $256^3 l.u.^3$ ($\sim 1.3 \text{ mm}^3$) sub-domain of a Bentheimer sandstone sample, under various reservoir conditions (i.e. Ca from 10^{-5} to 5×10^{-4} and $M = \{0.2, 0.8, 10\}$). Examining the flow patterns from the end state of each testing case (when the NW front reaches the W phase reservoir), it suggests that capillary fingering occurs even at high Ca and high M , which, according to the commonly seen classification for 2D micromodels, is deemed as in the stable displacement regime. In fact, all of the cases in $\alpha = 3.57 \times 10^{-2}$ resemble capillary fingering pattern, and so is the case for $\alpha = 10^{-4}$, except for the case of $Ca^* = 5 \times 10^{-4}$ and $M = 0.2$, which resembles more of a viscous fingering feature. Nonetheless, since the flow-pattern classification is scale dependent, simulations in much larger domain size is needed before more definite conclusion can be reached. The use of (Ca, M) phase diagram to characterise the displacement regimes for the flow in 3D natural rocks might be insufficient, and currently extensive research has been done to explore the alternative approaches, for example, the recent work by Schlüter et al. (2016)

demonstrated the classification of the flow regime by fitting to a power law of the saturation dependent Euler characteristics.

5. During the drainage processes, constant Haines jumps have been observed for all of the cases, and some of the Haines jumps lead to (Roof-type) snap-off. The velocity profiles of these Haines jumps were measured. At this stage, due to the relatively small sample size, a clear correlation between the fluid properties and the peak Haines jump velocity is not yet achieved: for the case of $\alpha = 3.57 \times 10^{-2}$ where the average NW and W phase viscosities are on the order of $10^{-1} \sim 10^0$ mPa-s, it suggests that the invading NW phase plays a more dominant role and a less viscous NW fluid leads to higher peak Haines jump velocity, despite the various viscosity of the defending phase; for the case of $\alpha = 10^{-4}$, where the average NW and W phase viscosities are on the order of $10^1 \sim 10^2$ mPa-s, it seems that the viscosity of the W phase is also important, and the increase in NW fluid viscosity is balanced by the decrease in W phase viscosity, such that it gives the same peak Haines jump velocity as in the case of a less viscous NW phase. Future work is needed to measure more Haines jump velocity data (including non-snap-off Haines jumps) both from simulations and experiments, using potentially more advanced automated front tracking techniques or others, to achieve more comprehensive conclusions.
6. All of the snap-off events are characterised by the invading throats and the pore bodies where the ganglia reside, each of which is assigned with a throat label and single/groups of pore body labels. These labels are obtained by partitioning the pore space using a novel geometry-topology analysis via persistent homology. More specifically, each labelled pore body is assigned with a ‘birth’ and ‘death’ values to indicate its topological signature, i.e. the so-called ‘persistence’ (see more in section 5.4.4). We find that most of the snapped-off ganglia reside in the most highly ‘persistent’ pores or their directly neighbouring pores. At this stage, we were unable to make a more quantitative statement due to the small sample size. Future work is needed to include more snap-off data either from simulations (using a larger domain) or experiments so that more insightful information can be extracted from the topological persistence analysis.

Chapter 6

Conclusion and Future Work

The research presented here was focused on improving our understanding of multiphase lattice-Boltzmann modelling in practical applications. Based on the development of a numerically stable and convenient flux boundary condition that is capable of replicating the experimental condition more realistically, we calculated the drainage displacement patterns under various reservoir conditions to explore the consequence of using different sets of key LB parameters to model the same physical system and associated issue of different LB temporal resolutions, as well as the influence of large spurious velocity on the interface movement. These studies are of critical importance as they enable us to better evaluate whether the pore-scale LB modelling is a robust technique giving reliable results. Given the higher temporal resolution by LB method than that can be currently obtained from experiments, we also had a ‘zoomed-in’ investigation of the Haines jumps and snap-off, measured the Haines jump velocity, and characterised the geometric feature of the porous medium where the snap-off frequently happens. Moreover, from a pragmatic perspective, we explored the behaviour of multiphase LB models at low-resolution limit, since in practice, the 3D μ CT images of natural rocks (used as the LB simulation domain) rarely have both sufficient resolution and good field of view; the low-resolution behaviour of LB models has been qualitatively grouped into several types, and was carefully characterised to evaluate the potential consequence on the larger-scale porous media applications. Additionally, throughout our study, it was found that two major unresolved issues in the current LB models are the large interfacial spurious velocity and the non-physical attraction of dissolved NW phase on the solid surface. These two issues are not limited to low resolution cases, but they are not completely resolution independent, either. Although the two issues have been identified separately by some reported works, this thesis brings them together with other potential problems, and identifies them as being the most serious. The main results of each chapter are as follows:

Chapter 2 gave an introduction of the theoretical framework of lattice-Boltzmann methods. I first reviewed briefly the different levels of description of motion in the classical context of transport phenomena, and where the continuum Boltzmann transport equation, the predecessor of lattice-Boltzmann equation, fits in the hierarchy. I then discussed the derivation of the LB equation from the continuum Boltzmann equation based on the Gaussian-Hermite quadrature, and also incorporated a systematic

analysis of the unit conversion between physical and LB systems. The algorithmic implementation of two commonly used single-relaxation-time based multicomponent LB models, Shan-Chen and Rothman-Keller models, were introduced, which were used later in the low-resolution study in Chapter 3. I also discussed the multiple-relaxation-time based colour-gradient model, with a detailed Chapman-Enskog analysis recovering the macroscopic Navier-Stokes equation for momentum transport and continuity equation for mass transport. The Chapman-Enskog analysis also revealed some limitations of the current MRT model: (a) the pressure variation is currently coupled with the phase density, which may limit the use of the model on non-unitary density ratio applications; (b) the error terms in the recovered mass transport equation still needs rigorous examination to quantify its potential influence.

In Chapter 3 I explored the discretisation limits of two commonly used SRT-LB models, Shan-Chen (SC) and Rothman-Keller (RK) models, by pushing the fluid-fluid interfacial radius of curvature and the feature size of the simulation domain down to the discrete unit size of the computation grid. More specifically, I performed a series of small-scale artificial-geometry tests, with and without solid boundary, and qualitatively characterised the models' breakdown behaviour into three subgroup as listed in Table 3.1. Overall, both SRT-SC and SRT-RK models show reasonable accuracy in the Young-Laplace relation, with the interfacial mean curvature being pushed as big as $\sim 1.0 \text{ l.u.}^{-1}$. This indicates that both models are capable of simulating dynamic process such as drainage in an effective throat radius down to $\sim 2.0 \text{ l.u.}$. On the other hand, the simple-geometry tests did reveal several limitations of both models. For SC model, the most severe problem is its inherent miscibility, which not only violates the Kelvin solubility relation in most cases, but also causes numerical instability especially in narrow tubes; in contrast, the RK model promotes better phase separation and is generally more stable. Nevertheless, the wetting boundary condition in RK model causes non-physical attraction of the dissolved NW phase near the solid surface, and in some circumstance, the accumulated dissolved NW phase layer can lead to non-physical transport. Based on the characterisations, it indicates that RK model is more suitable for the practical applications with better immiscibility and numerical stability, and larger flexibility of matching various fluid properties. At the end of the chapter, RK model is thus used to perform drainage tests in a Bentheimer sandstone μ CT image, whose results largely confirm the observations of previous simple-geometry tests, with discrepancies in pressures in the porous medium consistent with the predictions from special geometries. The low-resolution behaviours of the two models were categorised into different breakdown types, and the detailed conclusion for each individual test can be found in section 3.7.

The dissolved NW phase problem found in the simple-geometry tests in Chapter 3 turns out to be a serious consideration for real porous medium simulations. Therefore, Chapter 4 is dedicated to study the cause of such non-physical attraction, the associated consequences as well as the proposed improved wettability models. For SC model, the non-physical behaviour of dissolved NW phase in the bulk W phase is

due to the imbalance between fluid-fluid cohesion force and fluid-solid adhesion force; and in RK model, the attraction is caused by the non-zero phase field gradient between bulk W fluid and the solid surface. In practical porous medium applications, the transport of non-physically accumulated thin NW phase layer eventually generates numerous ‘fake’ NW phase ganglia, which is apparently different from the known physical processes such as snap-off during Haines jump. Researchers have been well aware of such non-physical behaviour and have proposed several improved wettability models. Generally speaking, there are two major methods, i.e. the energy-based approach and the geometry-based approach, with the current problematic model falling into the former category. One of the state-of-the-art geometric methods is introduced in this chapter. Typically the energy-based method is algorithmically simpler, which is why it has been widely used, but it gives rise to the non-physical attraction. On the contrary, the geometric method can satisfy the prescribed contact angle with sufficient image resolution (and its low-resolution behaviour is yet to be validated), at the cost of complicated algorithm with extra computations of various surface normal vectors. Therefore, in the end, an alternative energy-based model with much simpler algorithm is also proposed; however, the new wetting model has not been validated through tests, and future work is needed to implement the model and characterise its behaviour.

In Chapter 5, the influence of spurious velocity on the interfacial movement was examined, after which a series of primary drainage simulations in a Bentheimer sandstone μ CT image under a range of viscosity ratios and capillary numbers were performed, with the focus of improving our understanding on the dynamics of Haines jumps and associated snap-off. It was found in the simple square tube characterisations that the zone of influence of the spurious velocity is confined only near the interface, and the bulk velocity field is preserved and complies well with the Hagen-Poiseuille relation. However, in real porous media, where there can be numerous narrow throats and small pore bodies, the widespread interfacial spurious currents dominate the velocity field; hence the Haines jump velocity must be measured indirectly either through the manual front tracking or the level-set method. A key point during the investigation is that, although LB spurious velocity scales with the LB surface tension, due to the coupled LB-to-physical unit conversion constraint, the physical spurious velocity does not change by different LB surface tension. What LB surface tension changes is the time conversion factor, i.e. the temporal resolution in the unit of physical time per LB iteration step. Different temporal resolutions significantly affect the initial transient behaviour of the simulation, which in complex 3D natural rocks, can lead to different displacement patterns, even if the same physical system is being modelled by different LB temporal resolutions.

After the characterisation of interfacial spurious currents, the drainage simulations were performed on a 256^3 l.u.³ (~ 1.3 mm³) sub-domain of a Bentheimer sandstone sample, with capillary number Ca ranging from 10^{-5} to 5×10^{-4} , and viscosity ratio $M = \{0.2, 0.8, 10\}$; the strongly wetting boundary condition ($\phi_s = -1.0$) is used to

avoid the potential non-physical attraction of dissolved NW phase and the generation of ‘fake’ NW bubbles; also, two sets of LB temporal resolutions were used for all Ca and M , which in total gave ten testing cases. Examining the flow patterns of the end state for each case suggests that capillary fingering occurs even at high Ca and high M , which, according to the classification for 2D micromodels, is deemed as in the stable displacement regime. Nevertheless, the flow-pattern classification is generally scale dependent, thus simulations in much larger domain size is needed before more definite conclusion can be reached. During drainage for all cases, Haines jumps have been constantly observed, some of which lead to (Roof-type) snap-off. The velocity profiles of these Haines jumps were measured indirectly by front tracking and level-set method. At this stage, due to the small sample size, a clear correlation between the fluid properties and the peak Haines jump velocity is not yet achieved: for the case of lower LB temporal resolution, where the average NW and W phase viscosities are on the order of $10^{-1} \sim 10^0$ mPa-s, it suggests that the invading NW phase plays a more dominant role and a less viscous NW fluid leads to higher peak Haines jump velocity, despite the various viscosity of the defending phase; for the case of higher LB temporal resolution, where the average NW and W phase viscosities are on the order of $10^1 \sim 10^2$ mPa-s, it appears that the viscosity of the W phase is also important, and the increase in NW fluid viscosity is balanced by the decrease in W phase viscosity, such that it gives the same peak Haines jump velocity as in the case of a less viscous NW phase. Furthermore, the location of all snap-off events were characterised by a novel geometry-topology analysis via persistent homology, which partitions the pore space of the medium into regions with numbered labels: each invading throat and the pore bodies where the ganglia reside were assigned with a throat label and single/groups of pore body labels. The labelled pore body is further assigned with a ‘birth’ and ‘death’ values to indicate its topological signature, i.e. the so-called ‘persistence’. The key finding was that most of the snapped-off ganglia reside in the most highly ‘persistent’ pores or their directly neighbouring pores, but due to the small sample size, it still needs more work to make a more quantitative statement.

Overall, the multiple-relaxation-time colour-gradient based LB model (introduced in section 2.4 and exclusively investigated in Chapter 5) is potentially a good candidate for the pore-scale simulation. However, there are still several issues in the current LB model that may limit its applicability and robustness, and the following future work is needed to address those issues:

1. Further investigation of the influence of the high-velocity spurious currents on the pore-scale displacement pattern and Haines jump dynamics through narrow throat is needed.
2. Immediately following the item above, future work of developing improved multicomponent LB models with reduced spurious current is also highly desirable. For another popular multicomponent LB model, the free-energy model, there are several published works reporting largely reduced spurious current or even

elimination to machine precision when the system reaches equilibrium (Connington and Lee, 2012). However, in terms of the dynamic behaviour, to the author's knowledge, there has not been any comprehensive study for the free-energy models. Therefore, more work is needed to explore the influence of the spurious current during the transient part of simulation and in dynamic simulations in general. For new users of LB methods, the free-energy model seems to be a good starting point, given its good behaviour (i.e. low spurious currents) in static simulations; but users should also be aware that free-energy model's dynamic behaviour is still subject to further examination.

3. Improved wettability model which can achieve the prescribed contact angle and more importantly eliminate the non-physical attraction of dissolved phase is another future direction. Recently there have been several reports on the geometric-based methods which claim that non-physical behaviour has been fixed when the domain resolution is sufficient; however there still lacks study on the low-resolution behaviour of such proposed models, since small geometry features and limited resolution are constantly encountered in practical applications. More importantly, future work is also needed to develop newer energy-based wettability model, since this model can be implemented more easily in terms of its algorithm.
4. For the current MRT-RK multicomponent model, more theoretical work is needed to decouple the pressure variation and the phase density (see more in section 2.4.1), so that the model can work more appropriately under non-unitary density ratios. In addition, the error term in the recovered macroscopic mass transport equation (see more in section 2.4.2) also needs further examination to evaluate its influence on the simulated fluid dynamics.

In terms of the study of the pore-scale displacement, there also needs some future work to advance our understanding, which includes as follows:

1. More Haines jump velocity profiles, including the non-snap-off Haines jumps, need to be measured so that more statistically meaningful, comprehensive correlation among fluid properties, reservoir conditions and peak Haines jump velocity can be concluded. This also requires the development (or find the existent ones) of more advanced phase front tracking techniques, instead of using the 'home-made' approaches implemented in this thesis.
2. In order to draw more insights of the connections between the geometric signatures of porous media and the snap-off frequency, more snap-off data, both from experiments and simulations (ideally performed in a larger domain size) is needed.
3. One of the big challenges in carbon dioxide sequestration is how the experiment can be managed to trap large NW clusters via non-Roof type snap-off. The

LB simulations can be a good candidate to address this issue from a theoretical perspective and can be used to guide the experiments.

Appendix A

Methods of Measuring Interfacial Curvature

Once the simulation data is generated, one of the key properties to be measured is the mean curvature of the interface, since if the simulation satisfies the Laplace's law, the capillary pressure between non-wetting (NW) and wetting (W) phases will be proportional to the mean curvature. In this work, we implemented two different approaches, the surface fitting and level-set methods, to measure the mean curvature, since measuring curvature is difficult for small radii.

A.1 Surface Fitting Method

The surface fitting method proceeds by thresholding the input fluid density function to localise the isosurface, which defines the fluid-fluid interface on the voxel grid. The input fluid density function is defined as:

$$\Phi(\mathbf{x}) = \frac{\rho_{\text{nw}}(\mathbf{x}) - \rho_{\text{w}}(\mathbf{x})}{\rho_{\text{nw}}(\mathbf{x}) + \rho_{\text{w}}(\mathbf{x})}, \quad (\text{A.1})$$

where $\rho_{\text{nw}}(\mathbf{x})$ and $\rho_{\text{w}}(\mathbf{x})$ are NW phase and W phase densities when the system reaches the equilibrium state. In fact, the definition of this input function is consistent with the phase field introduced in the RK model. In the neighbourhood of voxels on this isosurface, point clouds of sets of points are constructed by linear interpolation (seed points near the outer edges of the isosurface are disregarded). Then, a biquadratic surface is fitted to each point cloud, through Monge fitting using the CGAL library (The CGAL Project, 2017). The biquadratic surface is sufficient to determine the principal radii of the curvature. The calculated mean curvature values on all of the cloud points (on the isosurface) are averaged to obtain the mean curvature and associated standard deviations. More details of the surface fitting method can be found in Herring et al. (2017).

A.2 Level-set Method:

The level-set method is widely used in fluid mechanics, computational geometry and computer vision to track the front of a moving interface, perform shape and surface smoothing, and achieve shape detection and recognition etc. The method takes an implicit interface representation, also known as the implicit function $\phi(\mathbf{x})$, as the input to calculate the curvature. For example, the implicit function for a 3D bubble with the radius of R centred at the origin of the Cartesian coordinates is simply $\phi(\mathbf{x}) = x^2 + y^2 + z^2 - R^2$, and we have $\phi(\mathbf{x}) = 0$ at the interface, $\phi(\mathbf{x}) > 0$ inside the bubble, and $\phi(\mathbf{x}) < 0$ outside the bubble, respectively. To be consistent with the surface fitting method, the phase field defined in Eq. A.1 is used as the implicit function for the level-set method, which theoretically has the properties that $\Phi(\mathbf{x}) = 0$ at the interface, $\Phi(\mathbf{x}) < 0$ inside the W fluid and $\Phi(\mathbf{x}) > 0$ inside the NW fluid.

The mean curvature calculated in the level-set method depends on the first- and second-order spatial gradients of the implicit function $\Phi(\mathbf{x})$, which is given by (Osher and Fedkiw, 2003):

$$\begin{aligned} \kappa_H(\mathbf{x}) = & (\Phi_x^2 + \Phi_y^2 + \Phi_z^2)^{\frac{3}{2}} (\Phi_x^2 \Phi_{yy} - 2\Phi_x \Phi_y \Phi_{xy} + \Phi_y^2 \Phi_{xx} \\ & + \Phi_x^2 \Phi_{zz} - 2\Phi_x \Phi_z \Phi_{xz} + \Phi_z^2 \Phi_{xx} + \Phi_y^2 \Phi_{zz} - 2\Phi_y \Phi_z \Phi_{yz} + \Phi_z^2 \Phi_{yy}), \quad (\text{A.2}) \end{aligned}$$

where Φ_x and Φ_{xx} are the first and second partial derivatives of $\Phi(\mathbf{x})$ with respect to x-axis, respectively, and this applies similarly in the other two dimensions. Given the finite lattice size, there is no precisely defined phase interface which gives exactly $\Phi(\mathbf{x}) = 0$, but an abrupt transfer from a positive $\Phi(\mathbf{x})$ at the inner interface (on the side of NW fluid) to a negative $\Phi(\mathbf{x})$ at the outer interface (on the side of W fluid). Therefore the mean curvature values are extract from both the inner and outer surfaces. By averaging the extracted curvature values, the final mean curvature as well as associated standard deviations (over the inner and outer surfaces) can be obtained.

Appendix B

Challenge of Low-Resolution Contact Angle Measurement

As is mentioned in the main text, the contact angle in this work is derived from the mean curvature. When the tube size is big and the resolution is not a limiting factor, it is feasible to manually measure the contact angle. For example, the contact angle can be determined by measuring the angle between the tangent to a contour line representing the fluid-fluid interface and the side-wall of the tube, such as the ones shown in Figure B.1(a) and (b), where the cross-sectional profiles of the phase field of RK model at $R_{\text{tube}} = 30.0 \text{ } l.u.$ with the model parameters $\Phi_{\text{wall}} = -0.32$ and $\Phi_{\text{wall}} = -0.84$ are shown respectively. The corresponding contour lines represent the zero phase field.

However, for small tube sizes such as $R_{\text{tube}} \leq 4.0 \text{ } l.u.$ in the main text, it is challenging to consistently identify the intersection between the fluid-fluid and the fluid-solid boundaries, from which the contact angle can be measured. For example, Figure B.1(c) and (d) show the cross-sectional phase field profiles at $R_{\text{tube}} = 4.0 \text{ } l.u.$ with the same model parameters as in (a) and (b), respectively. Based on the curvature measurement by the surface fitting method, the mean curvatures in Figure B.1(c) and (d) are $\sim 0.16 \text{ } l.u.^{-1}$ and $\sim 0.47 \text{ } l.u.^{-1}$, corresponding to contact angles of 71° and 0° , respectively. If the contact angle were measured manually, we first need to find a well-defined intersection point between the fluid-fluid interface and the part of the contour line aligned with the side-wall of the tube. It can be seen that inconsistently choosing an intersection point for different wetting condition in Figure B.1(c) and (d) can lead to the same contact angle result. Firstly fitting a circle to the major fluid-fluid interface away from the fluid-solid boundary, and using the radius of the fitted circle as the radius of the mean curvature to derive the contact angle is a more accurate way of determining the contact angle for small tubes such as in Figure B.1(c) and (d). In fact, this is exactly how the contact angle is determined in the current work: the fundamental mechanism in the surface fitting method is to fit a sphere to the phase interface to find the mean curvature.

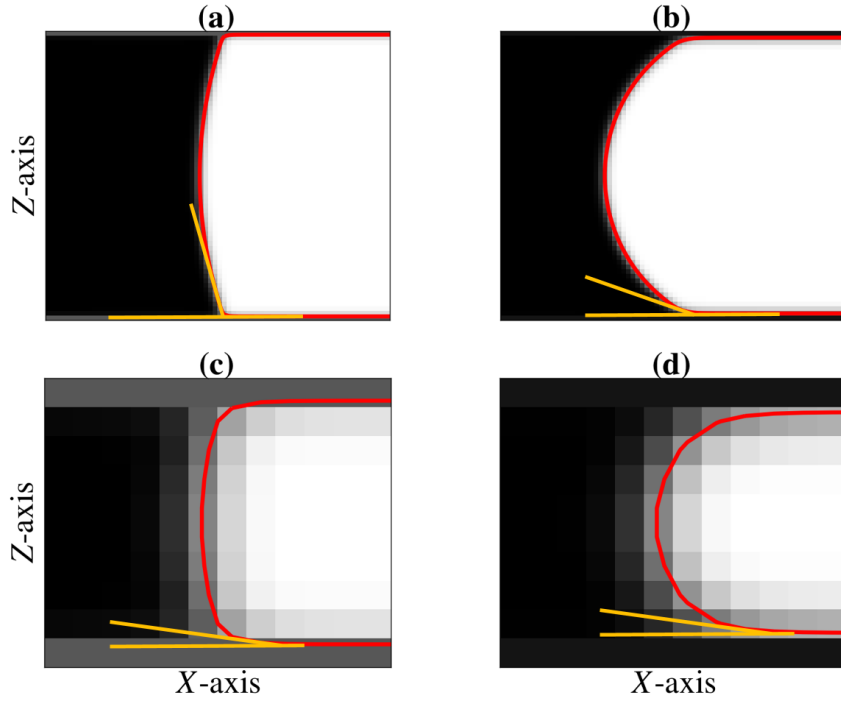


FIGURE B.1: The cross-sectional profile of the phase field of RK model at $R_{\text{tube}} = 30.0 \text{ l.u.}$, with the contour line showing the zero phase field at (a) $\Phi_{\text{wall}} = -0.32$, and (b) $\Phi_{\text{wall}} = -0.84$. Also, the cross-sectional profiles with the contour lines at $R_{\text{tube}} = 4.0 \text{ l.u.}$ are shown in (c) with $\Phi_{\text{wall}} = -0.32$, and (d) with $\Phi_{\text{wall}} = -0.84$. The simulation domain for (a) and (b) has a dimension of $(N_x, N_y, N_z) = (62, 62, 160)$, and for (c) and (d) has a dimension of $(N_x, N_y, N_z) = (10, 10, 80)$. The profile is extracted from the central plane at $y = 5$ for (a) and (b), and at $y = 31$ for (c) and (d).

Appendix C

Pressure Boundary Condition in Shan-Chen Model

In section 3.5.2, it has been introduced that for SC model, in order to maintain a relatively constant surface tension of the system during the fluid displacement process, the density components extracted from the flat tube test is used as the boundary conditions. However, for $R_{\text{tube}} = \{1.5, 2.0\}$, it is very difficult to maintain a constant surface tension, even though the boundary conditions are calibrated from the flat tube test, due to the large compressibility in the density.

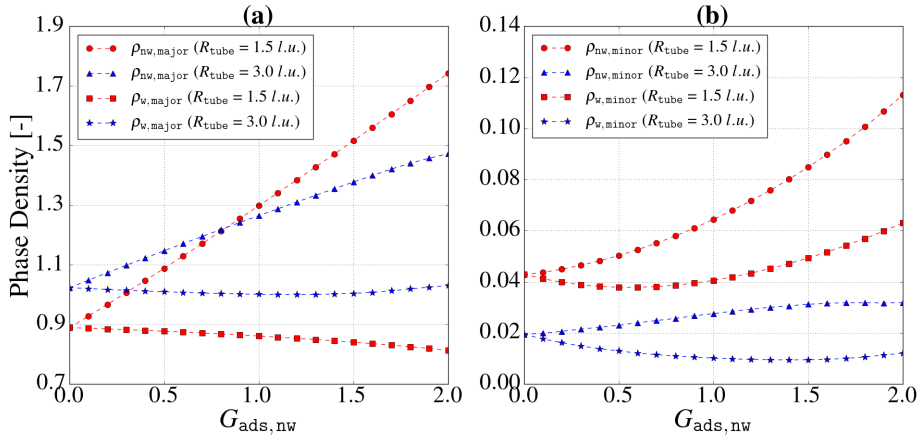


FIGURE C.1: Component densities of NW and W phase in the SC model as a function of wetting parameter $G_{\text{ads},\text{nw}}$ ($G_{\text{ads},\text{w}}$ is fixed at 0.0), extracted from the flat tube test at R_{tube} of 1.5 and 3.0 $l.u.$, respectively.

The density components against the model wetting parameter $G_{\text{ads},\text{nw}}$, extracted from the flat tube test at $R_{\text{tube}} = 1.5$ and 3.0 $l.u.$ are shown in Figure C.1. The case of $R_{\text{tube}} = 3.0 \text{ l.u.}$ is used as the boundary conditions for the primary drainage test for R_{tube} of 3.0 and 4.0 $l.u.$, and it resembles the trend shown in Schaap et al. (2007) (i.e. Figure 3.3 of the main text) until $G_{\text{ads},\text{nw}} \approx 1.5$. However, as $G_{\text{ads},\text{nw}}$ becomes larger, which corresponds to an increasing capillary pressure P_c , the (approximately) linearity correspondence between the density compressibility and P_c is gradually broken (especially for $\rho_{\text{w},\text{minor}}$), with the case of $R_{\text{tube}} = 1.5 \text{ l.u.}$ having an earlier onset. It can be seen that the trend in $\rho_{\text{w},\text{minor}}$ at $R_{\text{tube}} = 1.5 \text{ l.u.}$ is inverted after $G_{\text{ads},\text{nw}}$

$= 0.7$, indicating the actual surface tension keeps increasing for $G_{\text{ads}, \text{nw}} > 0.7$. Therefore, no matter how high the capillary pressure is set, the NW phase will not break through since the actual entry pressure keeps increasing correspondingly. Figure C.2 shows the PD curves at $R_{\text{tube}} = 1.5$ and 2.0 l.u. , where the density components at the boundaries are extracted from the flat tube test of $R_{\text{tube}} = \{1.5, 2.0\}$, respectively.

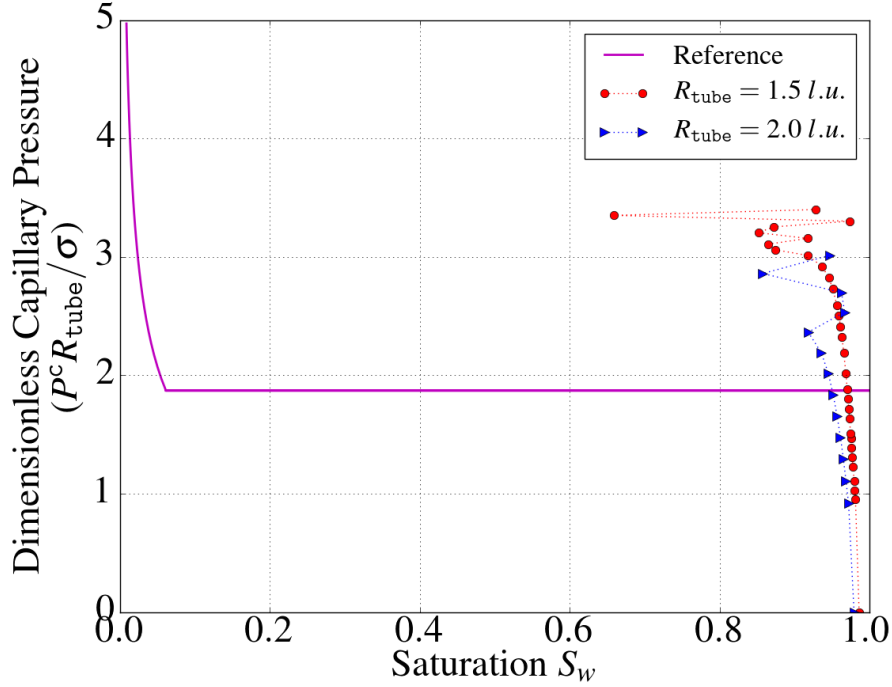


FIGURE C.2: Primary drainage curves for SC model at the tube size $R_{\text{tube}} = \{1.5, 2.0\} \text{ l.u.}$, where the boundary conditions are extracted from the flat tube test of $R_{\text{tube}} = \{1.5, 2.0\}$, respectively. P^c is the capillary pressure and σ is the surface tension. The W phase saturation S_w is calculated based on the grey-scale method (i.e. method (iv), see section 3.5.1). The entry pressure of the reference line is obtained from the flat tube test of $R_{\text{tube}} = 20.0 \text{ l.u.}$ of the SC model. The S_w beyond the entry pressure in the reference line is calculated according to equation (3.8).

Moreover, as is mentioned in the main text, the displacement will occur provided that $\rho_{\text{w}, \text{minor}}$ is fixed at a much smaller value than those extracted from the flat tube test. An example of a PD curve is shown in Figure C.3, where it shows that, although a displacement does take place, the system reaches several non-physical equilibrium states at $0.5 < S_w < 0.8$, which indicates that the surface tension is changed along the length of the tube (i.e. type II breakdown behaviour)

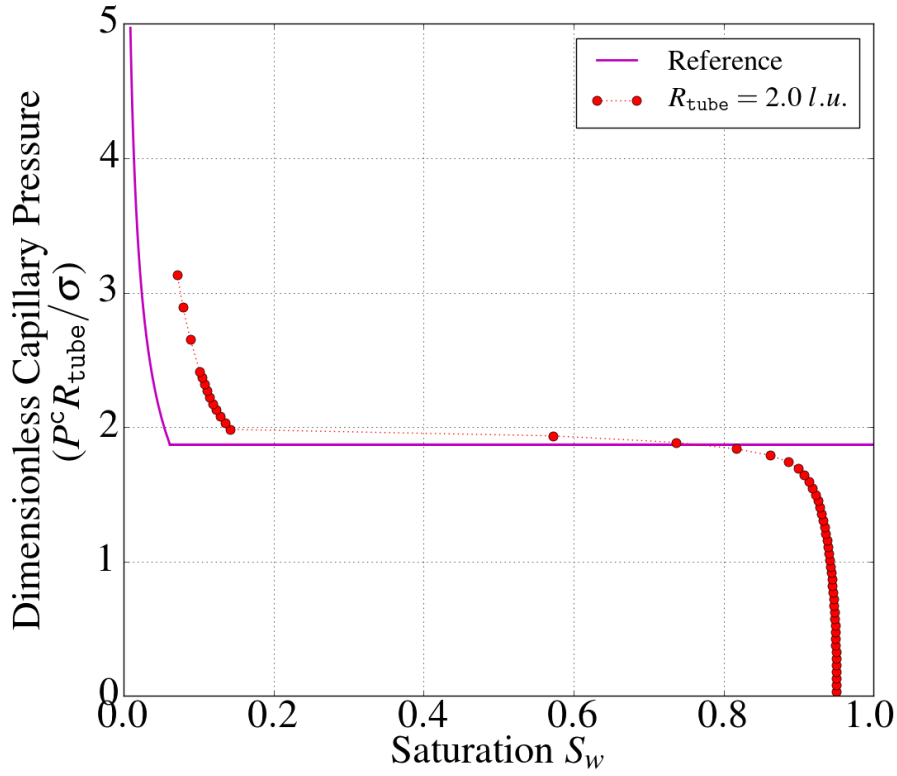


FIGURE C.3: Primary drainage curves for SC model at the tube size $R_{\text{tube}} = 2.0 \text{ l.u.}$, where the density components $\rho_{\text{nw},\text{major}}$, $\rho_{\text{nw},\text{minor}}$ and $\rho_{\text{w},\text{major}}$ at the boundaries are extracted from the flat tube test of $R_{\text{tube}} = 1.5 \text{ l.u.}$, and $\rho_{\text{w},\text{minor}}$ is fixed at 0.0005. P^c is the capillary pressure and σ is the surface tension. The W phase saturation S_w is calculated based on the grey-scale method (i.e. method (iv), see section 3.5.1). The entry pressure of the reference line is obtained from the flat tube test of $R_{\text{tube}} = 20.0 \text{ l.u.}$ of the SC models. The S_w beyond the entry pressure in the reference line is calculated according to equation (3.8).

Appendix D

Characterisation of Bentheimer Sandstone Sample

Pore and throat size analyses have been performed for a sub-domain of size 256^3 l.u.^3 from the Bentheimer sandstone samples in Herring et al. (2017). The resolution of the image is $4.95 \mu\text{m}/\text{l.u.}$, and the porosity of this sub-domain is 0.22. The dry image of the sample is processed based on the watershed partitioning and network statistical analysis; the detailed workflow is not repeated here, and readers are referred to Herring, Robins, and Sheppard (2019) for more details. In Figure D.1, the distribution of the pore and throat radii are shown in the lattice unit l.u. , and distributions are normalised by the total number of pores and throats, respectively.

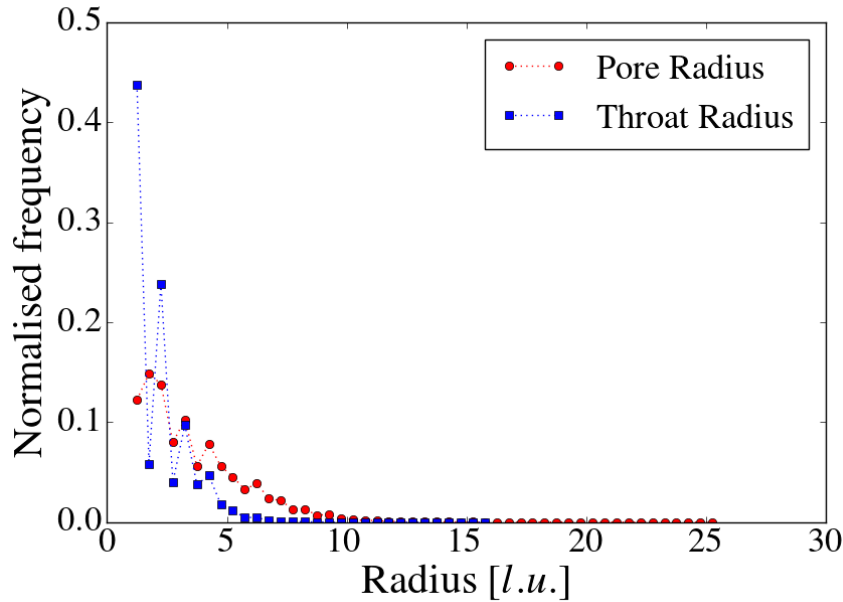


FIGURE D.1: The Pore and throat size distributions of the sub-domain of 256 l.u.^3 of the Bentheimer sandstone sample in (Herring et al., 2017).

Appendix E

Effect of Resolution on Dissolved Non-wetting Phase

It has been discussed that the generation of the non-physical non-wetting phase ganglia in the drainage simulation in the Bentheimer sandstone sample is irrelevant to the boundary condition, but is related to the contact angle. Here it shows that the non-physical phenomenon is also irrelevant to the resolution. It is already known that the ganglion comes from the transport of dissolved non-wetting phase at the solid surface, thus for nodes highlighted in the inset of Figure E.1, the dissolved non-wetting phase densities of RK model are plotted for contact angles from 0° to 90° . For all tube sizes, the density on corner nodes are generally larger than that on the normal fluid boundary nodes, since the corner boundary nodes have more solid neighbours and attract more dissolved non-wetting phase. Also, the dissolved non-wetting phase density becomes smaller as the contact angle becomes smaller. The dissolved densities on the normal fluid boundary nodes vary slightly for different tube sizes. For the corner boundary nodes, at the same contact angle, the dissolved density is larger for a larger tube size.

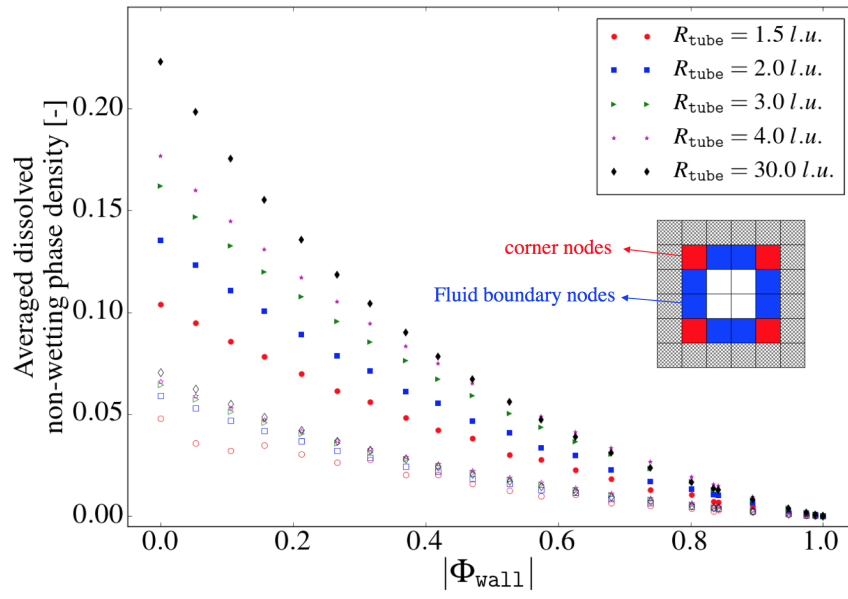


FIGURE E.1: The dissolved non-wetting phase density of RK model is plotted against the wetting boundary control parameter $|\Phi_{\text{wall}}|$ for different tube sizes. $|\Phi_{\text{wall}}|$ goes from 0.0 to 1.0, corresponding to the contact angle from 90° to 0° . The inset of a cross-section of the square tube illustrates the corner fluid nodes (in red) and the normal fluid boundary nodes (in blue). All solid symbols indicate the dissolved density on the corner nodes, and blank symbols indicate the dissolved density on the fluid boundary nodes.

Appendix F

Mean Curvature Measured by Level-set Method

F.1 Bubble Test

In section 3.3, the mean curvature results measured by the surface fitting method and the method proposed by Hou et al. (1997) are shown. Here the results measured by the level-set method and the surface fitting method are presented for completeness. The data is summarised in Figure F.1. For the surface fitting method, the error bars come from the standard deviations by averaging the measured mean curvature values at cloud points on the iso-surface (i.e. the fluid-fluid interface). For the level-set method, the standard deviations are due to averaging the curvature values over both the inner interface (on the side of NW phase) and the outer interface (on the side of W phase). As a result, it can be seen from Figure F.1 that the standard deviations of the level-set method is generally greater than those of the surface fitting method.

In Figure F.1(b) for RK model, it can be seen that the mean curvature of the smallest bubble given by the surface fitting method is greater than $2.0 \text{ } l.u.^{-1}$, corresponding to a bubble radius of less than one voxel. For such a small bubble, the NW phase density $\rho_{nw, major}$ is severely degraded, such that the region where $\Phi(\mathbf{x}) > 0.0$ (indicating the region occupied by NW phase) is limited in a cube of $2 \times 2 \times 2 \text{ } l.u.^3$; the surface fitting algorithm relies on both the input function $\Phi(\mathbf{x})$ and a segmented phase domain calculated based on $\Phi(\mathbf{x})$ (i.e. 1 for NW phase if $\Phi(\mathbf{x}) > 0.0$, and 2 for W phase if $\Phi(\mathbf{x}) < 0.0$). This is why the surface fitting algorithm gives an unrealistically high curvature value. Whereas for the level-set method, the final mean curvature value is averaged out because both the surface of the cube of $2 \times 2 \times 2 \text{ } l.u.^3$ (i.e. the inner interface) as well as the surface of the cube of $4 \times 4 \times 4 \text{ } l.u.^3$ (i.e. the outer interface) are considered; the outer interface usually gives smaller curvature values than the inner interface, therefore such an averaging process tends to even out the unrealistically high curvature values given by the inner interface. This is why in Figure F.1(d), the mean curvature of the smallest bubble given by the level-set method is not as large as in the case of the surface fitting method, but the associated standard deviation is inevitably big since the averaging is taken from two surfaces. Overall, the measured curvature values given by the surface fitting and the level-set method

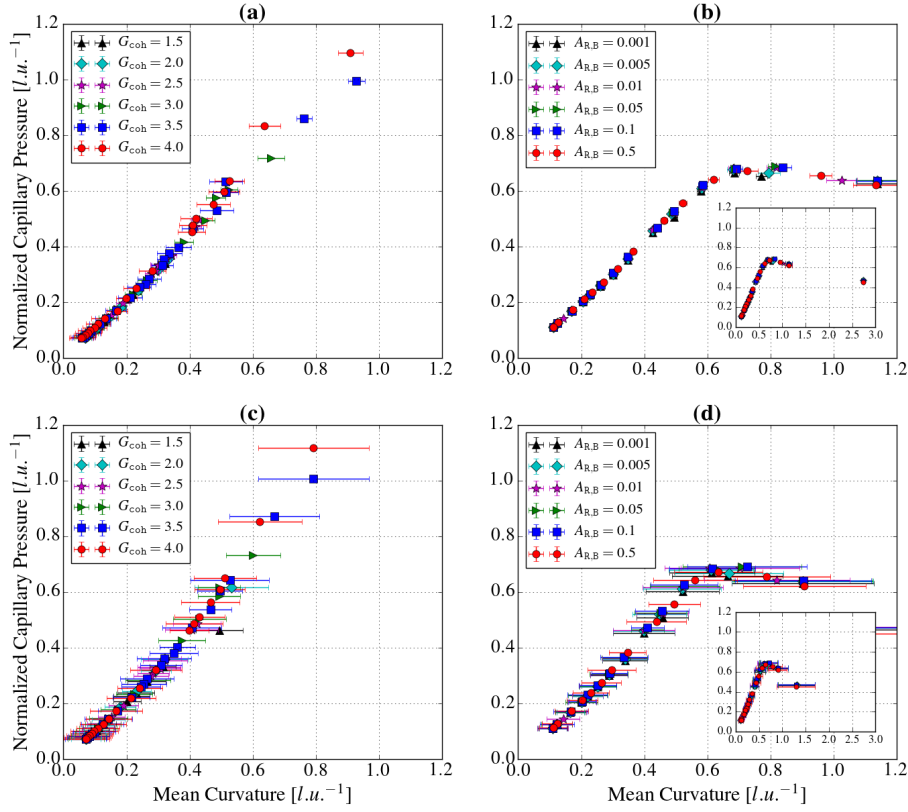


FIGURE F.1: The test of the Laplace's law, where the mean curvature is measured by the surface fitting method for (a) SC model, and (b) RK model. The mean curvature measured by the level-set method is shown for (c) SC model, and (d) RK model. The measured capillary pressure is normalised by the fitted surface tension for each G_{coh} and $A_{\text{R,B}}$. For RK model, the measured mean curvature for the smallest bubble given by both methods is greater than 1.2 l.u. , so the insets are used in (b) and (d), respectively, to show the full range of curvature values.

tend to converge for low curvature values, which is expected since the resolution is not a limiting factor. At large curvatures, the NW phase density degrades and this will affect the input function $\Phi(\mathbf{x})$, so the difference in the algorithms of two methods starts to play a role and the results begin to diverge.

F.2 Flat Tube Test

In this section, the capillary pressure - mean curvature relations measured by the surface fitting and the level-set methods are presented. The results are summarised in Figure F.2. The error bar of the capillary pressure is due to the calculation of the volume-averaged pressure. The error bar of the mean curvature in the surface fitting method is due to the averaging process of mean curvature values measured from all cloud points on the iso-surface. For the level-set method, this averaging

process is taken over both the inner interface (i.e. on the side of the NW phase) and the outer interface (i.e. on the side of the W phase), which is why the corresponding standard deviations are much greater than those in the surface fitting method. For $R_{\text{tube}} \leq 2.0 \text{ l.u.}$, the resolution is too low for the surface fitting method to extract enough cloud points, therefore the linear interpolation is applied to the original density data before the measurement is taken. For consistency, the level-set method uses the same interpolated density data. Based on the Figure F.2, it can be seen that the measurement results given by two methods have good agreement.

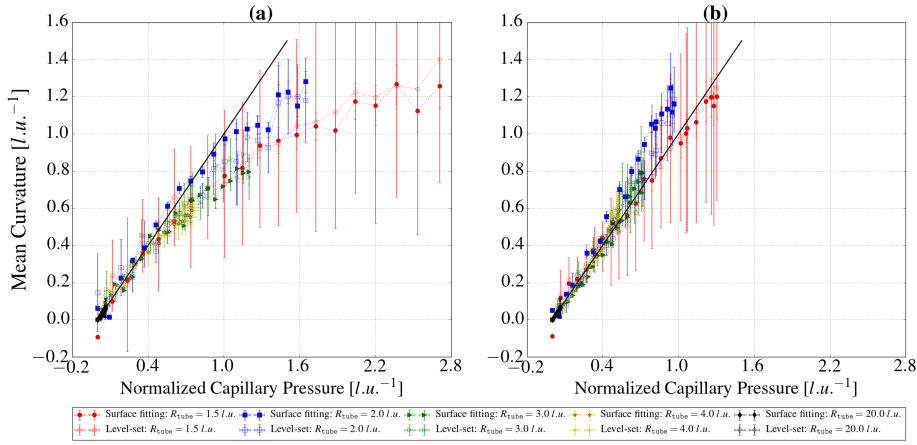


FIGURE F.2: The mean curvature - capillary pressure measurements for (a) SC model, and (b) RK model. The black line in each sub-plot is a prediction line, assuming a one-to-one correspondence between the mean curvature and the normalised capillary pressure. Note that for $R_{\text{tube}} = 1.5$ and 2.0 l.u. , the linear interpolation is applied to the original density data before the surface fitting and level-set method are performed.

F.3 Tilted Tube Test

For the tilted tube test, the capillary pressure - mean curvature relations measured by the surface fitting and the level-set methods are presented in Figure F.3. The averaging process in the level-set method involves both the inner and outer phase interface, whereas the surface fitting method takes averages over the reconstructed iso-surface. This explains why the standard deviations in level-set method is greater than those in the surface fitting method.

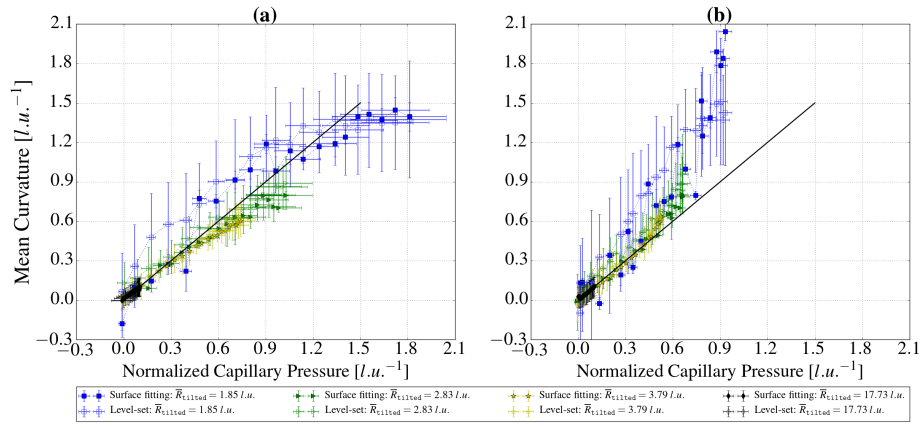


FIGURE F.3: The mean curvature - capillary pressure measurements for (a) SC model, and (b) RK model. The black line in each sub-plot is a prediction line, assuming a one-to-one correspondence between the mean curvature and the normalised capillary pressure. Note that for $\bar{R}_{\text{tilted}} = 1.85$ $l.u.$, the linear interpolation is applied to the original density data before the surface fitting and level-set method are performed.

Appendix G

Breakdown Examples of Primary Drainage in Square Tube

As is discussed in the main text, both Shan-Chen (SC) and Rothman-Keller (RK) models present some breakdown behaviour in the primary drainage tests in a square capillary tube. More specifically, in section 3.5.2, we investigate the influence of the pressure boundary condition on SC model's behaviour, and found that the invading non-wetting (NW) phase may snap off if the required entry pressure is high. This is a side effect of using density values from the static flat tube test as the pressure boundary condition. More discussion on this can be found in Appendix C. Figure G.1 shows an example of such snap-off process during the drainage of a square tube of $R_{\text{tube}} = 4.0 \text{ l.u.}$

Also, as is discussed in section 3.5.4, if the surface-to-volume ratio of the porous plate is too large, once the phase front of the invading NW phase approaches the porous plate, there is a leakage of the NW phase through the porous plate and NW phase bubble is generated in the wetting phase reservoir on the other side. This is due to non-physical attraction of the dissolved NW phase near the solid surface and more discussion can be found in Chapter 4. Figure G.2 shows an example of such leakage process during the drainage of a square tube of $R_{\text{tube}} = 4.0 \text{ l.u.}$

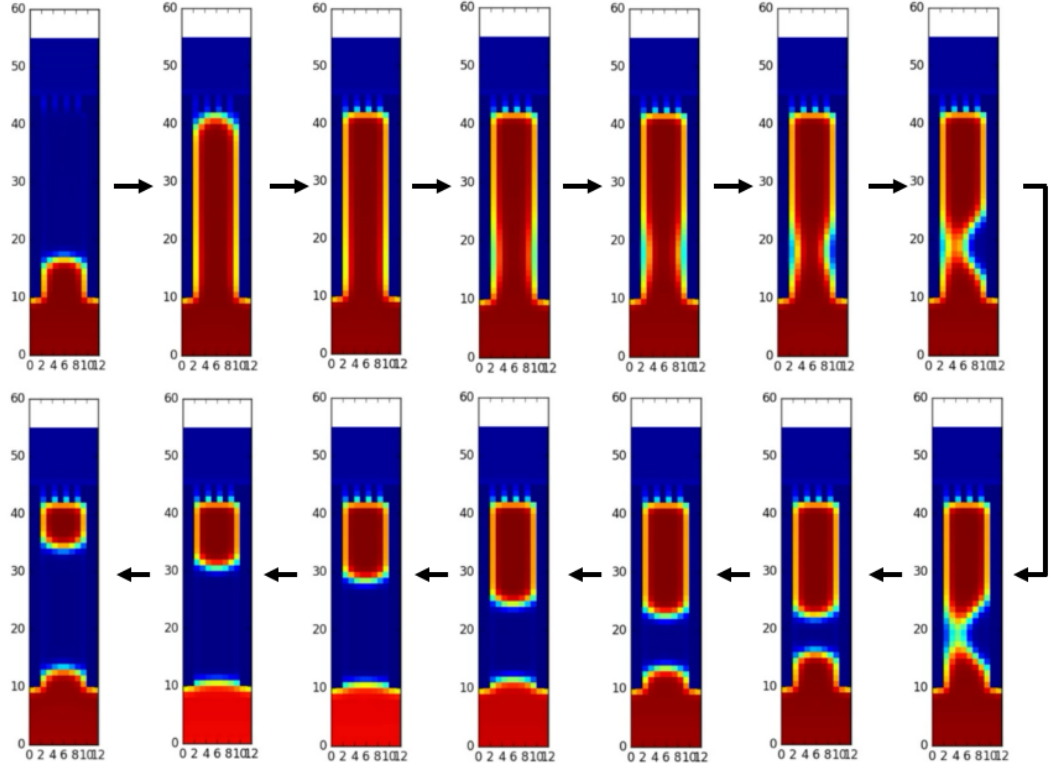


FIGURE G.1: Screen-shots of a breakdown process for SC model where the invading non-wetting phase snaps off after the entry in a primary drainage in square capillary tube. The black arrow indicate the time flow of the simulation. The two-dimensional phase distribution is extracted from three-dimensional simulations. The inscribed radius of the capillary tube is $R_{\text{tube}} = 4.0 \text{ l.u.}$. The inscribed radius of the single pore of the porous plate (R_{pore}) is 0.5 l.u. , and the thickness of the porous plate (L_{pore}) is 3.0 l.u. . The pressure values being applied to the inlet and the outlet of the domain come from the density values of static flat tube tests ($R_{\text{tube}} = 1.5 \text{ l.u.}$). The snap-off of the non-wetting phase occurs at the dimensionless capillary pressure P_c^d of 4.62 (See Table 3.4 of the main text).

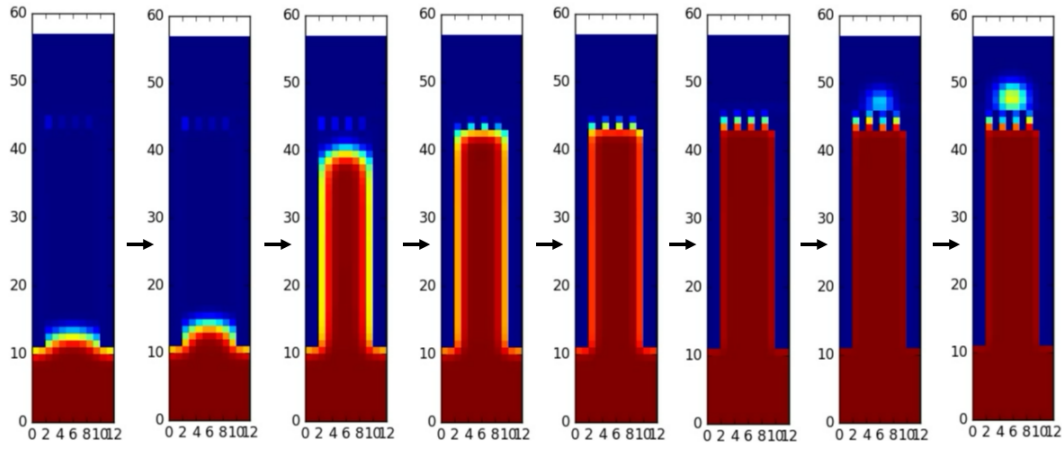


FIGURE G.2: Screen-shots of a breakdown process for RK model where the invading non-wetting phase leaks through the porous plate after the entry in a primary drainage in square capillary tube. The black arrow indicate the time flow of the simulation. The two-dimensional phase distribution is extracted from three-dimensional simulations. The inscribed radius of the capillary tube is $R_{\text{tube}} = 4.0 \text{ } l.u.$. The inscribed radius of the single pore of the porous plate (R_{pore}) is $0.5 \text{ } l.u.$, and the thickness of the porous plate (L_{pore}) is $3.0 \text{ } l.u.$. The non-physical leakage of the invading non-wetting phase through the porous plate occurs at the dimensionless capillary pressure P_c^d of 1.77, whereas theoretically the entry (dimensionless) pressure for $R_{\text{pore}} = 0.5 \text{ } l.u.$ is 14.16 (See Table 3.4 of the main text).

Appendix H

Snap-off Events During Drainage

In this appendix, the detailed snap-off processes are shown for all cases of $\alpha = 3.57 \times 10^{-2}$, according to Table 5.1 in Chapter 5. For the cases of $\alpha = 10^{-4}$, due to the use of more viscous fluids, the total time scale of the snap-off process is around one order of magnitude longer, and it is infeasible to simply ‘dump’ every pictorial-format snapshot of the saved data in here. Therefore, videos have been made for all of snap-off events of $\alpha = 10^{-4}$, and the media data can be accessed upon request.

The snapshots of the case 1, 3, 4 and 5 for $\alpha = 3.57 \times 10^{-2}$ is per 1000 LB time steps (i.e. ~ 0.89 ms), and the snap-off events are identified by identifier with the format as follows:

Case number/pore body labels/pore throat labels

where the pore body and throat labels are characterised based on geometry-topology analysis via persistent homology (Robins et al., 2015; Herring, Robins, and Sheppard, 2019).

For case 1, there are three snap-off events observed during drainage, and the snapshots of these events are shown in Figure H.1, H.2 and H.3, respectively. For case 3, there are in total seven consecutive snap-off events; since those snap-off events all occur in the same pore-body group via the same throat, only the first snap-off is shown in Figure.xx. For case 4, there are two snap-off events, which are shown in Figure H.5 and H.6, respectively. Lastly, for case 5, there are in total six snap-off events according to Table 5.1, and for snap-off events occurring between LB time of 1,589,000 *l.t.* and 1,620,000 *l.t.*, since it is in fact a series of break-up and coalescence events all occurring in the same pore bodies, the entire process is shown in Figure H.9, and the rest of two snap-off events are shown in Figure H.7 and H.8, respectively. It is noted that, the global capillary number that is used to specify each case is defined with respect to the more viscous fluid (consistent with the main body of the thesis), thus the notation Ca^* .

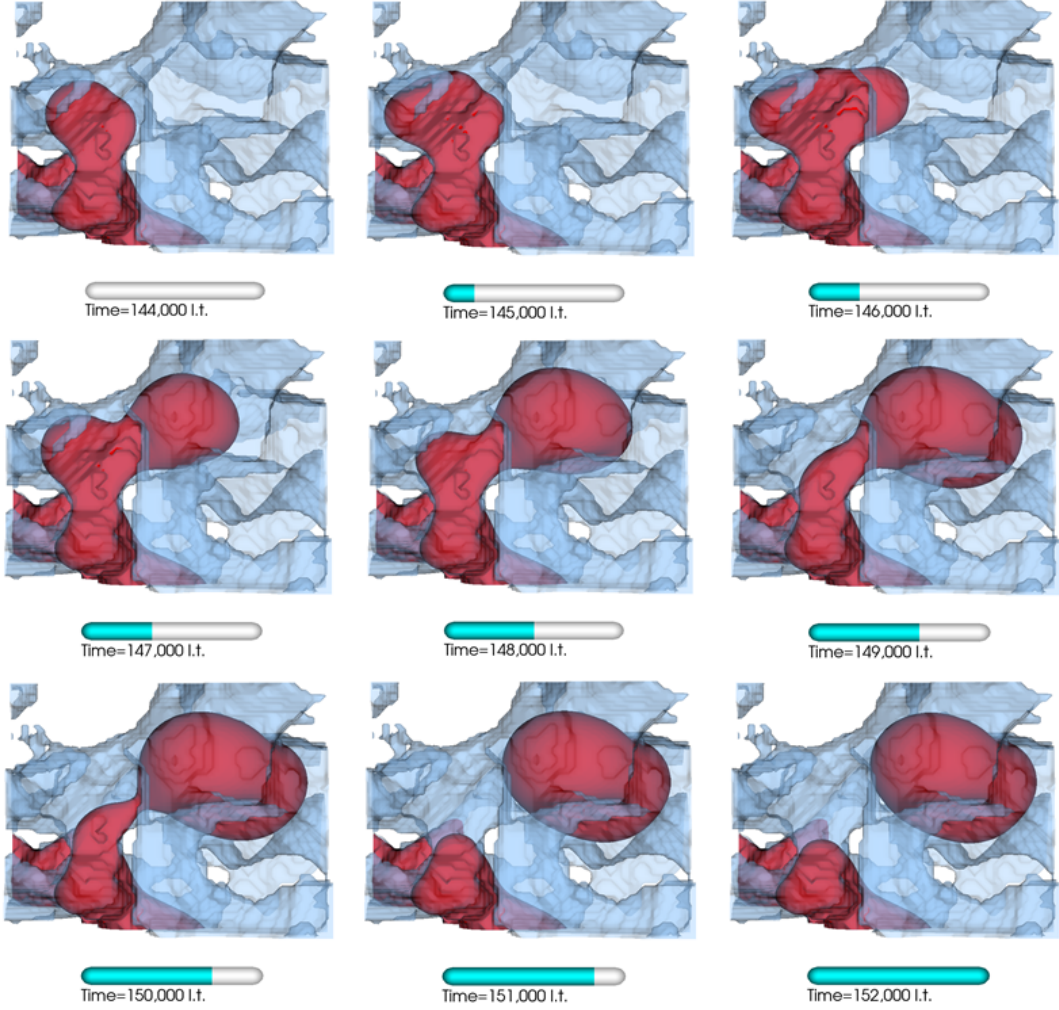


FIGURE H.1: Visualisation of snap-off process for LB primary drainage simulation with the snap-off event identifier 1/(5; 8)/752, which means it is case 1 ($Ca^* = 5 \times 10^{-4}$, $M = 0.2$), and the pore filling occurs in pore bodies with labels 5 and 8, through the invading throat with label 752.

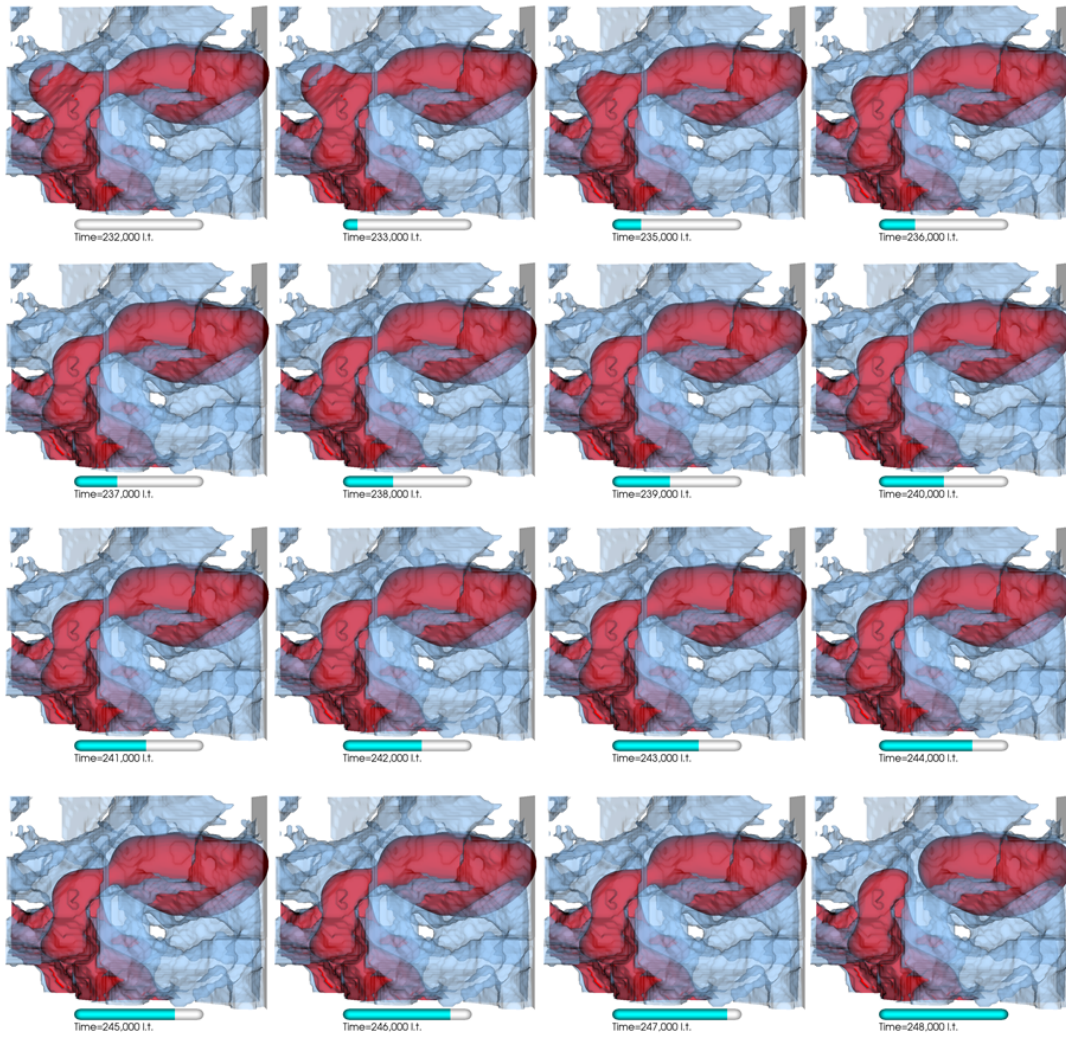


FIGURE H.2: Visualisation of snap-off process for LB primary drainage simulation with the snap-off event identifier 1/(5; 49; 55)/752, which means it is case 1 ($Ca^* = 5 \times 10^{-4}$, $M = 0.2$), and the pore filling occurs in pore bodies with labels 5, 49 and 55, through the invading throat with label 752.

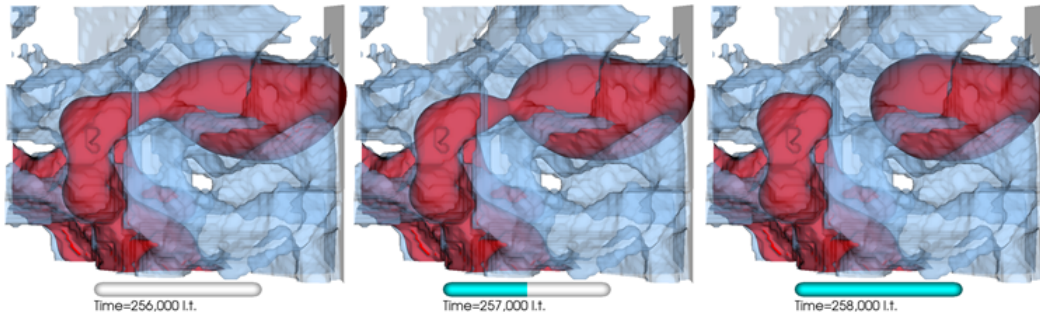


FIGURE H.3: Visualisation of snap-off process for LB primary drainage simulation with the snap-off event identifier 1/(5; 49; 55)/752, which means it is case 1 ($Ca^* = 5 \times 10^{-4}$, $M = 0.2$), and the pore filling occurs in pore bodies with labels 5, 49 and 55, through the invading throat with label 752.

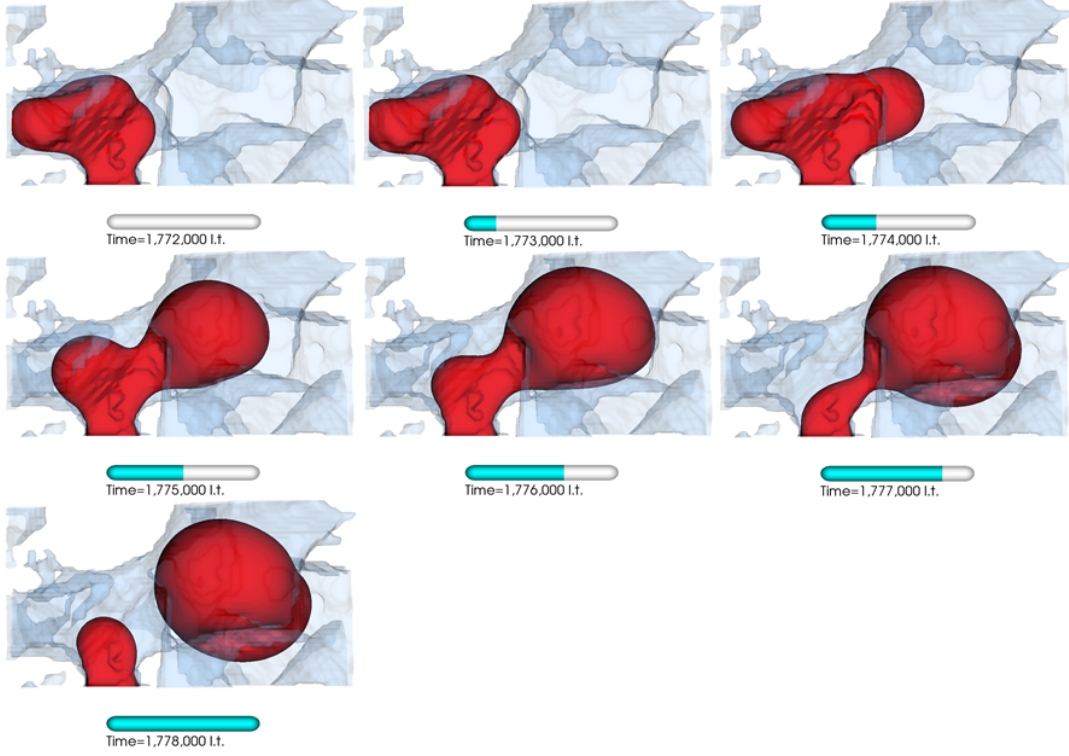


FIGURE H.4: Visualisation of snap-off process for LB primary drainage simulation with the snap-off event identifier 3/(5; 8)/752, which means it is case 3 ($Ca^* = 1.25 \times 10^{-5}$, $M = 0.8$), and the pore filling occurs in pore bodies with labels 5 and 8, through the invading throat with label 752.

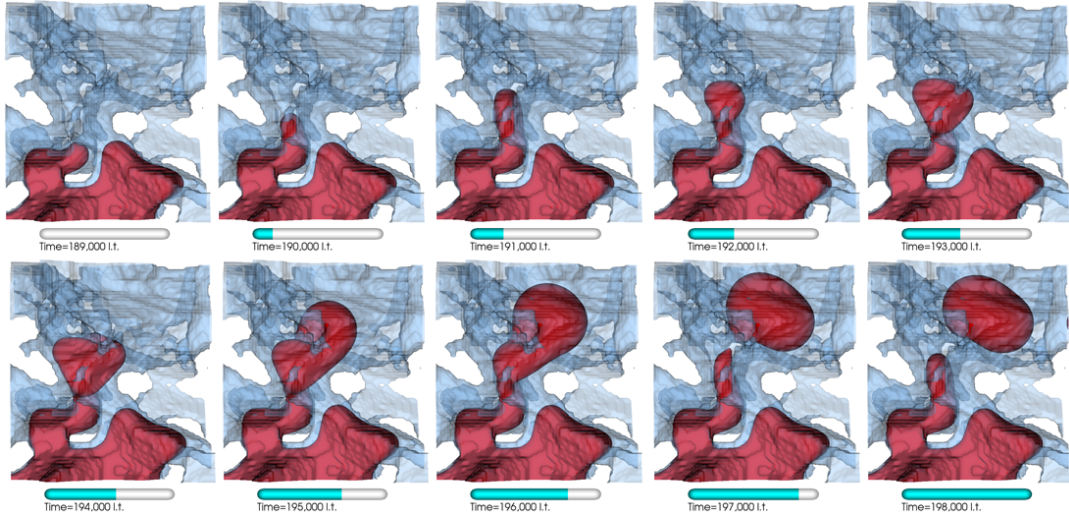


FIGURE H.5: Visualisation of snap-off process for LB primary drainage simulation with the snap-off event identifier 4/(15; 16)/709, which means it is case 4 ($Ca^* = 5 \times 10^{-4}$, $M = 10$), and the pore filling occurs in pore bodies with labels 15 and 16, through the invading throat with label 709.

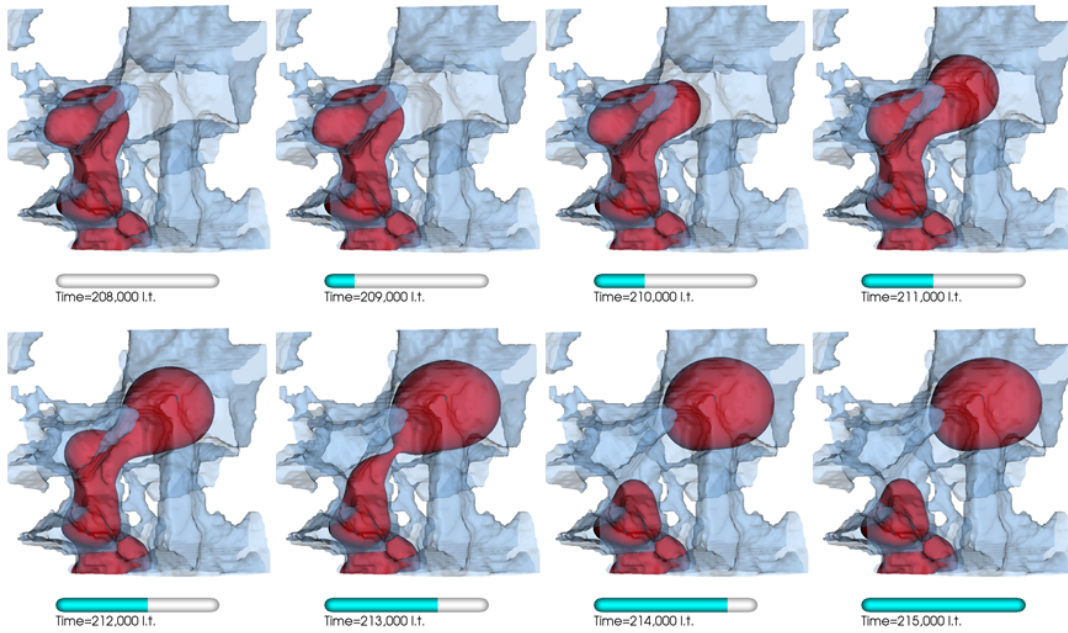


FIGURE H.6: Visualisation of snap-off process for LB primary drainage simulation with the snap-off event identifier 4/8/752, which means it is case 4 ($Ca^* = 5 \times 10^{-4}$, $M = 10$), and the pore filling occurs in pore bodies with label 8, through the invading throat with label 752.

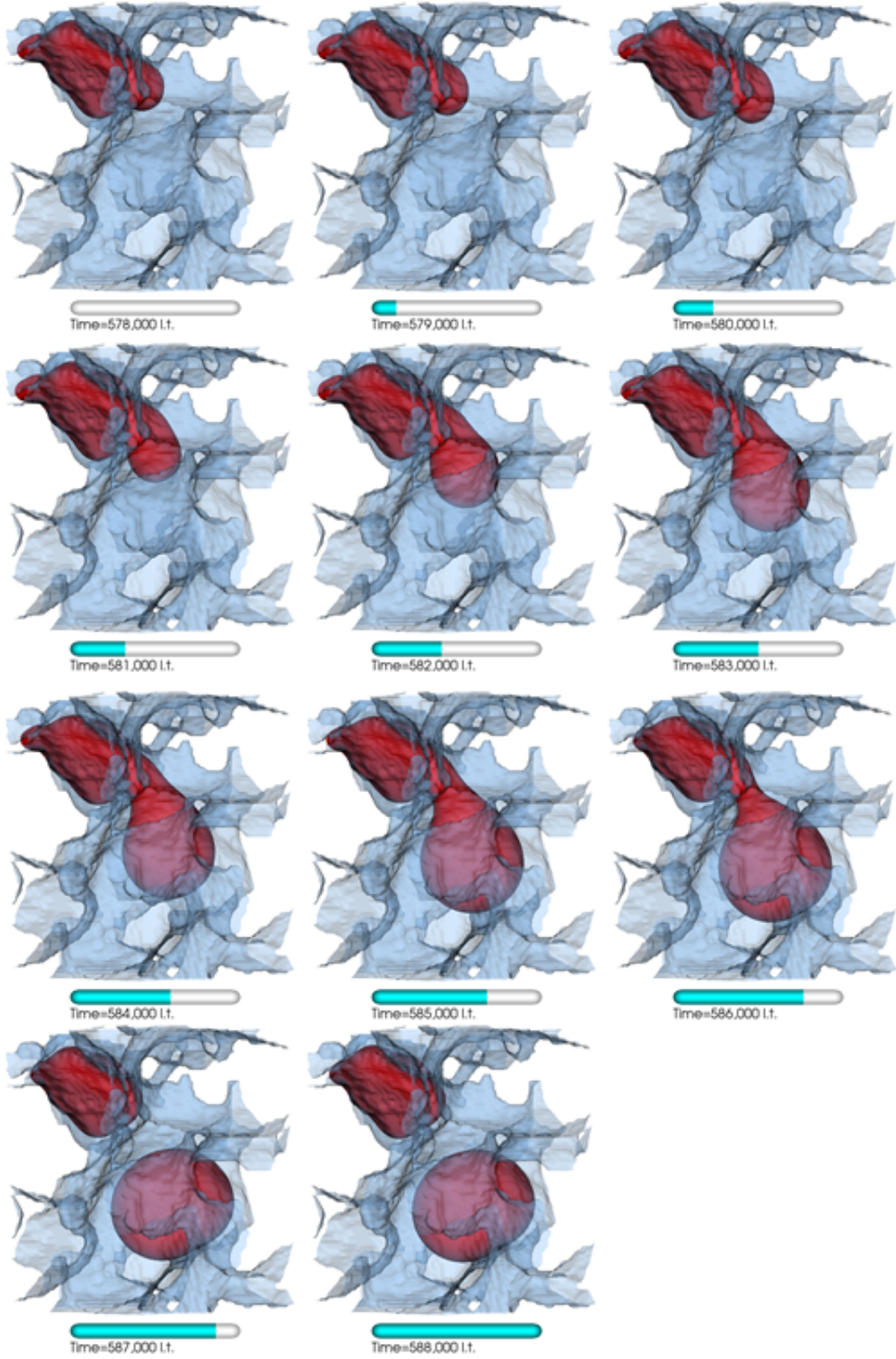


FIGURE H.7: Visualisation of snap-off process for LB primary drainage simulation with the snap-off event identifier 5/2/627, which means it is case 5 ($Ca^* = 5 \times 10^{-5}$, $M = 10$), and the pore filling occurs in pore bodies with label 2, through the invading throat with label 627.

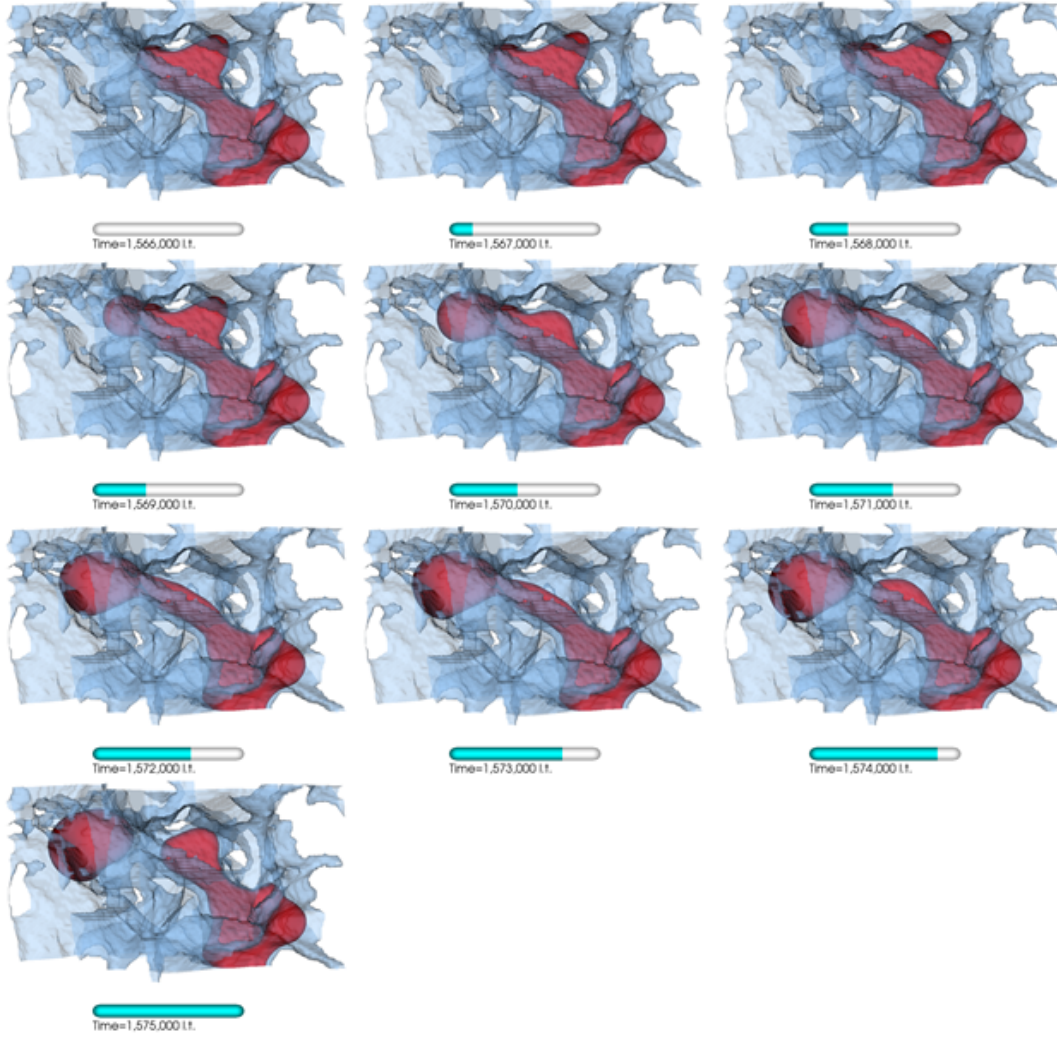


FIGURE H.8: Visualisation of snap-off process for LB primary drainage simulation with the snap-off event identifier 5/(15; 16)/646, which means it is case 5 ($Ca^* = 5 \times 10^{-5}$, $M = 10$), and the pore filling occurs in pore bodies with labels 15 and 16, through the invading throat with label 646. The process shown here corresponds to the snap-off event occurring at LB time of 1,574,000 *l.t.* (see Table 5.1 in Chapter 5).

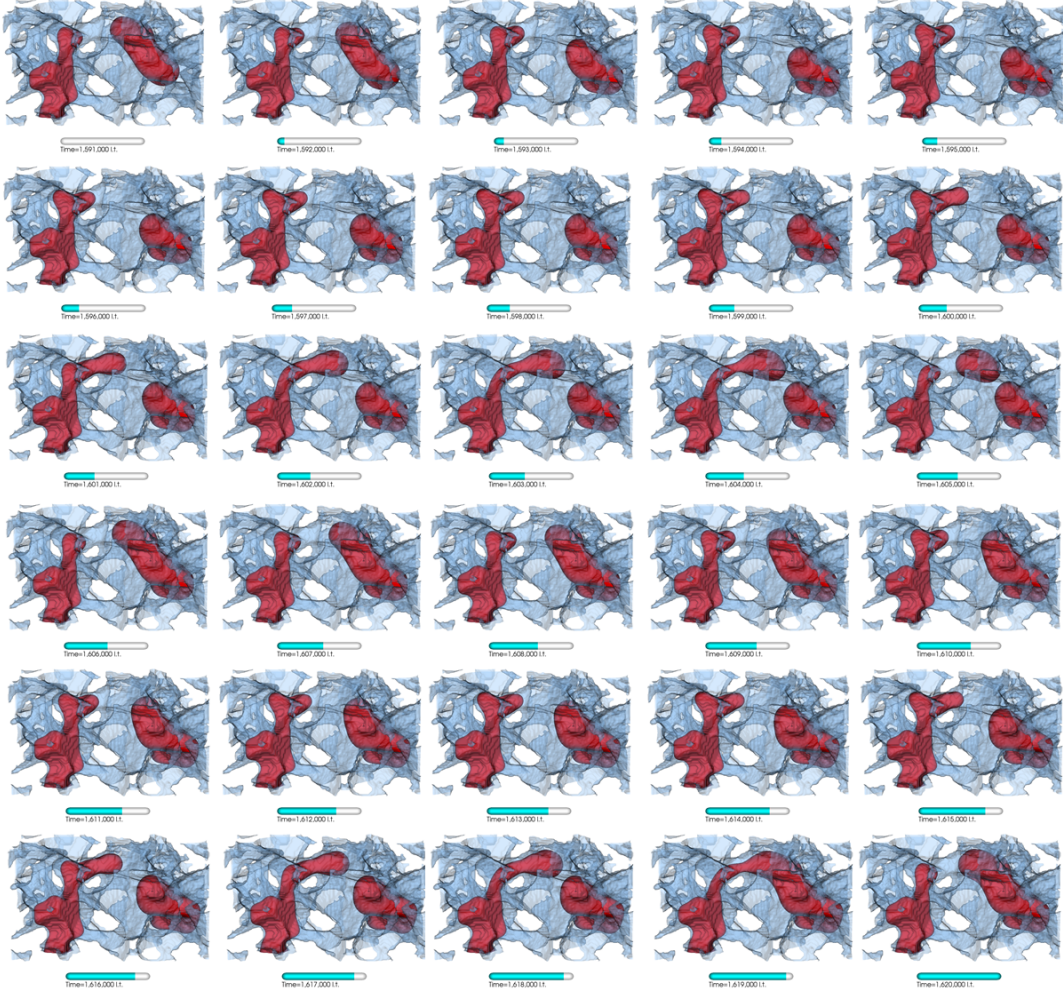


FIGURE H.9: Visualisation of the consecutive snap-off/reconnection cycle for LB primary drainage simulation with the snap-off event identifier 5/(15; 16)/646, which means it is case 5 ($Ca^* = 5 \times 10^{-5}$, $M = 10$), and the pore filling occurs in pore bodies with labels 15 and 16, through the invading throat with label 646. The events shown here correspond to the snap-off events occurring from LB time of 1,605,000 *l.t.* to 1,620,000 *l.t.* (see Table 5.1 in Chapter 5).

Appendix I

Young-Laplace Relation for Drainage in Square Tube

In this appendix, the supplementary results for section 5.2.1 and 5.2.2 are presented, to examine the Young-Laplace relation during the capillary filling and drainage processes. The phase pressure difference across the fluid interface, $p_n - p_w$ (normalised by LB surface tension) is plotted against the NW-W interface mean curvature, where the mean curvature is measured by the surface fitting method for $R_{\text{tube}} = \{5.0, 10.0\}$ $l.u.$. For $R_{\text{tube}} = 3.0$ $l.u.$, however, the mean curvature measured by the *in-situ* facility of LB code is extracted, since there are not enough surface cloud points for the surface fitting method to work, unless the interpolation is used. Figure I.1 and I.2 show the results for the capillary filling and the drainage processes, respectively. In particular, for the case of drainage, the colour of the symbols, from dark to light, corresponds to the prescribed global Ca from low to high.

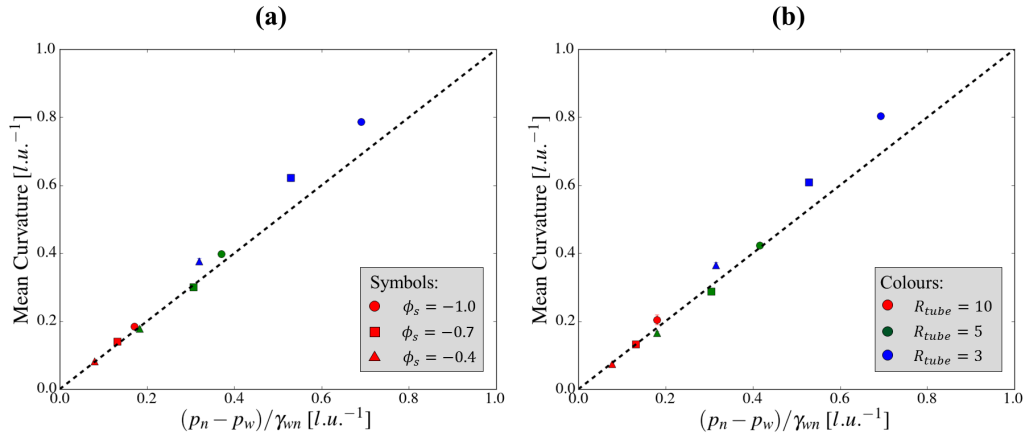


FIGURE I.1: Mean curvature measured by the surface fitting method is plotted against the phase pressure difference normalised by the LB surface tension, for capillary filling in a square tube, for (a) $\alpha = 10^{-2}$, and (b) $\alpha = 10^{-4}$. Both the mean curvature and the pressure difference are measured from the steady-state part of the simulation, where the mean values are calculated and presented in the figure, with the error bars indicating the standard deviations of the mean.

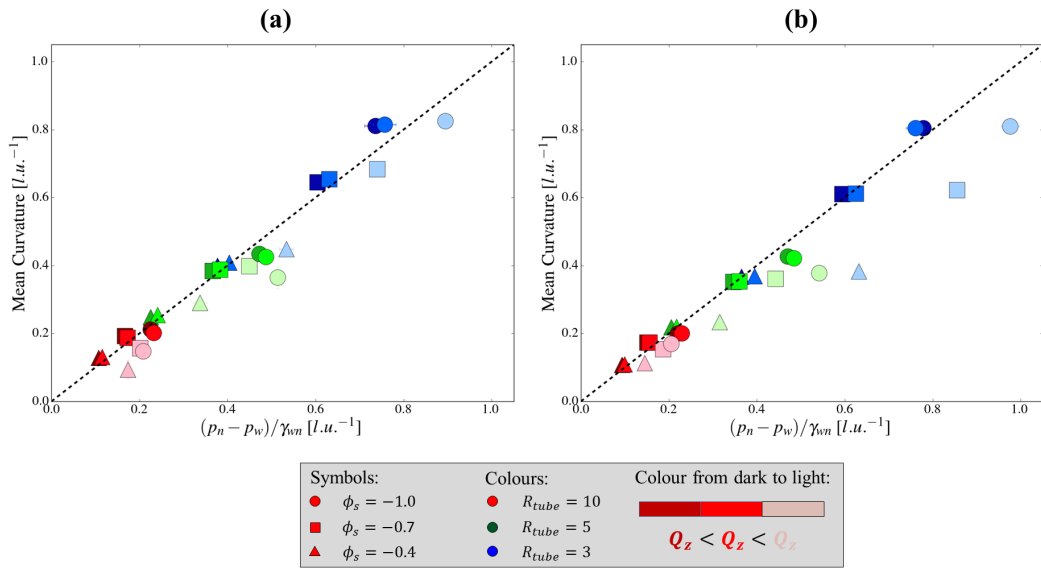


FIGURE I.2: Mean curvature measured by the surface fitting method is plotted against the phase pressure difference normalised by the LB surface tension, for drainage in a square tube, for (a) $\alpha = 10^{-2}$, and (b) $\alpha = 10^{-4}$. Both the mean curvature and the pressure difference are measured from the steady-state part of the simulation, where the mean values are calculated and presented in the figure, with the error bars indicating the standard deviations of the mean.

Bibliography

- [1] B. Ahrenholz et al. “Prediction of capillary hysteresis in a porous material using lattice-Boltzmann methods and comparison to experimental data and a morphological pore network model”. In: *Advances in Water Resources* 31.9 (2008), pp. 1151–1173. ISSN: 0309-1708. DOI: <http://doi.org/10.1016/j.advwatres.2008.03.009>. URL: <http://www.sciencedirect.com/science/article/pii/S0309170808000511>.
- [2] Cyrus K. Aidun and Jonathan R. Clausen. “Lattice-Boltzmann Method for Complex Flows”. In: *Annual Review of Fluid Mechanics* 42.1 (2010), pp. 439–472. DOI: [10.1146/annurev-fluid-121108-145519](https://doi.org/10.1146/annurev-fluid-121108-145519). URL: <http://dx.doi.org/10.1146/annurev-fluid-121108-145519>.
- [3] Takashi Akai, Branko Bijeljic, and Martin J. Blunt. “Wetting boundary condition for the color-gradient lattice Boltzmann method: Validation with analytical and experimental data”. In: *Advances in Water Resources* 116 (2018), pp. 56–66. ISSN: 0309-1708. DOI: <https://doi.org/10.1016/j.advwatres.2018.03.014>. URL: <http://www.sciencedirect.com/science/article/pii/S030917081731028X>.
- [4] F. O. Alpak et al. “A distributed parallel multiple-relaxation-time lattice Boltzmann method on general-purpose graphics processing units for the rapid and scalable computation of absolute permeability from high-resolution 3D micro-CT images”. In: *Computational Geosciences* 22.3 (2018), pp. 815–832. ISSN: 1573-1499. DOI: [10.1007/s10596-018-9727-7](https://doi.org/10.1007/s10596-018-9727-7). URL: <https://doi.org/10.1007/s10596-018-9727-7>.
- [5] F.O. Alpak, S. Berg, and I. Zacharoudiou. “Prediction of fluid topology and relative permeability in imbibition in sandstone rock by direct numerical simulation”. In: *Advances in Water Resources* 122 (2018), pp. 49–59. ISSN: 0309-1708. DOI: <https://doi.org/10.1016/j.advwatres.2018.09.001>. URL: <http://www.sciencedirect.com/science/article/pii/S0309170818304366>.
- [6] Giorgio Amati, Sauro Succi, and Renzo Piva. “Massively Parallel Lattice-Boltzmann Simulation of Turbulent Channel Flow”. In: *International Journal of Modern Physics C* 08.04 (1997), pp. 869–877. DOI: [10.1142/S0129183197000746](https://doi.org/10.1142/S0129183197000746).
- [7] D. M. Anderson, G. B. McFadden, and A. A. Wheeler. “DIFFUSE-INTERFACE METHODS IN FLUID MECHANICS”. In: *Annual Review of Fluid Mechanics* 30.1 (1998), pp. 139–165. DOI: [10.1146/annurev.fluid.30.1.139](https://doi.org/10.1146/annurev.fluid.30.1.139). URL: <https://doi.org/10.1146/annurev.fluid.30.1.139>.

- [8] Matthew Andrew, Branko Bijeljic, and Martin J. Blunt. “Pore-by-pore capillary pressure measurements using X-ray microtomography at reservoir conditions: Curvature, snap-off, and remobilization of residual CO₂”. In: *Water Resources Research* 50.11 (2014), pp. 8760–8774. ISSN: 1944-7973. DOI: [10.1002/2014WR015970](https://doi.org/10.1002/2014WR015970). URL: <http://dx.doi.org/10.1002/2014WR015970>.
- [9] Ryan T. Armstrong and Steffen Berg. “Interfacial velocities and capillary pressure gradients during Haines jumps”. In: *Phys. Rev. E* 88 (4 2013), p. 043010. DOI: [10.1103/PhysRevE.88.043010](https://link.aps.org/doi/10.1103/PhysRevE.88.043010). URL: <https://link.aps.org/doi/10.1103/PhysRevE.88.043010>.
- [10] Ryan T. Armstrong, Mark L. Porter, and Dorte Wildenschild. “Linking pore-scale interfacial curvature to column-scale capillary pressure”. In: *Advances in Water Resources* 46 (2012), pp. 55–62. ISSN: 0309-1708. DOI: <https://doi.org/10.1016/j.advwatres.2012.05.009>. URL: <http://www.sciencedirect.com/science/article/pii/S0309170812001443>.
- [11] Ryan T. Armstrong et al. “Beyond Darcy’s law: The role of phase topology and ganglion dynamics for two-fluid flow”. In: *Phys. Rev. E* 94 (4 2016), p. 043113. DOI: [10.1103/PhysRevE.94.043113](https://link.aps.org/doi/10.1103/PhysRevE.94.043113). URL: <https://link.aps.org/doi/10.1103/PhysRevE.94.043113>.
- [12] Ryan T. Armstrong et al. “Porous Media Characterization Using Minkowski Functionals: Theories, Applications and Future Directions”. In: *Transport in Porous Media* (2018). ISSN: 1573-1634. DOI: [10.1007/s11242-018-1201-4](https://doi.org/10.1007/s11242-018-1201-4). URL: <https://doi.org/10.1007/s11242-018-1201-4>.
- [13] Yan Ba et al. “Color-gradient lattice Boltzmann model for simulating droplet motion with contact-angle hysteresis”. In: *Phys. Rev. E* 88 (4 2013), p. 043306. DOI: [10.1103/PhysRevE.88.043306](https://link.aps.org/doi/10.1103/PhysRevE.88.043306). URL: <https://link.aps.org/doi/10.1103/PhysRevE.88.043306>.
- [14] Yan Ba et al. “Three dimensional simulations of droplet formation in symmetric and asymmetric T-junctions using the color-gradient lattice Boltzmann model”. In: *International Journal of Heat and Mass Transfer* 90 (2015), pp. 931–947. ISSN: 0017-9310. DOI: <https://doi.org/10.1016/j.ijheatmasstransfer.2015.07.023>. URL: <http://www.sciencedirect.com/science/article/pii/S0017931015007322>.
- [15] Stig Bakke and Pål-Eric Øren. “3-D Pore-Scale Modelling of Sandstones and Flow Simulations in the Pore Networks”. In: *SPE Journal* 2 (1997), pp. 136–149. ISSN: 2.
- [16] C. Bradford Barber, David P. Dobkin, and Hannu Huhdanpaa. “The Quickhull algorithm for convex hulls”. In: *ACM TRANSACTIONS ON MATHEMATICAL SOFTWARE* 22.4 (1996), pp. 469–483.

- [17] R. Benzi, S. Succi, and M. Vergassola. “The lattice Boltzmann equation: theory and applications”. In: *Physics Reports* 222.3 (1992), pp. 145–197. ISSN: 0370-1573. DOI: [http://dx.doi.org/10.1016/0370-1573\(92\)90090-M](http://dx.doi.org/10.1016/0370-1573(92)90090-M). URL: <http://www.sciencedirect.com/science/article/pii/037015739290090M>.
- [18] Steffen Berg et al. “Real-time 3D imaging of Haines jumps in porous media flow”. In: *Proceedings of the National Academy of Sciences* 110.10 (2013), pp. 3755–3759. ISSN: 0027-8424. DOI: [10.1073/pnas.1221373110](https://doi.org/10.1073/pnas.1221373110). URL: <http://www.pnas.org/content/110/10/3755>.
- [19] Massimo Bernaschi et al. “A flexible high-performance Lattice Boltzmann GPU code for the simulations of fluid flows in complex geometries”. In: *Concurrency and Computation: Practice and Experience* 22.1 (2010), pp. 1–14. ISSN: 1532-0634. DOI: [10.1002/cpe.1466](https://doi.org/10.1002/cpe.1466). URL: <http://dx.doi.org/10.1002/cpe.1466>.
- [20] Serge Beucher and Christian Lantuéjoul. *Use of Watersheds in Contour Detection*. workshop published. Sept. 1979. URL: <http://cmm.ensmp.fr/~beucher/publi/watershed.pdf>.
- [21] P. L. Bhatnagar, E. P. Gross, and M. Krook. “A Model for Collision Processes in Gases. I. Small Amplitude Processes in Charged and Neutral One-Component Systems”. In: *Phys. Rev.* 94 (3 1954), pp. 511–525. DOI: [10.1103/PhysRev.94.511](https://doi.org/10.1103/PhysRev.94.511). URL: <https://link.aps.org/doi/10.1103/PhysRev.94.511>.
- [22] Martin J. Blunt. “Flow in porous media - pore-network models and multiphase flow”. In: *Current Opinion in Colloid & Interface Science* 6.3 (2001), pp. 197–207. ISSN: 1359-0294. DOI: [http://doi.org/10.1016/S1359-0294\(01\)00084-X](https://doi.org/10.1016/S1359-0294(01)00084-X). URL: <http://www.sciencedirect.com/science/article/pii/S135902940100084X>.
- [23] Martin J. Blunt et al. “Pore-scale imaging and modelling”. In: *Advances in Water Resources* 51 (2013). 35th Year Anniversary Issue, pp. 197–216. ISSN: 0309-1708. DOI: [http://doi.org/10.1016/j.advwatres.2012.03.003](https://doi.org/10.1016/j.advwatres.2012.03.003). URL: <http://www.sciencedirect.com/science/article/pii/S0309170812000528>.
- [24] A.J. Briant. “Lattice Boltzmann simulations of contact line motion in a liquid-gas system”. In: *Philosophical Transactions of the Royal Society of London A: Mathematical, Physical and Engineering Sciences* 360.1792 (2002). Ed. by P. Papatzacos and J. M. Yeomans, pp. 485–495. ISSN: 1364-503X. DOI: [10.1098/rsta.2001.0943](https://doi.org/10.1098/rsta.2001.0943). URL: <http://rsta.royalsocietypublishing.org/content/360/1792/485>.
- [25] Nianzheng Cao et al. “Physical symmetry and lattice symmetry in the lattice Boltzmann method”. In: *Phys. Rev. E* 55 (1 1997), R21–R24. DOI: [10.1103/PhysRevE.55.R21](https://doi.org/10.1103/PhysRevE.55.R21). URL: <https://link.aps.org/doi/10.1103/PhysRevE.55.R21>.

- [26] Cyril Caubit et al. "Evaluation Of The Reliability of Prediction of Petrophysical Data Through Imagery and Pore Network Modelling". In: *Petrophysics* 50 (2009), pp. 322–334.
- [27] Carlo Cercignani. "The Boltzmann Equation". In: *The Boltzmann Equation and Its Applications*. New York, NY: Springer New York, 1988. ISBN: 978-1-4612-1039-9. DOI: [10.1007/978-1-4612-1039-9_2](https://doi.org/10.1007/978-1-4612-1039-9_2). URL: https://doi.org/10.1007/978-1-4612-1039-9_2.
- [28] Sydney Chapman, David Burnett, and Thomas George Cowling. *The mathematical theory of non-uniform gases*. English. 3rd Ed. Cambridge : Cambridge University Press, 1970. ISBN: 9780521408448.
- [29] Li Chen et al. "A critical review of the pseudopotential multiphase lattice Boltzmann model: Methods and applications". In: *International Journal of Heat and Mass Transfer* 76 (2014), pp. 210 –236. ISSN: 0017-9310. DOI: <http://doi.org/10.1016/j.ijheatmasstransfer.2014.04.032>. URL: <http://www.sciencedirect.com/science/article/pii/S0017931014003378>.
- [30] Peng Chen. "The lattice Boltzmann method for fluid dynamics: Theory and applications". MA thesis. Ecole Polytechnique Federale de Lausanne: Department of Mathematics, 2011.
- [31] Shiyi Chen and Gary D. Doolen. "LATTICE BOLTZMANN METHOD FOR FLUID FLOWS". In: *Annual Review of Fluid Mechanics* 30.1 (1998), pp. 329–364. DOI: [10.1146/annurev.fluid.30.1.329](http://dx.doi.org/10.1146/annurev.fluid.30.1.329). URL: <http://dx.doi.org/10.1146/annurev.fluid.30.1.329>.
- [32] Shiyi Chen et al. "Magnetohydrodynamics computations with lattice gas automata". In: *Journal of Statistical Physics* 68.3 (1992), pp. 533–556. ISSN: 1572-9613. DOI: [10.1007/BF01341761](https://doi.org/10.1007/BF01341761). URL: <https://doi.org/10.1007/BF01341761>.
- [33] Yu Chen et al. "Lattice Boltzmann Simulation of Particle Motion in Binary Immiscible Fluids". In: *Communications in Computational Physics* 18.3 (2015), pp. 757–786. DOI: [10.4208/cicp.101114.150415a](https://doi.org/10.4208/cicp.101114.150415a).
- [34] Chung Chieh. *Cyberspace Chemistry: Physical Properties of Water*. [Online; accessed 2017-12-20]. 2009. URL: <http://www.science.uwaterloo.ca/~cchieh/cact/applychem/waterphys.html>.
- [35] Bastien Chopard et al. *A Lattice Boltzmann modeling of blood flow in cerebral aneurysms*. Tech. rep. 2010. URL: <http://eccomas2012.conf.tuwien.ac.at/home.html>.
- [36] Kevin Connington and Taehun Lee. "A review of spurious currents in the lattice Boltzmann method for multiphase flows". In: *Journal of Mechanical Science and Technology* 26.12 (2012), pp. 3857–3863. ISSN: 1976-3824. DOI: [10.1007/s12206-012-1011-5](http://dx.doi.org/10.1007/s12206-012-1011-5). URL: <http://dx.doi.org/10.1007/s12206-012-1011-5>.

- [37] R. Cornubert, D. d’Humieres, and D. Levermore. “A Knudsen layer theory for lattice gases”. In: *Physica D: Nonlinear Phenomena* 47.1 (1991), pp. 241–259. ISSN: 0167-2789. DOI: [http://dx.doi.org/10.1016/0167-2789\(91\)90295-K](http://dx.doi.org/10.1016/0167-2789(91)90295-K). URL: <http://www.sciencedirect.com/science/article/pii/016727899190295K>.
- [38] O. Delgado-Friedrichs, V. Robins, and A. P. Sheppard. “Skeletonization and Partitioning of Digital Images Using Discrete Morse Theory”. In: *IEEE Transactions on Pattern Analysis and Machine Intelligence* 37.3 (2015), pp. 654–666. ISSN: 0162-8828. DOI: [10.1109/TPAMI.2014.2346172](https://doi.org/10.1109/TPAMI.2014.2346172).
- [39] D. d’Humières. “Generalized Lattice-Boltzmann Equations”. In: *Progress in Astronautics and Aeronautics* (1992), pp. 450–458. DOI: [10.2514/5.9781600866319.0450.0458](https://doi.org/10.2514/5.9781600866319.0450.0458). URL: <https://arc.aiaa.org/doi/abs/10.2514/5.9781600866319.0450.0458>.
- [40] D. d’Humières, M’hamed Bouzidi, and Pierre Lallemand. “Thirteen-velocity three-dimensional lattice Boltzmann model”. In: *Phys. Rev. E* 63 (6 2001), p. 066702. DOI: [10.1103/PhysRevE.63.066702](https://doi.org/10.1103/PhysRevE.63.066702). URL: <https://link.aps.org/doi/10.1103/PhysRevE.63.066702>.
- [41] D. d’Humières, P. Lallemand, and U. Frisch. “Lattice Gas Models for 3D Hydrodynamics”. In: *EPL (Europhysics Letters)* 2.4 (1986), p. 291. URL: <http://stacks.iop.org/0295-5075/2/i=4/a=006>.
- [42] D. d’Humières et al. “Multiple relaxation time lattice Boltzmann models in three dimensions”. In: *Philosophical Transactions of the Royal Society of London. Series A: Mathematical, Physical and Engineering Sciences* 360.1792 (2002), pp. 437–451. DOI: [10.1098/rsta.2001.0955](https://doi.org/10.1098/rsta.2001.0955). URL: <https://royalsocietypublishing.org/doi/abs/10.1098/rsta.2001.0955>.
- [43] Hang Ding and Peter D. M. Spelt. “Wetting condition in diffuse interface simulations of contact line motion”. In: *Phys. Rev. E* 75 (4 2007), p. 046708. DOI: [10.1103/PhysRevE.75.046708](https://doi.org/10.1103/PhysRevE.75.046708). URL: <https://link.aps.org/doi/10.1103/PhysRevE.75.046708>.
- [44] Herbert Edelsbrunner, David Letscher, and Afra Zomorodian. “Topological Persistence and Simplification”. In: *Discrete & Computational Geometry* 28.4 (2002), pp. 511–533. ISSN: 1432-0444. DOI: [10.1007/s00454-002-2885-2](https://doi.org/10.1007/s00454-002-2885-2). URL: <https://doi.org/10.1007/s00454-002-2885-2>.
- [45] Robert P Ewing and Brian Berkowitz. “Stochastic pore-scale growth models of DNAPL migration in porous media”. In: *Advances in Water Resources* 24.3 (2001). Pore Scale Modeling, pp. 309–323. ISSN: 0309-1708. DOI: [https://doi.org/10.1016/S0309-1708\(00\)00059-2](https://doi.org/10.1016/S0309-1708(00)00059-2). URL: <http://www.sciencedirect.com/science/article/pii/S0309170800000592>.

- [46] U. Frisch, B. Hasslacher, and Y. Pomeau. “Lattice-Gas Automata for the Navier-Stokes Equation”. In: *Phys. Rev. Lett.* 56 (14 1986), pp. 1505–1508. DOI: [10.1103/PhysRevLett.56.1505](https://link.aps.org/doi/10.1103/PhysRevLett.56.1505). URL: <https://link.aps.org/doi/10.1103/PhysRevLett.56.1505>.
- [47] Irina Ginzburg and D. d’Humières. “Multireflection boundary conditions for lattice Boltzmann models”. In: *Phys. Rev. E* 68 (6 2003), p. 066614. DOI: [10.1103/PhysRevE.68.066614](https://link.aps.org/doi/10.1103/PhysRevE.68.066614). URL: <https://link.aps.org/doi/10.1103/PhysRevE.68.066614>.
- [48] Harold Grad. “On the kinetic theory of rarefied gases”. In: *Communications on Pure and Applied Mathematics* 2.4 (1949), pp. 331–407. DOI: [10.1002/cpa.3160020403](https://onlinelibrary.wiley.com/doi/abs/10.1002/cpa.3160020403). URL: <https://onlinelibrary.wiley.com/doi/abs/10.1002/cpa.3160020403>.
- [49] Sybren Ruurds de Groot and P. Mazur. *Non-Equilibrium Thermodynamics*. New York, NY: Dover, Jan. 1984, 867p. ISBN: 0-486-64741-2.
- [50] Daryl Grunau, Shiyi Chen, and Kenneth Eggert. “A lattice Boltzmann model for multiphase fluid flows”. In: *Physics of Fluids A: Fluid Dynamics* 5.10 (1993), pp. 2557–2562. DOI: [10.1063/1.858769](http://dx.doi.org/10.1063/1.858769). URL: <http://dx.doi.org/10.1063/1.858769>.
- [51] Denis Gueyffier et al. “Volume-of-Fluid Interface Tracking with Smoothed Surface Stress Methods for Three-Dimensional Flows”. In: *Journal of Computational Physics* 152.2 (1999), pp. 423–456. ISSN: 0021-9991. DOI: <http://dx.doi.org/10.1006/jcph.1998.6168>. URL: <http://www.sciencedirect.com/science/article/pii/S002199919896168X>.
- [52] Andrew K. Gunstensen et al. “Lattice Boltzmann model of immiscible fluids”. In: *Phys. Rev. A* 43 (8 1991), pp. 4320–4327. DOI: [10.1103/PhysRevA.43.4320](https://link.aps.org/doi/10.1103/PhysRevA.43.4320). URL: <https://link.aps.org/doi/10.1103/PhysRevA.43.4320>.
- [53] Zhaoli Guo and Chang Shu. *Lattice Boltzmann Method and Its Applications in Engineering*. WORLD SCIENTIFIC, 2013. DOI: [10.1142/8806](https://www.worldscientific.com/doi/abs/10.1142/8806). URL: <https://www.worldscientific.com/doi/abs/10.1142/8806>.
- [54] Zhaoli Guo, Chuguang Zheng, and Baochang Shi. “Discrete lattice effects on the forcing term in the lattice Boltzmann method”. In: *Phys. Rev. E* 65 (4 2002), p. 046308. DOI: [10.1103/PhysRevE.65.046308](https://link.aps.org/doi/10.1103/PhysRevE.65.046308). URL: <https://link.aps.org/doi/10.1103/PhysRevE.65.046308>.
- [55] J. Habich et al. “Performance analysis and optimization strategies for a D3Q19 lattice Boltzmann kernel on nVIDIA GPUs using CUDA”. In: *Advances in Engineering Software* 42.5 (2011), pp. 266–272. ISSN: 0965-9978. DOI: <http://doi.org/10.1016/j.advengsoft.2010.10.007>. URL: <http://www.sciencedirect.com/science/article/pii/S0965997810001274>.

- [56] William B. Haines. “Studies in the physical properties of soil. V. The hysteresis effect in capillary properties, and the modes of moisture distribution associated therewith”. In: *The Journal of Agricultural Science* 20.1 (1930), 97–116. DOI: [10.1017/S002185960008864X](https://doi.org/10.1017/S002185960008864X).
- [57] I. Halliday, A. P. Hollis, and C. M. Care. “Lattice Boltzmann algorithm for continuum multicomponent flow”. In: *Phys. Rev. E* 76 (2 2007), p. 026708. DOI: [10.1103/PhysRevE.76.026708](https://doi.org/10.1103/PhysRevE.76.026708). URL: <https://link.aps.org/doi/10.1103/PhysRevE.76.026708>.
- [58] I. Halliday et al. “Interfacial micro-currents in continuum-scale multi-component lattice Boltzmann equation hydrodynamics”. In: *Computer Physics Communications* 219 (2017), pp. 286–296. ISSN: 0010-4655. DOI: <https://doi.org/10.1016/j.cpc.2017.06.005>. URL: <http://www.sciencedirect.com/science/article/pii/S001046551730187X>.
- [59] Stuart Harris. *An introduction to the theory of the Boltzmann equation*. Mineola, NY : Dover, 2004. ISBN: 0-486-43831-7.
- [60] Jens Harting et al. “Large-scale lattice Boltzmann simulations of complex fluids: advances through the advent of computational Grids”. In: *Philosophical Transactions of the Royal Society of London A: Mathematical, Physical and Engineering Sciences* 363.1833 (2005), pp. 1895–1915. ISSN: 1364-503X. DOI: [10.1098/rsta.2005.1618](https://doi.org/10.1098/rsta.2005.1618). URL: <http://rsta.royalsocietypublishing.org/content/363/1833/1895>.
- [61] Xiaoyi He and Li-Shi Luo. “Theory of the lattice Boltzmann method: From the Boltzmann equation to the lattice Boltzmann equation”. In: *Phys. Rev. E* 56 (6 1997), pp. 6811–6817. DOI: [10.1103/PhysRevE.56.6811](https://doi.org/10.1103/PhysRevE.56.6811). URL: <https://link.aps.org/doi/10.1103/PhysRevE.56.6811>.
- [62] M. Hecht and J. Harting. “Implementation of on-site velocity boundary conditions for D3Q19 lattice Boltzmann simulations”. In: *Journal of Statistical Mechanics: Theory and Experiment* 1 (2010), p. 01018. DOI: [10.1088/1742-5468/2010/01/P01018](https://doi.org/10.1088/1742-5468/2010/01/P01018).
- [63] Johan Olav Helland et al. “Footprints of spontaneous fluid redistribution on capillary pressure in porous rock”. In: *Geophysical Research Letters* 44.10 (2017), pp. 4933–4943. DOI: [10.1002/2017GL073442](https://doi.org/10.1002/2017GL073442). URL: <https://agupubs.onlinelibrary.wiley.com/doi/abs/10.1002/2017GL073442>.
- [64] A. L. Herring, V. Robins, and A. P. Sheppard. “Topological Persistence for Relating Microstructure and Capillary Fluid Trapping in Sandstones”. In: *Water Resources Research* 55.1 (2019), pp. 555–573. DOI: [10.1029/2018WR022780](https://doi.org/10.1029/2018WR022780). URL: <https://agupubs.onlinelibrary.wiley.com/doi/abs/10.1029/2018WR022780>.

- [65] A.L. Herring et al. “Observations of nonwetting phase snap-off during drainage”. In: *Advances in Water Resources* 121 (2018), pp. 32–43. ISSN: 0309-1708. DOI: <https://doi.org/10.1016/j.advwatres.2018.07.016>. URL: <http://www.sciencedirect.com/science/article/pii/S0309170818302793>.
- [66] Anna L. Herring et al. “Effect of fluid topology on residual nonwetting phase trapping: Implications for geologic CO₂ sequestration”. In: *Advances in Water Resources* 62 (2013), pp. 47–58. ISSN: 0309-1708. DOI: <https://doi.org/10.1016/j.advwatres.2013.09.015>. URL: <http://www.sciencedirect.com/science/article/pii/S0309170813001760>.
- [67] Anna L. Herring et al. “Flow rate impacts on capillary pressure and interface curvature of connected and disconnected fluid phases during multiphase flow in sandstone”. In: *Advances in Water Resources* 107 (2017), pp. 460–469. ISSN: 0309-1708. DOI: <http://dx.doi.org/10.1016/j.advwatres.2017.05.011>. URL: <http://www.sciencedirect.com/science/article/pii/S0309170816307011>.
- [68] A. P. Hollis, I. Halliday, and R. Law. “Kinematic condition for multicomponent lattice Boltzmann simulation”. In: *Phys. Rev. E* 76 (2 2007), p. 026709. DOI: <https://link.aps.org/doi/10.1103/PhysRevE.76.026709>. URL: <https://link.aps.org/doi/10.1103/PhysRevE.76.026709>.
- [69] Shuling Hou et al. “Evaluation of Two Lattice Boltzmann Models for Multiphase Flows”. In: *Journal of Computational Physics* 138.2 (1997), pp. 695–713. ISSN: 0021-9991. DOI: <http://dx.doi.org/10.1006/jcph.1997.5839>. URL: <http://www.sciencedirect.com/science/article/pii/S0021999197958393>.
- [70] Shuling Hou et al. “Simulation of Cavity Flow by the Lattice Boltzmann Method”. In: *J. Comput. Phys.* 118.2 (May 1995), pp. 329–347. ISSN: 0021-9991. DOI: [10.1006/jcph.1995.1103](http://dx.doi.org/10.1006/jcph.1995.1103). URL: <http://dx.doi.org/10.1006/jcph.1995.1103>.
- [71] Haibo Huang and Xi-yun Lu. “Relative permeabilities and coupling effects in steady-state gas-liquid flow in porous media: A lattice Boltzmann study”. In: *Physics of Fluids* 21.9 (2009), p. 092104. DOI: [10.1063/1.3225144](https://doi.org/10.1063/1.3225144). URL: <https://doi.org/10.1063/1.3225144>.
- [72] Haibo Huang, Michael C. Sukop, and Xi-Yun Lu. *Multiphase Lattice Boltzmann Methods: Theory and Application*. John Wiley & Sons, Ltd, 2015. ISBN: 9781118971444. DOI: [10.1002/9781118971451](http://dx.doi.org/10.1002/9781118971451). URL: <http://dx.doi.org/10.1002/9781118971451>.
- [73] Haibo Huang, Lei Wang, and Xiyun Lu. “Evaluation of three lattice Boltzmann models for multiphase flows in porous media”. In: *Computers & Mathematics with Applications* 61.12 (2011), pp. 3606–3617. ISSN: 0898-1221. DOI: <http://>

- doi.org/10.1016/j.camwa.2010.06.034. URL: <http://www.sciencedirect.com/science/article/pii/S0898122110004487>.
- [74] Haibo Huang et al. “Proposed approximation for contact angles in Shan-and-Chen-type multicomponent multiphase lattice Boltzmann models”. In: *Phys. Rev. E* 76 (6 2007), p. 066701. DOI: [10.1103/PhysRevE.76.066701](https://doi.org/10.1103/PhysRevE.76.066701). URL: <https://link.aps.org/doi/10.1103/PhysRevE.76.066701>.
- [75] Kerson Huang. *Statistical Mechanics*. 2nd Edition. New York: John Wiley & Sons, 1987.
- [76] Zu-Qia Huang and E-Jiang Ding. *Transport Theory*. Simplified Chinese. Second Edition. Beijing : China Science Publishing and Media, 2008. ISBN: 978-7-03-020772-2.
- [77] Jacob N. Israelachvili. *Intermolecular and Surface Forces*. Third Edition. San Diego: Academic Press, 2011, p. 520. ISBN: 978-0-12-375182-9. DOI: <https://doi.org/10.1016/B978-0-12-375182-9.10026-0>. URL: <http://www.sciencedirect.com/science/article/pii/B9780123751829100260>.
- [78] David Jacqmin. “Calculation of Two-Phase Navier-Stokes Flows Using Phase-Field Modeling”. In: *Journal of Computational Physics* 155.1 (1999), pp. 96–127. ISSN: 0021-9991. DOI: <http://dx.doi.org/10.1006/jcph.1999.6332>. URL: <http://www.sciencedirect.com/science/article/pii/S0021999199963325>.
- [79] David Jacqmin. “Contact-line dynamics of a diffuse fluid interface”. In: *Journal of Fluid Mechanics* 402 (2000), 57–88. DOI: [10.1017/S0022112099006874](https://doi.org/10.1017/S0022112099006874).
- [80] Fabian Jansen and Jens Harting. “From bijels to Pickering emulsions: A lattice Boltzmann study”. In: *Phys. Rev. E* 83 (4 2011), p. 046707. DOI: [10.1103/PhysRevE.83.046707](https://doi.org/10.1103/PhysRevE.83.046707). URL: <https://link.aps.org/doi/10.1103/PhysRevE.83.046707>.
- [81] M. Januszewski and M. Kostur. “Sailfish: A flexible multi-GPU implementation of the lattice Boltzmann method”. In: *Computer Physics Communications* 185.9 (2014), pp. 2350–2368. ISSN: 0010-4655. DOI: <https://doi.org/10.1016/j.cpc.2014.04.018>. URL: <http://www.sciencedirect.com/science/article/pii/S0010465514001520>.
- [82] Eric Jones, Travis Oliphant, Pearu Peterson, et al. *SciPy: Open source scientific tools for Python*. [Online; accessed 2017-03-25]. 2001. URL: <http://www.scipy.org/>.
- [83] D. Kandhai et al. “Lattice-Boltzmann hydrodynamics on parallel systems”. In: *Computer Physics Communications* 111.1 (1998), pp. 14–26. ISSN: 0010-4655. DOI: [http://dx.doi.org/10.1016/S0010-4655\(98\)00025-3](http://dx.doi.org/10.1016/S0010-4655(98)00025-3). URL: <http://www.sciencedirect.com/science/article/pii/S0010465598000253>.
- [84] Mehran Kardar. *Statistical Physics of Particles*. Cambridge University Press, 2007. DOI: [10.1017/CB09780511815898](https://doi.org/10.1017/CB09780511815898).

- [85] V. V. Khatavkar, P. D. Anderson, and H. E. H. Meijer. “Capillary spreading of a droplet in the partially wetting regime using a diffuse-interface model”. In: *Journal of Fluid Mechanics* 572 (2007), 367–387. DOI: [10.1017/S0022112006003533](https://doi.org/10.1017/S0022112006003533).
- [86] Mark A Knackstedt, Adrian P Sheppard, and Muhammad Sahimi. “Pore network modelling of two-phase flow in porous rock: the effect of correlated heterogeneity”. In: *Advances in Water Resources* 24.3 - 4 (2001), pp. 257–277. ISSN: 0309-1708. DOI: [http://doi.org/10.1016/S0309-1708\(00\)00057-9](http://doi.org/10.1016/S0309-1708(00)00057-9). URL: <http://www.sciencedirect.com/science/article/pii/S0309170800000579>.
- [87] M. Krafczyk et al. “Analysis of 3D transient blood flow passing through an artificial aortic valve by Lattice-Boltzmann methods”. In: *Journal of Biomechanics* 31.5 (1998), pp. 453–462. ISSN: 0021-9290. DOI: [https://doi.org/10.1016/S0021-9290\(98\)00036-0](https://doi.org/10.1016/S0021-9290(98)00036-0). URL: <http://www.sciencedirect.com/science/article/pii/S0021929098000360>.
- [88] A. Kuzmin and A.A. Mohamad. “Multirange multi-relaxation time Shan-Chen model with extended equilibrium”. In: *Computers & Mathematics with Applications* 59.7 (2010). Mesoscopic Methods in Engineering and Science, pp. 2260–2270. ISSN: 0898-1221. DOI: <https://doi.org/10.1016/j.camwa.2009.08.042>. URL: <http://www.sciencedirect.com/science/article/pii/S0898122109006300>.
- [89] Pierre Lallemand and Li-Shi Luo. “Theory of the lattice Boltzmann method: Dispersion, dissipation, isotropy, Galilean invariance, and stability”. In: *Phys. Rev. E* 61 (6 2000), pp. 6546–6562. DOI: [10.1103/PhysRevE.61.6546](https://doi.org/10.1103/PhysRevE.61.6546). URL: <https://link.aps.org/doi/10.1103/PhysRevE.61.6546>.
- [90] Jonas Latt et al. “Straight velocity boundaries in the lattice Boltzmann method”. In: *Phys. Rev. E* 77 (5 2008), p. 056703. DOI: [10.1103/PhysRevE.77.056703](https://doi.org/10.1103/PhysRevE.77.056703). URL: <https://link.aps.org/doi/10.1103/PhysRevE.77.056703>.
- [91] M. Latva-Kokko and Daniel H. Rothman. “Diffusion properties of gradient-based lattice Boltzmann models of immiscible fluids”. In: *Phys. Rev. E* 71 (5 2005), p. 056702. DOI: [10.1103/PhysRevE.71.056702](https://doi.org/10.1103/PhysRevE.71.056702). URL: <https://link.aps.org/doi/10.1103/PhysRevE.71.056702>.
- [92] M. Latva-Kokko and Daniel H. Rothman. “Scaling of Dynamic Contact Angles in a Lattice-Boltzmann Model”. In: *Phys. Rev. Lett.* 98 (25 2007), p. 254503. DOI: [10.1103/PhysRevLett.98.254503](https://doi.org/10.1103/PhysRevLett.98.254503). URL: <https://link.aps.org/doi/10.1103/PhysRevLett.98.254503>.
- [93] M. Latva-Kokko and Daniel H. Rothman. “Static contact angle in lattice Boltzmann models of immiscible fluids”. In: *Phys. Rev. E* 72 (4 2005), p. 046701. DOI: [10.1103/PhysRevE.72.046701](https://doi.org/10.1103/PhysRevE.72.046701). URL: <https://link.aps.org/doi/10.1103/PhysRevE.72.046701>.

- [94] Sébastien Leclaire et al. “Generalized three-dimensional lattice Boltzmann color-gradient method for immiscible two-phase pore-scale imbibition and drainage in porous media”. In: *Phys. Rev. E* 95 (3 2017), p. 033306. DOI: [10.1103/PhysRevE.95.033306](https://doi.org/10.1103/PhysRevE.95.033306). URL: <https://link.aps.org/doi/10.1103/PhysRevE.95.033306>.
- [95] Sébastien Leclaire et al. “Modeling of static contact angles with curved boundaries using a multiphase lattice Boltzmann method with variable density and viscosity ratios”. In: *International Journal for Numerical Methods in Fluids* 82.8 (2016). fld.4226, pp. 451–470. ISSN: 1097-0363. DOI: [10.1002/fld.4226](https://doi.org/10.1002/fld.4226). URL: <http://dx.doi.org/10.1002/fld.4226>.
- [96] Taehun Lee and Paul F. Fischer. “Eliminating parasitic currents in the lattice Boltzmann equation method for nonideal gases”. In: *Phys. Rev. E* 74 (4 2006), p. 046709. DOI: [10.1103/PhysRevE.74.046709](https://doi.org/10.1103/PhysRevE.74.046709). URL: <https://link.aps.org/doi/10.1103/PhysRevE.74.046709>.
- [97] Taehun Lee and Ching-Long Lin. “A Characteristic Galerkin Method for Discrete Boltzmann Equation”. In: *Journal of Computational Physics* 171.1 (2001), pp. 336 –356. ISSN: 0021-9991. DOI: <https://doi.org/10.1006/jcph.2001.6791>. URL: <http://www.sciencedirect.com/science/article/pii/S0021999101967919>.
- [98] Taehun Lee and Lin Liu. “Lattice Boltzmann simulations of micron-scale drop impact on dry surfaces”. In: *Journal of Computational Physics* 229.20 (2010), pp. 8045 –8063. ISSN: 0021-9991. DOI: <https://doi.org/10.1016/j.jcp.2010.07.007>. URL: <http://www.sciencedirect.com/science/article/pii/S0021999110003761>.
- [99] Roland Lenormand, Eric Touboul, and Cesar Zarcone. “Numerical models and experiments on immiscible displacements in porous media”. In: *Journal of Fluid Mechanics* 189 (1988), 165–187. DOI: [10.1017/S0022112088000953](https://doi.org/10.1017/S0022112088000953).
- [100] Huina Li, Chongxun Pan, and Cass T. Miller. “Pore-scale investigation of viscous coupling effects for two-phase flow in porous media”. In: *Phys. Rev. E* 72 (2 2005), p. 026705. DOI: [10.1103/PhysRevE.72.026705](https://doi.org/10.1103/PhysRevE.72.026705). URL: <https://link.aps.org/doi/10.1103/PhysRevE.72.026705>.
- [101] Qing Li, P. Zhou, and H. J. Yan. “Pinning–Depinning Mechanism of the Contact Line during Evaporation on Chemically Patterned Surfaces: A Lattice Boltzmann Study”. In: *Langmuir* 32.37 (2016). PMID: 27579557, pp. 9389–9396. DOI: [10.1021/acs.langmuir.6b01490](https://doi.org/10.1021/acs.langmuir.6b01490). URL: <https://doi.org/10.1021/acs.langmuir.6b01490>.
- [102] Hong Liang et al. “Lattice Boltzmann method for contact-line motion of binary fluids with high density ratio”. In: *Phys. Rev. E* 99 (6 2019), p. 063306. DOI: [10.1103/PhysRevE.99.063306](https://doi.org/10.1103/PhysRevE.99.063306). URL: <https://link.aps.org/doi/10.1103/PhysRevE.99.063306>.

- [103] S. V. Lishchuk, C. M. Care, and I. Halliday. “Lattice Boltzmann algorithm for surface tension with greatly reduced microcurrents”. In: *Phys. Rev. E* 67 (3 2003), p. 036701. DOI: [10.1103/PhysRevE.67.036701](https://doi.org/10.1103/PhysRevE.67.036701). URL: <https://link.aps.org/doi/10.1103/PhysRevE.67.036701>.
- [104] Haihu Liu, Albert J. Valocchi, and Qinjun Kang. “Three-dimensional lattice Boltzmann model for immiscible two-phase flow simulations”. In: *Phys. Rev. E* 85 (4 2012), p. 046309. DOI: [10.1103/PhysRevE.85.046309](https://doi.org/10.1103/PhysRevE.85.046309). URL: <https://link.aps.org/doi/10.1103/PhysRevE.85.046309>.
- [105] Haihu Liu and Yonghao Zhang. “Modelling thermocapillary migration of a microfluidic droplet on a solid surface”. In: *Journal of Computational Physics* 280 (2015), pp. 37–53. ISSN: 0021-9991. DOI: <https://doi.org/10.1016/j.jcp.2014.09.015>. URL: <http://www.sciencedirect.com/science/article/pii/S0021999114006512>.
- [106] Haihu Liu, Yonghao Zhang, and Albert J. Valocchi. “Lattice Boltzmann simulation of immiscible fluid displacement in porous media: Homogeneous versus heterogeneous pore network”. In: *Physics of Fluids* 27.5 (2015), p. 052103. DOI: [10.1063/1.4921611](https://doi.org/10.1063/1.4921611). URL: <http://dx.doi.org/10.1063/1.4921611>.
- [107] Haihu Liu et al. “Lattice Boltzmann modeling of contact angle and its hysteresis in two-phase flow with large viscosity difference”. In: *Phys. Rev. E* 92 (3 2015), p. 033306. DOI: [10.1103/PhysRevE.92.033306](https://doi.org/10.1103/PhysRevE.92.033306). URL: <https://link.aps.org/doi/10.1103/PhysRevE.92.033306>.
- [108] Haihu Liu et al. “Lattice Boltzmann phase-field modeling of thermocapillary flows in a confined microchannel”. In: *Journal of Computational Physics* 256 (2014), pp. 334–356. ISSN: 0021-9991. DOI: <https://doi.org/10.1016/j.jcp.2013.08.054>. URL: <http://www.sciencedirect.com/science/article/pii/S0021999113005986>.
- [109] Haihu Liu et al. “Multiphase lattice Boltzmann simulations for porous media applications”. In: *Computational Geosciences* 20.4 (2016), pp. 777–805. ISSN: 1573-1499. DOI: [10.1007/s10596-015-9542-3](https://doi.org/10.1007/s10596-015-9542-3). URL: <http://dx.doi.org/10.1007/s10596-015-9542-3>.
- [110] Haihu Liu et al. “Pore-scale simulation of liquid CO₂ displacement of water using a two-phase lattice Boltzmann model”. In: *Advances in Water Resources* 73 (2014), pp. 144–158. ISSN: 0309-1708. DOI: [http://doi.org/10.1016/j.advwatres.2014.07.010](https://doi.org/10.1016/j.advwatres.2014.07.010). URL: <http://www.sciencedirect.com/science/article/pii/S030917081400150X>.
- [111] Qin Lou, Mo Yang, and Hongtao Xu. “Wetting Boundary Condition in an Improved Lattice Boltzmann Method for Nonideal Gases”. In: *Communications in Computational Physics* 23.4 (2018), pp. 1116–1130. ISSN: 1991-7120. DOI: <https://doi.org/10.4208/cicp.0A-2016-0211>. URL: http://global-sci.org/intro/article_detail/cicp/12629.html.

- [112] Goran Lovric et al. “A multi-purpose imaging endstation for high-resolution micrometer-scaled sub-second tomography”. In: *Physica Medica* 32.12 (2016), pp. 1771–1778. ISSN: 1120-1797. DOI: <https://doi.org/10.1016/j.ejmp.2016.08.012>. URL: <http://www.sciencedirect.com/science/article/pii/S1120179716308997>.
- [113] Nicos S. Martys and Hudong Chen. “Simulation of multicomponent fluids in complex three-dimensional geometries by the lattice Boltzmann method”. In: *Phys. Rev. E* 53 (1 1996), pp. 743–750. DOI: [10.1103/PhysRevE.53.743](https://link.aps.org/doi/10.1103/PhysRevE.53.743). URL: <https://link.aps.org/doi/10.1103/PhysRevE.53.743>.
- [114] J. E. McClure et al. “Tracking interface and common curve dynamics for two-fluid flow in porous media”. In: *Journal of Fluid Mechanics* 796 (2016), pp. 211–232. DOI: [10.1017/jfm.2016.212](https://doi.org/10.1017/jfm.2016.212).
- [115] James E. McClure. “Microscale modeling of fluid flow in porous medium systems”. PhD thesis. Chapel Hill, NC: University of North Carolina at Chapel Hill, Aug. 2011.
- [116] James E. McClure et al. “An Adaptive Volumetric Flux Boundary Condition for Lattice Boltzmann Methods”. In: *ArXiv e-prints*, arXiv:1806.10589 (June 2018), arXiv:1806.10589.
- [117] James E. McClure et al. “Geometric state function for two-fluid flow in porous media”. In: *Phys. Rev. Fluids* 3 (8 2018), p. 084306. DOI: [10.1103/PhysRevFluids.3.084306](https://link.aps.org/doi/10.1103/PhysRevFluids.3.084306). URL: <https://link.aps.org/doi/10.1103/PhysRevFluids.3.084306>.
- [118] J.E. McClure, J.F. Prins, and C.T. Miller. “A novel heterogeneous algorithm to simulate multiphase flow in porous media on multicore CPU-GPU systems”. In: *Computer Physics Communications* 185.7 (2014), pp. 1865–1874. ISSN: 0010-4655. DOI: <https://doi.org/10.1016/j.cpc.2014.03.012>. URL: <http://www.sciencedirect.com/science/article/pii/S0010465514000927>.
- [119] J.E. McClure et al. “Approximation of interfacial properties in multiphase porous medium systems”. In: *Advances in Water Resources* 30.3 (2007), pp. 354–365. ISSN: 0309-1708. DOI: <https://doi.org/10.1016/j.advwatres.2006.06.010>. URL: <http://www.sciencedirect.com/science/article/pii/S030917080600100X>.
- [120] K. R. Mecke and H. Wagner. “Euler characteristic and related measures for random geometric sets”. In: *Journal of Statistical Physics* 64.3 (1991), pp. 843–850. ISSN: 1572-9613. DOI: [10.1007/BF01048319](https://doi.org/10.1007/BF01048319). URL: <https://doi.org/10.1007/BF01048319>.
- [121] A. A. Mohamad. “The Boltzmann Equation”. In: *Lattice Boltzmann Method: Fundamentals and Engineering Applications with Computer Codes*. London: Springer London, 2011, pp. 15–24. ISBN: 978-0-85729-455-5. DOI: [10.1007/978-0-85729-455-5_2](https://doi.org/10.1007/978-0-85729-455-5_2). URL: https://doi.org/10.1007/978-0-85729-455-5_2.

- [122] Francesca Nannelli and Sauro Succi. “The lattice Boltzmann equation on irregular lattices”. In: *Journal of Statistical Physics* 68.3 (1992), pp. 401–407. ISSN: 1572-9613. DOI: [10.1007/BF01341755](https://doi.org/10.1007/BF01341755). URL: <https://doi.org/10.1007/BF01341755>.
- [123] R.R. Nourgaliev et al. “The lattice Boltzmann equation method: theoretical interpretation, numerics and implications”. In: *International Journal of Multiphase Flow* 29.1 (2003), pp. 117–169. ISSN: 0301-9322. DOI: [https://doi.org/10.1016/S0301-9322\(02\)00108-8](https://doi.org/10.1016/S0301-9322(02)00108-8). URL: <http://www.sciencedirect.com/science/article/pii/S0301932202001088>.
- [124] Christian Obrecht et al. “Scalable lattice Boltzmann solvers for CUDA GPU clusters”. In: *Parallel Computing* 39.6-7 (2013), pp. 259–270. ISSN: 0167-8191. DOI: <https://doi.org/10.1016/j.parco.2013.04.001>. URL: <http://www.sciencedirect.com/science/article/pii/S0167819113000458>.
- [125] Travis E. Oliphant. *Guide to NumPy*. 2nd. USA: CreateSpace Independent Publishing Platform, 2015. ISBN: 151730007X, 9781517300074.
- [126] Stanley Osher and Ronald Fedkiw. *Level set methods and dynamic implicit surfaces (Applied Mathematical Sciences)*. 2003rd ed. Vol. 153. Springer New York, 2003.
- [127] Stanley Osher and James A Sethian. “Fronts propagating with curvature-dependent speed: Algorithms based on Hamilton-Jacobi formulations”. In: *Journal of Computational Physics* 79.1 (1988), pp. 12–49. ISSN: 0021-9991. DOI: [http://dx.doi.org/10.1016/0021-9991\(88\)90002-2](http://dx.doi.org/10.1016/0021-9991(88)90002-2). URL: <http://www.sciencedirect.com/science/article/pii/0021999188900022>.
- [128] C. Pan, M. Hilpert, and C. T. Miller. “Lattice-Boltzmann simulation of two-phase flow in porous media”. In: *Water Resources Research* 40.1 (2004). W01501. ISSN: 1944-7973. DOI: [10.1029/2003WR002120](http://dx.doi.org/10.1029/2003WR002120). URL: <http://dx.doi.org/10.1029/2003WR002120>.
- [129] Chongxun Pan, Jan F. Prins, and Cass T. Miller. “A high-performance lattice Boltzmann implementation to model flow in porous media”. In: *Computer Physics Communications* 158.2 (2004), pp. 89–105. ISSN: 0010-4655. DOI: <https://doi.org/10.1016/j.cpc.2003.12.003>. URL: <http://www.sciencedirect.com/science/article/pii/S0010465504000049>.
- [130] A. Parmigiani et al. “Pore-scale mass and reactant transport in multiphase porous media flows”. In: *Journal of Fluid Mechanics* 686 (2011), pp. 40–76. DOI: [10.1017/jfm.2011.268](https://doi.org/10.1017/jfm.2011.268).
- [131] G. G. Pereira et al. “Pore-scale network model for drainage-dominated three-phase flow in porous media”. In: *Transport in Porous Media* 24.2 (1996), pp. 167–201. ISSN: 1573-1634. DOI: [10.1007/BF00139844](https://doi.org/10.1007/BF00139844). URL: <https://doi.org/10.1007/BF00139844>.

- [132] Gerald G. Pereira. “Grayscale lattice Boltzmann model for multiphase heterogeneous flow through porous media”. In: *Phys. Rev. E* 93 (6 2016), p. 063301. DOI: [10.1103/PhysRevE.93.063301](https://doi.org/10.1103/PhysRevE.93.063301). URL: <https://link.aps.org/doi/10.1103/PhysRevE.93.063301>.
- [133] James Edward Pilliod and Elbridge Gerry Puckett. “Second-order accurate volume-of-fluid algorithms for tracking material interfaces”. In: *Journal of Computational Physics* 199.2 (2004), pp. 465 –502. ISSN: 0021-9991. DOI: [http://doi.org/10.1016/j.jcp.2003.12.023](https://doi.org/10.1016/j.jcp.2003.12.023). URL: <http://www.sciencedirect.com/science/article/pii/S0021999104000920>.
- [134] T. Pohl et al. “Performance Evaluation of Parallel Large-Scale Lattice Boltzmann Applications on Three Supercomputing Architectures”. In: *Supercomputing, 2004. Proceedings of the ACM/IEEE SC2004 Conference*. 2004, pp. 21–21. DOI: [10.1109/SC.2004.37](https://doi.org/10.1109/SC.2004.37).
- [135] C. M. Pooley and K. Furtado. “Eliminating spurious velocities in the free-energy lattice Boltzmann method”. In: *Phys. Rev. E* 77 (4 2008), p. 046702. DOI: [10.1103/PhysRevE.77.046702](https://doi.org/10.1103/PhysRevE.77.046702). URL: <https://link.aps.org/doi/10.1103/PhysRevE.77.046702>.
- [136] Mark L. Porter, Marcel G. Schaap, and Dorthe Wildenschild. “Lattice-Boltzmann simulations of the capillary pressure-saturation-interfacial area relationship for porous media”. In: *Advances in Water Resources* 32.11 (2009), pp. 1632 –1640. ISSN: 0309-1708. DOI: [http://doi.org/10.1016/j.advwatres.2009.08.009](https://doi.org/10.1016/j.advwatres.2009.08.009). URL: <http://www.sciencedirect.com/science/article/pii/S0309170809001328>.
- [137] Mark L. Porter et al. “Multicomponent interparticle-potential lattice Boltzmann model for fluids with large viscosity ratios”. In: *Phys. Rev. E* 86 (3 2012), p. 036701. DOI: [10.1103/PhysRevE.86.036701](https://doi.org/10.1103/PhysRevE.86.036701). URL: <https://link.aps.org/doi/10.1103/PhysRevE.86.036701>.
- [138] H.M Princen. “Capillary phenomena in assemblies of parallel cylinders”. In: *Journal of Colloid and Interface Science* 30.3 (1969), pp. 359 –371. ISSN: 0021-9797. DOI: [http://dx.doi.org/10.1016/0021-9797\(69\)90403-2](https://dx.doi.org/10.1016/0021-9797(69)90403-2). URL: <http://www.sciencedirect.com/science/article/pii/0021979769904032>.
- [139] Masa Prodanovic and Steven L. Bryant. “A level set method for determining critical curvatures for drainage and imbibition”. In: *Journal of Colloid and Interface Science* 304.2 (2006), pp. 442 –458. ISSN: 0021-9797. DOI: <https://doi.org/10.1016/j.jcis.2006.08.048>. URL: <http://www.sciencedirect.com/science/article/pii/S0021979706007764>.
- [140] Y. H. Qian, D. d’Humières, and P. Lallemand. “Lattice BGK Models for Navier-Stokes Equation”. In: *EPL (Europhysics Letters)* 17.6 (1992), p. 479. URL: <http://stacks.iop.org/0295-5075/17/i=6/a=001>.

- [141] Thomas Ramstad, Pål-Eric Øren, and Stig Bakke. “Simulation of Two-Phase Flow in Reservoir Rocks Using a Lattice Boltzmann Method”. In: *SPE Journal* 15 (2010), pp. 917–927. ISSN: 04.
- [142] T Reis and T N Phillips. “Lattice Boltzmann model for simulating immiscible two-phase flows”. In: *Journal of Physics A: Mathematical and Theoretical* 40.14 (2007), pp. 4033–4053. DOI: [10.1088/1751-8113/40/14/018](https://doi.org/10.1088/1751-8113/40/14/018). URL: <https://doi.org/10.1088/1751-8113/40/14/018>.
- [143] Vanessa Robins. “Towards computing homology from approximations”. In: *Topology Proceedings* 24 (Jan. 1999), pp. 503–532.
- [144] Vanessa Robins et al. “Percolating length scales from topological persistence analysis of micro-CT images of porous materials”. In: *Water Resources Research* 52.1 (2015), pp. 315–329. DOI: [10.1002/2015WR017937](https://agupubs.onlinelibrary.wiley.com/doi/abs/10.1002/2015WR017937). URL: <https://agupubs.onlinelibrary.wiley.com/doi/abs/10.1002/2015WR017937>.
- [145] J.G. Roof. “Snap-Off of Oil Droplets in Water-Wet Pores”. In: *Society of Petroleum Engineers Journal* 10.1 (1970). DOI: [10.2118/2504-PA](https://doi.org/10.2118/2504-PA).
- [146] Daniel H. Rothman. “Cellular-automaton fluids: A model for flow in porous media”. In: *GEOPHYSICS* 53.4 (1988), pp. 509–518. DOI: [10.1190/1.1442482](https://doi.org/10.1190/1.1442482). URL: <http://dx.doi.org/10.1190/1.1442482>.
- [147] Daniel H. Rothman and Jeffrey M. Keller. “Immiscible cellular-automaton fluids”. In: *Journal of Statistical Physics* 52.3 (1988), pp. 1119–1127. ISSN: 1572-9613. DOI: [10.1007/BF01019743](https://doi.org/10.1007/BF01019743). URL: <http://dx.doi.org/10.1007/BF01019743>.
- [148] J. S. Rowlinson and B. Widom. *Molecular Theory of Capillarity*. Dover Publications, New York 2002, 1982.
- [149] M. Sbragaglia et al. “Generalized lattice Boltzmann method with multirange pseudopotential”. In: *Phys. Rev. E* 75 (2 2007), p. 026702. DOI: [10.1103/PhysRevE.75.026702](https://link.aps.org/doi/10.1103/PhysRevE.75.026702). URL: <https://link.aps.org/doi/10.1103/PhysRevE.75.026702>.
- [150] Marcel G. Schaap et al. “Comparison of pressure-saturation characteristics derived from computed tomography and lattice Boltzmann simulations”. In: *Water Resources Research* 43.12 (2007). W12S06. ISSN: 1944-7973. DOI: [10.1029/2006WR005730](https://doi.org/10.1029/2006WR005730). URL: <http://dx.doi.org/10.1029/2006WR005730>.
- [151] S. Schlüter et al. “Pore-scale displacement mechanisms as a source of hysteresis for two-phase flow in porous media”. In: *Water Resources Research* 52.3 (2016), pp. 2194–2205. DOI: [10.1002/2015WR018254](https://doi.org/10.1002/2015WR018254). URL: <https://agupubs.onlinelibrary.wiley.com/doi/abs/10.1002/2015WR018254>.
- [152] Xiaowen Shan. “Analysis and reduction of the spurious current in a class of multiphase lattice Boltzmann models”. In: *Phys. Rev. E* 73 (4 2006), p. 047701. DOI: [10.1103/PhysRevE.73.047701](https://doi.org/10.1103/PhysRevE.73.047701). URL: <https://link.aps.org/doi/10.1103/PhysRevE.73.047701>.

- [153] Xiaowen Shan, Xue-Feng Yuan, and Hudong Chen. “Kinetic theory representation of hydrodynamics: a way beyond the Navier–Stokes equation”. In: *Journal of Fluid Mechanics* 550 (2006), 413–441. DOI: [10.1017/S0022112005008153](https://doi.org/10.1017/S0022112005008153).
- [154] Adrian P. Sheppard, Robert M. Sok, and Holger Averdunk. “Techniques for image enhancement and segmentation of tomographic images of porous materials”. In: *Physica A: Statistical Mechanics and its Applications* 339.1 (2004). Proceedings of the International Conference New Materials and Complexity, pp. 145–151. ISSN: 0378-4371. DOI: <https://doi.org/10.1016/j.physa.2004.03.057>. URL: <http://www.sciencedirect.com/science/article/pii/S037843710400370X>.
- [155] Kamaljit Singh et al. “Capillary-Dominated Fluid Displacement in Porous Media”. In: *Annual Review of Fluid Mechanics* 51.1 (2019), pp. 429–449. DOI: [10.1146/annurev-fluid-010518-040342](https://doi.org/10.1146/annurev-fluid-010518-040342). URL: <https://doi.org/10.1146/annurev-fluid-010518-040342>.
- [156] Michael C. Sukop and Dani Or. “Lattice Boltzmann method for modeling liquid-vapor interface configurations in porous media”. In: *Water Resources Research* 40.1 (2004). W01509, n/a–n/a. ISSN: 1944-7973. DOI: [10.1029/2003WR002333](https://doi.org/10.1029/2003WR002333). URL: <http://dx.doi.org/10.1029/2003WR002333>.
- [157] Michael C. Sukop et al. “Distribution of multiphase fluids in porous media: Comparison between lattice Boltzmann modeling and micro-x-ray tomography”. In: *Phys. Rev. E* 77 (2 2008), p. 026710. DOI: [10.1103/PhysRevE.77.026710](https://doi.org/10.1103/PhysRevE.77.026710). URL: <https://link.aps.org/doi/10.1103/PhysRevE.77.026710>.
- [158] The CGAL Project. *CGAL User and Reference Manual*. 4.10. CGAL Editorial Board, 2017. URL: <http://doc.cgal.org/4.10/Manual/packages.html>.
- [159] Willson C. S. White C. D. Nyman S. Bhattacharya J. Thompson K. E. and A. H. Reed. “Application of a New Grain-Based Reconstruction Algorithm to Microtomography Images for Quantitative Characterization and Flow Modelings”. In: *Society of Petroleum Engineers Journal* (2005). DOI: [10.2118/95887-MS](https://doi.org/10.2118/95887-MS).
- [160] J. Tölke and M. Krafczyk. “TeraFLOP computing on a desktop PC with GPUs for 3D CFD”. In: *International Journal of Computational Fluid Dynamics* 22.7 (2008), pp. 443–456. DOI: [10.1080/10618560802238275](https://doi.org/10.1080/10618560802238275). URL: <http://dx.doi.org/10.1080/10618560802238275>.
- [161] Jonas Tölke. “Implementation of a Lattice Boltzmann kernel using the Compute Unified Device Architecture developed by nVIDIA”. In: *Computing and Visualization in Science* 13.1 (2008), p. 29. ISSN: 1433-0369. DOI: [10.1007/s00791-008-0120-2](https://doi.org/10.1007/s00791-008-0120-2). URL: <https://doi.org/10.1007/s00791-008-0120-2>.
- [162] Jonas Tölke, Sören Freudiger, and Manfred Krafczyk. “An adaptive scheme using hierarchical grids for lattice Boltzmann multi-phase flow simulations”. In: *Computers Fluids* 35.8 (2006). Proceedings of the First International Conference for Mesoscopic Methods in Engineering and Science, pp. 820–830.

- ISSN: 0045-7930. DOI: <https://doi.org/10.1016/j.compfluid.2005.08.010>. URL: <http://www.sciencedirect.com/science/article/pii/S0045793005001441>.
- [163] Jonas Tölke, Giuseppe De Prisco, and Yaoming Mu. “A lattice Boltzmann method for immiscible two-phase Stokes flow with a local collision operator”. In: *Computers Mathematics with Applications* 65.6 (2013). Mesoscopic Methods in Engineering and Science, pp. 864–881. ISSN: 0898-1221. DOI: <https://doi.org/10.1016/j.camwa.2012.05.018>. URL: <http://www.sciencedirect.com/science/article/pii/S0898122112004178>.
 - [164] Jonas Tölke et al. “Lattice Boltzmann simulations of binary fluid flow through porous media”. In: *Philosophical Transactions of the Royal Society of London A: Mathematical, Physical and Engineering Sciences* 360.1792 (2002), pp. 535–545. ISSN: 1364-503X. DOI: [10.1098/rsta.2001.0944](https://doi.org/10.1098/rsta.2001.0944). URL: <http://rsta.royalsocietypublishing.org/content/360/1792/535>.
 - [165] Takeshi Tsuji, Fei Jiang, and Kenneth T. Christensen. “Characterization of immiscible fluid displacement processes with various capillary numbers and viscosity ratios in 3D natural sandstone”. In: *Advances in Water Resources* 95 (2016). Pore scale modeling and experiments, pp. 3–15. ISSN: 0309-1708. DOI: <https://doi.org/10.1016/j.advwatres.2016.03.005>. URL: <http://www.sciencedirect.com/science/article/pii/S0309170816300550>.
 - [166] H.-J. Vogel et al. “Comparison of a Lattice-Boltzmann Model, a Full-Morphology Model, and a Pore Network Model for Determining Capillary Pressure–Saturation Relationships”. In: *Vadose Zone Journal* 4.2 (2005), pp. 380–388. DOI: [10.2136/vzj2004.0114](https://doi.org/10.2136/vzj2004.0114). URL: <http://vzj.geoscienceworld.org/content/4/2/380>.
 - [167] H.J. Vogel and A. Kretzschmar. “Topological characterization of pore space in soil - sample preparation and digital image-processing”. In: *Geoderma* 73.1 (1996), pp. 23–38. ISSN: 0016-7061. DOI: [https://doi.org/10.1016/0016-7061\(96\)00043-2](https://doi.org/10.1016/0016-7061(96)00043-2). URL: <http://www.sciencedirect.com/science/article/pii/0016706196000432>.
 - [168] Lei Wang, Hai-bo Huang, and Xi-Yun Lu. “Scheme for contact angle and its hysteresis in a multiphase lattice Boltzmann method”. In: *Phys. Rev. E* 87 (1 2013), p. 013301. DOI: [10.1103/PhysRevE.87.013301](https://doi.org/10.1103/PhysRevE.87.013301). URL: <https://link.aps.org/doi/10.1103/PhysRevE.87.013301>.
 - [169] Edward W. Washburn. “The Dynamics of Capillary Flow”. In: *Phys. Rev.* 17 (3 1921), pp. 273–283. DOI: [10.1103/PhysRev.17.273](https://doi.org/10.1103/PhysRev.17.273). URL: <https://link.aps.org/doi/10.1103/PhysRev.17.273>.
 - [170] H.S. Wiklund, S.B. Lindström, and T. Uesaka. “Boundary condition considerations in lattice Boltzmann formulations of wetting binary fluids”. In: *Computer Physics Communications* 182.10 (2011), pp. 2192–2200. ISSN: 0010-4655. DOI:

- <https://doi.org/10.1016/j.cpc.2011.05.019>. URL: <http://www.sciencedirect.com/science/article/pii/S0010465511002098>.
- [171] Dorte Wildenschild and Adrian P. Sheppard. “X-ray imaging and analysis techniques for quantifying pore-scale structure and processes in subsurface porous medium systems”. In: *Advances in Water Resources* 51 (2013). 35th Year Anniversary Issue, pp. 217–246. ISSN: 0309-1708. DOI: <https://doi.org/10.1016/j.advwatres.2012.07.018>. URL: <http://www.sciencedirect.com/science/article/pii/S0309170812002060>.
- [172] Dieter A. Wolf-Gladrow. *Lattice-Gas Cellular Automata and Lattice Boltzmann Models - An Introduction*. First Edition. Berlin: Springer, Berlinpp, 2000, p. 308. ISBN: 3-540-66973-6.
- [173] Stephen Wolfram. “Cellular automaton fluids 1: Basic theory”. In: *Journal of Statistical Physics* 45.3 (1986), pp. 471–526. ISSN: 1572-9613. DOI: [10.1007/BF01021083](https://doi.org/10.1007/BF01021083). URL: <http://dx.doi.org/10.1007/BF01021083>.
- [174] Zhiyuan Xu, Haihu Liu, and Albert J. Valocchi. “Lattice Boltzmann simulation of immiscible two-phase flow with capillary valve effect in porous media”. In: *Water Resources Research* 53.5 (2017), pp. 3770–3790. ISSN: 1944-7973. DOI: [10.1002/2017WR020373](https://doi.org/10.1002/2017WR020373). URL: <http://dx.doi.org/10.1002/2017WR020373>.
- [175] Jianhui Yang and Edo S. Boek. “A comparison study of multi-component Lattice Boltzmann models for flow in porous media applications”. In: *Computers & Mathematics with Applications* 65.6 (2013), pp. 882–890. ISSN: 0898-1221. DOI: [http://doi.org/10.1016/j.camwa.2012.11.022](https://doi.org/10.1016/j.camwa.2012.11.022). URL: <http://www.sciencedirect.com/science/article/pii/S0898122112006839>.
- [176] Yuan Yu et al. “Color-gradient lattice Boltzmann modeling of immiscible two-phase flows on partially wetting surfaces”. In: *Proceedings of the Institution of Mechanical Engineers, Part C: Journal of Mechanical Engineering Science* 232.3 (2018), pp. 416–430. DOI: [10.1177/0954406217749616](https://doi.org/10.1177/0954406217749616). URL: <https://doi.org/10.1177/0954406217749616>.
- [177] Peng Yuan and Laura Schaefer. “Equations of state in a lattice Boltzmann model”. In: *Physics of Fluids* 18.4 (2006), p. 042101. DOI: [10.1063/1.2187070](https://doi.org/10.1063/1.2187070). URL: <http://dx.doi.org/10.1063/1.2187070>.
- [178] Pengtao Yue et al. “A diffuse-interface method for simulating two-phase flows of complex fluids”. In: *Journal of Fluid Mechanics* 515 (2004), pp. 293–317. DOI: [10.1017/S0022112004000370](https://doi.org/10.1017/S0022112004000370).
- [179] Ioannis Zacharoudiou and Edo S. Boek. “Capillary filling and Haines jump dynamics using free energy Lattice Boltzmann simulations”. In: *Advances in Water Resources* 92 (2016), pp. 43–56. ISSN: 0309-1708. DOI: <https://doi.org/10.1016/j.advwatres.2016.03.013>. URL: <http://www.sciencedirect.com/science/article/pii/S030917081630077X>.

- [180] Ioannis Zacharoudiou, Edo S. Boek, and John Crawshaw. “The impact of drainage displacement patterns and Haines jumps on CO2 storage efficiency”. In: *Scientific Reports* 8 (1 2018), p. 15561. ISSN: 2045-2322. DOI: [10.1038/s41598-018-33502-y](https://doi.org/10.1038/s41598-018-33502-y). URL: <https://doi.org/10.1038/s41598-018-33502-y>.
- [181] Ioannis Zacharoudiou et al. “Pore-filling events in single junction micro-models with corresponding lattice Boltzmann simulations”. In: *Journal of Fluid Mechanics* 824 (2017), 550–573. DOI: [10.1017/jfm.2017.363](https://doi.org/10.1017/jfm.2017.363).
- [182] Changyong Zhang et al. “Influence of Viscous and Capillary Forces on Immiscible Fluid Displacement: Pore-Scale Experimental Study in a Water-Wet Micromodel Demonstrating Viscous and Capillary Fingering”. In: *Energy & Fuels* 25.8 (2011), pp. 3493–3505. DOI: [10.1021/ef101732k](https://doi.org/10.1021/ef101732k). URL: <https://doi.org/10.1021/ef101732k>.
- [183] Wenhuan Zhang, Baochang Shi, and Yihang Wang. “14-velocity and 18-velocity multiple-relaxation-time lattice Boltzmann models for three-dimensional incompressible flows”. In: *Computers & Mathematics with Applications* 69.9 (2015), pp. 997 –1019. ISSN: 0898-1221. DOI: <https://doi.org/10.1016/j.camwa.2015.03.001>. URL: <http://www.sciencedirect.com/science/article/pii/S0898122115000966>.